Investigation of capillary effects on the grain scale by means of *in situ* experiments, imaging and numerical simulations

Habilitation thesis
Hamburg University of Technology

written by

Dr.-Ing. Marius Milatz

from Henstedt-Ulzburg

2022

Mitglieder des Habilitationsausschusses:

Univ.-Prof. Dr.-Ing. Jürgen Grabe
Univ.-Prof. Dr.-Ing. habil. Dr. h. c. Stefan Heinrich
Univ.-Prof. Dr. rer. nat. habil. Patrick Huber
Univ.-Prof. Dr. Nima Shokri
Univ.-Prof. Dr.-Ing. Kay Smarsly

Gutachter der Habilitationsschrift:

1. Gutachter: Univ.-Prof. Dr. rer. nat. habil. Patrick Huber, TUHH
2. Gutachter: Univ.-Prof. Dr.-Ing. habil. Sascha Henke, HSU Hamburg
3. Gutachter: Univ.-Prof. Dr.-Ing. habil. Ivo Herle, TU Dresden
4. Gutachter: Prof. Dr. Gioacchino (Cino) Viggiani, Univ. Grenoble Alpes

Tag des Habilitationskolloqiums: 01.12.2022

Investigation of capillary effects on the grain scale by means of in situ experiments, imaging and numerical simulations

von

Marius Milatz

Herausgegeben von

J. Grabe

Technische Universität Hamburg
Institut für Geotechnik und Baubetrieb

Veröffentlichungen des Instituts für
Geotechnik und Baubetrieb

56

Herausgeber:

Univ.-Prof. Dr.-Ing. Jürgen Grabe
Technische Universität Hamburg
Institut für Geotechnik und Baubetrieb
Harburger Schloßstraße 36
D – 21079 Hamburg
e-mail: *grabe@tuhh.de*

ISBN-13: 978-3-936310-58-0 (Erstausgabe)

DOI: 10.15480/882.4803

Lizenz: CC BY-NC-SA 4.0

Druckerei:

Druckzentrum Neumünster GmbH
Rungestraße 4
24537 Neumünster

In derselben Reihe erschienen:

1. J. Grabe (Hrsg.), 2000: Verbrennungsrückstände. Tagungsband, ISBN 3-936310-00-9

2. J. Grabe (Hrsg.), 2001: Schaden- und Risikomanagement im Tiefbau. Tagungsband, ISBN 3-936310-01-7

3. J. Grabe, 2003. Bodenmechanik und Grundbau. ISBN 3-936310-03-3

4. J. Grabe (Hrsg.), 2003: Euronormen in der Geotechnik – Was ändert sich? Tagungsband, ISBN 3-936310-04-1

5. J. Grabe (Hrsg.), 2003: Bodenverdichtung, Experimente - Modellierung - Geräteentwicklung - Baustellenberichte - F+E-Bedarf. Tagungsband, ISBN 3-936310-05-X

6. M. Kelm, 2004: Nummerische Simulation der Verdichtung rolliger Böden mittels Vibrationswalzen. Dissertation, ISBN 3-936310-06-8

7. J. Grabe (Hrsg.), 2004: Kaimauern - Messungen und Numerik. Tagungsband, ISBN 3-936310-07-6

8. J. Stein, 2005. Experimentelle und numerische Untersuchungen zum Düsenstrahlverfahren. Dissertation, ISBN 3-936310-09-2

9. J. Grabe (Hrsg.), 2005: Grenzschicht Wasser und Boden - Phänomene und Ansätze. Tagungsband, ISBN 3-936310-10-6

10. J. Grabe (Hrsg.), 2005: FEM in der Geotechnik - Qualität, Prüfung, Fallbeispiele - Tagungsband, ISBN 3-936310-11-4

11. B. Mardfeldt, 2006: Zum Tragverhalten von Kaikonstruktionen im Gebrauchszustand. Dissertation, ISBN 3-936310-12-2

12. J. Grabe (Hrsg.), 2006: Optimierung in der Geotechnik - Strategien und Fallbeispiele. Tagungsband, ISBN-13: 978-3-936310-13-9

13. T. Bierer, 2007: Bodenschwingungen aus Straßenverkehr auf unebener Fahrbahn im Zeitbereich - experimentelle und theoretische Untersuchungen. Dissertation, ISBN-13: 978-3-936310-14-6

14. J. Grabe (Hrsg.), 2007: Bemessen mit Finite-Elemente-Methoden. Tagungsband, ISBN-13: 978-3-936310-15-3

15. K.-P. Mahutka, 2008: Zur Verdichtung von rolligen Böden infolge dynamischer Pfahleinbringung und durch Oberflächenrüttler. Dissertation, ISBN-13: 978-3-936310-16-0

16. J. Grabe (Hrsg.), 2008: Seehäfen für Containerschiffe zukünftiger Generationen. Tagungsband, ISBN-13: 978-3-936310-17-7

17. F. König, 2008: Zur zeitlichen Traglastentwicklung von Pfählen und der nachträglichen Erweiterung bestehender Pfahlgründungen. Dissertation, ISBN-13: 978-3-936310-18-4

18. S. Henke, 2008: Herstellungseinflüsse aus Pfahlrammung im Kaimauerbau. Dissertation, ISBN-13: 978-3-936310-19-1

19. J. Grabe (Hrsg.), 2009: Spundwände – Profile, Tragverhalten, Bemessung, Einbringung und Wiedergewinnung. Tagungsband, ISBN-13: 978-3-936310-20-7

20. J. Dührkop, 2009: Zum Einfluss von Aufweitungen und zyklischen Lasten auf das Verformungsverhalten lateral beanspruchter Pfähle in Sand. Dissertation, ISBN-13: 978-3-936310-21-4

21. O. Möller, 2009: Zum Langzeit-Kompressionsverhalten weicher organischer Sedimente. Dissertation, ISBN-13: 978-3-936310-22-1

22. J. Grabe (Hrsg.), 2011: Ports of container ships of future generations. Tagungsband, ISBN-13: 978-3-936310-23-8

23. S. Kinzler, 2011: Zur Parameteridentifikation, Entwurfs- und Strukturoptimierung in der Geotechnik mittels numerischer Verfahren. Dissertation, ISBN-13: 978-3-936310-24-5

24. G. Qiu, 2012: Coupled Eulerian Lagrangian Simulations of Selected Soil-Structure Problems. Dissertation, ISBN-13: 978-3-936310-25-2

25. X. Ma, 2013: Nutzung der oberflächennahen Geothermie mittels Energiepfählen und Erdwärmesonden. Dissertation, ISBN-13: 978-3-936310-26-9

26. J. Grabe (Hrsg.), 2013: Proceedings of the Conference on Maritime Energy COME 2013. Tagungsband, ISBN-13: 978-3-936310-28-3

27. J. Grabe (Hrsg.), 2013: Bemessen mit numerischen Methoden. Tagungsband, ISBN-13: 978-3-936310-29-0

28. T. Pucker, 2013: Stoffmodell zur Modellierung von stetigen Materialübergängen im Rahmen der Optimierung geotechnischer Strukturen. Dissertation, ISBN-13: 978-3-936310-30-6

29. S. Henke, 2013: Untersuchungen zur Pfropfenbildung infolge der Installation offener Profile in granularen Böden. Habilitation, ISBN-13: 978-3-936310-31-3

30. J. Grabe (Hrsg.), 2014: Ports for Container Ships of Future Generations. Tagungsband, ISBN-13: 978-3-936310-32-0

31. J. Grabe (Hrsg.), 2014: Offshore Basishäfen, Tagungsband, ISBN-13: 978-3-936310-33-7

32. C. Rudolph, 2015. Untersuchungen zur Drift von Pfählen unter zyklischer, lateraler Last aus veränderlicher Richtung, Dissertation, ISBN-13: 978-3-936310-34-4

33. J. Grabe (Hrsg.), 2015: Morphodynamics 2015, Tagungsband, ISBN-13: 978-3-936310-35-1

34. T. Hamann, 2015: Zur Modellierung wassergesättigter Böden unter dynamischer Belastung und großen Bodenverformungen am Beispiel der Pfahleinbringung, Dissertation, ISBN-13: 978-3-936310-36-8

35. B. Schümann, 2015: Beitrag zum dynamischen Dreiphasenmodell für Boden auf Basis der Finite-Elemente-Methode, Dissertation, ISBN-13: 978-3-936310-37-5

36. M. Milatz, 2015: Untersuchungen zum Einfluss der Kapillarität auf das hydraulisch-mechanische Verhalten von granularer Tragschichten für Verkehrswege, Dissertation, ISBN-13: 978-3-936310-38-2

37. H. Kaya, 2016: Bodenverschleppung und Spaltbildung infolge der Einbringung von Profilen in Dichtungsschichten aus Ton, Dissertation, ISBN-13: 978-3-936310-39-9

38. J. Grabe (Hrsg.), 2017: Proceedings of the Conference on Maritime Energy COME 2017. Tagungsband, ISBN-13: 978-3-936310-40-5

39. B. Kocak, 2017: Zur numerischen Modellierung von hydraulisch-mechanisch gekoppelten Prozessen in gesättigten granularen Böden mittels Smoothed Particle Hydrodynamics, Dissertation, ISBN-13: 978-3-936310-41-2

40. K. Siegl, 2017: Zur Pfahldynamik von gerammten Großrohrpfählen und der daraus resultierenden Wellenausbreitung in Wasser und im Meeresboden, Dissertation, ISBN-13: 978-3-936310-42-9

41. J. Grabe (Hrsg.), 2017: Numerical Methods in Geotechnics, Tagungsband, ISBN-13: 978-3-936310-43-6

42. J. Grabe (Hrsg.), 2018: Digitale Infrastruktur und Geotechnik (DIG 2018), Tagungsband, ISBN-13: 978-3-936310-44-3

43. D. Osthoff, 2018: Zur Ursache von Schlosssprengungen und zu einbringbedingten Lageabweichungen von Spundwänden, Dissertation, ISBN-13: 978-3-936310-45-0

44. E. Heins, 2018: Numerical based identification of the pile-soil interaction in terms of the axial pile bearing capacity, Dissertation, ISBN-13: 978-3-936310-46-7

45. K.-F. Seitz, 2021: Zur Topologieoptimierung von geotechnischen Strukturen und zur Tragfähigkeitssteigerung des Baugrunds durch Scherfugenverfestigung, Dissertation, ISBN-13: 978-3-936310-47-4

46. D. Plenker, 2021: Physical and numerical investigations of the dynamic interaction of saturated granulates and fluid, Dissertation, ISBN-13: 978-3-936310-48-1

47. J. Grabe, J.-O. Backhaus & P. Vogel, 2021: Bauprojektmanagement, ISBN-13: 978-3-936310-49-8

48. M. Kanitz, 2021: Experimental and numerical investigations of particle-fluid systems in geotechnical engineering, Dissertation, ISBN-13: 978-3-936310-50-4

49. J.-O. Backhaus, 2021: A methodology for the numeric time-cost forecast and pareto optimization of large injection projects in tunneling, Dissertation, ISBN-13: 978-3-936310-51-1

50. S. N. Sinduri, 2021: Optimisation of deep compaction as liquefaction mitigation measure, Dissertation, ISBN-13: 978-3-936310-52-8

51. J. Bubel, 2022: Zum Versagen von Unterwasserböschungen im Seegang, Dissertation, ISBN-13: 978-3-936310-53-5

52. J. Grabe (Hrsg.), 2022: Adaptive Structures At Shore, Tagungsband, ISBN-13: 978-3-936310-54-2

53. J. Grabe (Hrsg.), 2022: Numerische Methoden in der Geotechnik, Tagungsband, ISBN-13: 978-3-936310-55-9

54. J. Grabe (Hrsg.), 2022: Processes in natural and technical Particle-Fluid-Systems (PintPFS), Tagungsband, ISBN-13: 978-3-936310-56-6

55. T. Törzs, 2022: Zum hydraulisch-mechanisch gekoppelten Verhalten teilgesättigter granularer Geomaterialien infolge hydraulischer und mechanischer Beanspruchungen, Dissertation, ISBN-13: 978-3-936310-57-3

Vorwort des Herausgebers

Ich habe die Freude den Werdegang von Marius Milatz nun schon seit vielen Jahren zu begleiten. Zuerst als interessierter Student, dann als sehr befähigter Doktorand und seit ein paar Jahren als Postdoktorand. Seine Habilitationsschrift ist hervorragend geschrieben. Sie zeigt mit welchem ungezügelten Interesse und mit welcher Kreativität Marius Milatz sich in die komplexe Mechanik teilgesättigter Böden einarbeitet, neue Versuchstechniken und Methoden entwickelt, diese anwendet und interpretiert. Mit der Computertomografie gewinnt er dabei neue Einblicke in die Interaktion von Partikeln, Wasser und Luft und lässt uns daran in Wort und Schrift teilhaben. Sein Vortrag zur Habilitation und die anschließende Diskussion hat allen Zuhörern und insbesondere den Mitgliedern der Habilitationskommission große Freude bereitet.

Ich wünsche Marius Milatz weiterhin alles Gute. Ich bin sicher, dass noch eine große wissenschaftliche Karriere vor ihm liegt.

Hamburg, 22. Dezember 2022

Jürgen Grabe

Author's preface and acknowledgements

This habilitation thesis would certainly not exist without the appreciation, the encouragement, the scientific exchange, and discussions that I have experienced from many sides in the last years of my postdoctoral research.

First of all, I would like to acknowledge Hamburg University of Technology and the German Research Foundation (Deutsche Forschungsgemeinschaft, DFG) for funding my research in the framework of *DFG Research Training Group GRK 2462 "Processes in natural and technical Particle-Fluid-Systems" (PintPFS)*. In the creative environment of this interdisciplinary research training group, guided by my doctoral adviser Prof. Dr.-Ing. Jürgen Grabe to whom I am especially indebted for all the years of assistance and encouragement, I was given the opportunity to follow my research ideas, to improve my teaching skills, and to get in touch with the most interesting people from very different fields of research. Further thanks go to the other seven professors and all PhD students who constitute the research training group PintPFS at TUHH. Their support in the technical environment of their labs as well as their advice are gratefully acknowledged.

I would like to thank Prof. Dr. Gioacchino (Cino) Viggiani as well as Dr. Edward (Eddy) Andò for the great discussions, the warm reception, and assistance during the CT experiments at Laboratoire 3SR in Grenoble as well as during the writing of related publications. The visits to Grenoble and especially Eddy's help in setting up and running CT experiments as well as in using "Python magic" are very much acknowledged.

Further thanks on the field of scientific imaging go to Dr. Lukas Helfen and Dr. Alessandro Tengattini who assisted me during my research visit at the Institut Laue-Langevin (ILL) in Grenoble for a neutron CT experiment and to Dr. Felix Beckmann and Dr. Julian Philipp Moosmann from Helmholtz-Zentrum Hereon who supervised us during synchrotron-based CT experiments at Deutsches Elektronen-Synchrotron (DESY) in Hamburg.

Regarding the Lattice Boltzmann simulations, I would like to express my gratitude to Prof. Dr. Krishna Kumar, Dr. Reihaneh Hosseini, and Qiuyu (Amber) Wang at the department of Civil, Architectural and Environmental Engineering at The University of Texas at Austin. During our regular web-based meetings, you have taught me many insights into the LBM, its formulation, and generally, into C++ coding, and I will always remember the inspiring and cordial atmosphere during our interesting sessions.

At the Institute of Geotechnical Engineering and Construction Management, my home institute in Hamburg, I would furthermore like to thank our senior engineer Dr.-Ing. Hans Mathäus Stanford for the all-time sophisticated discussions on scientific questions much beyond the scope of my research and his encouraging words. Furthermore, I would like to thank my direct colleagues, *i. e.*, all PhD students, our secretary in the office, the team in the lab, our student assistants, and curious students.

Last but not least, my most cordial thanks are saved for my family, my girlfriend and my friends. You have given me the opportunity to follow and realise my dreams by always believing in me.

Hamburg, December 2022

Marius Milatz

Schlagwörter:

Teilgesättigte granulare Böden, Kapillareffekte, Partikelskala, *in situ*-Experimente, Einplatinencomputer, Bildgebung, Computertomografie (CT), numerische Simulationen

Keywords:

Unsaturated granular soils, capillary effects, grain scale, *in situ* experiments, single-board computers, imaging, computed tomography (CT), numerical simulations

Contents

1 Introduction **1**

1.1 Motivation 1

1.1.1 The beauty and relevance of capillarity in nature 3

1.1.2 Practical meaning of capillary effects 4

1.1.3 The charm of imaging experiments in solving open questions 5

1.2 Scope and outline of the thesis 8

2 Fundamentals and state of the art **9**

2.1 Fundamentals of capillarity 9

2.1.1 Capillarity as a physical principle 9

2.1.2 Capillary forces 13

2.2 Water retention behaviour of soils 16

2.2.1 Microscopic origins of water retention behaviour 16

2.2.2 Measurement of water retention behaviour 19

2.2.3 Modelling of water retention behaviour 20

2.3 Flow in a capillary system 21

2.3.1 Macroscopic approach to fluid flow in unsaturated soils 21

2.3.2 Microscopic approach to fluid flow in unsaturated soils 22

2.4 Hydro-mechanical behaviour of unsaturated soils 24

2.4.1 The quest for χ 24

2.4.2 Hydro-mechanical lab testing of unsaturated soils 26

2.5 Short introduction to imaging methods 27

2.5.1 Overview 27

2.5.2 Simple camera-based imaging experiments 28

2.5.3 Microscopy 29

2.5.4 Radiographic imaging methods 29

2.5.5 Computed tomography 32
2.5.6 Other imaging techniques 36
2.6 Numerical modelling and simulation of capillary effects in unsaturated soils 36
2.6.1 Continuum approach on the macroscopic scale 37
2.6.2 Discrete particle approach on the microscopic scale 38
2.6.3 Boltzmann's approach on the mesoscopic scale 39
2.6.4 Multiscale approaches 40

3 Characterisation of experimental materials 41
3.1 Materials used in the experiments 41
3.1.1 Hamburg Sand 41
3.1.2 Soda-lime glass beads 42
3.1.3 Water and air 43
3.2 Hydro-mechanical behaviour 46

4 Development of miniaturised testing devices for imaging experiments 49
4.1 Hard- and software for creating individual testing apparatuses 49
4.2 Miniaturised uniaxial compression apparatus 52
4.2.1 Field of application 52
4.2.2 Technical details 52
4.2.3 Specimen preparation 54
4.2.4 Selected results 54
4.3 Miniaturised flow cell apparatus for measurement of the WRC 57
4.3.1 Field of application 57
4.3.2 Technical details 58
4.3.3 Specimen preparation 58
4.3.4 Selected results 60
4.4 Miniaturised direct shear device 61
4.4.1 Field of application 61
4.4.2 Technical details 62
4.4.3 Specimen preparation 65
4.4.4 Selected results 65
4.5 Particle separation experiment 65
4.5.1 Field of application 65
4.5.2 Technical details 66
4.5.3 Specimen preparation 69
4.5.4 Selected results 69

5 *In situ* 4D experiments with full-field CT imaging 71

5.1 Principles of *in situ* CT experiments 71

5.2 4D uniaxial compression of unsaturated sand and glass bead specimens . . 73

5.2.1 Experimental set-up 74

5.2.2 Testing procedure 75

5.2.3 Evaluation of macroscopic hydro-mechanical behaviour 78

5.2.4 Evaluation and analysis of CT data 79

5.3 4D water retention experiments on sand and glass beads 85

5.3.1 Experimental set-up at Laboratoire 3SR 85

5.3.2 Experimental set-up at Institut Laue-Langevin 85

5.3.3 Testing procedure 87

5.3.4 Evaluation of macroscopic water retention behaviour 90

5.3.5 Evaluation and analysis of CT data 91

6 Microscopic insights into the behaviour of unsaturated granular media 97

6.1 Hydro-mechanical behaviour during uniaxial compression 97

6.1.1 Evolution of phase distributions and discrete water clusters 97

6.1.2 Evolution of interfacial areas 103

6.1.3 Discrete grain motion, strain fields, and coupling to pore saturation 104

6.1.4 Evolution of grain contacts 107

6.2 Capillary bridge mechanics 109

6.2.1 Monotonic straining of capillary bridges 109

6.2.2 Cyclic straining and compression of a capillary bridge 113

6.3 Water retention behaviour 117

6.3.1 Phase distributions during cyclic drainage and imbibition 117

6.3.2 Analysis of discrete fluid clusters 121

6.3.3 Analysis of interfacial areas and contact lines 124

6.3.4 Pore scale analysis of contact angles and radii of curvature 125

6.3.5 Discrete analysis of grain motion and pore-based hydraulic effects . 128

6.4 Links between microscopic and macroscopic soil behaviour 132

6.4.1 Water retention behaviour 132

6.4.2 Mechanical behaviour 133

7 Outlook on further applications of imaging experiments 137
7.1 Synchrotron-based CT imaging of direct shear tests . . . 137
7.2 Investigation of soil-structure interaction on the microscale . . . 141
7.3 Soil mechanical experiments with CT imaging . . . 141
7.4 Physical computing and its experimental applications in teaching . . . 142

8 On the way to a virtual soil lab for simulations on the grain scale 145
8.1 Introduction . . . 145
8.2 Generation of numerical models based on CT data . . . 146
8.2.1 Meshing study of a single grain of sand . . . 146
8.2.2 Pore scale meshes for CFD simulations . . . 147
8.3 Combined FDEM simulation of particle interaction . . . 148
8.3.1 Free fall study of a meshed sand grain . . . 148
8.3.2 Simulation of a sand column collapse . . . 148
8.4 Multiphase LBM simulation of capillary phenomena on the pore scale . . . 151
8.4.1 Capillary bridges and contact angles . . . 153
8.4.2 Water retention behaviour . . . 154
8.4.3 Comments on similarity between LBM model and physical "reality" 160

9 Summary and outlook 165
9.1 Summary of results . . . 165
9.1.1 *In situ* imaging experiments . . . 165
9.1.2 Hydraulic and mechanical behaviour of unsaturated soils . . . 166
9.2 Outlook, open questions, and work ahead . . . 170

Bibliography 173

Symbols and units 185

A List of abbreviations 191

B Further selected results 193
B.1 Deviatoric strain during uniaxial compression . . . 193
B.2 Volumetric strain during uniaxial compression . . . 195
B.3 Evolution of grain contacts during uniaxial compression . . . 197
B.4 Monotonic straining of capillary bridges . . . 200

B.5 Evolution of air phase during cyclic drainage and imbibition 202
B.6 Evolution of water phase during cyclic drainage and imbibition 203
B.7 Evolution of water and air clusters during cyclic drainage and imbibition . 204
B.8 Characterisation of air clusters by sphericity 206
B.9 Visualisation of discrete grain motion during primary drainage 207
B.10 Synchrotron-based CT imaging of direct shear test 209

C Multiphase Lattice Boltzmann Method **211**
C.1 Fundamentals of single-phase LBM 211
C.2 Extension to single-component multiphase LBM 214
C.3 Implementation of the single-component multiphase LBM 217

D Research data **219**

Chapter 1

Introduction

1.1 Motivation

Within the scope of my time as a postdoctoral researcher at Hamburg University of Technology (TUHH), I was given the opportunity to live my credo which is to follow a path of lifelong learning. As mentioned in the acknowledgements section, many people, far beyond my own university, have supported me and taught me interesting insights into the beautiful physical behaviour of granular media which will be the main topic of this habilitation thesis.

During my work as a PhD student, I started to develop an interest in research on the hydraulic and mechanical behaviour of unsaturated granular soils which I could fortunately extend in the later postdoc years. The unsaturated or partially saturated state represents a niche in soil mechanics—from the point of view of the practitioner as well as of the theoretical soil mechanics researcher—although most soils of the top soil layers encountered in nature exist in the unsaturated state. I have never fully understood the reason for this niche existence of unsaturated soil mechanics. One reason might be that the fundamental theories in soil mechanics have been developed for water saturated and dry states for which experiments and calculations could be done with less uncertainties in the past. I would not dare to declare that unsaturated soil mechanics is more complex than the classical soil mechanics field, but to my eyes, it is the more general approach to soil mechanics because unsaturated soils include nearly all states that natural soils, granular soils as well as cohesive soils, can be found to occupy between the dry, the unsaturated, and the fully saturated state. Also *gassy soils* with stable gas bubbles in the pore water can be grouped into the field of unsaturated soil mechanics. Furthermore, a topical intersection with *frozen soils* is given due to the mechanical interaction of frozen liquid bonds with soil grains.

It is this variety of research fields in the domain of unsaturated soil mechanics that has always fascinated me. Especially, the experimental investigation of the unsaturated soil behaviour includes many interesting aspects as special techniques need to be developed to reveal either small or hidden effects, *e. g.*, the small and fragile impact of capillary pressure in coarse granular soils. Therefore, in unsaturated soil mechanics, classical experimental

set-ups, such as the triaxial or direct shear test, have to be extended by consideration of special techniques for the measurement or control of matric suction or degree of saturation.

From the point of view of continuum mechanics, soil mechanical tests are typically considered to represent *element tests*, seeking to measure and describe the soil behaviour under the assumption of homogeneous stress and strain fields and, more generally, of homogeneous state variables and boundary conditions. Although this approach is totally suitable for practical needs with element tests representing an idealised model to arrive at solutions, a closer look at real experimental boundary conditions and at the grain scale of the soil fabric, describing geometrical properties of soil grain assemblies, as well as phase distributions in the unsaturated case leads to the question whether the soil specimen conditions are really as homogeneous as we assume them to be. It is this microscopic perspective on soils with special emphasis on capillary effects in the unsaturated state, studied on the grain or pore scale, that I will focus on in this habilitation thesis. With the help of non-destructive imaging techniques, originating from medical science and further developed for materials science, we can nowadays "look" into the microcosm of soils as a source of the macroscopic soil behaviour that we measure in our traditional experiments and that we homogenise in our continuum mechanics approaches. The key method here is computed tomography (CT), an imaging method for reconstruction of three-dimensional volumes of matter. This method can also be applied for the imaging of *in situ* experiments, *i. e.*, experiments performed *in situ* (in place) inside of a CT environment. Besides other much simpler, but also powerful, imaging methods, the *in situ* CT approach is followed in this thesis and is generally applied to study unsaturated granular soils. *In situ* CT experiments can be used for the collection of "4D data" (*i. e.*, 3D spatial and temporal information) during soil mechanical experiments in order to investigate the microscopic origin of the macroscopic soil behaviour, such as single particle motion as well as changes in the phase distribution.

Thinking again of the field of unsaturated soil mechanics, this thesis focuses on granular soils represented by the group of sands in nature whose particles are large enough to be sufficiently resolved by modern X-ray CT scanners and furthermore, where capillary effects result in the still visible "liquid morphologies" (Scheel *et al.*, 2008) that develop on the pore or grain scale, *e. g.*, in the fascinating shape of capillary bridges. In cohesive soils, which are not treated here, further more complex effects are present leading to a material behaviour that not only originates from capillarity, but also from chemical phenomena. Examples are the very high suction levels of several megapascals that can be encountered in cohesive soils as well as swelling and shrinkage effects.

With this in mind, this thesis is not to be seen as a complete work on unsaturated granular soil mechanics, but as the outcome of my postdoctoral research on the promising application of imaging techniques from materials science combined with *in situ* experiments using dedicated custom-built set-ups. An attempt will be made to characterise and outline the method of *in situ* imaging experiments for fundamental research on geomaterials, but also for practical geotechnical research based on different examples. With regard to unsaturated soils, a procedure to quantitatively describe and analyse their hydro-mechanical behaviour by means of *capillary state variables* that can be measured on the pore scale by imaging is proposed. The thesis is intended as motivation for other researchers to take on the track to answer further open and exciting questions on this field.

1.1.1 The beauty and relevance of capillarity in nature

In nature, capillarity leads to the formation of droplets and bubbles of beautiful shapes in which the human eye can frequently rejoice. More important still for essential needs of life, capillary structures, such as water droplets, represent the water supply for plants and animals as shown in Figure 1.1, whereas air bubbles act as air supply. The latter is known from the life of the water spider, a diving arachnid that is able to breathe under water from an air bubble adhering to its abdomen. Evolution has also led to the development of specialised hydrophobic leaf surfaces being repulsive to water droplets. This is known as the "lotus effect", applied in industry for hydrophobic material surfaces.



Figure 1.1: Insects in between nearly spherical water droplets on a plant leaf with hydrophobic surface properties at Raakmoor, a swampy nature reserve in Hamburg

Capillarity is highly interwoven with the development of geometric structures of fluid phases in contact with the solid phase. The quantitative measurement of these geometries, such as the shape properties of a droplet or capillary bridge, always minimising their surface (energies), in a pore or in between sand grains is the key to analyse and understand the acting of surface tension.

Furthermore, capillarity leads to capillary rise of water in capillary tubes of plants, but

also in the maze-like pore space of soils. This causes the rise of groundwater above the phreatic line, creating the unsaturated vadose zone where the pore space of the soil is partially filled with air and water. This changes the soil's permeability for water and air flow as well as its shear strength and stiffness as compared to the water saturated or dry state. These capillary effects of water rise can be described by simple mathematical relations under idealised conditions, such as in the well-known model of a glass capillary tube described later on in this thesis, which, however, become more complex and need to be addressed by empirical laws when formulated for real soil conditions.

Due to the maximum pressure difference (maximum vacuum/suction or underpressure) of one atmosphere or one bar on Earth, the maximum capillary rise is theoretically limited to a negative water head of *ca.* 10 m (approximately −100 kPa of underpressure). At this suction level, air bubbles would start to nucleate and stop the water rise in pore channels, *e. g.*, in trees. Nevertheless, higher growing plants are able to supply their topmost regions with water which is still not fully understood. The reason here is believed to exist in a strong (actually measured) tension in the plant sap (Debenedetti, 1997) and in additional transpiration suction caused by evaporation of water from the plant leaves (Tötzke, 2009). As an example, this combined pumping effect allows the coastal redwood trees *Sequoia sempervirens* to transport water from the roots to their treetops in heights of frequently more than 80 m above the ground as impressively pictured in Figure 1.2. This "capillary pump" represents a fascinating invention of nature, but it also makes clear, how strongly life depends on water and what disturbances of a safe water supply would mean.

1.1.2 Practical meaning of capillary effects

Regarding practical problems from the field of soil mechanics, geotechnical engineering, but also from other disciplines of engineering, capillary effects in unsaturated soils and other materials play a similarly significant role.

From the point of view of construction industry, capillary rise in soils, foundations, and masonry can lead to wet cellar walls and related building physics problems, such as mould infestation and increased heat transfer. Furthermore, rising moisture can lead to different other forms of structural damage, *e. g.*, due to frost weathering.

In unsaturated soils, the reduced permeability at low degrees of saturation strongly influences the ground water flow which can be applied technically in capillary barriers, *e. g.*, for sealings of waste disposal sites. Besides this, knowledge of unsaturated flow is important for the understanding of contaminant or solute transport. Regarding mechanical effects, capillary cohesion leads to a shear strength reserve of earthen structures, such as dikes and embankments, historical loam buildings, *e. g.*, parts of the Chinese Wall, and sand sculptures. Besides the reinforcing effects due to plant roots, capillary cohesion, also known as "apparent cohesion", is responsible for an increase of the stability of slopes. Due to heavy rain events, the apparent cohesion vanishes which can lead to catastrophic slope failures and landslides. Under the threat of climate change and the increasing chaotic weather phenomena, especially slope failures and the protection against rising water levels by means of dikes represent related future challenges in geotechnical and hydraulic engineering.

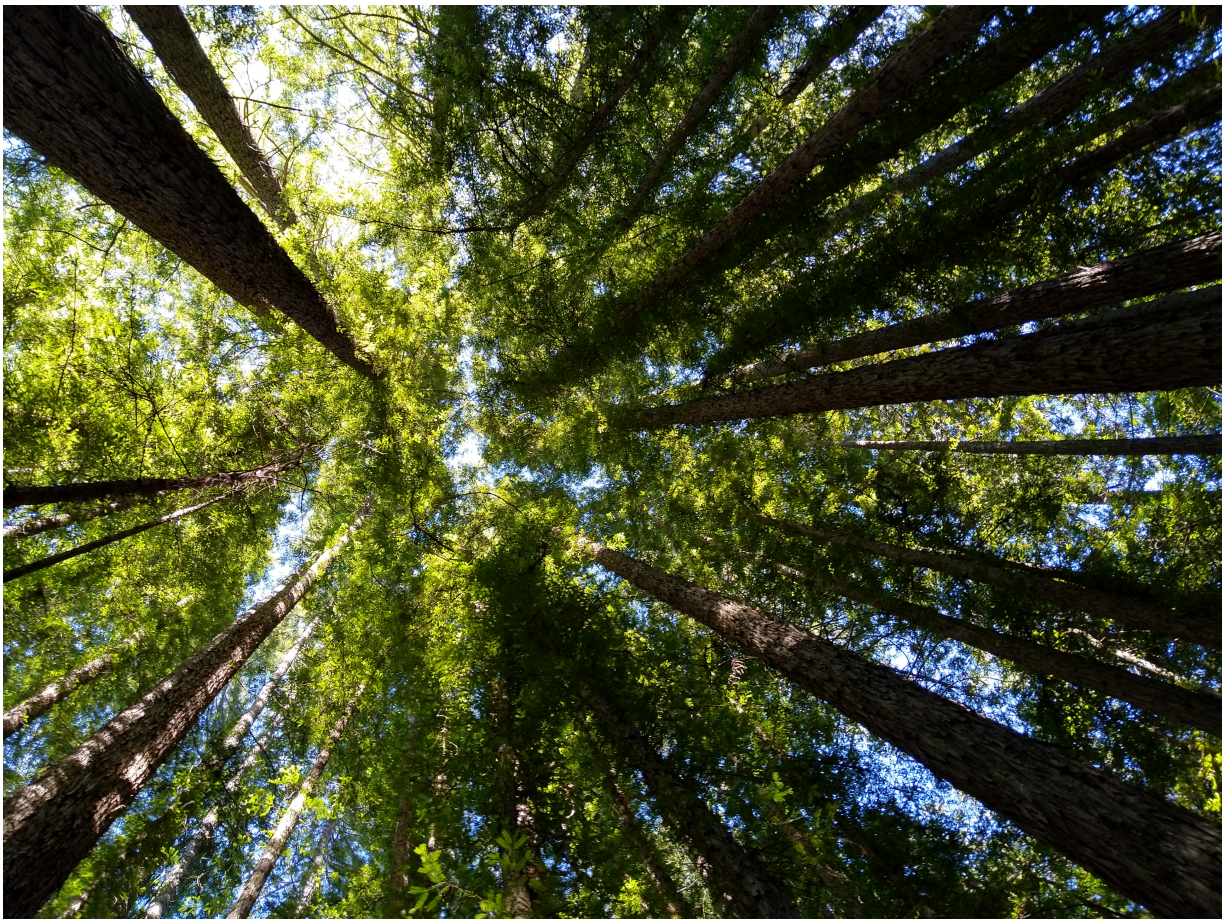


Figure 1.2: A view into the green treetops of various coastal redwood (mammoth) trees *Sequoia sempervirens* at Muir Woods National Monument, California, USA. Due to combined capillary rise and evaporation, liquid water under strong tension even reaches the tips of this highest tree species on Earth

Another technical meaning of capillary effects is given by their influence on clogging soils which result in many problems in mechanised tunneling. The influence of different water contents and of suction on soil adhering to technical structures, such as the cutting wheel and excavation tools of tunnel boring machines, is still not fully understood.

In the field of process engineering, many technical applications and production methods are based on capillary effects. Examples are given by moist aggregation or agglomeration processes where capillary pressure and liquid bridges create adhering granulates and where wettability, *i. e.*, a liquid's ability to wet a solid surface, dictates the coating of particles or surfaces with either hydrophilic or hydrophobic properties.

1.1.3 The charm of imaging experiments in solving open questions

Imaging experiments represent a non-destructive method to record quantitative information for the investigation of different physical processes. In the field of soil mechanics and

geotechnical engineering, this includes the mechanical response of soils in loading tests or their hydraulic behaviour during interaction with different fluids, *e. g.*, in flow experiments.

As we will see in the main chapters of this thesis, imaging experiments can be run in 2D or 3D imaging mode with different spatial and temporal resolutions to resolve and measure different grain or pore scale properties. As an example, the capillary bridge in Figure 1.3 can be studied by means of 2D imaging in order to characterise the hydro-mechanical interaction of water with moving particles and the involved capillary forces.

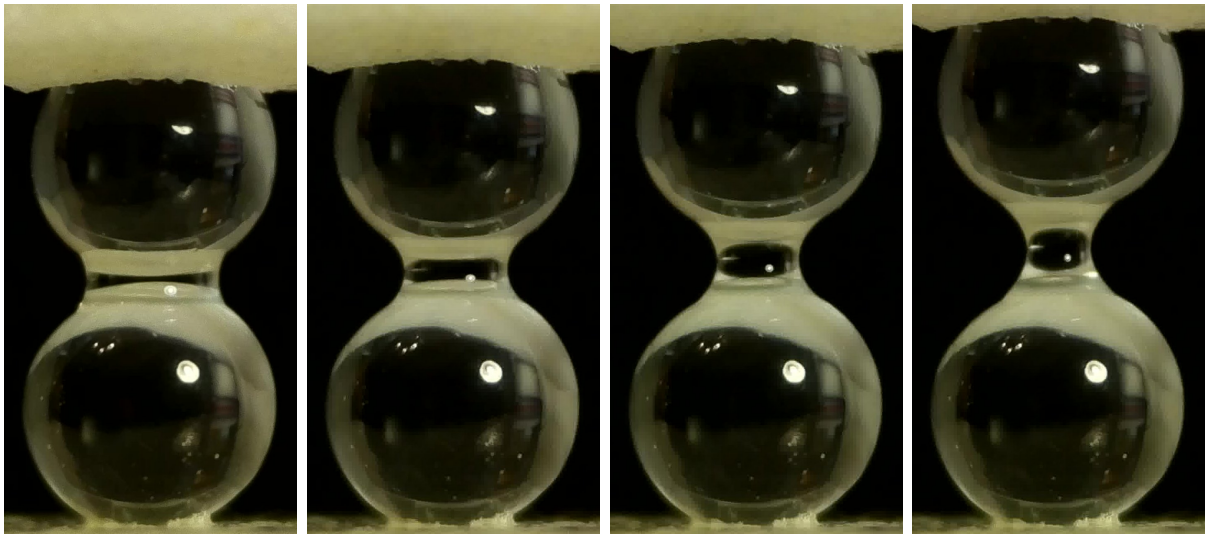


Figure 1.3: Straining experiment of a capillary bridge in between two glass beads with a diameter $d \approx 2$ mm

By means of 3D imaging methods with sensitivity to different phases, deeper insights into the phase distribution inside measurement volumes can be obtained. Figure 1.4 shows the reconstructed phase distributions from CT scans of unsaturated columns of sand and glass beads with individual water clusters highlighted in different colours.

With the help of suitable imaging experiments, very different processes in soils as multi-phase materials can be investigated. Furthermore, the acquisition of a time series of images makes it possible to study changes in microscopic properties, such as particle contacts or the phase distribution, and to relate them to the macroscopic mechanical or hydraulic boundary conditions, *e. g.*, caused by mechanical loading or fluid flow.

The acquired image data can be analysed systematically in order to answer research questions concerning the relationship between microscopic and macroscopic behaviour or concerning the hydro-mechanical coupling in soils, such as the influence of partial saturation on stiffness, shear strength, and volume change. Finally, image data can also act as input for numerical simulations on the grain or pore scale. Therefore, imaging techniques and the corresponding methods of analysis represent important tools for soil mechanical or geotechnical research to improve our understanding of physical processes and our methods for their numerical simulation.

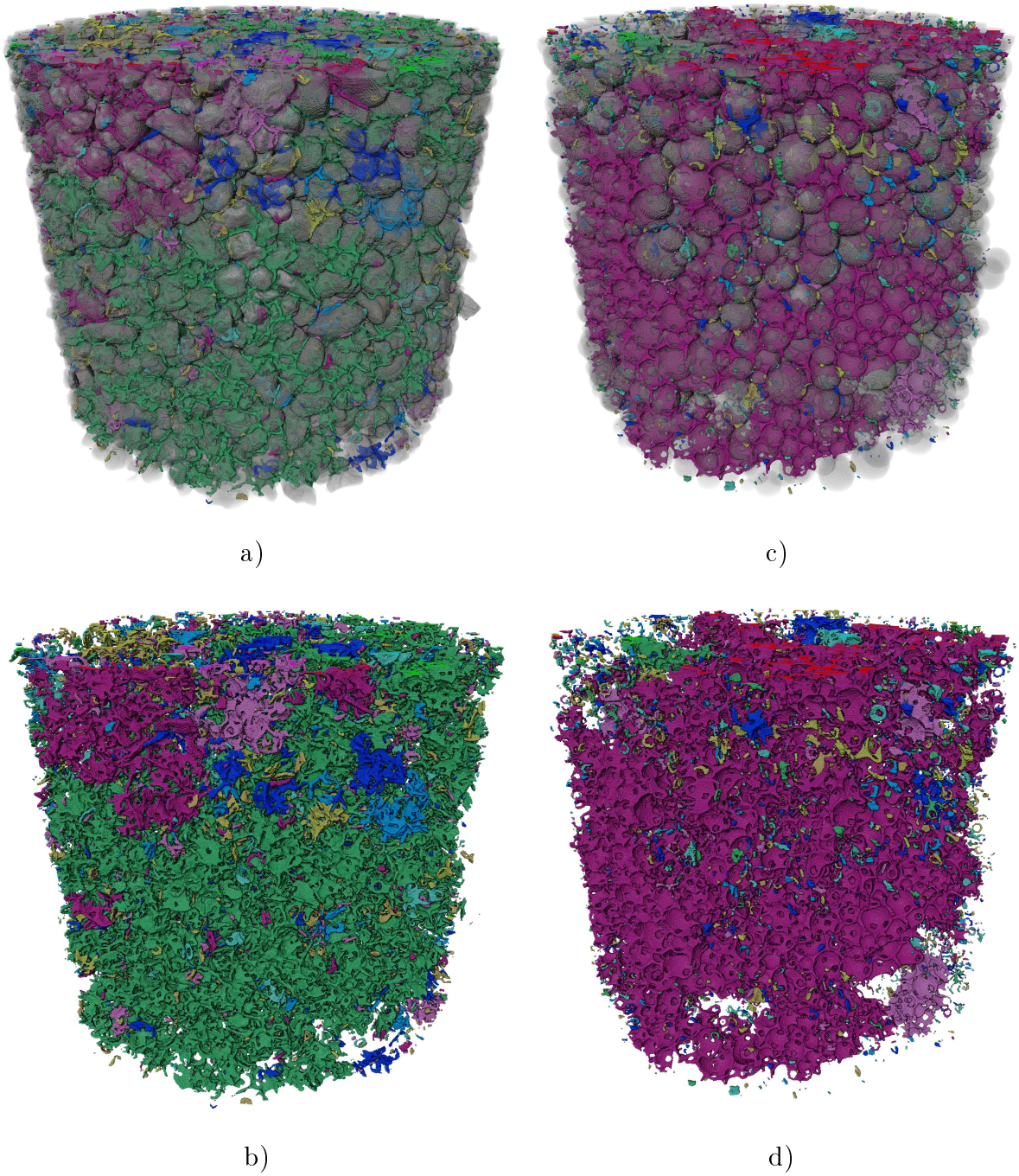


Figure 1.4: Reconstructed 3D CT data of free-standing unsaturated sand and glass bead columns. Independent connected water clusters are labelled and distinguished by different colours. Solid phase made opaque. a) Sand and water, b) water clusters without sand, c) glass beads and water, d) water clusters without glass beads

1.2 Scope and outline of the thesis

State-of-the-art non-destructive imaging techniques, such as computed tomography, allow the spatially and temporally highly resolved imaging of physical processes. Within the scope of this thesis, the benefits of such imaging methods are combined with custom-built miniaturised experiments for *in situ* testing, resulting in "*in situ* imaging experiments" in order to measure and analyse the hydraulic and mechanical soil behaviour on the grain or pore scale. This work mainly focuses on the capillary effects in unsaturated granular soils and on their investigation by means of hydraulic or mechanical experimental set-ups. Capillary effects can be quantitatively described and incorporated into models using different *capillary state variables*, as we name them here, which are measured by means of CT. The granular soils are represented by sand and glass beads. Beyond this focus, further applications of *in situ* CT experiments for research as well as teaching in different fields of soil mechanics and geotechnical engineering will be outlined. In order to bridge the gap between experiments and numerical simulations, an outlook on the application of image data for direct numerical simulation of the mechanical and hydraulic behaviour of granular materials is given.

This habilitation thesis is structured as follows: After this introduction, Chapter 2 gives an overview on fundamentals of capillarity and unsaturated soil mechanics as well as imaging experiments. In the related sections of this chapter, many advantages of imaging experiments compared to traditional experiments will be shown. In Chapter 3, the different materials investigated in the experiments will be briefly presented along with the most important material properties. The following Chapters 4 and 5 are dedicated to the development of custom-built miniaturised soil mechanical testing devices for *in situ* imaging experiments as well as to their application in CT environments. Besides information about the technical design of the set-ups, selected experimental results are given. In the core Chapter 6, microscopic insights into the soil behaviour on the grain or pore scale as derived from the available data are showcased and discussed in order to answer the guiding research questions behind every experiment. Chapter 7 gives an outlook on further applications of imaging experiments with the aim to illustrate what is or what can be possible in other current projects and in future research. Furthermore, Chapter 8 gives insights into numerical work seeking to establish a link between experiments and numerical modelling of the unsaturated soil behaviour. As so much local and temporal information can be drawn from *in situ* CT experiments, the application of the collected data as input for so-called "virtual soil labs" is proposed. This allows the direct simulation of soil mechanical problems based on digitised or virtual soils which is important in research, teaching, and engineering practice. Therefore, Chapter 8 illustrates and discusses numerical applications for simulations on the grain or pore scale including the Finite-Discrete Element Method and the Multiphase Lattice Boltzmann Method. The thesis closes with a summary of results and an outlook in Chapter 9 where open research questions as a starting point for further scientific work will be given. Further selected results, theoretical details on the applied Multiphase Lattice Boltzmann Method as well as information about access to open research data related to this thesis are given in the Appendix.

Chapter 2

Fundamentals and state of the art

2.1 Fundamentals of capillarity

2.1.1 Capillarity as a physical principle

Granular soils, such as sands, characterise a large part of the Earth's surface in many countries. Therefore, they represent an important natural building ground and material in geotechnical engineering. Due to the availability of water in the porous system of surface-near soils, originating from ground water flow or precipitation, a large portion of natural soils is generally "unsaturated" or partially saturated, *i. e.*, neither fully dry, nor water saturated.

Due to the physical principle of capillarity, pore water is imbibed into the porous system of a soil and retained against gravity, forming a three-phase system consisting of the solid grain skeleton, *i. e.*, the porous matrix, the liquid phase (water) and the gaseous phase (air). In physics, liquids and gases are typically referred to as fluids.

In a natural capillary system, on which we focus here, water forms the so-called wetting phase, while air represents the nonwetting phase. The wetting properties of a liquid or gas depend on their contact angle with regard to a contacting surface or some other phase. If the contact angle is less than 90 degrees, a fluid is called wetting. If the contact angle is larger or equal, the fluid is nonwetting, with the fluid surface being repelled by the contacting surface. Figure 2.1 shows a water droplet on a solid surface in ambient air.

Under equilibrium of the different interfacial tensions γ_{12}, γ_{23}, and γ_{13}, a droplet with a wetting contact angle $\theta < 90°$ forms on the surface. The interfacial tensions originate from the intermolecular forces, which are different between the liquid and the solid, where the forces are either adhesive or repulsive, and inside the liquid, where cohesion attracts liquid molecules. Also interfacial tension inside the air-water interface originates from a balance of intermolecular forces which lead to a resulting tensile force at the interface where the resultant intermolecular attraction is not zero. According to Blunt (2017), "interfacial tension" is the more general term as compared to the term "surface tension" which is frequently used for γ. Strictly speaking, the term "surface tension" is reserved

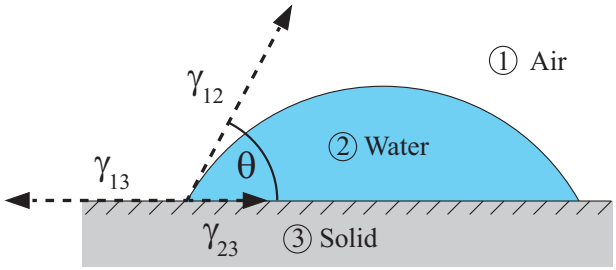


Figure 2.1: Water droplet in ambient air on a solid surface

to the interfacial tension between a liquid and its vapour in thermodynamic equilibrium. Furthermore, the liquid and its vapour should be chemically pure according to this definition of surface tension, *i. e.*, no other chemical compounds should be present. Keeping this differentiation in mind, in this work, we will apply both terms, interfacial tension and surface tension. The latter term will be frequently applied if we idealise the components to be pure and in thermodynamic equilibrium (which might not necessarily be the case for soils containing different minerals in the thermodynamically non-controlled environment of our experiments).

Contact angles $\theta > 90°$ can be found under natural conditions, *e. g.*, if a soil has become hydrophobic by biological influence (Karatza *et al.*, 2020), or in the case of the "lotus effect", *e. g.*, caused by hydrophobic surfaces of plant leaves, as depicted in Figure 1.1 in Chapter 1. Similar hydrophobic surfaces copied from natural conditions are used in many technical applications, where high contact angles can be achieved by surface treatment, such as the application of coatings.

As water and air are generally immiscible if excessive evaporation or boiling are neglected, capillary menisci form at the interface of air and water, with the water wetting the grain surfaces in a specific contact angle. Depending on the water content of the soil, the air phase in the porous system is either forming a closed front, especially around air entry when water is driven out of the pores, or forming a fully connected system of air ganglia during further water drainage. Furthermore, the air phase can become isolated in the form of air clusters or bubbles during imbibition when water re-enters the pores. When the pore space is mainly filled with connected air clusters, the pore water forms so-called capillary bridges connecting single grains and transferring capillary forces on the microscopic level. These forces originate from the interfacial tension γ inside the air-water interfacial area of the menisci, also known as "contractile skin" (Fredlund and Rahardjo, 1993), and represent a contribution to effective stress transferred through the grain skeleton in the unsaturated state.

On a macroscopic level, the capillary forces acting inside the interfaces of two immiscible fluids in a porous medium lead to capillary rise of pore water above the ground water table. In this hydraulic domain, pore water pressure is negative and equal to the capillary pressure that can be derived from the capillary rise. This capillary pressure p_c is also called soil suction, or more concrete, matric suction s, if only the portion caused by capillarity within the porous soil matrix is considered (Fredlund and Rahardjo, 1993). Therefore,

matric suction is the relevant suction contribution in granular soils, whereas in cohesive soils also osmotic suction contributes to total suction. Matric suction is then given as the difference of the pore air pressure u_a and pore water pressure u_w inside the soil, yielding

$$s = u_a - u_w \quad . \tag{2.1}$$

Following the soil mechanical sign convention, fluid pressures bear a positive mathematical sign. If the pore air pressure is equal to atmospheric pressure, which is set to zero as a reference pressure, matric suction is equal to negative pore water pressure.

The link between macroscopic pore water and pore air pressure or capillary pressure and microscopic surface tension and capillary forces inside a single capillary of radius r is derived from the Young-Laplace equation[1] as follows.

$$p_c = u_a - u_w = \frac{2\gamma \cos\theta}{r} \tag{2.2}$$

The equation results from vertical force equilibrium of the water meniscus in a capillary tube, as shown in Figure 2.2. Here, θ is the contact angle between wetting fluid and solid surface, *i. e.*, the surface of the capillary tube. The capillary pressure p_c represents the pressure difference of pore air pressure u_a and pore water pressure u_w on both sides of the capillary membrane, which represents a minimal surface.

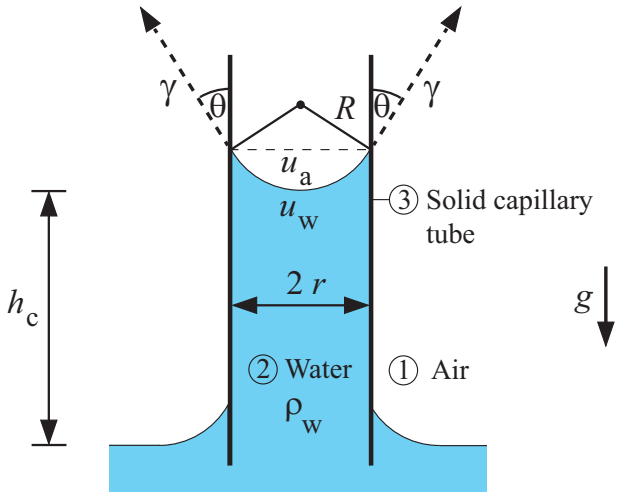


Figure 2.2: Capillary rise in a capillary tube placed in a water reservoir

In an environment with gravity, the resulting force from capillary pressure or matric suction, lifting a water column in a capillary tube, must correspond to the weight of the hanging water and the height of the capillary rise h_c, so that the equilibrium liquid rise in the tube can be calculated as

$$h_c = \frac{2\gamma \cos\theta}{\rho_w g r} \quad , \tag{2.3}$$

[1] Named after the British polymath Thomas Young (1773–1829) and the French scholar and polymath Pierre-Simon Laplace (1749–1827).

where ρ_w is the density of water and g is gravitational acceleration.

It is clearly visible that the capillary rise h_c increases with decreasing capillary radius r, which is the reason for higher capillary fringes above the ground water table in fine grained soils, *e. g.*, silts and clays, compared to coarse grained soils, such as sands, where the capillary rise reaches heights of only a few decimetres.

It must be noted that capillary action also works without gravity, *e. g.*, in space. This can be explained by the molecular origin of capillarity. A liquid surrounded by gas and in contact with a solid surface moves and deforms around the contact line of the three present phases until equilibrium between the adhesive forces at the contact line and the cohesive forces in the liquid volume acting on the liquid molecules is reached. Under the given circumstances, a minimal interfacial surface is formed. This also leads to capillary menisci as well as capillarity-driven flow in low or zero gravity environments as proven by many research projects conducted by NASA, *e. g.*, focusing on the optimisation of liquid-bearing containers in space, where capillarity might cause problems.

With the help of the definition of the radius of curvature of the meniscus R as well as the relationship $r = R\cos\theta$, Equation 2.2 can be transformed to

$$p_c = u_a - u_w = \frac{2\gamma}{R} \quad , \tag{2.4}$$

allowing to calculate capillary pressure p_c or matric suction s from a capillary curvature in a capillary tube. This possibility is very useful since no ideal capillary tubes with regular radii r exist in the irregularly shaped pore space of soils with a multitude of pore necks and throats of different sizes.

In a more general case where the capillary meniscus is not spherical, the curvature term $1/R$ can be substituted by mean curvature H according to

$$H = \frac{1}{R_1} + \frac{1}{R_2} \quad , \tag{2.5}$$

with R_1 and R_2 being the main radii of mean curvature. This allows to calculate capillary pressure from mean curvature as

$$p_c = \gamma H \quad . \tag{2.6}$$

In a granular medium, such as a packing of sand or of glass beads, with the latter representing a model soil, the capillary effects explained before and illustrated for special boundary conditions, such as in the capillary tube model, are more diverse as shown in Figure 2.3. Due to the presence of a multitude of different pores and pore throats in between individual grains as well as changing material surfaces, especially in natural sands, typically consisting not only of quartz, a large variety of capillary structures develops in the pore space. This leads to statistical distributions of radii of curvature as well as contact angles on the pore level and to the presence of larger water clusters and smaller capillary bridges. In the literature, different geometries of capillary water clusters in granular media, consisting of regular shaped grains, such as glass bead packings, have been classified as "liquid morphologies" which represent repeating constituent building blocks (Scheel *et al.*, 2008).

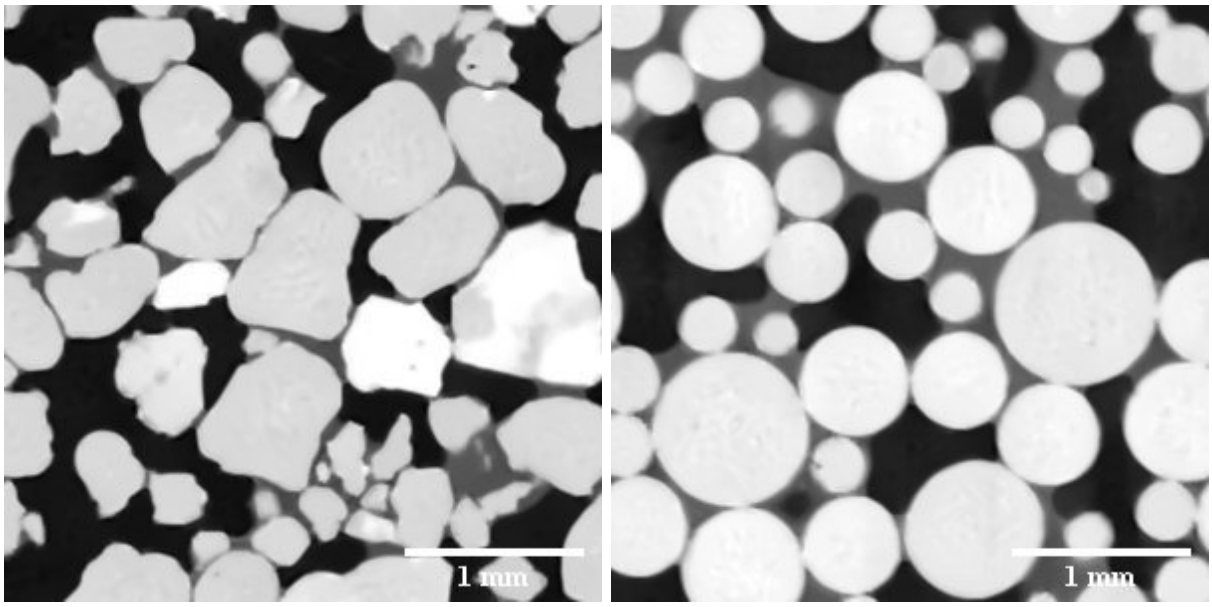


Figure 2.3: Distribution of pore water in a sand specimen (left) and polydisperse glass bead specimen (right) after mixing of dry granular material with water shown in greyscale images (3.3 mm × 3.3 mm) from laboratory X-ray CT at a voxel size of 11 μm

2.1.2 Capillary forces

The definition of microscopic capillary properties, such as mean curvature or the contact angle, opens the door to theoretical formulations of capillary forces which can be calculated for assumed capillary bridge geometries. Due to the meaning of capillary forces for the mechanical behaviour of granular materials, several authors have studied capillary forces in liquid bridges theoretically and experimentally (Schubert, 1982; Mielniczuk *et al.*, 2015; Bozkurt *et al.*, 2017; Shi *et al.*, 2018; Hueckel *et al.*, 2020; Agarwal *et al.*, 2019). While theoretical models derive the adhesive effects of capillary bridges based on a mathematical description of capillary bridge geometry, experiments seek to measure capillary forces. On the experimental side, mainly mechanical tensile tests have been proposed where single liquid bridges or more complex liquid cluster geometries are strained.

Following the description by Schubert (1982), approximating the geometry of a capillary bridge by an axisymmetric body characterised by the two main radii of curvature R_1 and R_2 in between two also axisymmetric particles as shown in Figure 2.4, the capillary force F_c can be derived as

$$\begin{aligned} F_\mathrm{c} &= F_\gamma + F_{p_\mathrm{c}} \\ &= -2\pi R_2 \gamma \sin\alpha + \pi R_2^2 p_\mathrm{c} \\ &= -2\pi R_2 \gamma \sin\alpha + \pi R_2^2 \gamma \left(1/R_1 + 1/R_2\right). \end{aligned} \tag{2.7}$$

Further important prerequisites underlined by Schubert (1982) are static conditions, a negligible influence of gravity on the capillary bridge as well as homogeneous contact

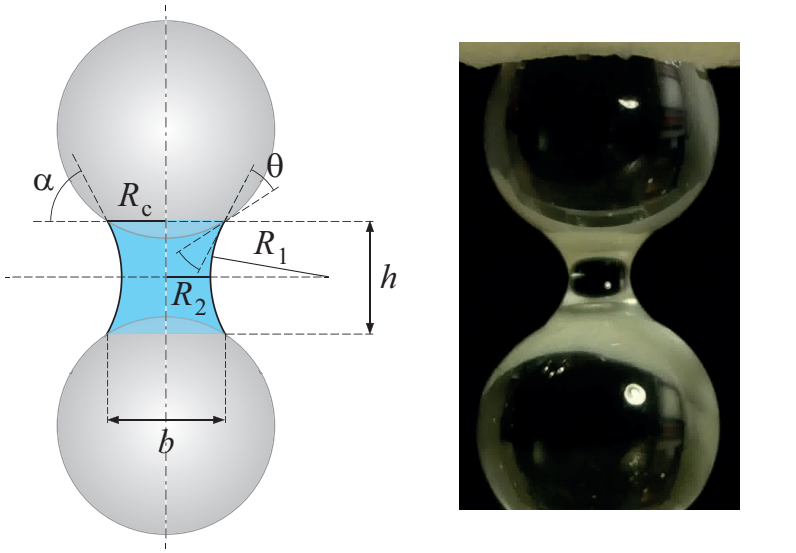


Figure 2.4: Idealised model of an axisymmetric capillary bridge in comparison to a real capillary bridge in between glass beads with a diameter of *ca.* 2 mm

angles at all contact lines. Furthermore, the capillary pressure is assumed to be constant inside the capillary bridge. If capillary pressure is constant, no internal flow will occur, and also the mean curvature must be constant in every point of the minimal surface according to the Young-Laplace equation (Willett *et al.*, 2007).

The capillary force can be either calculated at the neck of the capillary bridge (its thinnest region in Figure 2.4), where the meniscus slope angle $\alpha = 90°$ and R_2 is the inner mean radius of curvature of the liquid bridge as shown in Figure 2.4, or at the contact line, where R_2 equals the projected radius of the contact line R_c and α develops according to the wetting contact conditions. Irrespective of the region along the capillary bridge axis where the transferred force in a real liquid bridge is determined, the same capillary force must be obtained due to equilibrium conditions. This must not necessarily be the case when Equation 2.7 is applied as it is formulated for a model liquid bridge under idealising geometric assumptions. The characterisation of the capillary bridge geometry by two constant radii of curvature presented here is also known as the "toroidal approximation" (Willett *et al.*, 2007) which violates a constant mean curvature along the bridge surface, but which allows a simple calculation of capillary force at the "neck" or "gorge" of the liquid bridge. In the literature, further more accurate models exist which better approximate the true geometry of capillary bridges.

In Equation 2.7 we find two components of static capillary force F_c which is attractive for positive values in the sign convention followed here. The first term F_γ originates from surface tension acting parallel to the air-water interface. This term always leads to an attractive (positive) force contribution (therefore the negative sign in front of this term due to negative R_2). The second component F_{p_c} originates from capillary pressure p_c that can either be positive or negative, depending of the capillary bridge geometry modelled

by R_1 and R_2, leading to attraction or repulsion in the sign convention applied here.

It is important to note that according to Schubert (1982) the inner capillary radius R_2 is always negative, while the outer radius R_1 can either be positive or negative, leading to either positive (attractive) or negative (repulsive) capillary pressures, depending on the geometry of the capillary bridge. If the capillary bridge takes the shape of a sphere (convex capillary bridge or droplet), *i. e.*, R_1 and R_2 are both negative, the total capillary force F_c can become negative (repulsive).

With the help of the simple toroidal model presented above, theoretical static capillary forces can be calculated for known geometry and contact conditions of an idealised capillary bridge in between two particles or plates. However, if the capillary bridge is moving with a certain velocity, an additional viscous term contributing to total capillary force might become necessary (Shi *et al.*, 2018). Based on Equation 2.7 and the liquid bridge model from Figure 2.4, the different contributions of surface tension and capillary pressure to the total force are calculated for different geometry ratios h/b of the ideal liquid bridge and plotted in Figure 2.5. Besides $\gamma = 0.07275$ N/m, a constant width $b = 1$ mm of the liquid bridge and a constant meniscus slope angle at the contact line of $\alpha = 40°$ are assumed in the calculations. Please note that the liquid volume in these calculations with much simplified kinematics is not at all considered to be constant. In reality, the continuity condition of a constant liquid bridge volume would lead to an adjustment of contact angles and of course of the length of contact line or width of the liquid bridge b during elongation of the bridge when h is increased.

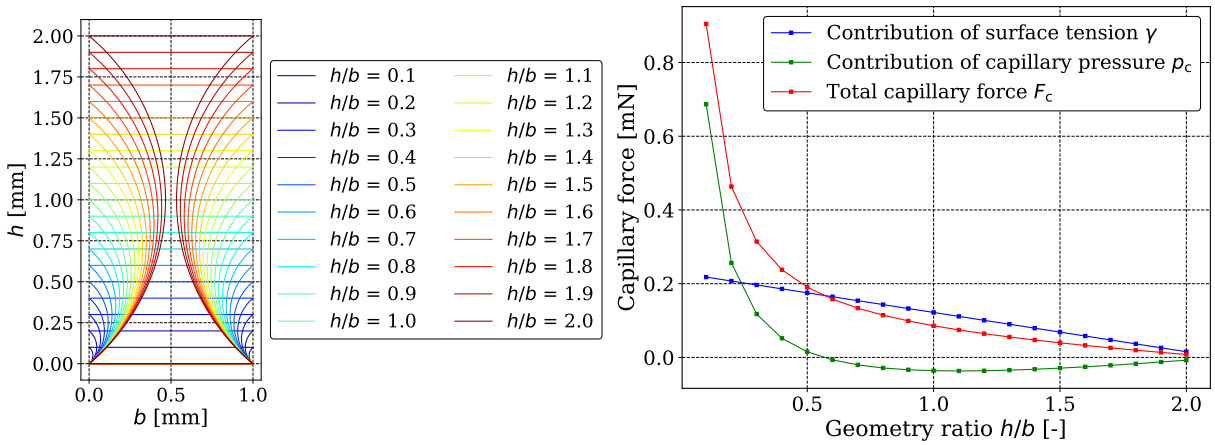


Figure 2.5: Geometry variation of a model capillary bridge at different geometry ratios h/b (left) and resulting components of total capillary force (right)

The variation of geometry ratio h/b of the liquid bridge reveals a positive total capillary force, *i. e.*, tension, in between the considered values $0.1 \leq h/b \leq 2.0$. As the liquid bridge is increasing in height h, the total capillary force is non-linearly approaching zero. The model yields high tensional capillary forces for low geometry ratios, *i. e.*, for short or compact liquid bridges. While the contribution of surface tension to the total capillary force is positive and decreasing linearly with increasing geometry ratio, the contribution of

capillary pressure causes the non-linear slope of the total capillary force. Interestingly, the capillary pressure can assume negative values if h/b increases, physically meaning excess pore water pressures, which is due to the sign convention of the radii of curvature and their relationship in the definition of mean curvature. To sum up, the geometry variation of the model liquid bridge reveals high tension forces for compact liquid bridges with a low geometry ratio h/b, while an increase in height apparently leads to a reduction of capillary force until the bridge fails.

The rupture length, representing the length of particle separation at which a capillary bridge breaks, has amongst others been studied by Lian *et al.* (1993), resulting in the simple empirical equation

$$l_{\mathrm{r}} = (1 + 0.5\,\theta)\, V_{\mathrm{liq}}^{\frac{1}{3}} \quad . \tag{2.8}$$

This equation describes the rupture length l_{r} of a capillary bridge in between two equally sized spheres and is valid for contact angles $\theta < 40°$. According to this equation, the rupture length depends on the contact angle (in radians) and on the liquid volume V_{liq}. Further models for calculation of the rupture length are presented and discussed in Willett *et al.* (2007).

In a granular assembly typically a variety of different liquid bridges and also larger water clusters with non-ideal shapes will be present as shown in Figure 1.4 in Chapter 1. This makes an analytical approach to contact force calculation very complicated. Nevertheless, the macroscopic effective stress due to capillarity can theoretically be considered as the outcome of a statistical distribution of contact forces averaged over the contact surfaces between liquid and solid phase.

2.2 Water retention behaviour of soils

2.2.1 Microscopic origins of water retention behaviour

Due to the characteristic pore size distribution, which is itself influenced by density, grain shapes, and grain size distribution, a soil volume theoretically encounters a multitude of different capillary pressures on the microscale, resulting in a macroscopic capillary pressure as the averaged effect of the whole considered soil volume. On this macroscopic level the microscopic capillary effects lead to a measurable water retention curve, when degree of saturation S_{r} is plotted *vs.* capillary pressure or matric suction. An exemplary water retention curve of a sand is shown in Figure 2.6. Its features will be explained in detail in the following.

The characteristic S-shaped water retention curve reflects the drainage and imbibition phenomena happening on the microscale. The entire saturation range is typically divided into three different regimes, depending on the connectivity and distribution of pore water. In the capillary regime, where the pores are still filled with water, however under natural conditions with occluded air bubbles, an increase in matric suction leads to air entry into the pores upon primary drainage. When the macroscopic matric suction overcomes the capillary resistance for air entry, the so-called air entry value (AEV) is reached and

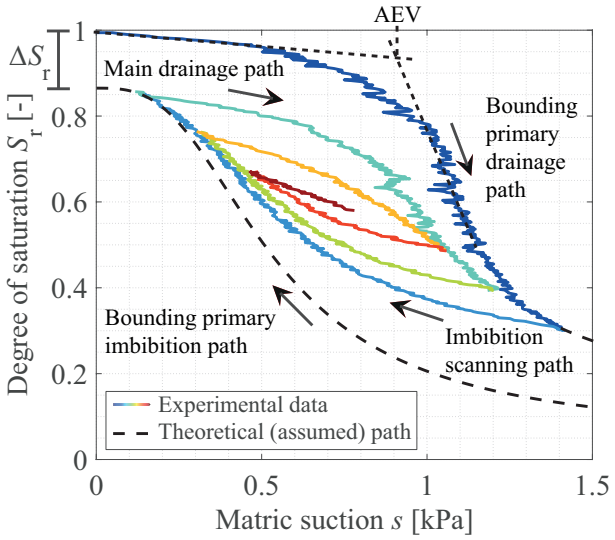


Figure 2.6: Water retention curve of a medium coarse to coarse grained sand with different consecutive hydraulic paths measured with the method proposed in Milatz (2020a)

the initially water-filled pores begin to empty. When drainage continues, connected pore channels begin to further fill with air, creating a network of pore air volumes and vice versa disconnected water clusters, which is called the funicular regime. At very low degree of saturation capillary bridges of isolated pore water around grain contacts are formed, which is called the pendular regime. As these water menisci can be hardly driven out of the grain skeleton by a further increase of suction, a theoretical residual saturation S_{res} is frequently observed for water retention curves at very high matric suction. However, this saturation can be expelled by complete drying of the soil, *e. g.*, in an oven. Fredlund and Xing (1994) assume a suction of 10^6 kPa as the maximum suction where the soil is entirely dry.

The mechanisms of drainage as described above occur on the so-called primary drainage path of a soil, starting from full water saturation. When a consecutive imbibition process takes place, a different macroscopic hydraulic path in the s-S_{r} space is measured, revealing the so-called hysteresis effect of the macroscopic water retention curve. The hysteresis effect leads to a hydraulic path-dependence in unsaturated soils, with hydraulic history developing between a bounding primary drainage and a bounding primary imbibition path as shown in Figure 2.6. Upon reversal of the flow direction, a multitude of so-called drainage and imbibition scanning paths can be observed, with the hydraulic state in the s-S_{r} space asymptotically approaching the bounding primary drainage or primary imbibition paths. Closed scanning cycles of drainage and imbibition take the shape of ellipses as shown in Figure 2.6. Owing to the hysteresis effect, the hydraulic history of a soil must be known in order to accurately describe its current hydraulic state as different suction levels exist for the same degree of saturation on the different hydraulic paths.

Due to air entrapment on the microscopic level, the full water saturation is usually not reached again when matric suction becomes zero upon imbibition, leaving a gap ΔS_{r} which is illustrated in Figure 2.6. Different theoretical microscopic mechanisms of air entrapment

are described in Bear (1979) and Lins (2009). Essentially, air can get entrapped by the effect of bypassing when water flows around air clusters, leaving them locked inside smaller voids or in dead ends. The effect of entrapped air is believed to be one possible microscopic reason for the existence of hysteresis (Bear, 1979). After air entrapment, a further drainage event leads to the so-called main drainage curve that runs asymptotically into the bounding primary drainage curve. If air entrapment is assumed to be irreversible, further drainage events are theoretically bounded by this main drainage curve.

Another theoretical explanation for the hysteretic effect can be seen in different contact angles between pore water and solid grains, which is known as contact angle-hysteresis (de Gennes *et al.*, 2004). Experiments on single droplets moving on an inclined plane indicate differences between the contact angles of an advancing and a receding fluid droplet θ_{adv} and θ_{rec}, with $\theta_{\mathrm{rec}} < \theta_{\mathrm{adv}}$ as shown in Figure 2.7.

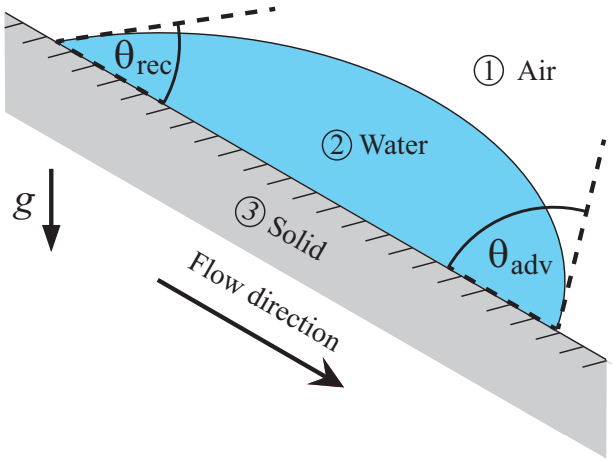


Figure 2.7: Moving water droplet in ambient air on an inclined solid plane

In accordance with Equation 2.2, this observation leads to a higher capillary pressure or matric suction for a receding water meniscus upon drainage compared to an advancing meniscus upon imbibition inside the same capillary. Also the radii of meniscus curvature are different with smaller radii of curvature for drainage and larger radii for imbibition processes which is illustrated in Figure 2.8.

Soil compaction leads to a decrease in void space and a reduction of average capillary radius. In agreement with Equations 2.2 and 2.3, this results in generally higher capillary pressures. Therefore, the water retention curve shows a density- or void ratio-dependence with higher capillary pressures and higher AEVs measured for lower void ratios at the same degree of saturation.

Traditionally, water retention curves are measured and modelled under the assumption of equilibrium between matric suction and degree of saturation and for quasi-static flow conditions, *i. e.*, for a very low flow rate. Accordingly, the aforementioned contact angles θ represent static contact angles. Due to viscous and dynamic effects, the static contact angle of a wetting fluid on a surface might be changed for fast flow events leading to a so-called dynamic contact angle. The difference of dynamic and static contact angles

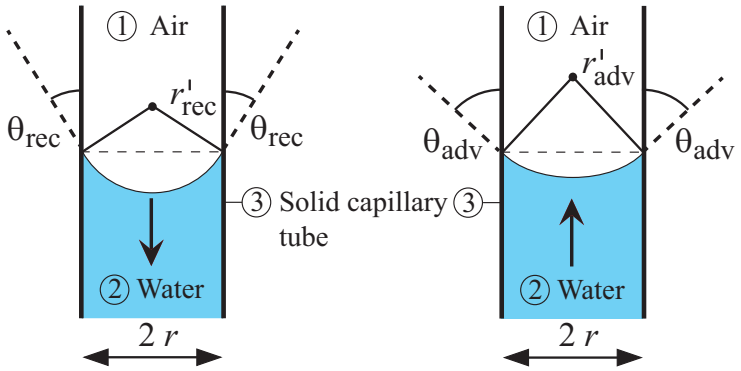


Figure 2.8: Movement of a water meniscus in a capillary tube: Drainage (left) and imbibition (right)

represents an explanation for transient flow effects leading to transient or dynamic water retention curves (Hassanizadeh *et al.*, 2002; Diamantopoulos and Durner, 2012; Milatz *et al.*, 2018b). These water retention curves can be measured for non-equilibrium flow conditions and generally deviate from static equilibrium soil water retention curves. If the flow rate is low enough, transient water retention curves and static water retention curves become the same.

2.2.2 Measurement of water retention behaviour

A multitude of different laboratory experiments have been developed for the measurement of the water retention curve. Due to varying suction ranges in coarse grained and fine grained soils, different methods for the application of matric suction and measurement of water content or degree of saturation have been developed. An overview of some frequently used methods for suction control for the measurement of the WRC is given by Vanapalli *et al.* (2008).

Focusing on granular soils, such as sands, with a typical low suction range much below 100 kPa, or one atmosphere of negative pore water pressure that can occur under natural conditions, methods to control negative pore water pressures are frequently applied for suction control. In order to measure the equilibrium water retention curve, the hanging water column method, standardised in ASTMD6836-16 (2016), is frequently applied. According to this method, matric suction in the form of a negative water head is applied to a soil specimen through a porous filter plate with a defined AEV in different suction steps. For every suction step the pore water outflow until equilibrium is measured in order to calculate the specimen degree of saturation. The reconstruction of the WRC by equilibrium s-S_r-data is tedious and time-consuming because the unsaturated flow requires more equilibrium time with decreasing specimen degree of saturation. Especially for the investigation of higher-order scanning paths, an experiment may have to run for several weeks. An acceleration of flow experiments for the measurement of the WRC can be achieved by the application of microporous filter membranes instead of solid porous plates as proposed by Nishimura *et al.* (2012). The filter membranes can provide an appropriate

AEV in order to prevent air from entering into the drainage system while at the same time allowing higher flow rates as compared to solid porous filter stones.

Another approach for the measurement of the WRC is given by the vice versa procedure of changing the specimen water content or degree of saturation by application of forced pore water flow and measuring the corresponding response of matric suction with the help of an embedded tensiometer sensor. With the help of such flow cell-based methods, transient quasi-static or dynamic water retention curves can be measured depending on the applied flow rate (Mirzaei and Das, 2013; Milatz, 2015; Zhuang, 2017; Milatz *et al.*, 2018b; Milatz *et al.*, 2018a; Milatz, 2020a). The miniaturised flow cell apparatus for the automated continuous measurement of transient WRCs of granular media discussed in Milatz (2020a) is used for the CT experiments to be presented in Chapter 5.

Several authors have already applied X-ray computed tomography for the investigation of the WRC from a microscopic point of view (Higo *et al.*, 2015; Khaddour, 2015; Khaddour *et al.*, 2018; Kido *et al.*, 2020; Thakur *et al.*, 2020; Milatz *et al.*, 2022b). In many experiments the hanging water column method is used to set different levels of degree of saturation and matric suction in the investigated specimens. After equilibration of degree of saturation, CT images are taken to analyse the microscopic phase distribution for different hydraulic states. Furthermore, microscopic interfacial properties, as given by the interfacial areas or curvatures of menisci, have already been measured using conventional X-ray CT by Wang *et al.* (2019) or by synchrotron-based CT by Culligan *et al.* (2004), Armstrong *et al.* (2012), and Schlüter *et al.* (2016). Contact angles have been measured based on CT data in a porous sand stone by Andrew *et al.* (2014) revealing a statistical distribution of contact angles. The availability of high quality imaging data with high local and temporal resolutions is important in order to analyse microscopic flow and material properties, such as pore scale wettability, on a statistical basis. However, publicly available image data from flow experiments are still rare. Two data sets from flow cell experiments on glass beads and on a limestone have been published by Schlüter *et al.* (2016) and Singh *et al.* (2018). These data are analysed with focus on the evolution of contact angles during pore emptying events by Mascini *et al.* (2020).

2.2.3 Modelling of water retention behaviour

Generally, two different types of models can be distinguished in the mathematical modelling of the water retention behaviour of soils. These are physical models and empirical models (Lins, 2009). Physical models make the attempt to predict the water retention behaviour based on different soil properties. Due to the dependence of the water retention curve on the pore size distribution, which is itself related to the grain size distribution of a soil, parameters of the grain size distribution curve can be used to predict the water retention curve. An example of an empirical model making use of the relationship between grain size distribution and water retention curve is given by the model proposed by Aubertin *et al.* (2003).

Empirical models fit experimental data based on a mathematical modelling approach and curve fitting parameters. Classical empirical approaches which are used to model a single hydraulic path of the water retention curve are the models presented by Brooks and Corey

(1964), van Genuchten (1980), and Fredlund and Xing (1994). In order to model higher complexity with hydraulic path dependence due to the hysteresis effect, more sophisticated modelling approaches have been presented by different authors, *e. g.*, Li (2005), Pedroso and Williams (2010) and Fuentes and Triantafyllidis (2013).

Being one of the most widely used mathematical models for the water retention curve, the van Genuchten (1980) model is reproduced here as

$$S_{\mathrm{e}}(s) = \frac{1}{(1 + (\alpha s)^n)^m} \quad . \tag{2.9}$$

In the standard form, it allows to calculate effective, *i. e.*, normalised, degree of saturation S_{e} as a function of matric suction s, but it can also be inverted. The parameter α is related to the reciprocal value of the AEV, while n and m are exponents. Very frequently, $m = 1 - 1/n$ is set in order to reduce the number of free model parameters. The effective degree of saturation is defined as

$$S_{\mathrm{e}} = \frac{S_{\mathrm{r}} - S_{\mathrm{res}}}{S_{\mathrm{max}} - S_{\mathrm{res}}} \tag{2.10}$$

in dependence on the residual degree of saturation S_{res} and the maximum degree of saturation S_{max} which allows to consider air entrapment if $S_{\mathrm{max}} < 1$.

2.3 Flow in a capillary system

2.3.1 Macroscopic approach to fluid flow in unsaturated soils

The WRC also plays a key role for multiphase flow in porous media. More than one century ago, scientists have already been aware of the difference between flow under unsaturated conditions and flow in the fully saturated state. Using the example of unsaturated soils, a reduction of water degree of saturation leads to a significant decrease in water permeability as the presence of air limits the flow paths available for pore water, which is of course also an example of microscopic flow effects governing the macroscopic hydraulic behaviour. Darcy's law, a continuum approach to laminar flow in porous media, stating the proportionality of the flow rate to a pressure gradient with a permeability as coefficient of proportionality, has been extended very early in soil science by Buckingham (1907) to include the physics of multiphase flow in a macroscopic approach suitable to solve practical engineering problems. The reduction of the coefficient of permeability upon decreasing degree of saturation can be modelled with the help of a relative permeability. This value, ranging between zero and one, can be calculated as a function of degree of saturation or matric suction, either following empirical approaches (Brooks and Corey, 1964; Fredlund and Rahardjo, 1993) or statistical approaches, also using models for the WRC to derive closed solutions for the unsaturated permeability (Childs and Collis-George, 1950; Burdine, 1953; Mualem, 1976).

Similar to the WRC, the measurement of unsaturated hydraulic conductivity is complex and time-consuming. Typically, flow experiments are performed, extending Darcy's law to

the unsaturated state where a difference in matric suction causes flow that is measured to calculate the coefficient of permeability. A convenient method to simultaneously measure the WRC and derive the unsaturated hydraulic conductivity during drainage of a soil is the evaporation test (Peters and Durner, 2008; Schindler *et al.*, 2010) in which matric suction is continuously measured in a soil column in two heights (resulting in the pressure gradient) during slow water flow caused by free evaporation at the specimen top.

2.3.2 Microscopic approach to fluid flow in unsaturated soils

Besides the macroscopic point of view on flow processes in the experimental and modelling approaches presented above, also microscopic investigations are pursued because hydraulic processes on the pore scale dictate the macroscopic behaviour regarding capillary pressure, degree of saturation, and flow of the wetting or nonwetting phase. A recent overview of theoretical, experimental, and numerical approaches to a better understanding of capillary flow in porous media is given by Singh *et al.* (2019).

Many of the findings regarding flow behaviour on the pore scale originate from so-called *microfluidic* experiments in which the drainage and imbibition of different fluids in artificial or natural porous systems is investigated. The experiments are designed for measurement and imaging of the complete pore scale flow behaviour, classically under 2D conditions, *e. g.*, in a Hele-Shaw cell[2]. However, recent 3D imaging methods, such as conventional laboratory X-ray CT and synchrotron-based CT are increasingly applied to obtain 3D insights. The research on this field is frequently driven by interests from the oil-industry with the aim of oil recovery from porous rock where a high residual saturation of the oil phase is undesirable.

Generally, gravity-driven density flow can be distinguished from capillary flow on the pore scale. The latter is entirely driven by capillary effects without the influence of gravity and fluid viscosity leading to a movement of the wetting phase into the configuration that corresponds to a minimum of energy regarding its interface to the nonwetting phase in the pore space. Under natural conditions, both gravity-driven and capillary flow and all corresponding physical effects, gravity, viscosity, and capillarity, are overlapping, however, physical boundary conditions and the relationship of material properties may exist that support the dominance of the one or the other of the two named flow conditions. The dominating flow conditions typically lead to different flow patterns named capillary fingering, viscous fingering, and stable displacement that can be observed in porous media (Singh *et al.*, 2019). While capillary fingering and viscous fingering lead to the formation of more or less branching fingers of the invading fluid into the pore space which is initially filled by the defending fluid, stable displacement flow patterns are rather characterised by smooth interfaces. An experimental study on the dominance of the different flow patterns is presented and extensively discussed by Méheust *et al.* (2002).

Two dimensionless quantities are applied in fluid mechanics to distinguish prevailing physical effects leading to a corresponding type of flow (Li *et al.*, 2018). With the help of the

[2]Flow experiment named after Henry Selby Hele-Shaw (1854–1941), a British engineer and professor at the University of Liverpool.

dimensionless Eötvös number Eo, also known as Bond number Bo, defined as

$$Eo = Bo = \frac{\Delta\rho g L^2}{\gamma} \quad , \tag{2.11}$$

the relationship between the magnitudes of gravitational forces and capillary forces for a specific flow situation can be described. $\Delta\rho$ represents the difference in density of the two present phases, g is the gravitational acceleration, L is a characteristic length, and γ is surface tension. The dimensionless quantity allows to compare different flow situations, with a high Eötvös or Bond number indicating a system where gravitational forces are dominating the flow physics. Capillary forces dominate the flow if the Eötvös or Bond number is less than one.

Another important dimensionless quantity is capillary number Ca, defined as

$$Ca = \frac{\eta v}{\gamma} \quad . \tag{2.12}$$

The capillary number is computed from the dynamic viscosity η of the wetting fluid, the average velocity v of the fluid interface or front as well as surface tension γ and represents the relationship of viscous forces in the numerator and capillary forces in the denominator. For very low capillary number (different references from oil recovery research name a limiting value of 10^{-5}), capillary forces dominate the flow.

For pore scale studies, also the following definition of capillary number is found in literature (Méheust *et al.*, 2002).

$$Ca = \frac{\eta v L^2}{\gamma \kappa} \quad , \tag{2.13}$$

where L is typical pore size, and κ is the permeability of the porous medium. Also the prevalent occurrence of different flow patterns, such as viscous or capillary fingering, can be derived from capillary number, with capillary fingering occurring for $Ca << 1$ and viscous fingering occurring for $Ca >> 1$ (Méheust *et al.*, 2002).

Nevertheless, not all physical effects influencing the microscopic flow can be characterised thoroughly by the named dimensionless quantities and still open questions exist. Especially, the local flow dynamics including sudden bursts of capillary pressure due to rapid emptying or filling of pores, the so-called Haines jumps (Haines, 1930) named after the early soil physicist William Burgess Haines, who is also known to have discovered hydraulic hysteresis in soils (Keen, 1963), are not fully understood yet. An important factor influencing capillary flow patterns on the pore scale is the wettability of the solid phase that can be described by the contact angle of the wetting fluid at the solid surface. However, in natural porous media there is obviously no single contact angle, but a statistical distribution to be found on the pore scale (Andrew *et al.*, 2014). Besides the contact angles, that are also known to show contact angle-hysteresis, the ratio of fluid viscosities as well as the local geometry and boundary conditions of the interfaces between fluids and solids seem to influence pore scale processes (Singh *et al.*, 2019).

2.4 Hydro-mechanical behaviour of unsaturated soils

2.4.1 The quest for χ

The contribution of capillarity to the effective stress principle as proposed by Terzaghi has been an important question of research. In order to model effective stress in unsaturated soils, different models have been established that allow to calculate effective stress based on the hydraulic state as reflected by the water retention curve.

Starting with Bishop (1959), different researchers have developed equations for the formulation of effective stress in unsaturated soils. These equations can be applied to calculate the contribution of degree of saturation and matric suction to effective stress, which underlines the importance of the WRC as a key function, not only for the hydraulic behaviour, but also for the mechanical stress state of unsaturated soils.

From a microscopic point of view, matric suction as well as the interfacial tension in water clusters or capillary bridges act on the grain skeleton depending on the current phase distribution which can be described by degree of saturation. Therefore, it was Bishop's approach, given in Equation 2.14, to weigh the contribution of matric suction to effective stress with the help of the Bishop parameter χ which is related to degree of saturation.

$$\sigma' = \sigma - u_\mathrm{a} + \chi(u_\mathrm{a} - u_\mathrm{w}) = \sigma + \chi s \text{ if } u_\mathrm{a} = 0 \text{ and if } s = -u_\mathrm{w} \quad , \tag{2.14}$$

where σ' and σ represent effective stress and total stress, respectively. Due to the implication that χ has to satisfy the conditions $\chi = 0$ for $S_\mathrm{r} = 0$ and $\chi = 1$ for $S_\mathrm{r} = 1$, χ is frequently assumed to be equal to S_r.

According to the suction stress concept proposed by Lu and Likos (2006) and Lu *et al.* (2010), the impact of capillary effects on effective stress can be expressed by the so-called suction stress σ_s which is given as

$$\sigma_\mathrm{s} = S_\mathrm{e} s = \frac{S_\mathrm{r} - S_\mathrm{res}}{S_\mathrm{max} - S_\mathrm{res}} s \quad . \tag{2.15}$$

In this original approach for suction stress, we find the parameter χ equal to effective degree of saturation S_e.

Further following the suction stress concept, effective stress can be expressed as

$$\sigma' = \sigma + \sigma_\mathrm{s} \quad . \tag{2.16}$$

The parameter χ has been the focus of many discussions in unsaturated soil mechanics because from a microscopic point of view, it represents all influences of the phase distribution as well as the interfacial properties on effective stress. Therefore, different researchers have proposed to include the interfacial areas in the effective stress formulation for unsaturated soils. While the interface between solid and pore water transfers suction to the grains, the interface between pore air and pore water is characterised by surface tension, and the corresponding capillary forces act on the soil grains via the menisci occurring at lower degrees of saturation.

In their derivation of suction stress, Lu *et al.* (2010) present Equation 2.17 that also includes the effect of the interfacial areas A_i per volume V and their respective interfacial surface energies (or surface tensions) γ_i of the different interfaces i = (air, water), (solid, water) and (solid, air) on effective stress.

$$\sigma_\mathrm{s} = S_\mathrm{e} s + \Sigma_i \gamma_i \frac{\partial A_i}{\partial V} \tag{2.17}$$

If the influence of the interfaces is neglected, which might be the case for the capillary and funicular regimes according to Lu *et al.* (2010), the suction stress formulation given in Equation 2.15 is restored.

A similar formulation for suction stress including the influence of air-water interfacial area or nonwetting-wetting fluid interfacial area per total volume a^nw is presented by Nikooee *et al.* (2013) in the form of

$$\sigma_\mathrm{s} = S_\mathrm{e} s + k^\mathrm{nw} a^\mathrm{nw} \quad , \tag{2.18}$$

where k^nw represents a material parameter related to air-water surface tension γ, and a^nw is specific air-water interfacial area (per total volume) according to Nikooee *et al.* (2013).

Applying Equation 2.18 to the effective stress formulation, the Bishop parameter can be derived according to

$$\chi = S_\mathrm{e} + \frac{k^\mathrm{nw} a^\mathrm{nw}}{s} \quad , \tag{2.19}$$

adding a term for the contribution of specific air-water interfacial area to the influence of effective saturation.

Also taking account of the effect of interfacial energies, Equation 2.20 was presented by Gray *et al.* (2009) based on previous thermodynamic considerations of the effective stress state in unsaturated porous media (Gray and Schrefler, 2001).

$$\begin{aligned} \sigma' &= \sigma - [\chi_\mathrm{sw} - n(\chi_\mathrm{sw} - S_\mathrm{r})](u_\mathrm{w} + \Gamma_\mathrm{sw} J_\mathrm{sw}) \\ &+ [1 - \chi_\mathrm{sw} + n(\chi_\mathrm{sw} - S_\mathrm{r})](u_\mathrm{a} + \Gamma_\mathrm{sa} J_\mathrm{sa}) \quad , \end{aligned} \tag{2.20}$$

where Γ_sw and Γ_sa represent the interfacial energies of the solid-water and solid-air interface and J_sw and J_sa stand for the mean curvatures of the solid-water and solid-air interface.

If the curvature terms in Equation 2.20 are neglected, the Bishop parameter can be described as

$$\chi \approx (1 - n)\chi_\mathrm{sw} + n S_\mathrm{r} \quad , \tag{2.21}$$

considering the effect of the fraction of wetted solid surface area $\chi_\mathrm{sw} = a^\mathrm{sw}/a^\mathrm{s}$ and degree of saturation weighed by porosity n. Here, a^sw represents the specific solid-water interfacial area (per total volume), while a^s describes the specific solid surface area (per total volume) according to Wang *et al.* (2019).

With the help of a model for the water retention curve as well as for the development of interfacial areas *vs.* degree of saturation or suction, the equations above can be used to describe the effective stress state in unsaturated soils. As effective stress is also the key to shear strength and volume change behaviour, this underlines the importance of a thorough understanding of the water retention behaviour and the interplay of phases on the micro- and macroscale.

2.4.2 Hydro-mechanical lab testing of unsaturated soils

Starting from the half of the last century, many experimental techniques have been developed to investigate the effects of partial saturation on the mechanical properties of soils, such as shear strength and stiffness (Donald, 1956; Fredlund *et al.*, 1978; Fredlund and Rahardjo, 1993). Traditionally, element tests, such as the triaxial test, are performed with special focus on the control and measurement of matric suction or degree of saturation (Bishop, 1961; Vanapalli *et al.*, 2008; Delage *et al.*, 2008; Craciun and Lo, 2009) and the concept of the stress state variables (Fredlund and Morgenstern, 1977; Fredlund and Rahardjo, 1993) has been widely applied to derive effective stress and shear strength in unsaturated soils for practical applications in geotechnical engineering. Special techniques for the measurement and control of suction, *e. g.*, tensiometer sensors, the hanging water column method (ASTMD6836-16, 2016) or the axis translation technique (Hilf, 1956), have been implemented in traditional soil mechanical experiments, such as the direct shear test (Donald, 1956; Likos *et al.*, 2010; Purwana *et al.*, 2011; Wang *et al.*, 2019) or simple shear test (Tombolato *et al.*, 2008; Milatz and Grabe, 2015). Many of these experiments could deliver valuable continuum-based information on the macroscopic shear and volume change behaviour of unsaturated soils, however, without being able to evaluate interior or local processes occurring inside the specimens. Many open questions regarding the validity of element test conditions, such as homogeneity of strain fields, but also of water content and matric suction, remain unanswered if a pure macroscopic approach is followed.

This is why many researchers have already started to apply imaging techniques, such as X-ray computed tomography, to investigate local microscopic processes in unsaturated soils during mechanical experiments. Starting from pure imaging of the soil structure with the availability of early medical CT scanners, *e. g.*, Petrovic *et al.* (1982), the development of CT scanners for industrial purposes and materials science led the way to many imaging applications in mechanical soil testing. After the pioneering work of Desrues *et al.* (1996), triaxial tests with parallel CT imaging have revealed many interesting insights into the shear behaviour of soils, *e. g.*, Tani (1997), Otani *et al.* (2000), Hall *et al.* (2010), Andò (2013), Andò *et al.* (2013), Salvatore *et al.* (2016), Wiebicke (2020). Besides triaxial tests, also one-dimensional compression (oedometer) tests have been run in CT scanning environments, *e. g.*, Nadimi and Fonseca (2019), Yan and Shi (2015) and Zhao *et al.* (2015), focussing on grain crushing. Furthermore, other problems related to soil mechanics, such as plant and root growths as well as soil freezing, have been investigated by means of X-ray CT imaging (Viggiani *et al.*, 2015).

Beyond interesting insights into the "micro-to-macro" behaviour of granular soils, the research works highlighted above also illustrate many developments in the treatment and analysis of image data which allows to capture whole processes in "4D experiments" (3D + time) and to extract quantitative measurements, such as the development of strain fields or the tracking of single particle displacements and rotations by image correlation (Bay *et al.*, 1999; Hall *et al.*, 2010; Stamati *et al.*, 2020). Also the development of grain fabric has been measured based on X-ray CT data (Wiebicke *et al.*, 2017a; Wiebicke, 2020).

Regarding the mechanical testing of unsaturated soils, with the aim to investigate the influence of degree of saturation and matric suction on the macroscopic shear behaviour

as well as to investigate the change of microscopic properties, such as capillary bridges, triaxial tests have been run in X-ray CT scanners by Higo *et al.* (2013), Khaddour (2015), Kido and Higo (2019) and Kido and Higo (2020). Milatz *et al.* (2021b) have investigated the hydro-mechanical behaviour of different unsaturated granulates at low stress state by means of uniaxial compression tests in a laboratory X-ray CT scanner. Furthermore, the hydro-mechanical phenomenon of capillary collapse, describing the collapse of metastable unsaturated grain skeletons upon imbibition, has been studied with X-ray CT by Bruchon *et al.* (2013) and Moscariello *et al.* (2018) allowing to identify the local soil-water interaction leading to the dissolution of capillary bridges and closure of larger pores.

To sum up, for the investigation of the influence of microscopic structures, such as the interfacial areas, on effective stress and the macroscopic behaviour of unsaturated soils, a non-destructive experimental method as given by computed tomography is urgently needed as outlined by Wang *et al.* (2019). As an example, Wang *et al.* (2019) could measure a relationship of air-water interfacial area and solid-water interfacial area *vs.* degree of saturation for a packing of glass beads by CT imaging. A comparison of the χ-parameter, as discussed in Section 2.4.1, calculated from suction-controlled direct shear tests, has revealed that the formulation given by Equation 2.21 seems to represent a good approximation of χ, making use of the fraction of wetted solid surface area χ_{sw} (Wang *et al.*, 2019).

2.5 Short introduction to imaging methods

2.5.1 Overview

Imaging is a very popular method in various scientific fields and applications because it allows to capture local and temporal information of an object or process of interest. Images contain information stored on a grid, with data cells being addressed as pixels (px) in 2D or voxels (vx) in 3D, and therefore represent a structured format bearing quantitative information that can be explored by image analysis. Another important aspect of imaging as a measurement tool is the fact that it is typically working without contact to the object of interest which can thus be observed without disturbance. Therefore, imaging can be counted to the non-destructive experimental methods.

If a series of images is captured to follow a process, not only local data, but also temporal information can be drawn from the image sequence, allowing to investigate transient processes at a given temporal resolution. As the sampling of data at a certain image size and a desired resolution, *e. g.*, number of pixels per mm, takes time, frequently, a compromise between resolution and imaging time needs to be found. Furthermore, all imaging methods suffer from image noise influencing the image quality or signal, so that the quality of an image or imaging method can be characterised by a so-called signal-to-noise ratio. The noise is originating from the object to be imaged or from ambient factors of influence, such as light conditions or technical issues, *e. g.*, in the process of digitising the captured information which is in the simplest case transported by light.

Thanks to the fast development of optical instruments as well as software, many imaging techniques for the extraction of local and temporal information are available today. Some imaging techniques very common in science are listed and briefly explained in the following.

- (High speed) camera set-ups (2D)
- Microscopy (2D and 3D)
- Radiography (2D)
- Computed tomography (3D)

2.5.2 Simple camera-based imaging experiments

Digital cameras are frequently applied in imaging experiments to capture 2D images of planar surfaces in order to observe processes, *e. g.*, in model tests which are frequently applied for physical modelling in soil mechanics and geotechnical research. In this field, sand box experiments are very common in which soil mechanical phenomena, such as the formation of a shear zone behind a moving wall mobilising active or passive earth pressure, can be observed with suitable camera set-ups which also include appropriate lighting as shown in Figure 2.9.

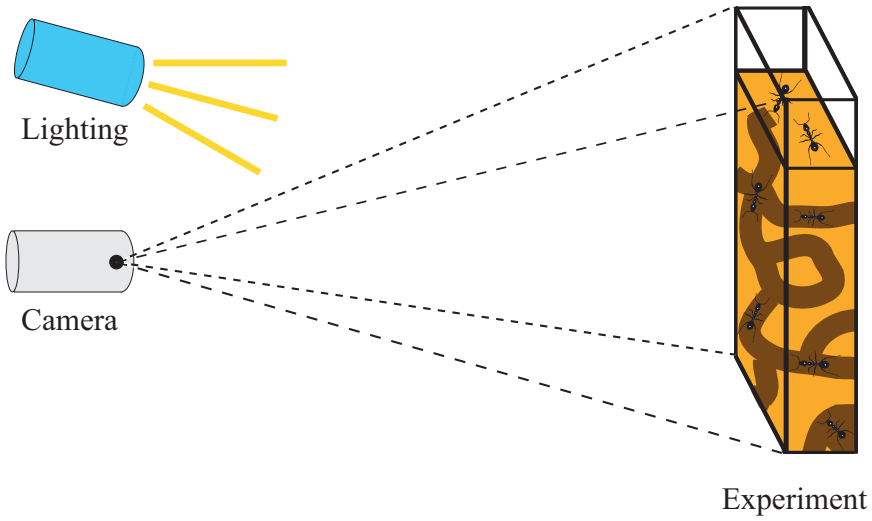


Figure 2.9: Principle of a camera-based imaging experiment

Depending on the frame rate, slow to fast temporal processes can be captured to either obtain qualitative insights into 2D processes or extract quantitative measurements by more sophisticated image analysis techniques, such as the tracing of objects of interest or the Particle Image Velocimetry (PIV). PIV, originally a method from fluid mechanics designed to measure flow velocities from a series of images taken of 2D channel flow with tracer particles, has frequently been applied in geotechnical engineering to map velocities,

displacements, and strains onto 2D soil surfaces imaged by camera set-ups in element or model tests (White *et al.*, 2003; White *et al.*, 2005). Furthermore, also soil properties, such as liquid degrees of saturation in granular media, can be quantitatively measured from image data (Flores, 2010; Parera *et al.*, 2020).

2.5.3 Microscopy

Beginning with the invention of the light microscope several hundred years ago, microscopy has developed to a standard imaging method in many fields of science. Depending on the physical principle used for generating images, various kinds of microscopy are distinguished today. Main techniques of microscopy include the classical *light microscopy*, *electron microscopy*, including *transmission electron microscopy* (TEM) and *scanning electron microscopy* (SEM), *scanning probe microscopy* (SPM) and the field of *X-ray microscopy* combining X-ray CT with lenses for magnification. The different microscopy techniques can be applied for the acquisition of 2D and in some cases also 3D images with resolutions in very different length scales.

2.5.4 Radiographic imaging methods

Radiographic imaging methods are based on the interaction of different kinds of radiation with matter. In its classical application, this imaging method allows to extract two dimensional structural information from a sample which is passed through by the imaging radiation. In general, contrast in the obtained images is achieved by attenuation of the used radiation when it interacts with the sample to be imaged.

A milestone in radiography, the science of radiographic imaging, was the discovery of X-rays by Wilhelm Conrad Röntgen[3] in 1895. Röntgen was working as a physics professor in Würzburg, Germany, when he discovered a new type of radiation capable of penetrating solid matter. His discovery, so relevant for medical use, was honored with the very first Nobel Prize in Physics in the year 1901.

X-rays are a type of ionising radiation in the invisible electromagnetic spectrum of light. Due to its small wavelength, the radiation can pass through dense matter but is attenuated due to different physical effects, namely the photoelectric effect, Compton scattering and electron pair formation, depending on the energy level of the X-ray photons. The main sources of X-ray attenuation are caused by an interaction with electrons in the electron shells of atoms inside the sample. Either X-ray photons are absorbed by these electrons, causing a photoelectron to be emitted (photoelectric effect) and leaving the corresponding atom in an ionised, *i. e.*, charged, state, or they are scattered (Andò, 2013; Tengattini *et al.*, 2021). At lower X-ray energies as applied in laboratory X-ray imaging, the photoelectric effect dominates the absorption effects. This main interaction between X-ray photons and electrons leads to the relationship between atomic number and X-ray attenuation: The higher the atomic number of an element, indicating the number of electrons in the electron

[3] Wilhelm Conrad Röntgen (1845–1923): German physicist who discovered the "X-radiation" (X-rays), a form of high-energy electromagnetic radiation.

hull of its uncharged atoms, the higher the attenuation of X-ray photons. Therefore, materials with higher density, such as metals, lead to a higher X-ray attenuation, which allows to use them for X-ray radiation protection, but on the other hand complicates the imaging of their inner structure. The absorption of X-ray photons furthermore depends on their energy level, with higher energies generally leading to weaker absorption, however, also with other energy-dependent effects occurring due to the interaction with electrons contained in discrete electron hull layers around an atom nucleus at different energy levels.

Right after the discovery of X-rays, medical applications could profit from X-ray imaging as already foreseen by Wilhelm Conrad Röntgen who illustrated the medical use of his discovery with the help of an X-ray radiography of people's hands, impressively showing the contrast between bones, surrounding flesh, and also metallic rings.

Due to different densities in samples to be imaged by X-rays, contrast is obtained allowing to distinguish the different materials by their attenuation effect on the emitted radiation. The attenuation of homogeneous (monochromatic) radiation on its one-dimensional path through homogeneous matter is described by the Beer-Lambert law[4]

$$I(x) = I_0 e^{-\mu x} \quad , \tag{2.22}$$

with the current intensity $I(x)$ of the radiation, *e. g.*, photons per area and time, after a travel distance x through the matter depending on the initial intensity I_0 of the radiation and an exponential decay term with the product of x and the linear attenuation coefficient μ as exponent.

A radiographic imaging set-up generally consists of the radiation source and a detector. The sample to be imaged is placed in between source and detector, with areas of different X-ray attenuation coefficient leading to contrast in the detected image. Typical X-ray sources known from medical applications are X-ray tubes which contain a vacuum and allow to accelerate electrons from the cathode by thermionic emission to collide with a target which forms the anode in an electrical acceleration circuit at high voltage as shown in Figure 2.10.

Due to the collision of the electrons with the target which is typically made of a very dense material, such as tungsten (wolfram), their energy is transformed into heat and X-ray photons which leave the X-ray tube in a conical shape as defined by the surface and angle of the target and further radiation shielding. This behaviour leads to an X-ray cone beam typical for many X-ray tubes. The emission of X-ray photons at different energies caused by the deceleration of electrons when colliding with dense matter is known as bremsstrahlung. Besides the bremsstrahlung, also a material-specific characteristic radiation is caused by electrons leaving their atomic electron hulls and shifting in them when hit by the X-rays. Both effects lead to the occurrence of an X-ray spectrum emitted by an X-ray tube. This means the radiation is not monochromatic, but contains a variety of different wavelengths, frequencies or energies, characteristic of the kind of material used for the anode and with the peak energy generally depending on the applied acceleration voltage between cathode and anode target, whereas the applied current controls the intensity

[4]Named after the German mathematician, chemist and physicist August Beer (1825–1863) and the Swiss-French polymath Jean-Henri Lambert (1728–1777).

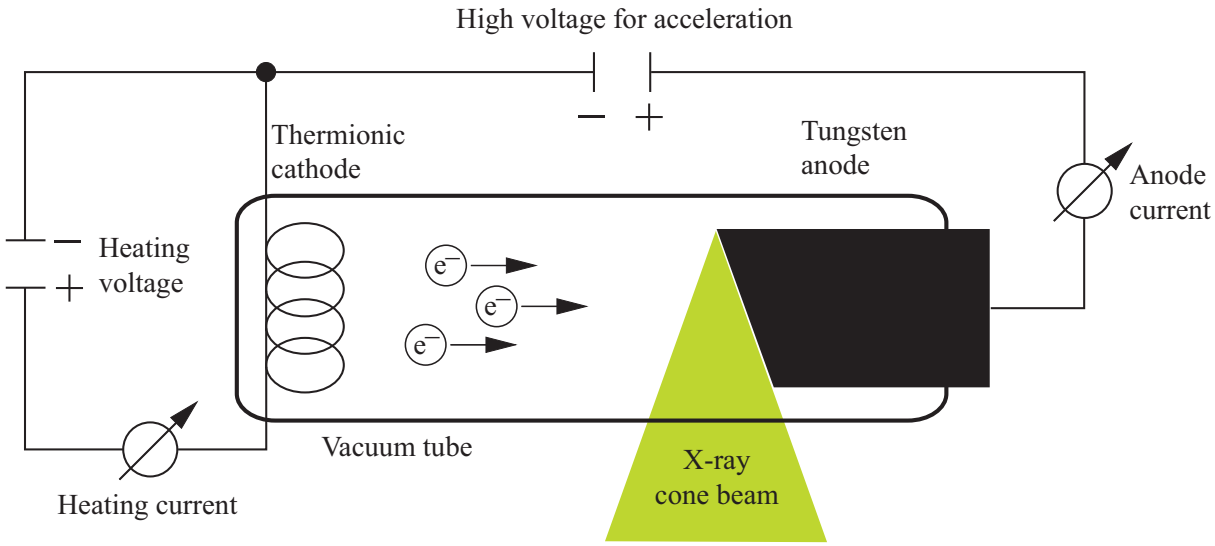


Figure 2.10: Principle of an X-ray tube

or flux of photons I_0 in the emitted X-ray beam. Depending on the energy level, soft and hard X-ray light is distinguished and applied for different imaging purposes, *e. g.*, for imaging of soft and hard matter. Especially for imaging of living tissue in medicine, soft X-rays are preferred, whereas materials science frequently requires hard X-rays at high energies to radiate through dense matter. With knowledge of the X-ray energy at which a material to be imaged delivers the maximum attenuation, the applied X-ray energy can be selected equal or close to the corresponding energy to make use of this optimum of attenuation in order to achieve or enhance a material-specific contrast. For this purpose, also contrast enhancing agents can be applied, such as iodine, to dope water for a better contrast (Wildenschild *et al.*, 2002; Wildenschild *et al.*, 2005).

For the detection or visualisation of X-rays, formerly radiation sensitive films or luminescent screens were applied. In modern X-ray machines for medical and scientific purposes, X-ray detectors are used which are based on a digital principle. Typically, so-called scintillators are applied to transform incoming X-ray energy into visible light which can be detected and digitised by an image sensor as used in a digital camera. Imaging detectors are characterised by their number of pixels as discrete radiation detecting elements and by pixel size. Furthermore, the read out speed and properties of light exposure times, needed to measure sufficient signal quality, represent important properties of an image detector because they influence acquisition time (Andò, 2013).

Besides X-rays, also other types of ionising radiation have been used in radiographic imaging. A prominent example that is more and more applied in imaging is neutron radiography. Unlike X-rays, neutrons are atomic nuclei constituent particles with a mass, but with no electrical charge. Neutrons can be produced in reactors by nuclear fission of atomic nuclei and are therefore rather rare for scientific imaging (Tengattini *et al.*, 2021).

Due to their different mechanisms of interacting with matter, neutrons yield promising perspectives for the imaging of materials that cannot be achieved by X-rays. While X-rays

are mainly attenuated by dense materials, mainly interacting with the orbital electrons of atoms, neutrons interact with the atomic nuclei and are therefore attenuated depending on the properties of the nuclei. With increasing relative size of the nucleus of an element the attenuation of neutrons increases, creating contrast when imaging materials that are translucent and thus "invisible" to X-rays. Especially water is highly attenuating neutrons while being relatively translucent for X-rays. An interesting aspect is the isotope-sensitive attenuation of neutrons. An example is also given by water that can be found in a regular and a heavier configuration in nature, made up of the stable isotopes hydrogen or the much rarer deuterium which vary in the composition of their atomic nuclei. The application of both forms of liquid water in neutron-based imaging experiments thus allows for interesting insights as different contrast can be achieved, *e. g.*, during the mixing of the different kinds of water. Furthermore, neutrons allow to image and differentiate between metal composites which are highly attenuating X-rays. Owing to their sensitivity when radiating through water, neutrons can be used for many imaging applications in the research on geomaterials as proposed by Tengattini *et al.* (2021).

2.5.5 Computed tomography

The invention of computed tomography by the physicist Allan MacLeod Cormack[5] and the electrical engineer Godfrey Newbold Hounsfield[6] in the 1970s extended two dimensional radiographies to the third dimension, which led to a new imaging method for diagnosis in medicine and a Nobel Prize in Physiology or Medicine for both inventors in the year 1979. After the invention of computed tomography, many medical X-ray CT scanners were developed and the new imaging technique has expanded into all fields of science and industry until today. While CT is used for the investigation of new materials in materials science, also standard industry applications have emerged, *e. g.*, for damage detection in fabricated parts with need for high failure safety, such as airplane parts or components for medical apparatuses.

The principle of CT is the measurement of various radiographies of the three-dimensional object of interest from different angles of view and the following reconstruction of a three-dimensional tomography image from calculated two-dimensional cross sections (tomographies) yielding a density distribution of the object. Three-dimensional images are obtained from individual tomography images reconstructed as cross sectional slices of the object in different heights. The method is named computed tomography as the tomographies are reconstructed by computational methods. The computed CT value or magnitude of X-ray attenuation in every coordinate of the reconstructed cross section correlates to its internal material density distribution, which allows different materials to be identified.

The general layout of a CT scanner consists of an X-ray source and a detector. Either the source and the detector rotate around the fixed sample to be imaged or the sample itself is placed on a rotation stage with source and detector being fixed while radiographies for different rotation angles of the sample are captured as shown in Figure 2.11. While

[5] Allan MacLeod Cormack (1924–1998): South African American physicist.
[6] Godfrey Newbold Hounsfield (1919–2004): English electrical engineer.

the first option is used for medical applications on live patients, the second approach is frequently used in laboratory CT applications, *e. g.*, for materials science. In CT systems with cone beam geometry a geometric magnification of the object to be imaged is realised. The magnification can be set by varying the distance between sample and X-ray source. In the more sophisticated currently emerging X-ray microscopes, as combinations of X-ray CT scanners with properties of a microscope, further magnification can be achieved by X-ray lenses.

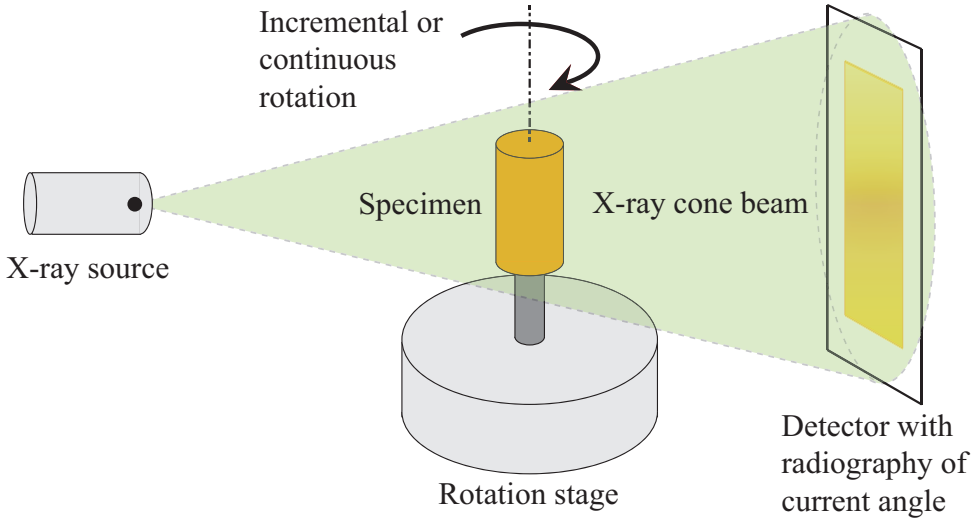


Figure 2.11: Principle of X-ray computed tomography

The reconstruction of three dimensional data from a multitude of two dimensional radiographies, *i. e.*, X-ray images measured for different angle increments, requires a mathematical algorithm named "filtered back-projection" which is based on the work of the Austrian mathematician Johann Radon[7], who described a linear integral transform in 1917 which was named the Radon transform afterwards. The name of the algorithm originates from the fact that a signal processing filter is involved in the mathematical procedure. The Radon transform transforms a bivariate function in cartesian coordinates $f(x,y)$ into a bivariate function in polar coordinates $Rf(t,\Theta)$ (Iske, 2018), with t being the radius or radial coordinate and Θ being the projection or polar angle.

To solve the reconstruction problem of computed tomography, *i. e.*, the reconstruction of an unknown two dimensional function from known line integrals of lines going through the function (Iske, 2018), the Radon transform is used in an inverted form, the inverse Radon transform. In X-ray computed tomography, the integrated effect of attenuation of an X-ray passing through a sample is directly measured as the loss in X-ray intensity according to the Beer-Lambert law. For a given X-ray beam path through a sample, the measured intensity or energy loss between emitted and detected X-ray is equal to the line integral of the unknown attenuation function $f(x,y) = \mu(x,y)$ along this path. The attenuation of X-ray beams through an object with elliptical cross section on a rotation stage placed in

[7] Johann Karl August Radon (1887–1956): Austrian mathematician.

between an idealised X-ray line source with parallel beam geometry and a detector with discrete read out units (pixels) is illustrated in Figure 2.12 for two angle increments. The set-up and principle of attenuation and reconstruction is similar for X-ray sources with cone beam geometry. Here, the reconstruction has to consider the different angles of X-ray paths included in the cone beam between point source and detector.

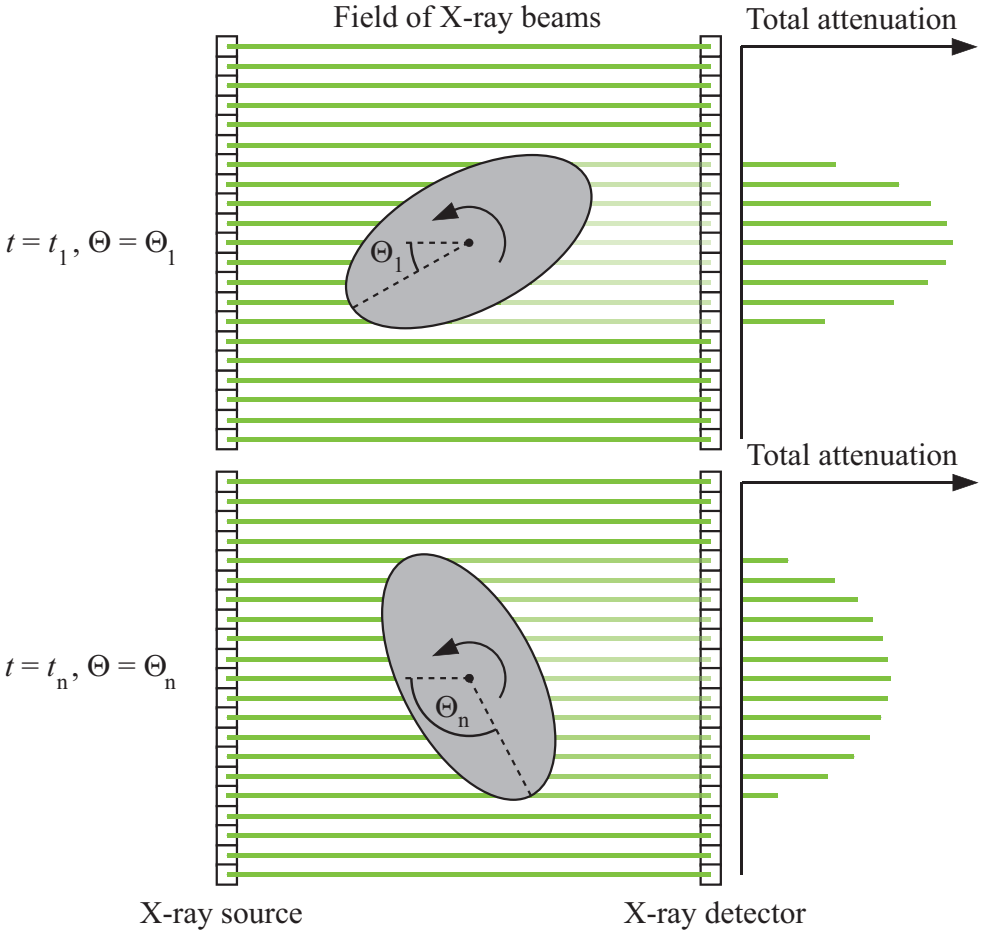


Figure 2.12: Principle of X-ray attenuation and data acquisition in an idealised tomography set-up with parallel beam geometry for two time steps t_1 and t_n and the corresponding projection angles Θ_1 and Θ_n

Every point represented by the coordinates (x,y) along the path of the X-ray through the sample contributes to the attenuation of X-ray energy. The task of the reconstruction algorithm is now to inversely calculate the unknown local attenuation coefficient $f(x,y) = \mu(x,y)$ in every desired discrete point (x,y) on a two dimensional grid in a cross section of the sample to be imaged for many X-ray beams, each of which comes with a measured line integral of total X-ray attenuation in the form of the Radon transform $Rf(t,\Theta)$ as shown in Figure 2.12. Hence, the Radon transform is directly measured as the total (integrated) X-ray attenuation in polar coordinates for every projection angle Θ. In order to obtain the X-ray attenuation μ in every point (x,y) along a single path in cartesian coordinates,

an inverse Radon transform of the measured data in polar coordinates is needed. By combining the information from many beams passing through the object of interest from different angles, the discretised distribution of attenuation on the two dimensional grid in cartesian coordinates $\mu(x,y)$ can be calculated, which is done in the filtered back-projection algorithm as a practical algorithm for solving the inverse Radon transform.

From the mathematical point of view, a so-called inverse problem has to be solved where discrete spatial information on the interior material distribution of an unknown object is to be derived from the integrated result of X-ray attenuation through the object from different angles. As only a finite number of angular projections can be measured, the reconstructed image represents a discretised approximation of reality, however, the accuracy and image quality can be improved to some extent by measuring more projections, *e. g.*, by reducing the angle increment. In practice, the image data contains noise from various sources and the data must be carefully filtered, which is suggested by the name "filtered back-projection". The full mathematical derivation and implementation of the filtered back-projection algorithm is described in detail in Iske (2018).

Besides tomography set-ups based on X-ray tubes, also other radiation sources and different types of radiation can be applied for CT imaging. A multitude of imaging possibilities comes with the application of synchrotron radiation, a very brilliant and monochromatic X-ray beam occurring as a side product of particle accelerators or synchrotrons. Unlike the cone beam emitted by classical X-ray tubes, synchrotron radiation is typically collimated with a very parallel beam geometry and is nearly monochromated so that it mainly contains photons with a single wavelength yielding a relatively homogeneous energy distribution or flux. There is no geometric magnification when synchrotron radiation is applied, and the image resolution must be set by the properties of the detector. Due to the high brilliance, which is a measure of beam quality, considering the flux of photons per beam cross section and time, the degree of collimation, and bandwidth of included wavelengths of the beam, synchrotron radiation has many advantages regarding imaging applications. Typically, short acquisition times with high spatial resolutions can be realised, however, the field of view is frequently limited to a few square millimetres as the beam is very concentrated.

There are different synchrotron radiation research facilities available worldwide where researchers can apply for beamtime. An example of such a facility with different imaging beamlines for materials science as well as biological and medical research is the German Electron Synchrotron (Deutsches Elektronen-Synchrotron, DESY) in Hamburg.

Alternatively to X-rays, also neutron radiation can be applied for CT imaging as described in Section 2.5.4 for radiography imaging. As an atomic reactor is required for the generation of stable neutron fluxes, neutron tomography is mainly available at large research facilities, such as the Institut Laue-Langevin (ILL) in Grenoble, where the most brilliant neutron source in the world is currently available. An innovative approach towards CT imaging is the combination of X-ray and neutron tomography as the different types of ionising radiation are sensitive to different properties of matter. An experimental research facility of this kind is the NeXT tomograph at the ILL (Tengattini *et al.*, 2020).

General problems of computed tomography arise from the compromise between signal-to-noise ratio, resolution, and acquisition time. Due to the imperfection of different compo-

nents in the imaging process, the acquired data is always influenced by statistical noise which typically requires data filtering to improve the signal-to-noise ratio. Besides noise, image data may contain so-called artefacts leading to single pixels or pixel groups with incorrect X-ray attenuation and correspondingly erroneous contrast or interpreted density of the sample. Known types of artefacts include ring artefacts, metal artefacts as well as movement artefacts. While ring artefacts are due to bad measurements of single malfunctioning or miscalibrated detector pixels, metal artefacts are caused by very dense inclusions of matter, such as iron, in a sample. Movement artefacts lead to blurred areas in a reconstructed image if a relative movement of the sample material happens. This might especially be the case when granular materials are imaged. In the case of polychromatic X-ray beams, as produced by X-ray tubes, so-called beam hardening can occur. If X-rays with a multitude of different energy levels pass through matter of varying density or thickness, mainly X-ray photons with higher energies will pass through and reach the detecting unit, whereas photons with less energy will be attenuated more. Thus the photon beam hardens up with regard to its mean energy level in areas with high material thickness leading to differences in the measured absorption contrast. To reduce the effects of beam hardening, special software corrections or monochromatic beams as in the case of synchrotron-based radiation can be applied. Image artefacts can be detected based on experience but can also be compensated for with the help of special image processing software.

2.5.6 Other imaging techniques

Due to the relevance of image data and non-destructive testing in many fields of research, many more imaging techniques have been developed. As this field is very diverse and still expanding, not all methods can be covered in this work. However, to mention another imaging technique besides the methods based on ionising radiation discussed above, Magnetic Resonance Imaging (MRI), which is based on totally different physical principles, is an emerging imaging technique in applications from materials science and engineering. In addition to CT, it might represent an interesting method for imaging applications in geomechanics. In this work, however, it is not further focussed on.

2.6 Numerical modelling and simulation of capillary effects in unsaturated soils

Numerical models and corresponding methods can be applied to simulate capillary effects in unsaturated soils on different length scales. Scientific questions focus on the modelling of the hydraulic and hydro-mechanical behaviour by means of mathematical equations which are solved numerically. In general, continuum and discrete models can be separated, although mixed formulations also exist in literature.

Continuum models are based on continuum theories on the macroscopic scale and typically include macroscopic constitutive models and soil properties, such as stiffness, shear

strength or permeability, to describe the mechanical and hydraulic soil behaviour. As discrete models focus on the physical behaviour of discrete quantities, such as single particles, and on their interaction, these models are rather working on the microscale. Therefore, it is convenient to add discrete models to the group of microscale or microscopic particle models. However, also upscaling methods, such as *coarse-graining*, exist for particle models, aiming to establish a link to the macroscopic behaviour. In between the microscopic and macroscopic length scales of modelling approaches, also mesoscale models may be grouped, *e. g.*, models based on Boltzmann's kinetic theory. Furthermore, hybrid or multiscale approaches which model soil behaviour on different length scales by linking different numerical methods can be identified.

Within the scope of this section, a brief overview on numerical modelling of capillary effects in unsaturated soils on different length scales and on the corresponding numerical methods for numerical simulations on this field is given.

2.6.1 Continuum approach on the macroscopic scale

The continuum approach to the modelling of unsaturated soil behaviour is based on different continuum theories. The considered physical problem is generally described by mathematical model equations describing the evolution and relationships of physical variables on a continuum level, typically by partial differential equations based on conservation equations. Besides these governing model equations, mathematical constitutive formulations, seeking to reproduce the macroscopic soil behaviour as derived from soil mechanical experiments based on the "element test philosophy"[8], must be mentioned as they represent the essence of the continuum modelling of material behaviour. These constitutive models, along with their model parameters, are generally calibrated based on dedicated laboratory tests to yield a realistic numerical material response of an assumed single soil element with homogeneously distributed continuum state variables, such as density, degree of saturation as well as suction, stress, and strain distribution. After calibration and validation based on experimental data, the constitutive models are applied for the modelling of material behaviour in larger simulation domains reflecting a studied boundary value problem to be solved.

A frequently applied numerical continuum method is the Finite Element Method (FEM) in which the governing model equations are solved by means of a discretisation of space. If temporal processes are modelled, also time is discretised using finite difference schemes. This procedure requires the assumption that the constitutive model formulated for a soil element is valid for the whole continuum over all length scales. In the most simple case, the constitutive model including the complete considered unsaturated material behaviour is applied with "standard" finite elements with displacement degrees of freedom for mechanical stress-strain analyses. An example of an early elastoplastic constitutive model

[8] Element test: Laboratory experiment seeking to submit soil specimens idealised as continuum elements with homogeneous properties to controlled boundary conditions in order to yield homogeneous physical specimen responses, *e. g.*, stress and strain fields in the case of mechanical tests, as a prerequisite for the formulation of deterministic mathematical constitutive models with corresponding model parameters.

for unsaturated soils is the "Barcelona Basic Model" (Alonso *et al.*, 1990), describing the mechanical behaviour of unsaturated soils under the influence of matric suction.

Another approach to the modelling of unsaturated soil behaviour can be seen in continuum models that include state variables of unsaturated soils on the level of their mathematical formulation. Prominent examples are continuum theories with additional degrees of freedom, such as liquid and gas pressures in order to account for capillary pressure and its influence on effective stress. One example is the $\boldsymbol{u}$-p-p formulation (Lewis and Schrefler, 1998; Zienkiewicz *et al.*, 1999) based on the early work regarding two-phase formulations by Zienkiewicz *et al.* (1980). The $\boldsymbol{u}$-p-p formulation is a fully coupled hydro-mechanical continuum model where the displacements of the solid phase $\boldsymbol{u}$ are coupled to the gas and liquid pressure. If the FEM is applied as a numerical method, finite elements with additional pressure degrees of freedom are required. The formulation furthermore includes a water retention model, coupling capillary pressure and degree of saturation, as well as a permeability model for unsaturated flow. The stress-strain behaviour of the solid phase is modelled with a soil mechanical constitutive model that can be formulated in effective stresses and with enhancements to include capillary effects, *e. g.*, by introduction of suction stress. Similar to the FEM, but with focus on large deformations of materials, the Material Point Method (MPM), originally proposed by Sulsky *et al.* (1994), can be enhanced to model unsaturated soils (Yerro *et al.*, 2015; Ceccato *et al.*, 2021).

2.6.2 Discrete particle approach on the microscopic scale

Besides the continuum approach, being very versatile and well applicable to the simulation of large practical engineering problems, also discrete or microscale models exist, allowing to obtain insights into the micromechanical or microhydraulic behaviour of unsaturated soils. Here, the terms "micromechanics" and "microhydraulics" refer to physical processes occurring on the particle or pore scale and to the corresponding numerical tools to model them.

A prominent example of a method to simulate the dynamic mechanical interaction of particulate materials on the particle or grain level is the Distinct or Discrete Element Method (DEM), firstly proposed by Cundall and Strack (1979). In the basic form of DEM, particles are modelled as spheres with elastic properties interacting with other particles and rigid walls at contact. The particle trajectories over time are solved via explicit integration of Newton's laws of motion, with particle-particle or particle-wall contacts leading to an exchange of contact forces and momentum. Micromechanical interactions upon particle contact, such as friction and damping, are accounted for by mechanical spring and dashpot models and corresponding material parameters. If non-spherical particles are to be modelled, extended formulations are required, such as the Level Set DEM (LS-DEM) where level set functions for the modelling of arbitrary particle geometries are used (Kawamoto *et al.*, 2016). Other numerical methods based on discrete elements are the DEM with Bonded-Particle Models (BPM) (Thomas and Bray, 1999; Potyondy, 2015) where arbitrary particle shapes are achieved through approximation by clusters of spheres which are bonded together, or the Combined Finite-Discrete Element Method (FDEM) presented by Munjiza (2004). The latter hybrid method approximates an arbitrary particle

shape by a multitude of finite elements and is very well suited for deriving mechanical particle scale models from CT data (Turner *et al.*, 2016; Nadimi and Fonseca, 2019; Thakur and Penumadu, 2020).

For the simulation of capillary effects, the DEM can be enhanced by the previously mentioned Bonded-Particle Models (BPM) in order to model cohesive behaviour or liquid bridges. The mechanical behaviour of such particle bonds can be controlled by constitutive laws controlling the elasticity or rupture strength of the bonds, *e. g.*, as a function of particle separation distance. Different levels of complexity of capillary bond models exist in literature. While capillary bonds can be modelled by simple force-displacement laws, also more complex models which even consider the geometry of capillary bridges and liquid clusters as well as their specific contact areas touching the solid phase exist for DEM-applications (Liu *et al.*, 2020).

2.6.3 Boltzmann's approach on the mesoscopic scale

As an alternative to conventional computational fluid dynamics (CFD) approaches, which are generally grouped to the continuum approach, the Lattice Boltzmann Method (LBM) has developed in the last decades as a powerful numerical tool to simulate fluid-structure interaction. Originating from cellular (gas) automata, used for the simulation of molecular gas dynamics problems, the modern LBM is based on the discretised form of the Boltzmann equation which is solved numerically on a lattice or grid. It originally describes the dynamic collision-based interaction of molecules or "particles" in gases in a statistical approach using a probability distribution of the particles' position and momentum based on Ludwig Eduard Boltzmann's[9] gas kinetic theory. The numerical method models fluid flow on a mesoscopic level which can be considered in between the pure particle scale and macroscopic level because particle density or momentum distributions are focused on, rather than individual particles or pure continuum properties. A comprehensive introduction to the origins of LBM and the numerical method itself is given by Krüger *et al.* (2017).

After first single-phase formulations, the LBM has been extended to simulate multiphase problems, such as flow processes as well as capillary effects along with the dynamic interaction of wetting and nonwetting fluids in porous media (Pan *et al.*, 2004; Schaap *et al.*, 2007; Huang *et al.*, 2015). Multiphase LBM models can be applied to study the water retention behaviour in granular media on a numerical basis as presented by Hosseini *et al.* (2021). Their numerical results indicate that the multiphase LBM is capable of reproducing the S-shaped water retention curve during imbibition of a liquid into an artificial pore space in between a packing of spheres. Due to its intrinsic numerical capability of reproducing capillary effects, the multiphase LBM can capture phase separation with sharp interfaces resulting in the formation of capillary structures in porous media, such as liquid clusters, capillary bridges, and gas bubbles, which resemble well to experimental results, *e. g.*, found in CT images.

[9] Ludwig Eduard Boltzmann (1844–1906): Austrian physicist and philosopher, considered as one of the founders of statistical mechanics.

2.6.4 Multiscale approaches

In a multiscale approach, different modelling techniques are coupled, linking multiple length scales. As an example of a coupling of meso- and microscale, the LBM can be coupled to the DEM, with fluid dynamics in a discretised pore space or a free water phase being modelled by LBM and the particle dynamics being simulated by DEM. Hydrodynamic forces as calculated by the LBM are added to the contact forces of the particles for the hydro-mechanical coupling (Cook *et al.*, 2004; Iglberger *et al.*, 2008). Focusing on geophysical hazards, such as landslides, Soundararajan (2015) presents a 2D coupled LBM-DEM technique to study liquid-saturated granular flow behaviour.

Chapter 3

Characterisation of experimental materials

In this work, capillary effects in different granular materials are investigated. These materials have been selected as representatives of different soils with relevance in geotechnical engineering and will be briefly described in this chapter together with the fluids used in most of the experiments.

3.1 Materials used in the experiments

3.1.1 Hamburg Sand

A representative of natural soils is "Hamburg Sand", a natural medium coarse to coarse-grained sand that is used as a model sand at TUHH. In order to continuously guarantee the same quality of the model soil, it is obtained from a gravel quarry (WIKA Sand und Kies GmbH & Co. KG) at Stade, Germany as a product labelled "Quarzsand (Körnung K4)".

The grain size distribution curve of Hamburg Sand is shown together with a microscopic image in Figure 3.1. Hamburg Sand contains rounded and also angular grains. Most of the grains are characterised by smooth surfaces and a well rounded shape as the main part is quartz sand. However, also other minerals, such as feldspar, are present. Grains consisting of non-quartz minerals are typically rather of a rough surface appearance with frequently sharp and broken edges.

Due to limited resolution of the CT scanners used in imaging experiments, the grain fraction smaller than 0.063 mm has been removed from the original material by washing the sand on a sieve. Furthermore, the main part of ion ore containing sand grains has been removed with a magnet in order to avoid metal artefacts in CT images.

Standard soil mechanical properties of Hamburg Sand are summarised in Table 3.1.

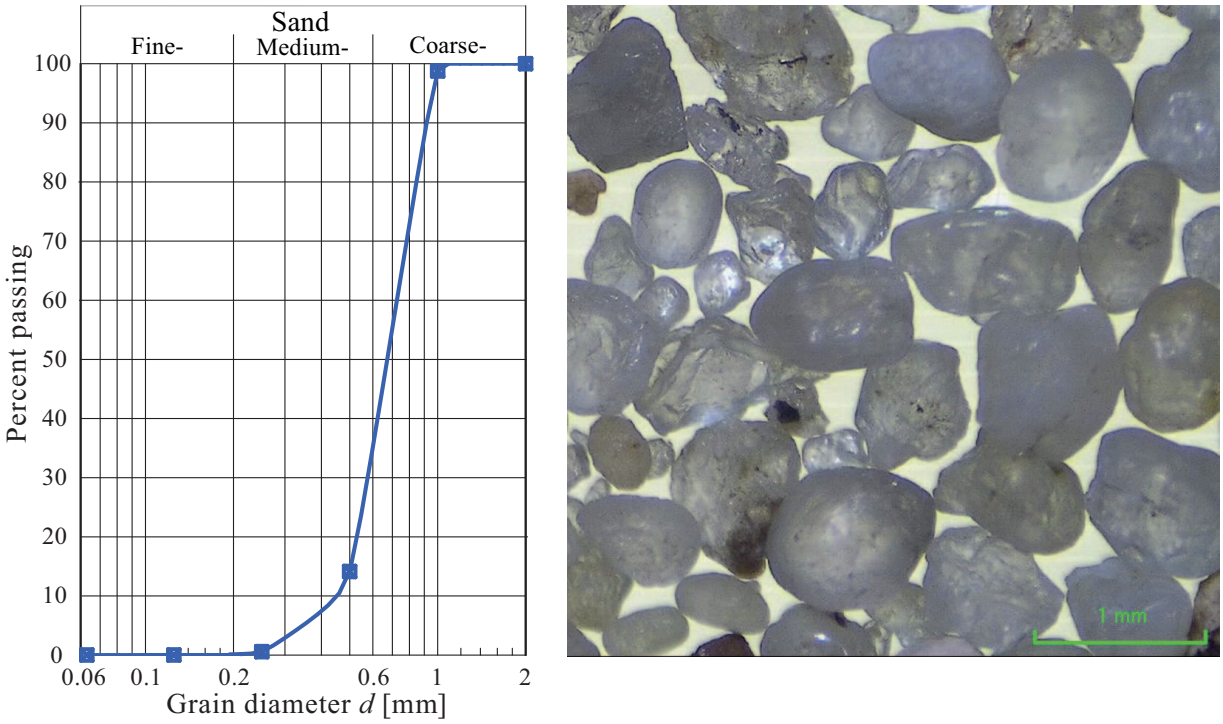


Figure 3.1: Grain size distribution and microscopic image of Hamburg Sand

Table 3.1: Selected soil mechanical properties of Hamburg Sand

ρ_s [g/cm^3]	e_{min} [-]	e_{max} [-]	d_{10} [mm]	d_{50} [mm]	d_{max} [mm]
2.64	0.52	0.805	0.45	0.68	2.0

ρ_s: grain density, e_{min}: min. void ratio
e_{max}: max. void ratio
d_{10}: grain diameter at 10% passing
d_{50}: grain diameter at 50% passing
d_{max}: max. grain diameter

3.1.2 Soda-lime glass beads

In order to investigate the influence of grain shape of irregular shaped and spherical particles, soda-lime glass beads, type S, manufactured by Sigmund Lindner GmbH, Germany, have been selected to represent rather ideal spherical particles in comparison to Hamburg Sand. These particles with smooth polished surfaces are available in different diameters and are characterised by a relatively high roundness ≥ 0.95 (here defined as ratio of minimum grain width to maximum grain length) according to their manufacturer. CT images confirm that not all grains are exact spheres. Furthermore, a very low quantity of mechanically damaged spheres as well as spheres containing occluded air bubbles can be identified.

As described in Milatz (2019), a mixture of different ranges of sphere diameters has been prepared to approximate the grain size distribution of Hamburg Sand. If nothing else is mentioned, this mixture is considered and simply named as "glass beads" in this work. The grain size distribution of this mixture of soda-lime glass beads is illustrated in Figure 3.2 together with a microscopic image of a particle assembly.

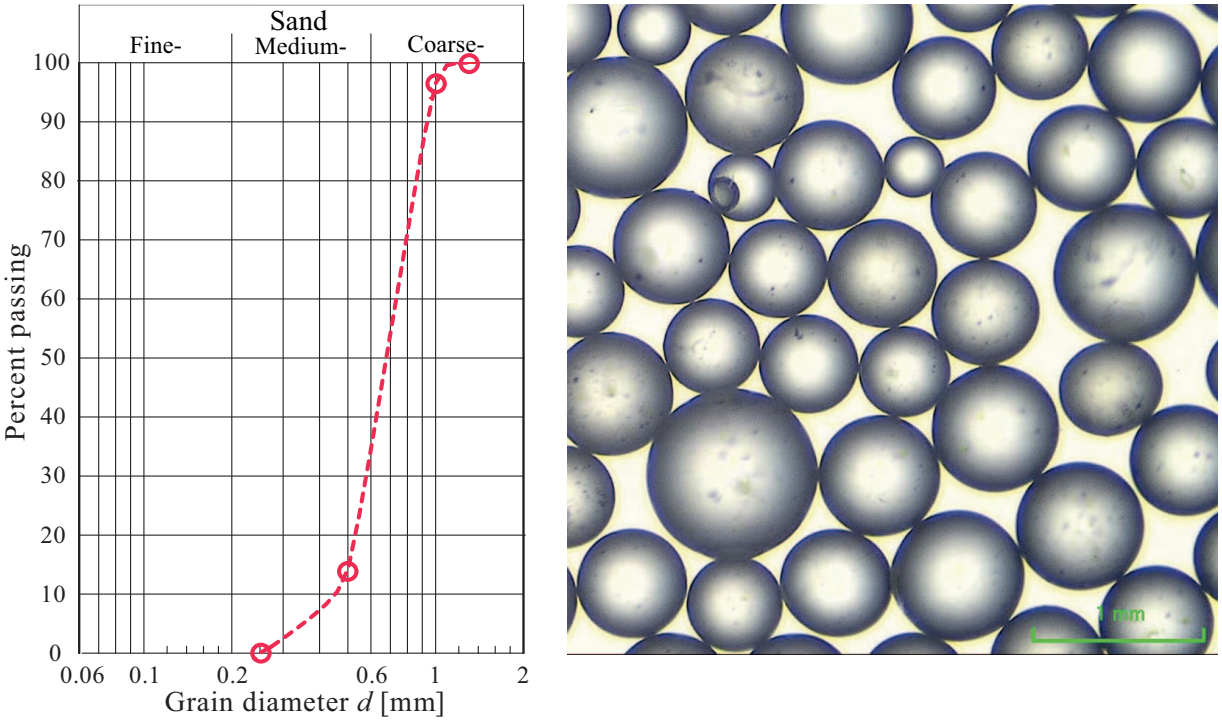


Figure 3.2: Grain size distribution and microscopic image of a glass bead mixture with grain size distribution adapted to Hamburg Sand

Standard soil mechanical properties of the glass beads studied in this work are summarised in Table 3.2.

Table 3.2: Selected soil mechanical properties of the mixture of glass beads

ρ_s [g/cm^3]	e_{min} [-]	e_{max} [-]	d_{10} [mm]	d_{50} [mm]	d_{max} [mm]
2.50	0.555	0.679	0.45	0.68	1.3

3.1.3 Water and air

In this work, the natural capillary behaviour of the fluids air and water interacting with granular materials is investigated. Different physical and chemical phenomena influence the properties of water in nature but also in our experiments. Firstly, the surface tension of water as one of the most important liquid properties regarding capillary effects is

dependent on temperature as shown in Figure 3.3. Please recall that strictly speaking, the applied term "surface tension" refers to thermodynamic equilibrium of chemically pure liquid and its surrounding vapour as discussed in Chapter 2. The more general term would be "interfacial tension".

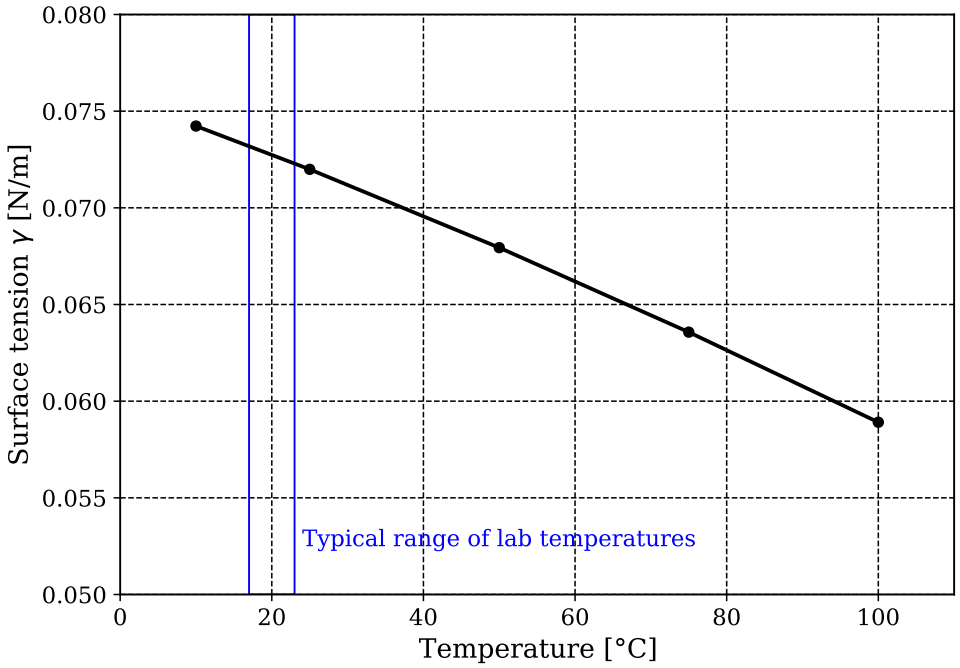


Figure 3.3: Dependence of surface tension of water on the temperature from Butt *et al.* (2003)

Furthermore, chemical solutes, surfactants (surface-active agents), and other impurities influence the surface tension (Butt *et al.*, 2003; Myers, 2006). As compared to the temperature, the presence of such impurities of water can lead to an even more pronounced impact on the magnitude of surface tension. An impressive example is the effect of soap reducing the surface tension so much that aquatic insects cannot use the water surface for floating any longer. The effect of different impurities is hard to measure from the chemical point of view, *e. g.*, refer to Posner *et al.* (1952), Butt *et al.* (2003) or Russo and Hoffmann (2010), as its measurement requires meticulous chemical lab experiments using ingredients of highest purities. Such "chemical lab conditions" and a control of the actually present interfacial tension can usually not be achieved in soil mechanical experiments due to the complexity of this task and especially, when mineral-containing soils are present. An impression of the sensitivity of the surface tension of water is given by the curve in Figure 3.4. The data reflect the pronounced reduction of surface tension of water-alcohol mixtures at a controlled temperature of 25 °C with increasing alcohol content as measured by Bircumshaw (1922).

As an attempt to control the chemical properties of water in all experiments, we use de-ionised water at laboratory temperatures of *ca.* 20±3 °C which is common for a soil mechanical lab. Despite the lab air conditioning, different water temperatures can lead

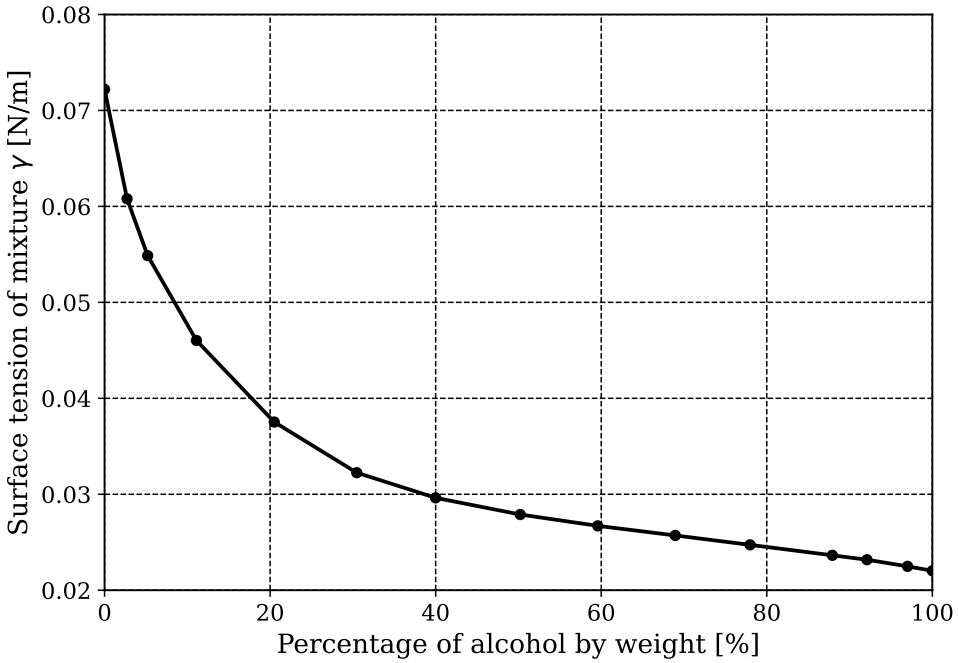


Figure 3.4: Dependence of surface tension of water-alcohol mixtures at a temperature of 25 °C on the weight percentage of alcohol from Bircumshaw (1922)

to slight variations in surface tension which are not explicitly controlled in the presented experiments. The effect of varying lab temperatures on surface tension of water is highlighted in Figure 3.3. Furthermore, in order to assess the surface tension of the "lab water" used in the experiments, measurements based on the Wilhelmy plate method are taken using a Force Tensiometer-K100 (manufactured by Krüss) as illustrated in Figure 3.5. In the Wilhelmy plate experiment, surface tension is calculated from the reaction force measured on a thin plate which is wetted by the tested liquid forming a meniscus. Prior to each measurement, the Wilhelmy plate is carefully cleaned by tap water, ethanol, and de-ionised water. Before its mounting in the force tensiometer, the Wilhelmy plate is finally flame treated with a Bunsen burner. In the experiments, de-ionised water from the soil mechanical research lab at TUHH is tested. After measurement of the surface tension of this water, Hamburg Sand and glass beads are added to verify the individual influence of these granular materials on surface tension.

The results of several measurements with varying number of samples N in Figure 3.5 reveal a mean surface tension $\gamma = 54.35$ mN/m of the de-ionised water sample which is much lower than the nominal value of pure water. The variation of surface tension in a series of N experiments is found to be low as judged by the given error bars highlighting the standard deviation of measured surface tension. Interestingly, the application of *ca.* three teaspoons of Hamburg Sand or glass beads to the tested water leads to an increase of surface tension as shown in Figure 3.5. While surfactants or alcohols generally reduce surface tension, the presence of solved ions, *e. g.*, from salts or from silica reactions possibly occurring in the tested granular materials in contact with water, is known to increase surface tension

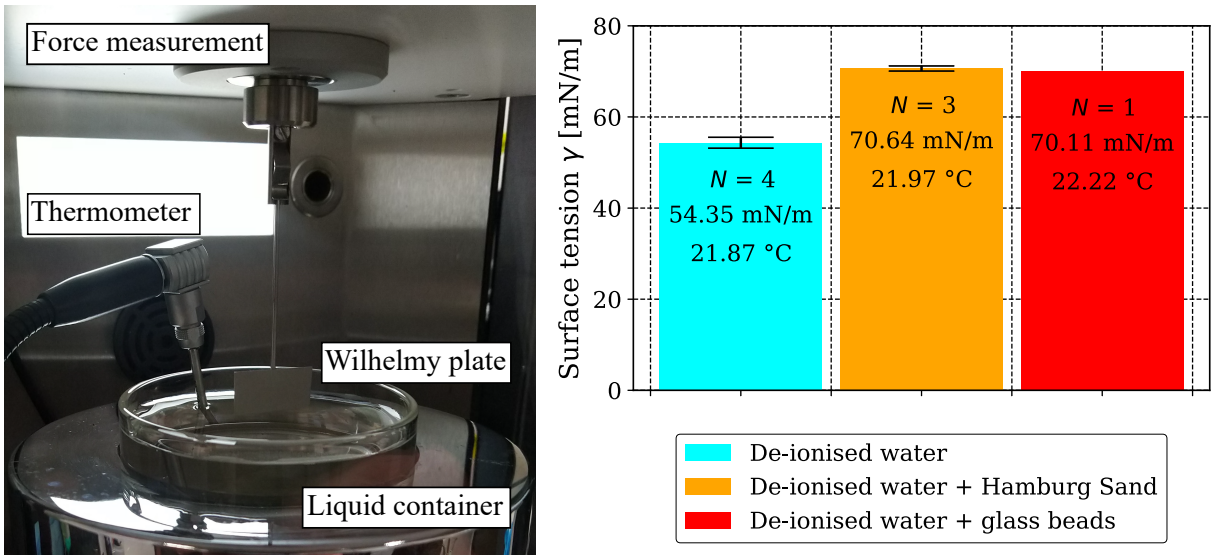


Figure 3.5: Measurement of surface tension by means of Wilhelmy plate method (left) and measured surface tension for de-ionised "lab water" and its mixture with Hamburg Sand and glass beads (right)

(Levin and Flores-Mena, 2001; Wang *et al.*, 2018).

The air "used" in all experiments represents the unfiltered ambient air in the lab at typical temperatures of *ca.* 20 ±3 °C. As in most cases no air pressure is controlled, it is supposed to be equivalent to the atmospheric air pressure. However, strictly speaking, this is only the case in a porous medium if the air phase is connected and continuous.

3.2 Hydro-mechanical behaviour

For the characterisation of hydro-mechanical behaviour, standard drained triaxial tests according to DIN 18137-2:2011-04 have been performed resulting in effective friction angles of $\varphi' = 33.9°$ ($e_0 = 0.65$) for Hamburg Sand and $\varphi' = 22.3°$ ($e_0 = 0.6$) for glass beads.

The water retention behaviour as a key function of hydro-mechanical behaviour in the unsaturated state has been measured with the help of Hyprop evaporation tests, based on the work by Peters and Durner (2008) and Schindler *et al.* (2010) and manufactured by UMS GmbH/Meter Group. The evaporation method allows to measure equilibrium primary drainage paths of the initially water saturated granular materials as shown in Figure 3.6 for Hamburg Sand and glass beads. The water retention curves are fitted with the van Genuchten (1980) model according to Equation 2.9 in Chapter 2 using the parameters indicated in Table 3.3.

Compared to other soils with finer grains, the impact of capillary effects in Hamburg Sand and glass beads can be classified as rather low if the suction level at typical degrees of saturation is applied for classification. The water retention curves of both materials show AEVs below 1 kPa, with higher suction being present in Hamburg Sand at the same

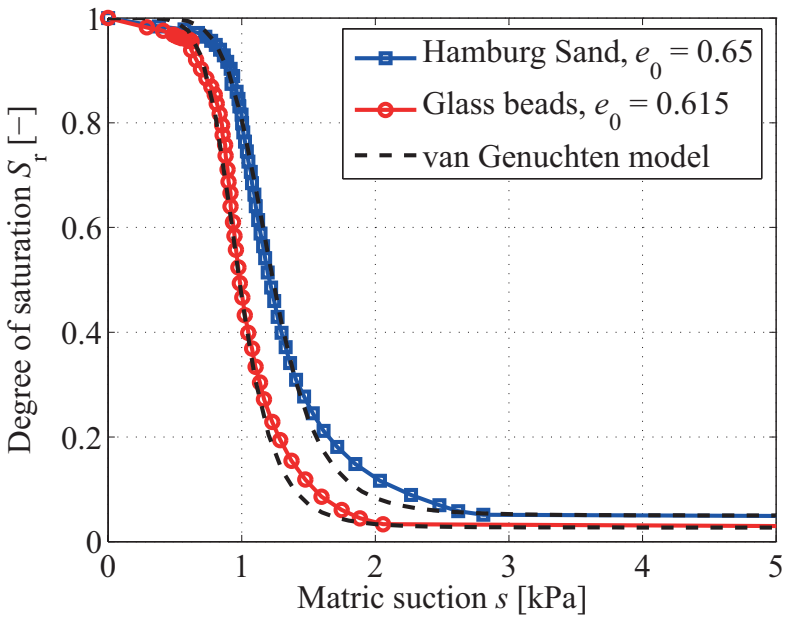


Figure 3.6: Equilibrium primary drainage paths of the water retention curve of Hamburg Sand and glass beads from Milatz *et al.* (2021b) measured with the Hyprop evaporation test and fitted by the van Genuchten model (van Genuchten, 1980)

Table 3.3: Parameters of the van Genuchten model

Material	α [1/kPa]	n [-]	S_{res} [-]
Hamburg Sand	0.847	7.3	0.050
Glass beads	1.053	7.7	0.027

$\alpha, n, (m = 1 - 1/n)$: fitting parameters (van Genuchten, 1980),
S_{res}: residual degree of saturation

saturation level as in the glass beads. It should be noted that the WRCs are shifting towards higher suction when void ratio is decreased and towards lower suction if void ratio is increased according to the density-dependence of the WRC. Furthermore, both materials show hysteretic WRCs for cyclic drainage and imbibition which is described in detail in Milatz (2020a) and in following chapters of this work.

Chapter 4

Development of miniaturised testing devices for imaging experiments

The design of miniaturised experimental set-ups requires knowledge in the field of measurement technology, electrical engineering, and also informatics as the set-ups typically consist of mechanical and electronic hardware components and software. The recent developments in the availability of single-board computers (Milatz, 2019; Milatz, 2020b), circuit boards for all kinds of purposes as well as open hard- and software and their documentation on the internet have made it possible for everyone to solve problems related to automation, robotics, and control engineering. The exchange of ideas and technical documentation is boosted by the maker scene, by internet forums, and data repositories, which is very useful from the point of view of research and education. In these fields, individual technical solutions for research can be designed and students can be taught practical programming in an illustrative way based on "physical computing".

The possibility to conduct soil mechanical experiments in a CT scanning environment, such as a laboratory X-ray CT scanner or a CT system based on synchrotron radiation or neutrons, opens the door to a better understanding of hydraulic or mechanical processes and furthermore allows to quantitatively measure and analyse microscopic properties in four dimensions. In this chapter, the idea of such "4D experiments", *i. e.*, physical *in situ* experiments with collection of data over 3 spatial dimensions plus time as the fourth dimension, is outlined focusing on unsaturated soils. Accordingly, different specialised experimental set-ups, representing the centre pieces of imaging experiments of various complexity, will be highlighted, roughly following the chronology of their development.

4.1 Hard- and software for creating individual testing apparatuses

The mechanical testing of materials represents a large field of applications in engineering research. In geotechnical engineering, testing equipment for the measurement of shear strength and stiffness of geomaterials is required. Depending on the type of mechanical

test, the measurement or control of forces or displacements as well as stresses and strains is typically of concern. Furthermore, in hydraulic experiments, the flow of fluids, such as water and air, as well as corresponding pressures need to be controlled or measured. For this purpose, special dosing pumps and pressure sensors can be applied.

For the design of individual testing environments as outlined in this chapter, an open hard- and software approach is followed which allows to realise very customised and typically low-cost applications based on easily accessible hardware components and open software.

For the experimental test control of all proposed experimental devices, a single-board computer has been selected. As outlined in Milatz (2020b), single-board computers have encountered a renaissance in the last decade due to the availability of cheap and versatile models on the market, the documentation of many technical applications on the internet, and their use in school and undergraduate teaching as well as in research.

In this work, the *Raspberry Pi* single-board computer has been selected as the main piece of hardware for the control of different experiments. The miniaturised computer in the size of a credit card was originally designed by the Raspberry Pi Foundation to boost digitalisation and programming in school education (*Raspberry Pi* 2022) following the physical computing approach which includes illustrative projects, *e. g.*, from the field of robotics or electrical engineering. As illustrated in Figure 4.1, the single-board computer can be connected to different peripheral devices allowing to control actuators or to read out sensors.

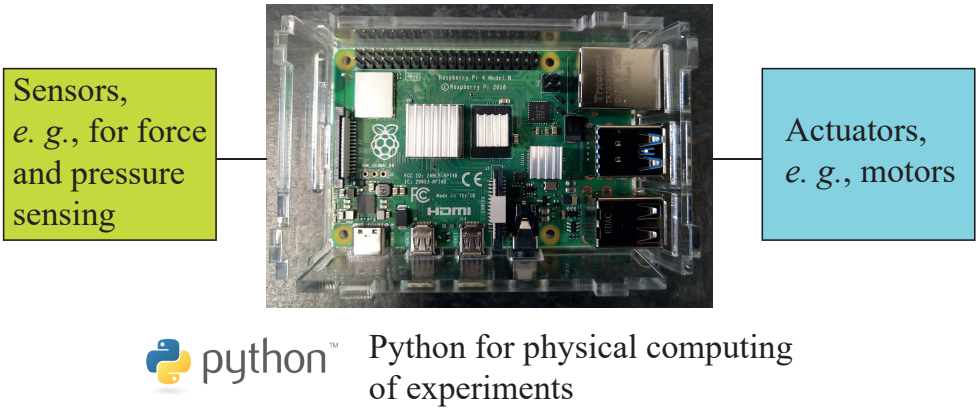


Figure 4.1: Application of the Raspberry Pi single-board computer for physical computing tasks

Besides the success story of single-board computers, also open and well-documented programming languages with the aim to reach a large community in teaching and research are available today. One example is the Python programming language, firstly released in 1991 with the aim to create a new, well-readable, and versatile programming language. Python is distributed with the Raspberry Pi and will also be used in this work for hardware control and data logging as illustrated in Figure 4.1.

For displacement controlled loading as well as the control of water flow, motors are needed to drive loading plates as well as pumps. Stepper motors represent a valuable selection as

they allow to prescribe rotation angles in an incremental and very repeatable way. In the experimental set-ups presented in the following, stepper motors are used to apply linear motion to loading plates in mechanical experiments and to drive linear spindle drives in syringe pumps which apply a certain flow in hydraulic experiments.

As an interface between the single-board computer and the stepper motor, a motor driver board is applied which encodes the digital signals issued by the single-board computer and transforms them into motor movements. The digital signals can be directly turned on and off by means of Python scripts and dedicated functions to control motors in different experiments. An example of such a Python script is published in Milatz (2020a) to control a syringe pump.

Both for the linear motion of loading plates and syringe pump plungers, stepper motors in combination with a linear worm or spindle drive have been considered (Milatz, 2019; Milatz, 2020a). Depending on the step resolution of the motor and the selected kind of spindle, *e. g.*, an M5-threaded steel rod with its individual pitch, different resolutions of displacement or pumping volume control per motor step can be achieved. When the applied number of steps is known in the software, the displacement control of mechanical loading plates or volumetric dosing control of syringe pumps can be calibrated and applied to calculate the prescribed displacements and volume changes with sufficient accuracy depending on the specimen dimensions and selected kind of application.

With regard to the sensing of mechanical or hydraulic quantities, the measurement of forces, pressures, and corresponding displacements is of importance in geotechnical engineering applications. In all set-ups presented in this work, load cells and pressure sensors are applied which can be connected to the Raspberry Pi single-board computer's General Purpose Input/Output (GPIO) pins. Those pins represent the electronic interface to most peripheral devices. As the I^2C-interface implemented in the Raspberry Pi to process external data can only handle digital input data, the analog signals from typical load cells or pressure sensors need to be converted. For this purpose, a 16-bit analog-to-digital converter (A/D-converter or ADC) is applied allowing to translate the frequently used analog voltage output data of sensors to a digital scale which can be processed in the Python software.

As the *in situ* testing of unsaturated granular media under very low confining pressures requires the resolution of very low forces as well as relatively low matric suction, load cells and pressure sensors with sensing ranges of only a few newtons or kilopascals, respectively have been selected. These miniaturised sensors typically need an external power source which is delivered by a stabilised laboratory power supply and provide a voltage output with a signal being proportional to the physical variable to be measured. All sensing devices are individually calibrated and the calibration is carefully implemented in the Python software used to read and log sensor data.

In all experimental set-ups presented in the following, very different hardware components have been selected and combined to meet the individual needs of each single experiment. Therefore, it is underlined that careful testing and calibration of all hardware and software components is urgently needed. Although the control of linear motion with stepper motors is relatively fail-proof due to their accuracy and repeatability of rotation angles, all linear drives have been thoroughly tested and calibrated by comparison of prescribed motor

movements to independent measurements. The same holds true for force or pressure measurements using load cells or pressure sensors in combination with ADCs. While load cells are calibrated with the help of dead weights with known masses, pressure sensors for the measurement of matric suction are calibrated by means of a hanging water column apparatus similar to the device presented in ASTMD6836-16 (2016) allowing to apply small underpressures with an accuracy of 1 mm of hanging water head.

4.2 Miniaturised uniaxial compression apparatus

4.2.1 Field of application

In order to study the shear behaviour of unsaturated granular materials under nearly zero confining pressure, a miniaturised uniaxial compression apparatus has been designed (Milatz, 2019). The uniaxial compression test, a standard test in soil mechanics mainly applied for the investigation of the uniaxial compression strength as well as undrained shear strength of cohesive soils, has been selected because it allows to apply shear to a laterally unconfined soil specimen, *i. e.*, at quasi zero confining pressure. From the point of view of unsaturated granular soils where typically very low matric suction leads to capillary cohesion of only a few kilopascals, the capillary effects dominate the mechanical stress state in such an experiment as the confinement pressure is negligible. Accordingly, the uniaxial compression test allows to study the effect of degree of saturation and suction on shear strength without having the relatively small capillary effects being masked by confining pressure.

The designed apparatus is small enough to be placed in an environment for *in situ* CT experiments (Milatz and Grabe, 2019) allowing to gather further insights into the shear behaviour as well as volume change of unsaturated granular media on the grain scale which will be reported in chapters 5 and 6.

4.2.2 Technical details

The uniaxial compression apparatus, named the "UNSAT-*Pi*", consists of a miniaturised compression device with a displacement controlled loading mechanism driven by a stepper motor, a miniature load cell, and a Raspberry Pi 3 B single-board computer for experimental control and data logging. The experimental design, calibration, testing, and first experimental results are fully described in Milatz (2019) and in Milatz (2020b). The experimental set-up around the UNSAT-*Pi* is illustrated in Figure 4.2.

The wiring diagram, showing all hardware components and their connections, is given in Figure 4.3. For wiring, jumper cables with female or male connectors as shown in Figure 4.2 are used allowing to build simple electrical circuits without soldering.

In the prototype version of the uniaxial compression apparatus, a small stepper motor (manufactured by Changzhou Fulling Motor Co., Ltd., China) with 512 steps per rotation (step angle of *ca.* 0.7°), connected to an ULN 2003 driver board for applications in robotic

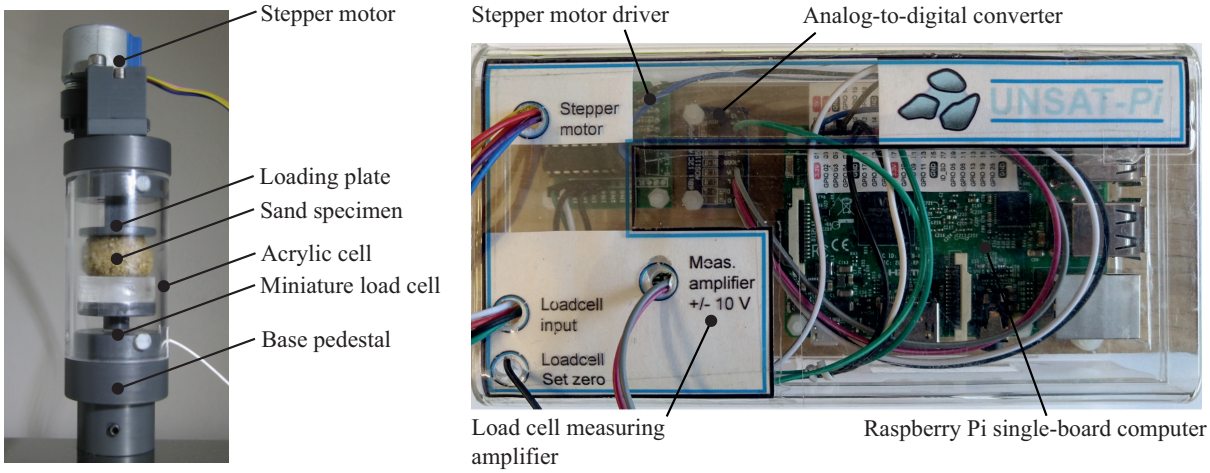


Figure 4.2: Details of the UNSAT-*Pi* set-up including the miniaturised uniaxial compression apparatus with sheared unsaturated sand specimen (left) and a single-board computer for experimental control and data logging (right) from Milatz (2020b)

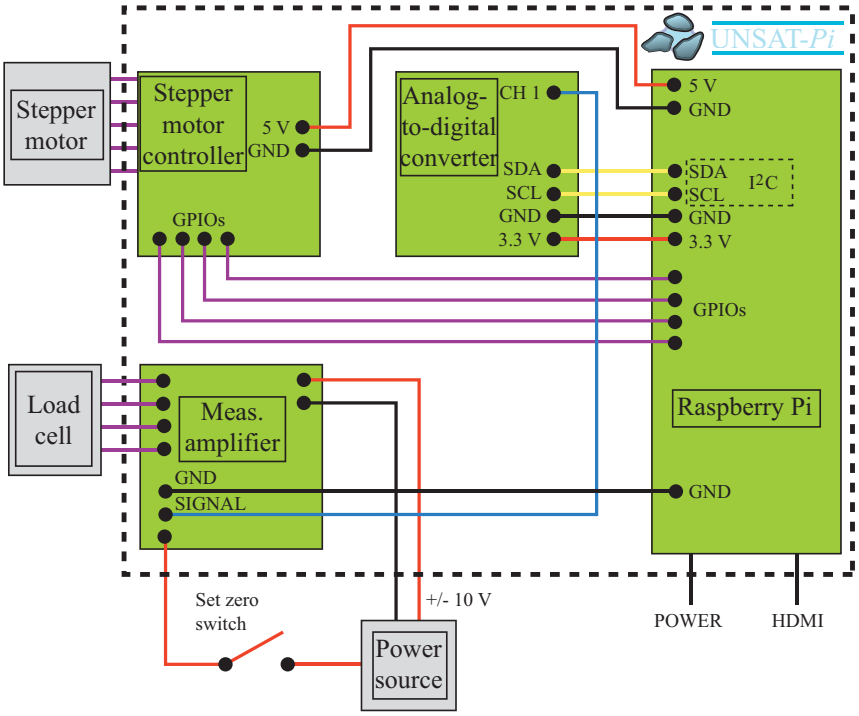


Figure 4.3: Wiring diagram showing the components and connections forming the UNSAT-*Pi* experimental set-up for miniaturised uniaxial compression tests (Milatz, 2020b)

toys, is implemented for the displacement controlled movement of the vertical loading plate. In a later development, a NEMA 17 stepper motor with 200 steps per rotation (step angle of 1.8°), driven by a *DRV8825 stepper motor controller board*, is applied. The driver boards are connected to the GPIO pins of the applied single-board computer

allowing to initiate motor steps with the control software.

The axial force is measured with a miniature load cell with a range of 25 N (KM10z, ME-Meßsysteme, Germany). The analog output data of the load cell is translated to a digital signal by a 16-bit *ADS1115 analog-to-digital converter* (Adafruit learning system). The load cell is calibrated by dead weights that are stacked on the loading plate, resulting in an individual calibration of the force measurement that can be used in the software.

For the measurement of the specimen diameter during uniaxial compression in laboratory experiments, images of the specimen deformation can be taken with a supplementary camera equipment. This allows to assess the specimen volume change and specimen cross sectional area in order to calculate axial stress in the middle of the specimen.

The Python software used for experimental control allows to set a target displacement at a given displacement rate while at the same time logging the applied displacement and measured forces to file. While the specimens are sheared continuously in experiments under lab conditions, the *in situ* CT experiments require a step-wise loading procedure to capture CT images in between loading steps.

4.2.3 Specimen preparation

The uniaxial compression apparatus allows to investigate the shear behaviour of soil specimens with a maximum diameter of up to 30 mm at a maximum height of *ca.* 40 mm. In different applications, unsaturated glass bead and sand specimens, with diameters and heights of 20 mm as well as diameters and heights of 12 mm have been tested where the smaller specimen dimensions have been selected in *in situ* CT experiments.

Free-standing laterally unconfined unsaturated granular soil columns for uniaxial compression tests are prepared by mixing the desired dry mass of the granular material, corresponding to a selected initial porosity, with the selected amount of water in order to reach the target initial gravimetric water content w or degree of saturation of the specimens. After careful mixing and homogenisation, *e. g.*, by stirring in a ceramic bowl, the material is filled in a special hollow cylinder in layers which are individually scarified with a screw driver to avoid the formation of segregated layers. Especially glass beads tend to segregation. The different layers of granular material are carefully compacted with a piston until the selected specimen height is reached. Finally, free-standing specimens are obtained by slowly pushing the specimens out of the hollow cylinder. The whole procedure requires some practice, but finally allows to create unsaturated laterally unconfined specimens with fixed dimensions in a repeatable way.

4.2.4 Selected results

The specimen shapes during continuous uniaxial compression of a specimen of Hamburg Sand and glass beads with initial diameter and height of 20 mm are illustrated in Figure 4.4.

The measured macroscopic stress-strain relationships as well as the development of specimen cross sectional area as an indicator of volumetric behaviour are shown in Figure 4.5

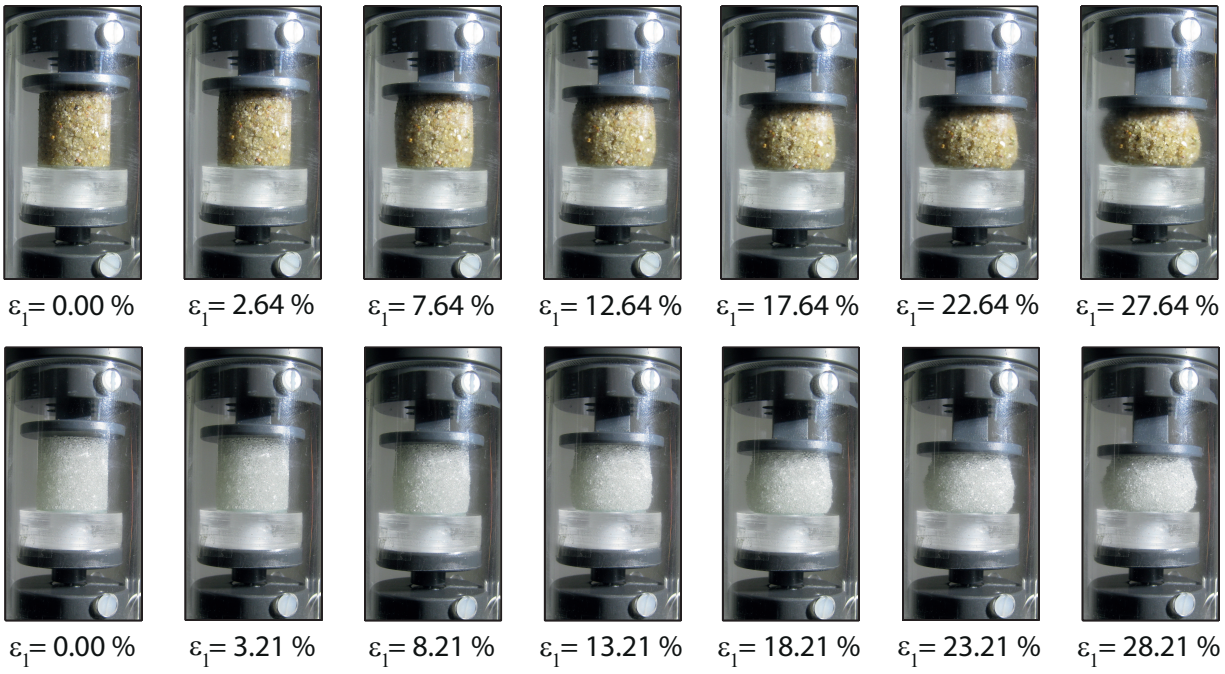


Figure 4.4: Uniaxial compression of an unsaturated specimen of Hamburg Sand at $e_0 = 0.65$ and $S_r = 0.671$ (top) and glass beads at $e_0 = 0.614$ and $S_r = 0.675$ (bottom) from Milatz (2019)

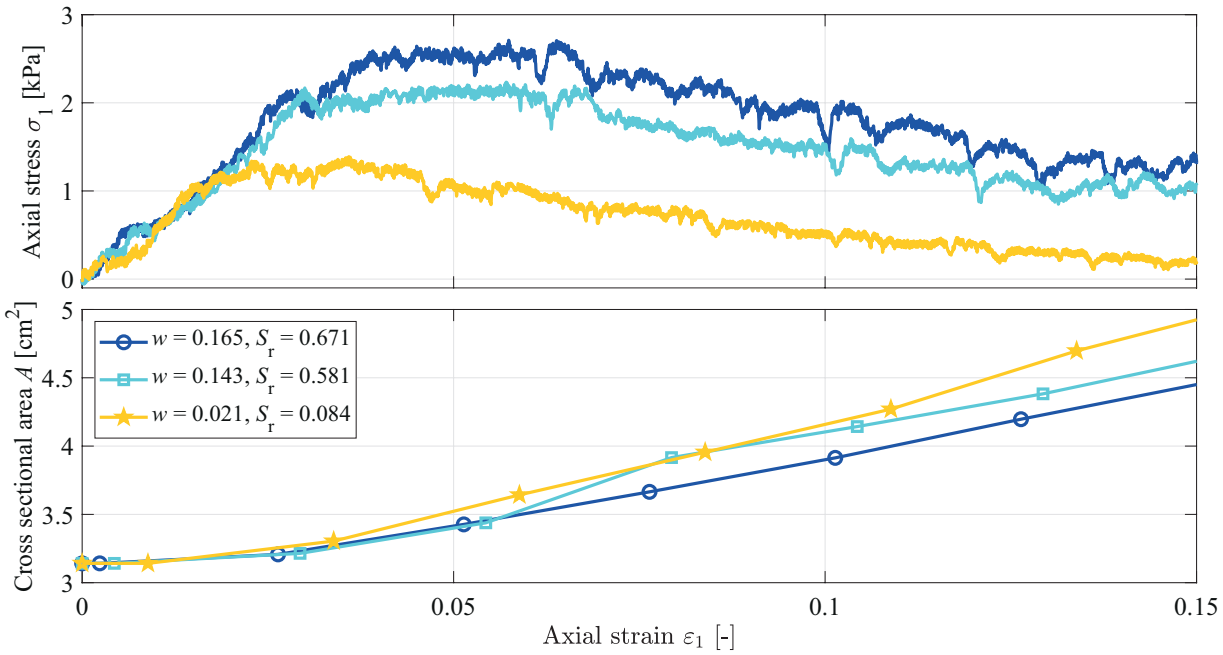
for specimens of Hamburg Sand and glass beads at different water contents and degrees of saturation, respectively. Axial stress is calculated from the axial force and the current specimen cross sectional area which is derived from the specimen diameter measured in a series of photographs taken during uniaxial compression.

A clear dependence of uniaxial compression strength σ_{max} on the initial degree of saturation is visible for both granular materials. The uniaxial compression strength increases with increasing degree of saturation as shown in Figure 4.6. The shear strength due to capillary cohesion c_c is much more pronounced in the sand compared to the glass beads. Regarding the volumetric behaviour represented by the development of the specimens' cross sectional area, a trend of increasing dilatancy with decreasing water content is revealed, especially for the sand specimens. The dilatant behaviour is slightly more pronounced in the sand compared to the glass beads.

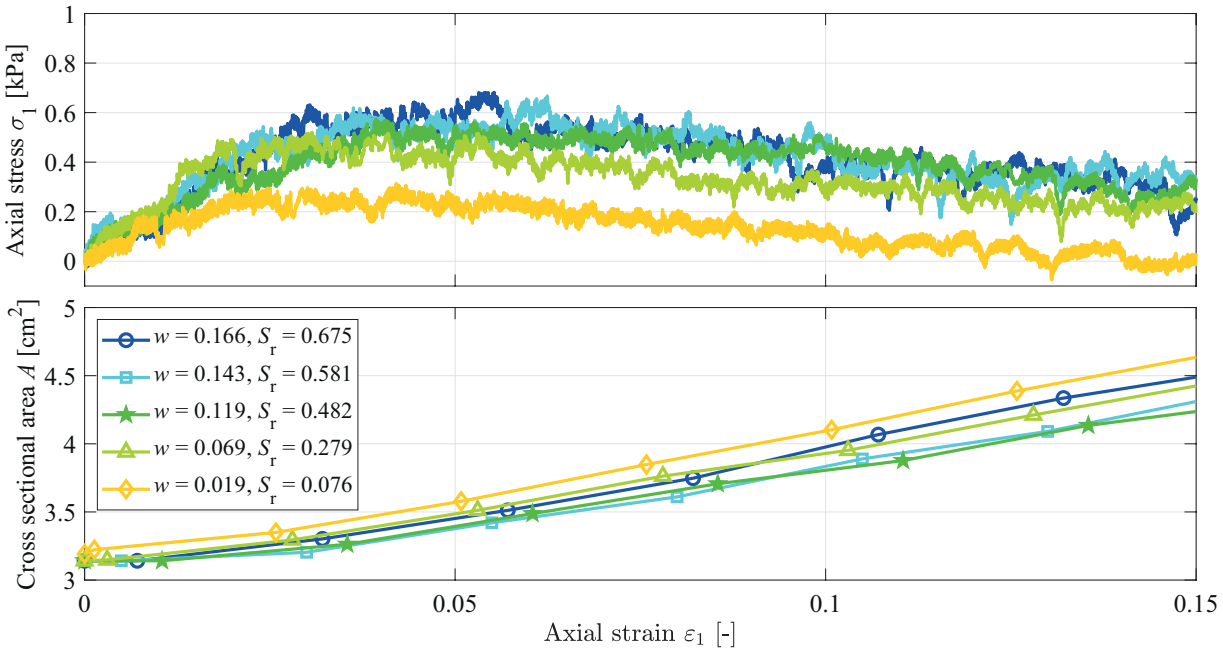
The measured uniaxial compression strength σ_{max} is further evaluated to derive capillary cohesion according to

$$c_c = \frac{1}{2}\sigma_{max}(\cos\varphi' - (1 - \sin\varphi')\tan\varphi') \tag{4.1}$$

based on the Mohr-Coulomb failure criterion as shown in Milatz (2019). The calculated capillary cohesion, also shown in Figure 4.6, follows the same trend as uniaxial compression strength as it rises with increasing degree of saturation. A maximum value is reached for a relatively high degree of saturation which should theoretically coincide with the saturation



(a)



(b)

Figure 4.5: Shear behaviour of unsaturated Hamburg Sand (a) and glass bead specimens (b) at different water contents from uniaxial compression tests using the set-up presented in Milatz (2019)

at the AEV. It must be noted, that the capillary cohesion and therefore the uniaxial compression strength vanish for $S_r = 0$ and for $S_r = 1$.

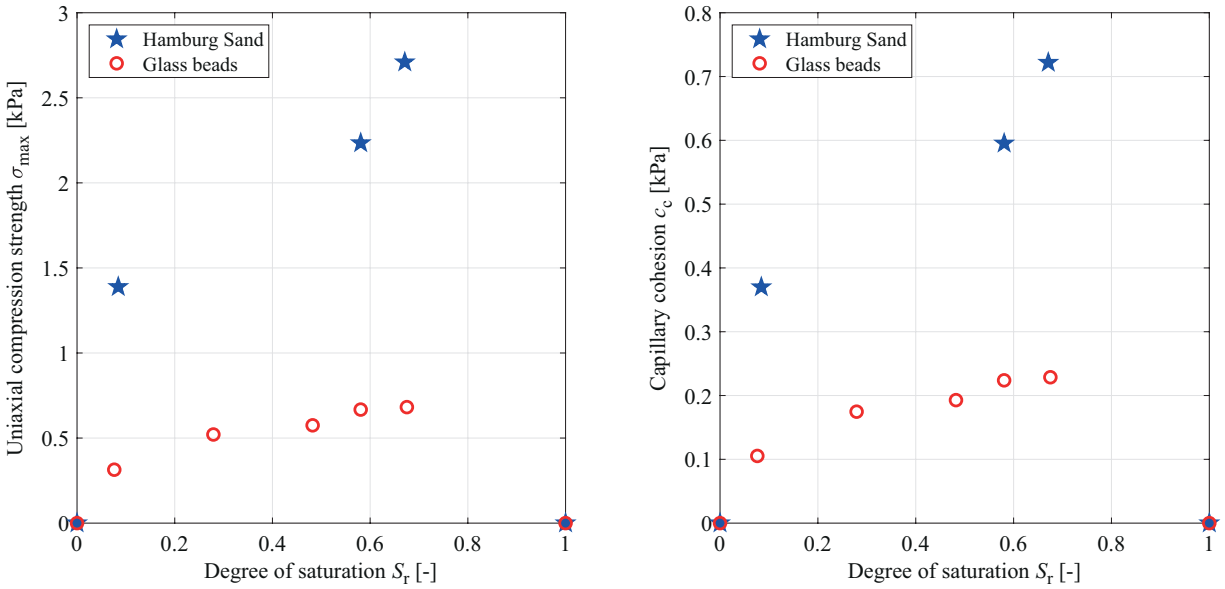


Figure 4.6: Measured uniaxial compression strength (left) and calculated capillary cohesion (right) from uniaxial compression tests on Hamburg Sand and glass beads presented in Milatz (2019)

4.3 Miniaturised flow cell apparatus for measurement of the WRC

4.3.1 Field of application

As the measurement of the water retention curve with conventional suction controlled methods is a meticulous and time consuming task, especially when different hydraulic paths are to be measured for the investigation of hysteresis upon reversals of flow direction, a new flow controlled experimental device was developed based on different preliminary studies (Milatz, 2015; Milatz *et al.*, 2016). The final version of the experimental set-up, named the UNSAT-*Pi* 2, allows to prescribe consecutive hydraulic cycles to a soil specimen in order to measure the hysteretic WRC transiently in a quasi automated way (Milatz, 2020a).

In the transient water retention experiments, pore water is continuously extracted from or injected into a small cylindrical soil specimen contained in a flow cell. Unlike other conventional methods, matric suction is not controlled, but measured as a response to a forced change of degree of saturation. By adjusting the flow rate of pore water (and the permeability of applied filter plates and membranes), it can be decided if equilibrium or non-equilibrium (dynamic) water retention curves are measured (Milatz *et al.*, 2018b).

4.3.2 Technical details

Similar to the uniaxial compression device described before, the flow cell apparatus is designed in a miniaturised format for *in situ* CT experiments. The main element of hardware is a Raspberry Pi 3 B+ single board computer (the version following the model B mentioned above) for control of the peripheral hardware and for data logging. Hardware components include a 3D-printed syringe pump based on the design by Wijnen *et al.* (2014), and a system of two low-cost pressure sensors applied for suction measurement in the drainage system underneath a filter plate covered by a filter membrane below the soil specimen. The plunger of the 1 ml syringe clamped into the syringe pump is moved by a NEMA 17 stepper motor via an M5-threaded steel rod yielding a very fine resolution of $2.174 \cdot 10^{-3}$ mm^3 per motor step. The syringe pump is individually calibrated by comparing the dosed amount of water to the water volume measured by weighing on a laboratory balance as further detailled in Milatz (2020a). The change of matric suction is measured with two pressure sensors with a range of ±34.75 kPa, the first of which measures the negative water pressure in the drainage system of the flow cell, while the second sensor logs the ambient (zero) air pressure. Matric suction is derived as the differential pressure of both sensors using the differential signal for annihilation of electrical noise. Prior to their use in experiments, the pressure sensors are verified and calibrated with the help of a hanging water column apparatus which applies small suction steps to which the sensor readings can be compared. Further details on the layout of hardware components are given in full account in Milatz (2020a). The experimental set-up as well as the UNSAT-*Pi* 2 are illustrated in Figure 4.7. The corresponding wiring diagram is reproduced in Figure 4.8.

The different transient cycles in which pore water is drained out of or imbibed into the flow cell are coded in a Python script controlling the stepper motor of the syringe pump and recording the pore water volume change data and pore water pressure data from the pressure sensors to file. This allows to run test programs for the automated measurement of arbitrary hydraulic paths forming a hysteretic water retention curve of the investigated granular material.

Besides experiments under lab conditions, the set-up has been applied for *in situ* water retention tests with parallel CT imaging at Laboratoire 3SR in Grenoble using a lab X-ray source (Milatz *et al.*, 2022b) and at the Institut Laue-Langevin in Grenoble using combined X-ray and neutron-tomography (Milatz *et al.*, 2019). In a further developed version, it has recently been applied for synchrotron-based CT imaging at DESY[1].

4.3.3 Specimen preparation

Small cylindrical specimens of granular material with a diameter and height of 12 mm are prepared by pluviating the dry material into the flow cell already containing some deionised water. The granular material is carefully poured into the water for sedimentation. Care is taken that the water level is always above the surface of pluviated granular material to minimise air entrapment. In the filling procedure, the material is carefully stirred and

[1] Beamtime-proposal I-20210425 "Synchrotron-based tomography of changing pore scale capillary effects during transient water retention experiments on granular media"

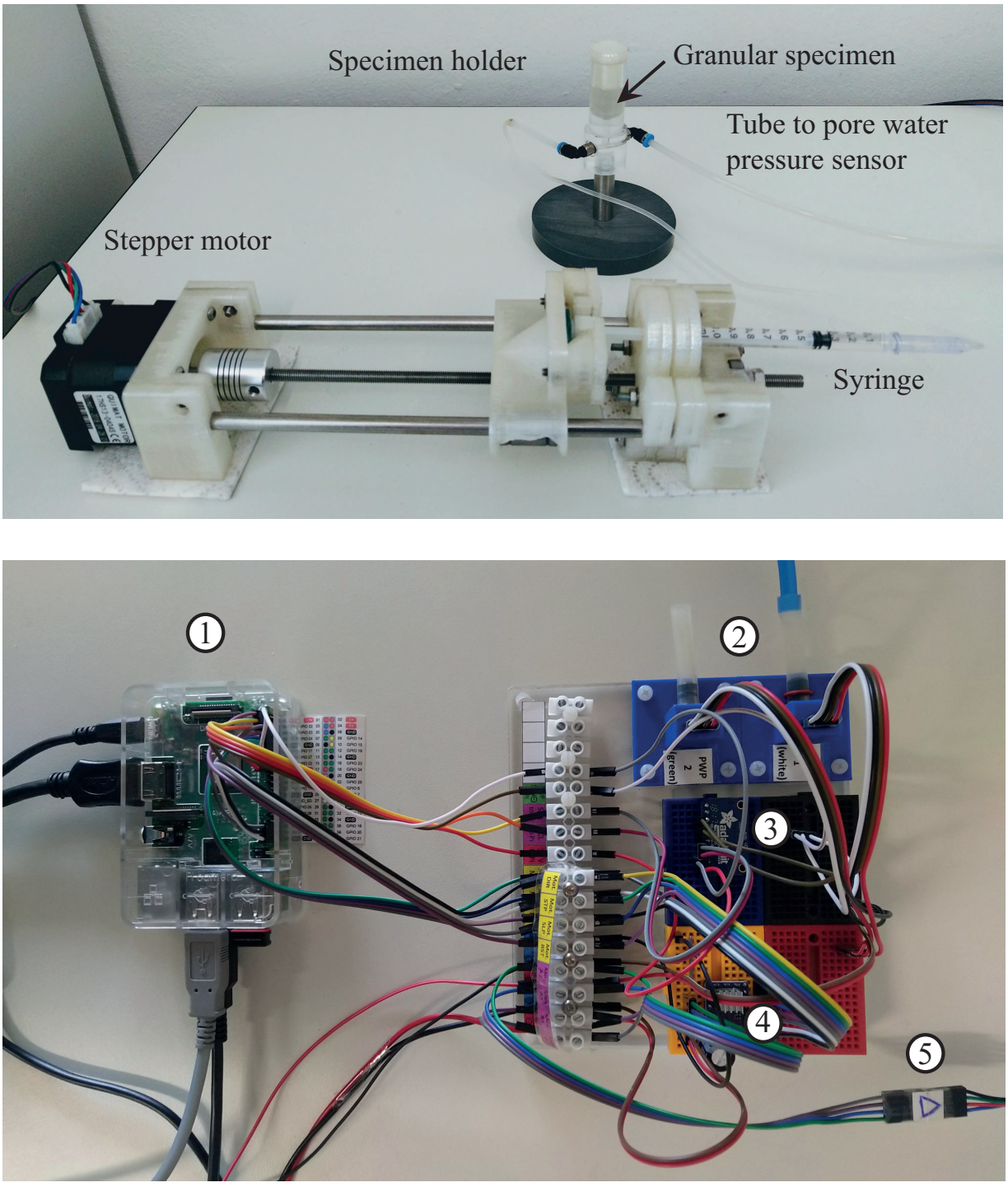


Figure 4.7: Miniaturised apparatus for the measurement of the WRC with flow cell and syringe pump (top) and UNSAT-*Pi* 2 for experimental control and data logging (bottom). ① Raspberry Pi 3 Model B+, ② Pore water pressure sensors, ③ ADC, ④ Stepper motor driver, ⑤ Cable to syringe pump (Milatz, 2020b)

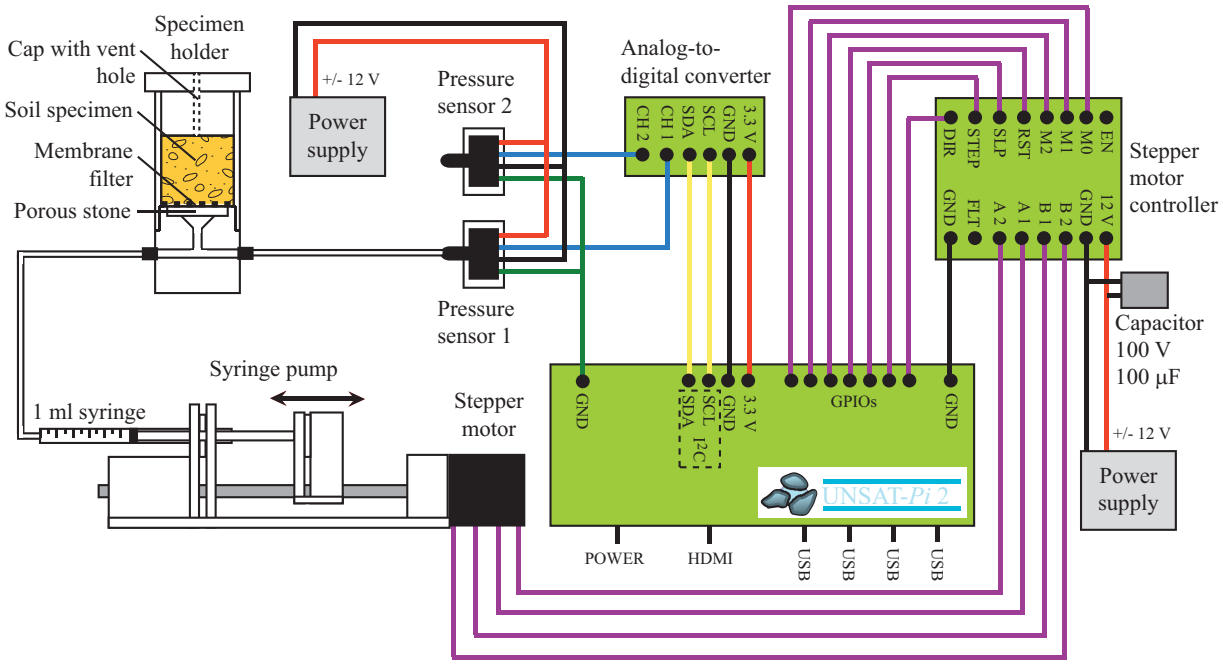


Figure 4.8: Wiring diagram, showing the components and connections forming the UNSAT-*Pi* 2 experimental set-up for miniaturised water retention tests (Milatz, 2020a)

shuffled with the tip of a screw driver to prevent the formation of segregated layers. In order to reach the desired specimen height, the material can be densified with a piston if needed. Glass beads tend to compact towards maximum density easier than sand when filled into the flow cell. Before the start of an experiment, the surface of the specimen is carefully smoothed and a top cap is placed on the specimen surface to apply a small vertical load. This helps to prevent specimen movements in CT experiments. The top cap has a central bore hole to connect the specimen top to the ambient air while at the same time minimising evaporation. A circumferential groove in the top cap allows to reduce capillary rise of pore water from the specimen top in the slit between flow cell walls and top cap.

4.3.4 Selected results

Typical results of a cyclic water retention test on Hamburg Sand with 14 consecutive hydraulic steps are illustrated in Figure 4.9. The experiment ran autonomously during a time period of more than 8 hours at a relatively low flow rate (close to equilibrium conditions) of $\frac{\partial V_\mathrm{w}}{\partial t} = 0.0597\ \frac{\mathrm{mm}^3}{\mathrm{s}}$ corresponding to $\frac{\partial S_\mathrm{r}}{\partial t} \approx 0.000112\ \frac{1}{\mathrm{s}}$. In response to the applied change of degree of saturation, matric suction is changing in a non-linear way, also showing path-dependence due to hysteresis of the water retention behaviour. The logged data of degree of saturation and matric suction can be combined to a water retention curve as shown in Figure 4.10. The experimental method allows to measure the full hysteresis behaviour of the tested soil. Besides higher-order scanning paths, rarely measured so far, also the effect of air entrapment can be studied. The hydraulic main imbibition path

after primary drainage indicates an entrapped air saturation of $S_a \approx 0.1$ as matric suction approaches 0 kPa.

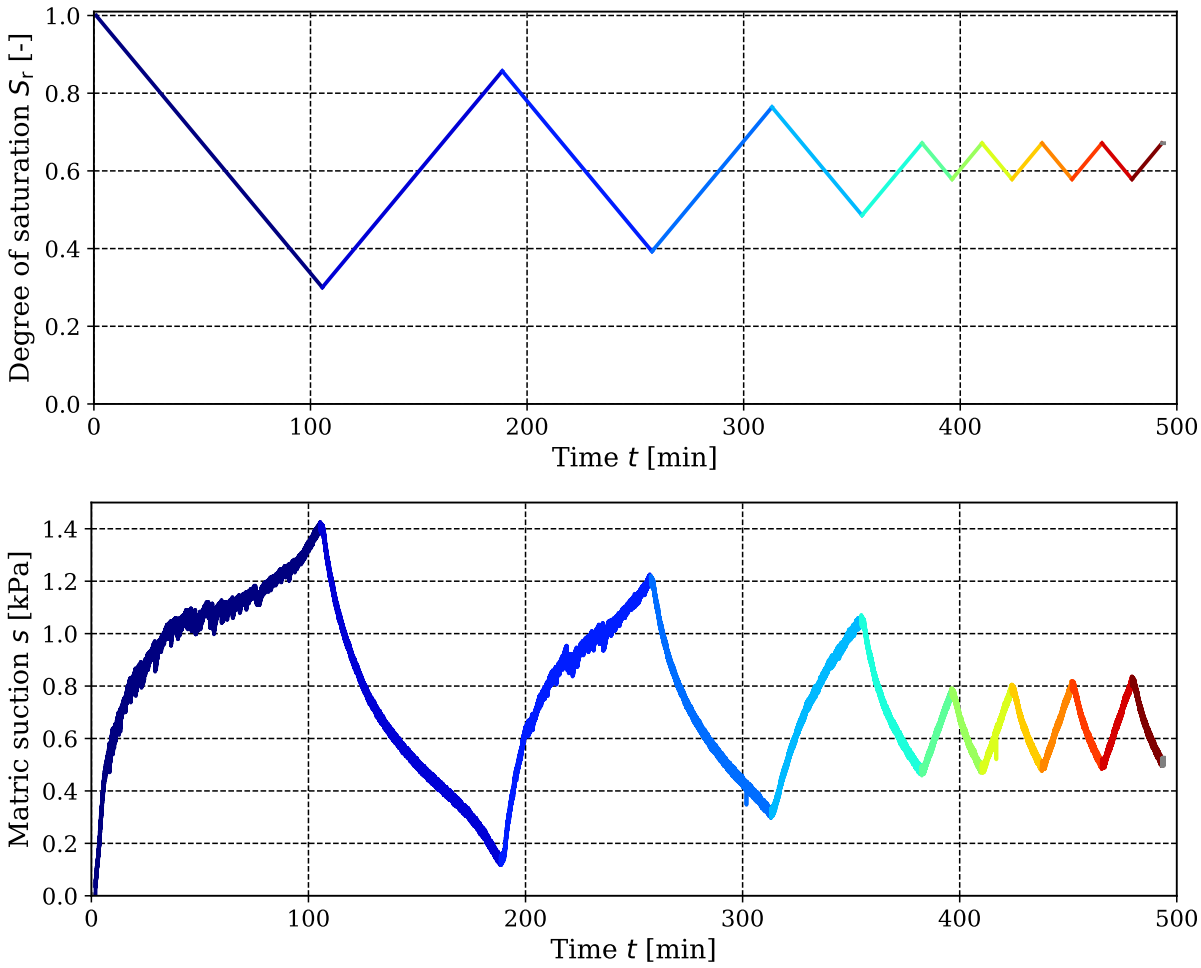


Figure 4.9: Temporal change of degree of saturation (top) and measured response of matric suction (bottom) during a cyclic water retention experiment on a specimen of Hamburg Sand ($e_0 = 0.65$). Each colour represents a different hydraulic step

4.4 Miniaturised direct shear device

4.4.1 Field of application

Besides the free evolution of shear zones in a triaxial test or in a uniaxial compression test as presented before, direct shearing enforces a shear zone in a soil in order to measure or study shear strength based on a rather controlled failure plane. Also frequently used in geotechnical engineering practice, the direct shear test, *e. g.*, standardised in DIN EN ISO 17892-10:2019-04, allows to measure peak and residual shear strength. Due to the

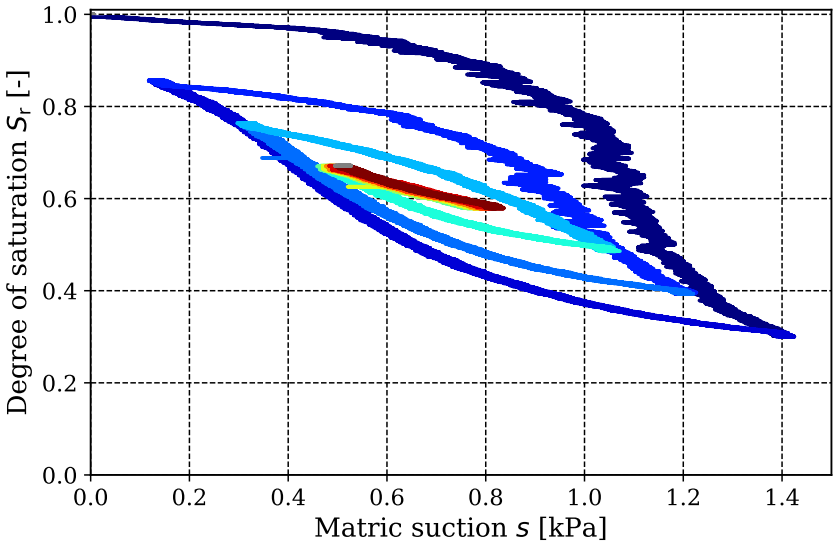


Figure 4.10: Transient water retention curve with 14 hydraulic steps measured on a specimen of Hamburg Sand ($e_0 = 0.65$)

simplicity of the test set-up, basically only consisting of a shear drive to apply linear displacement, of a load cell for the measurement of the resulting shear force, and of a vertical loading mechanism for the application of a normal force, the direct shear test has been selected as another interesting soil mechanical experiment to study the shearing of unsaturated granular media in *in situ* tests with CT imaging of the shear zone. In the few first applications of the only recently developed device, it is focused on the influence of capillarity on shear strength and volume change inside and close to a prescribed shear zone in specimens of Hamburg Sand and glass beads.

4.4.2 Technical details

A prototype of a miniaturised direct shear apparatus was custom-built for application in *in situ* CT experiments. The set-up has been tested under lab conditions and could be applied during a beamtime at DESY for synchrotron-based CT imaging of shearing processes in unsaturated granular media. Its basic technical layout is illustrated in Figure 4.11.

The experimental set-up does not strictly conform to the DIN standard, especially regarding the specimen dimensions inside the shear box. In the current set-up, specimens with a height to diameter ratio of $h/d = 5$ mm/16 mm and $h/d = 10$ mm/16 mm can be sheared with the shear plane being located at the half specimen height. During displacement controlled shearing, low vertical stresses are applied by dead weights. As the apparatus is intended for *in situ* testing in a CT environment, its small dimensions represent a compromise between the standardised geometry recommended in the DIN standard to ensure negligible boundary effects and the possibility to obtain full field CT images. Thus, the measured shear forces might be influenced by confinement effects, not leading to representative macroscopic shear strengths. However, the overall specimen response,

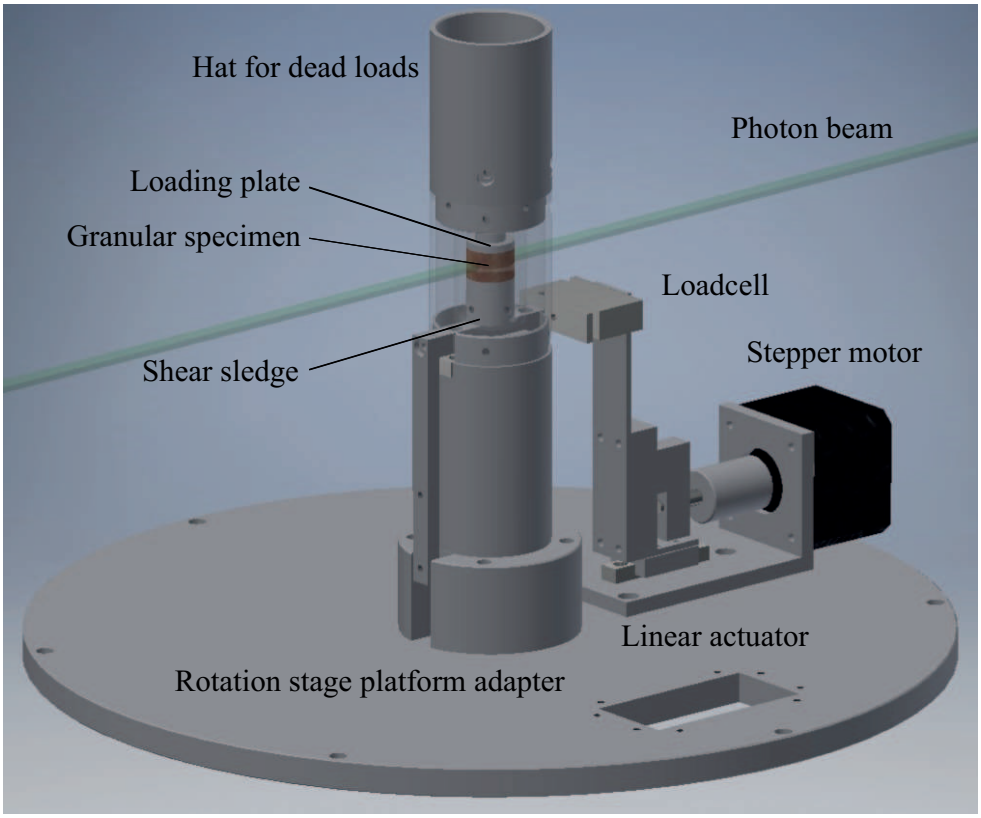


Figure 4.11: Technical layout of the miniaturised direct shear apparatus for *in situ* CT experiments using synchrotron radiation

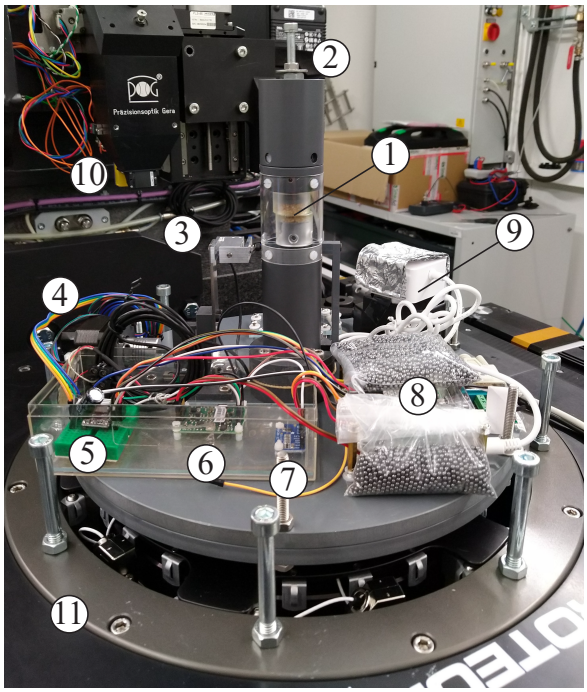
e. g., the change in specimen height due to dilation as well as grain movements inside and outside of the shear plane and the related changes in water clusters or liquid bridges, are supposed to be captured by the CT images in order to study the coupled processes.

The soil specimen is located in a shear box made of a hollow cylinder that is split horizontally to apply direct shear by lateral movement of the lower hollow cylinder section. The thickness of the shear slit can be adjusted and was fixed to *ca.* 0.1 mm by using a plastic foil as a spacer. The adjusted slit thickness prevents smaller grains inside a specimen from entering the slit and from increasing friction. The lower hollow cylinder is mounted on a horizontal sledge moving on a ball bearing to reduce friction in the shear direction. Vertical load is applied by dead weights on top of the loading plate which can move vertically in a guide equipped with ball bearings to minimise friction.

For a small distance between X-ray source and specimen centre in laboratory CT scanners, the specimen is placed on a tower that is centred on the rotation stage by an adapter plate. The shear sledge is pushed by the sensing end of an S-shaped load cell which itself is moved by a linear guide actuated by a stepper motor. The shear displacement is applied via the rotation of an M5-threaded rod leading to a feed of 0.8 mm per full rotation. The stepper motor is a NEMA 17 stepper motor driven by a *DRV8825 stepper motor controller board* allowing to apply microstepping. A full rotation is discretised by 200

full motor steps. With a maximum microstepping of factor 32, the minimum displacement resolution is 0.8 mm/200/32 = 0.000125 mm/step. In the presented experiments, a coarser microstepping factor of 16 is applied leading to a step resolution of 0.8 mm/200/16 = 0.00025 mm/step. The load cell is a miniature force sensor with a measurement range of ±5 N of type KD34s which is connected to a measurement amplifier of type GSV-1L, both manufactured by ME-Meßsysteme GmbH. The load cell can be changed if a lower measurement range and resolution are needed. Together with the applied 16-bit ADC of type *ADS1115 analog-to-digital converter*, distributed by Adafruit learning system, a resolution of force measurement of *ca.* 0.000172 N/bit is achieved.

The whole experiment is programmed in a Python script for controlling the stepper motor and for data logging of the shear displacement and measured shear force. Under lab conditions, monotonic shearing is applied while step-wise shearing with intermediate breaks for CT imaging is programmed in *in situ* CT experiments. Software and peripheral hardware are linked by a Raspberry Pi 4 B single-board computer which is also placed on the rotation stage to minimise the length of cable connections and possible disturbances of data measurement. A detailed view of the experimental set-up during shearing of a Hamburg Sand specimen at DESY with all hardware components is given in Figure 4.12. During the synchrotron-based CT imaging at DESY, the power supply of the single-board computer, the load cell and the stepper motor, all placed on the rotation stage, has been secured by two cables that could curl up during rotation for imaging and that were drawn back during back rotation by counter weights attached to the cables which ran over a pulley.



① Hamburg Sand specimen in shear box
② Axial loading system
③ Load cell
④ Stepper motor
⑤ Motor driver board
⑥ Measurement amplifier
⑦ ADC
⑧ Raspberry Pi with radiation protection
⑨ Power supply
⑩ Beam optics
⑪ Rotation stage

Figure 4.12: Experimental set-up during the shearing of a Hamburg Sand specimen at the P07 High Energy Materials Science beamline at DESY

4.4.3 Specimen preparation

While dry specimens can be easily pluviated into the shear box through a funnel, unsaturated specimens to be sheared at constant initial water content are first mixed and then filled in using a spoon and a funnel. For all specimens, the initial void ratio and degree of saturation are fixed by filling in a calculated amount of dry granular material which is previously mixed with the amount of water needed for a desired degree of saturation in the case of unsaturated specimens. The specimens are carefully compacted in layers which are roughened to prevent the formation of layers until the target specimen height is reached. During specimen preparation, the shear box is locked in order to prevent a relative displacement between the lower and upper hollow cylinder. After the desired specimen height is reached, the specimen top surface is smoothed prior to applying the loading piston with the selected dead weight corresponding to a fixed vertical stress level. In the shear step, the shear box is unlocked and then driven forward with displacement control.

4.4.4 Selected results

The direct shear apparatus has been tested under lab conditions in monotonic shear experiments. Figure 4.13 shows the measured shear stress *vs.* shear displacement for six exemplary tests on dry Hamburg Sand at different vertical stress levels σ. The sand specimens with an initial height of 10 mm have been prepared with an initial void ratio of $e_0 = 0.7$ and have been sheared monotonically to a maximum shear displacement of 3.5 mm at an average shear velocity of 0.365 mm/min.

The shear stress response at the same vertical stress levels is repeatable and a clear dependence of maximum shear stress as well as initial slope of shear stress *vs.* shear displacement (reflecting shear stiffness) on the stress level is visible. However, rather high shear stresses are measured in comparison to the applied vertical stresses, leading to a much elevated friction angle. This is most likely due to the strong confinement of the relatively small specimens inside the miniaturised shear box. Although not measured, the specimen height is noticed to increase in all direct shear tests as the specimens dilate which also might lead to an increase in confinement and interlocking of the sand grains inside the shear box.

4.5 Particle separation experiment

4.5.1 Field of application

Although liquid bridges have been studied for more than 200 years if the works by Young and Laplace are seen as the origin, their behaviour is still not fully understood as it is governed by different physical and chemical principles. As an example, liquid bridges encounter differences in their static and dynamic physical behaviour. Furthermore, the microscopic properties of wetted solid surfaces, such as roughness, as well as the direction

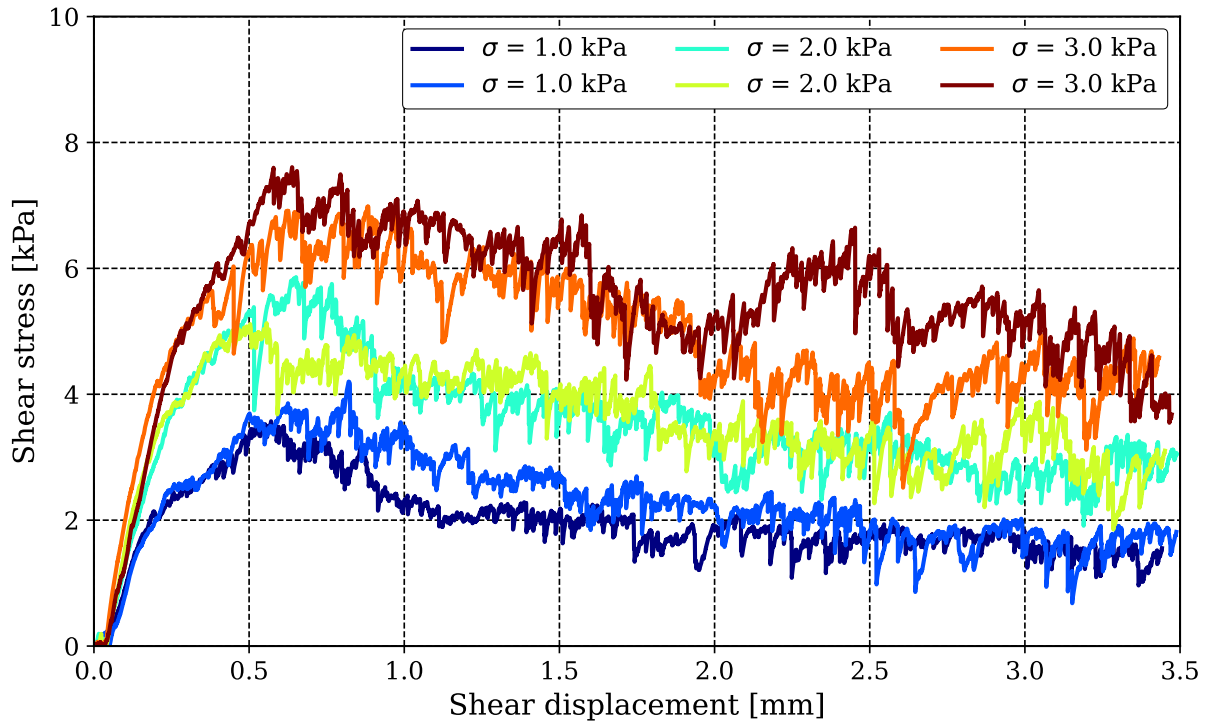


Figure 4.13: Shear stress *vs.* shear displacement measured in miniaturised direct shear tests on dry Hamburg Sand specimens at different stress levels σ

of interface movement determine the contact angles, and from the chemical point of view, surface tension depends on temperature and especially on the considered liquid.

For the investigation of the behaviour of single capillary bridges during relative grain movement as shown in Figure 1.3 in Chapter 1, a miniaturised testing apparatus has been designed. The experiment requires some experimental practice due to the handling of single grains and small amounts of water, but is very suitable for application in student projects. Questions of research are the development of capillary bridge geometry during straining which can be characterised by the length of the contact line, the radii of curvature as well as contact angles as defined in Figure 2.4 in Chapter 2. Furthermore, the quantification of capillary forces during cyclic elongation and compression as well as the rupture length of capillary bridges are of interest. The experiments focus on the granular materials studied in this work, *i. e.*, real capillary bridges in between pairs of glass beads and Hamburg Sand grains are studied on the natural scale, which requires magnification in the imaging procedure.

4.5.2 Technical details

A NEMA 17 stepper motor as described in the previous set-ups is applied together with a gear pinion and toothed rack, transforming the gear pinion's rotation into an upward or downward movement for the separation of single glass beads or sand grains with a

displacement resolution of *ca.* 0.0057 mm per motor step. The particle movement and capillary bridge geometry are measured in an image-based approach with the help of a digital camera and a microscope lens (25 mm zoom, magnification 10×–200×). The Raspberry Pi High Quality Camera (V1.0 2018) is applied in the imaging set-up as it allows to capture images and movies in HD-quality. A Raspberry Pi 4 B single-board computer is used for control of the motor and image acquisition. A schematic drawing of the imaging experiment and its technical components is shown in Figure 4.14.

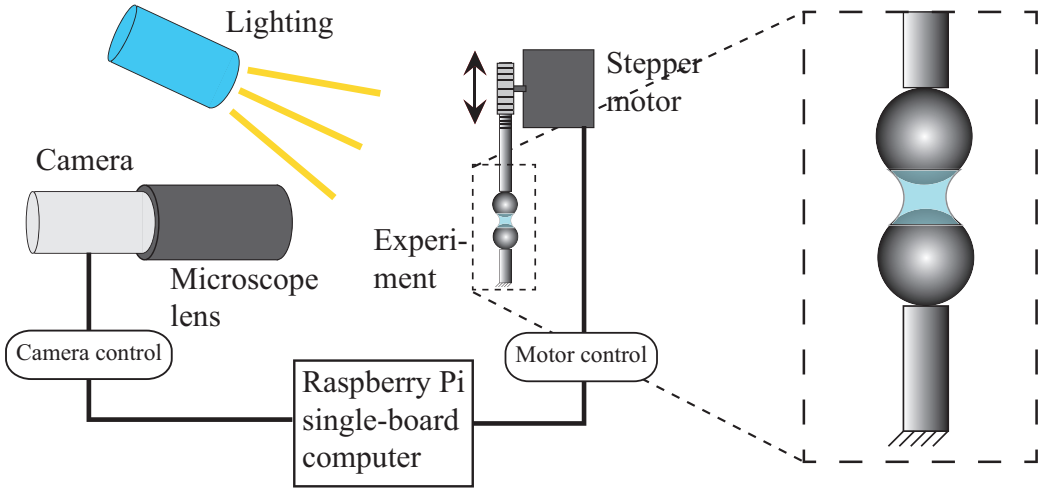


Figure 4.14: Set-up for the image-based investigation of mechanical capillary bridge behaviour in particle separation experiments

For the direct measurement of capillary forces, the lower grain can be placed on a laboratory balance which logs the time series of force measurements to a PC. In selected experiments with force measurement, a Sartorius BP 211 D laboratory balance with a resolution of 0.01 mg is used.

With the help of a Python program, the desired particle movement, either monotonic or cyclic particle separation, is controlled while at the same time a video is recorded at a frame rate of *ca.* 10 frames/s. After the experiment, the open-source multimedia software *ffmpeg* is run to extract individual images from the video. As the video is recorded in parallel to the experiment, the time step of each image can be calculated from the duration of the experiment and number of individual image frames as stripped by ffmpeg. In experiments with parallel force measurement, the Python program controlling the mechanical experiment and the program for the logging of the balance data are started simultaneously to have the same time stamp in both data.

In the evaluation process, capillary bridge properties, such as the different geometric length measures as well as contact angles, are measured with the open-source software *ImageJ/Fiji* in combination with a *MATLAB* program allowing to extract different measures directly from the images by manually fitting circles to the capillary curvatures according to the toroidal capillary bridge model. Physical measurements in the length unit mm are extracted from the raw measurements in image pixels with the help of a known scale

in mm/px that is calculated for each imaging experiment. For contact angle measurement, the manual angle tool in *ImageJ/Fiji* is used. With the applied digital camera and the microscope lens typical resolutions of 2.8 to 3.6 μm/px are achieved. While lengths and displacements can be measured very accurately at this resolution, the resolution of manual angle measurements is typically limited to a few degrees. This is mainly due to uncertainties at the phase boundaries and due to the changing perspective during grain movement. The experimental set-up and the evaluation procedure are highlighted in Figure 4.15 showing the separation of two glass beads with $d \approx 2$ mm and the measurement of a left and right radius of curvature R_1 as well as four contact angles. The final R_1 is obtained by averaging of the two measured angles, while the inner radius of curvature R_2 is calculated from both measured values of R_1 and the known locations of the left (red) and right (green) fitted circles. Assuming an ideal symmetric liquid bridge, a single representative contact angle can be obtained as the mean of the four measured contact angles. In the evaluation of the experiments, the capillary force and its contributions from capillary pressure and surface tension are mainly calculated with Equation 2.7 in Chapter 2 based on the geometric measures and the toroidal approximation, but it can also be directly measured using a lab balance.

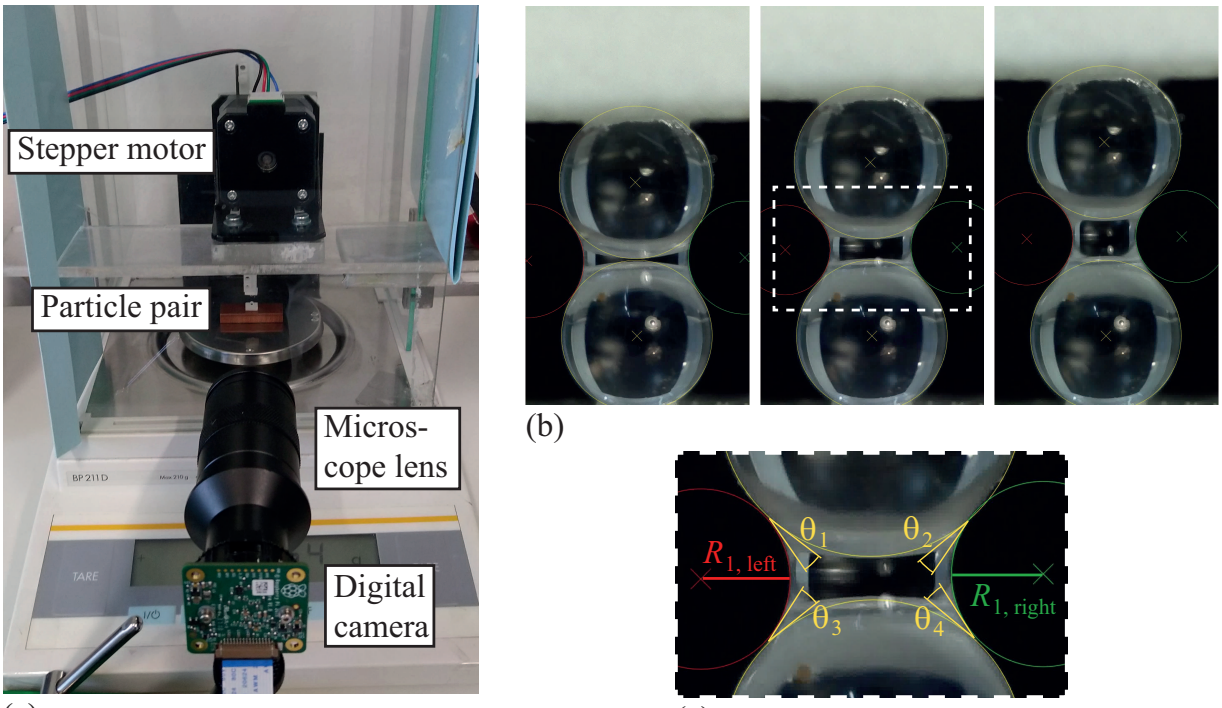


Figure 4.15: (a) Photograph of the particle separation experiment with technical components placed on a lab balance, (b) time frames during elongation of a capillary bridge in between two glass beads with $d \approx 2$ mm showing the fitted circles and (c) detail of measurement of outer radius of curvature R_1 and contact angle θ from the images

4.5.3 Specimen preparation

Prior to experiments, single particle pairs are selected based on considered characteristics, *e. g.*, particle diameter and roundness. Care is taken not to change the surface properties of the particles which must be cleaned before the experiments. The particle pair is then fixed by means of double sided tape or putty on the lower platform and on the upper moving end of the actuator. Before the start of an experiment, a water droplet is placed on the lower particle and the top particle is moved down to create an initial capillary bridge. In experiments with a lab balance for force measurement, the capillary force at the moment of capillary bridge formation is already recorded in order to capture the initial tensile force between the upper and lower grain and its following change.

4.5.4 Selected results

Selected results of a separation experiment on a capillary bridge in between two glass beads with $d \approx 2$ mm with monotonic increase of particle separation distance are given in Figure 4.16. In the experiment, the initial water volume has been calculated as a body of revolution based on the initial bridge geometry as $V_{\mathrm{liq}} = 0.122$ mm^3. The separation velocity was $v_{\mathrm{sep}} \approx 0.09$ mm/s. Figure 4.16 shows the evolution of measured radii of curvature R_1 and R_2 as well as the dimensionless capillary force F^* calculated according to

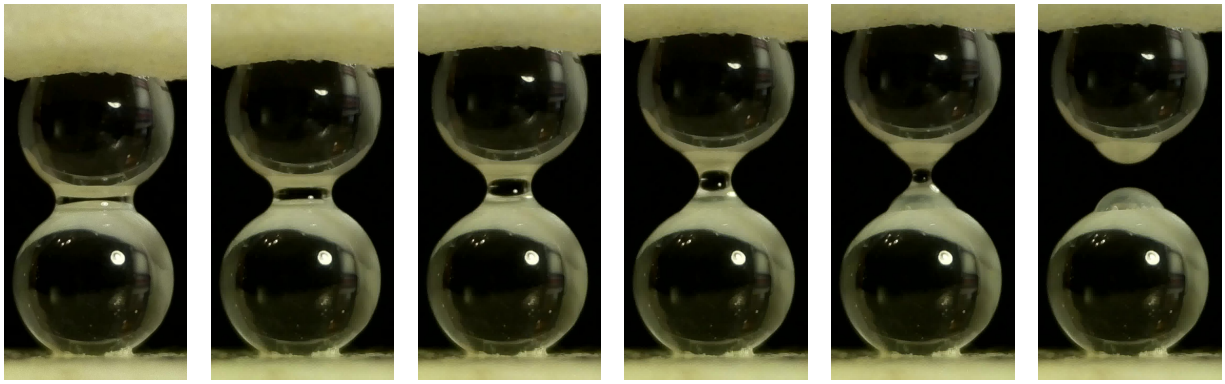
$$F^* = \frac{F}{2\,\pi\,R\,\gamma} \tag{4.2}$$

and its contributing parts from capillary pressure and surface tension. The results are plotted *vs.* dimensionless particle separation l^* defined as

$$l^* = \frac{l}{R} \quad . \tag{4.3}$$

The dimensionless values are calculated from surface tension γ, separation distance l, and particle radius R. Note that if the dimensionless force is based on geometric properties measured from the images, the surface tension in F^* cancels out as it appears in F in the numerator as well as in the denominator.

The experimental results highlight the role of the main radii of curvature which highly depend on the initial geometry of the capillary bridge and its volume and which change during the particle separation. The different contributions to capillary force are exclusively calculated from the radii of curvature according to Equation 2.7. The impact of surface tension as well as particle size are eliminated by expressing the forces in a dimensionless way according to Willett *et al.* (2007). Based on the relationship of R_1 and R_2, capillary pressure inside the capillary bridge is either positive (suction) or negative (excess water pressure) leading to a positive or negative contribution to the overall capillary force. In the experiment shown here, the contribution of capillary pressure turns from positive to negative values as the particle separation increases until failure of the studied capillary bridge at a rupture length $l_{\mathrm{r}} \approx 0.634$ mm. The contribution of surface tension is always positive and initially more than twice as high as the contribution of capillary pressure. Further results of particle separation experiments will be presented and discussed in Chapter 6.



$l = 0.023$ mm $l = 0.187$ mm $l = 0.358$ mm $l = 0.530$ mm $l = 0.634$ mm After rupture

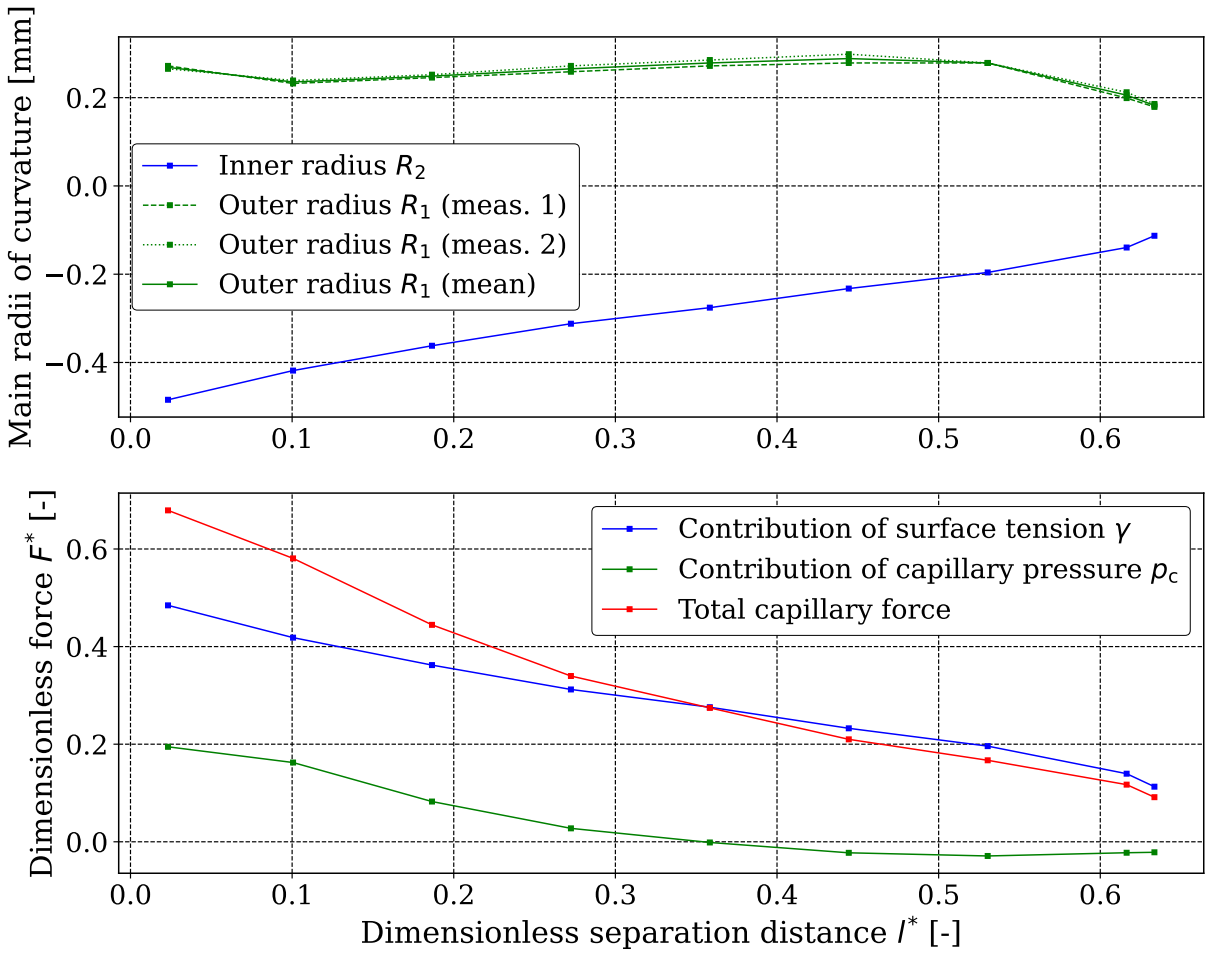


Figure 4.16: Results of a particle separation experiment on glass beads with $d \approx 2$ mm until rupture of the capillary bridge

Chapter 5

In situ 4D experiments with full-field CT imaging

In this chapter, the application of miniaturised experimental set-ups in 4D *in situ* CT experiments is highlighted based on different experimental campaigns pursued at Laboratoire 3SR, Université Grenoble Alpes and at the Institut Laue-Langevin in Grenoble, France. In the experiments, full-field CT data, *i. e.*, capturing the complete specimen volume, have been recorded. The implementation of the hardware set-ups in a CT scanning environment as well as special requirements for *in situ* testing regarding experimental control and parallel image acquisition are focused on. Furthermore, the image processing and analysis procedures required to extract and study quantitative measurements on the grain or pore scale will be outlined in detail.

5.1 Principles of *in situ* CT experiments

Focusing on typical engineering applications, *in situ* CT experiments are applied to observe the distribution of matter in a temporal process. This includes the structural change of materials during mechanical loading, *e. g.*, resulting in particle displacements, deformations or fracturing, the flow of liquids and gases in porous media or the transformation of substances in chemical reactions. Many more applications from technical fields of research exist.

As compared to experiments running in a conventional laboratory environment, many aspects of experimental procedures need to be adjusted for the special requirements of *in situ* CT imaging which are briefly explained in the following.

First of all, special testing environments need to be designed for *in situ* CT imaging experiments as outlined in Chapter 4. These must fit onto the rotation stage of the selected CT scanning system. Very frequently, weight limitations exist. Furthermore, care needs to be taken to consider all aspects of accessibility for specimen preparation and testing. Moreover, a thorough collision check of all hardware parts during specimen rotation must be accounted for. The materials of which the specimen environment is made

should be selected carefully in order not to hinder the path of the radiation through the desired specimen field of view. Although various manufacturers of special CT systems for *in situ* testing including dedicated sample environments, *e. g.*, for mechanical testing or cooling of specimens, are emerging on the market to respond to the growing research interest on this field, in many cases, tailor-made solutions need to be developed directly by researchers.

In the imaging process, different aspects of hardware-interaction need to be considered. If no sliding contacts for the transfer of electrical signals onto the rotation stage are available, flexible cables, *e. g.*, connecting sensors and actuators on the rotation stage to a control unit, should be able to curl up during image acquisition without disturbing the experimental set-up or the electrical signals to be transferred and read.

With known imaging set-up, as characterised by the beam geometry and scanning positions of the specimen relative to the radiation source and detector, the desired tomography volume, including the specimen or process of interest, as well as the local resolution can be selected *a priori*. Especially the position of movable parts or of the modified specimen needs to be considered. Therefore, preliminary experiments are frequently helpful.

After planning of the geometric and local aspects of *in situ* CT imaging, the temporal resolution must be selected and set taking account of the duration of processes of interest. As scanning time is typically influenced by the chosen field of view and image resolution, a compromise between local and temporal resolution is frequently needed. Preliminary CT scans are highly recommended in order to determine the optimal scan settings for the best image quality in terms of signal-to-noise ratio and phase contrast.

Depending on the temporal process to be imaged and on the desired spatial resolution of the results, various techniques can be applied to reduce scan time. Amongst others, these include a reduction of projections to be acquired together with the application of sophisticated reconstruction algorithms working on a reduced number of projections as well as "onflight imaging". In the latter technique, frequently applied in synchrotron-based CT, projections are measured continuously without halting the investigated process and without stopping the specimen rotation. Reconstructions can then be made at arbitrary time intervals using the corresponding projections. Furthermore, X-ray microscopes as outlined in Chapter 2 allow to focus on a selected subvolume of interest during a process, thus reducing the need to scan the full specimen.

Synchrotron radiation can be applied for fast and spatially highly resolved CT imaging. The use of synchrotron radiation, especially at high energies, requires special materials of sample environments stable to X-rays because the energy of the beam can be so intense that acrylic cells *etc.* are progressively degraded and can finally be destroyed if the exposure is long enough. An X-ray stable material, frequently used due to its durability, is the organic thermoplastic polymer Polyether ether ketone (PEEK). Furthermore, direct synchrotron radiation and back-scattered radiation are harmful for electronic components which should be shielded by leaden protective covers. Another problem with synchrotron radiation is the potential degassing of water contained in specimens, leading to occluded gas bubbles, which is generally undesirable.

If neutrons are used in imaging experiments, the different attenuation laws as compared to X-rays need to be considered in the planning of the experimental set-up (Tengattini *et al.*,

2021). The materials used for the testing environments should be well selected according to these laws. While neutrons easily pass through aluminium walls, they are strongly attenuated by hydrogen-containing materials and also by boron which is frequently used for neutron shielding, *e. g.*, of electronic components. Furthermore, neutron radiation is known to "activate" some chemical elements, *i. e.*, components of the experimental set-up consisting of those elements are possibly becoming radioactive themselves during the experiments, limiting their re-usability. These aspects require careful radiation protection measures for all sensitive components in an experimental set-up.

If special research facilities, such as synchrotrons, are selected for imaging experiments, the beamtime, granted after a highly competitive application process, is frequently very limited. Furthermore, the practical work on site can be intense, as allocated beamtime shifts run all around the clock. Therefore, a profound planning of the experiments, including preliminary tests and enough scientific personnel on site to support each other and sharing shifts, is urgently needed.

In the case of long-time experiments with requested high fidelity of spatial measurements, temperature changes in the scanning chamber of CT scanners and the corresponding temperature strain in the specimen or in testing apparatuses can be problematic. As a solution to this problem, a climate control in combination with massive hardware parts should be used. Furthermore, software-based solutions allowing to correct images which are influenced by temperature shifts can be an option (Andò, 2013).

The software control of customised testing environments for *in situ* CT experiments should be tailor-made to control the experiment during loading steps and CT imaging steps. A certain degree of manual interaction is frequently needed. However, if possible, an interaction of the experimental software with the CT software should be realised, *e. g.*, by communicating the start and end of a CT scan to the loading system (Milatz *et al.*, 2022b).

5.2 4D uniaxial compression of unsaturated sand and glass bead specimens

The miniaturised uniaxial compression apparatus as described in Chapter 4 has been applied to study the uniaxial compression of laterally unconfined specimens of Hamburg Sand and glass beads in an experimental campaign using the Laboratoire 3SR X-ray tomograph described in Viggiani *et al.* (2015).

The experiments described in the following focus on the micro- to macroscale shear behaviour of granular soils at quasi zero confining pressure allowing to investigate the influence of low capillary effects on the macroscopic volume change and shear strength. For the investigation of the influence of shearing on the different *capillary state variables* measured on the microscale, such as the distributions of phases as well as interfacial areas, and the macroscale shear behaviour, a series of six *in situ* CT experiments, reported in full account in Milatz *et al.* (2021b), is run.

The guiding research questions, proposed in Milatz *et al.* (2021b), are as follows:

1) How does capillarity affect the macroscopic effective stress?

2) What is the relationship between the microscopic capillary system, described by air-water distribution and degree of saturation, and measured shear strength and volumetric response on a macroscopic level?

3) How do grain scale quantities, such as number and size of water clusters, location of capillary bridges, and interfacial areas, evolve during macroscopic shearing as grains rearrange?

5.2.1 Experimental set-up

In order to answer the different research questions, the Unsat-*Pi* set-up described in Chapter 4 is installed in the X-ray tomograph at Laboratoire 3SR at Université Grenoble Alpes (Viggiani *et al.*, 2015) to analyse the uniaxial compression of unsaturated Hamburg Sand and glass beads. The set-up is fitted on the rotation stage in the scanning chamber as shown in Figure 5.1. Cables connecting the hardware on the rotation stage to the Raspberry Pi single-board computer placed beside the rotation stage are carefully guided above the top of the uniaxial compression apparatus out of view of the X-rays or are positioned directly on the rotation stage to coil up during its motion.

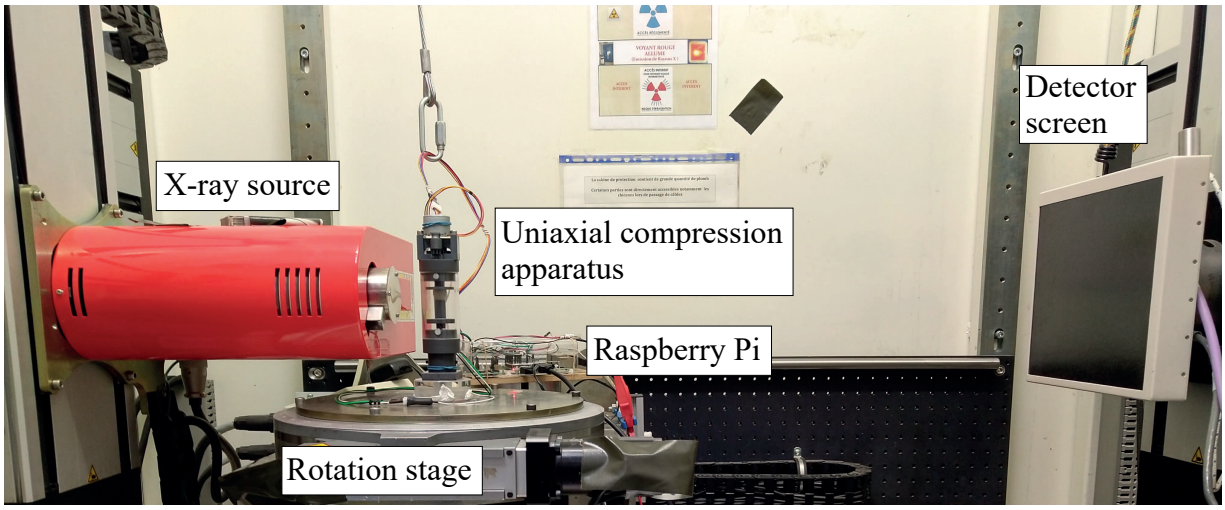


Figure 5.1: Experimental set-up for the *in situ* uniaxial compression tests

Tomographies of the full specimen volume, including portions of the top and bottom loading plates, are obtained with the scan settings indicated in Table 5.1. In order not to disturb the sensitive unsaturated soil specimens, the acceleration and deceleration of the rotation stage are limited and the rotation speed is reduced to *ca.* 10°/min. 1200 projections/360° in continuous rotation mode are measured for the reconstruction of the tomography volume, resulting in a scan time of *ca.* 36 min for each individual scan.

Table 5.1: Settings of CT scans

X-ray tube voltage	120 kV
X-ray tube current	82 μA
Projections/360° revolution	1200
Isotropic voxel size	11 μm
Averaging	4
Acquisition time per scan	$\approx$ 0.6 h
Acquisition mode	Continuous rotation

5.2.2 Testing procedure

Unsaturated specimens of Hamburg Sand and glass beads are prepared according to the procedure described in Section 4.2.3. Due to low amounts of pore water and granular material needed for the preparation of small specimens with height and diameter of only 12 mm, a lab balance with a resolution of 0.0001 g is used for balancing of water and grains. After mixing and homogenisation of these components, the specimens are compacted in layers and shaped with the preparation tool shown in Figure 5.2.

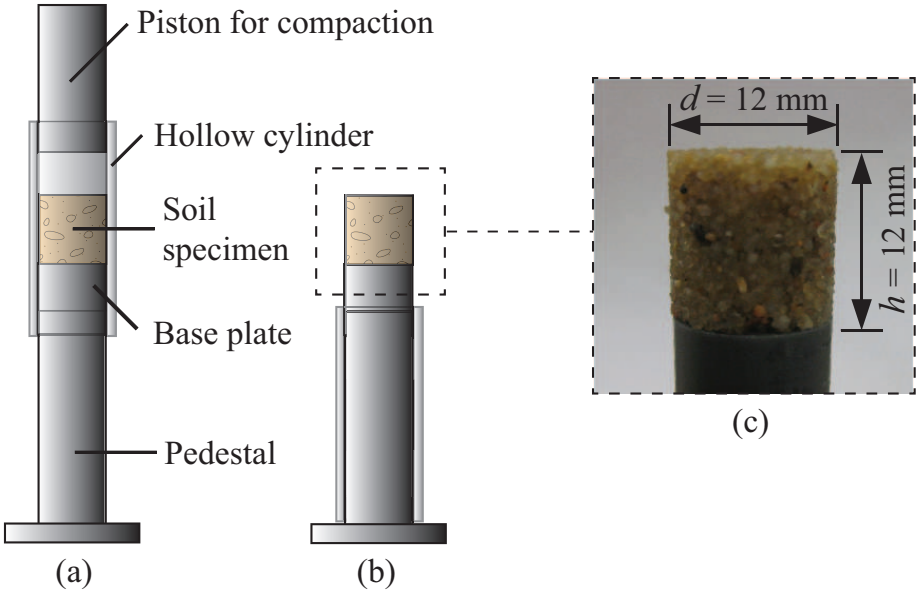


Figure 5.2: Specimen preparation for *in situ* uniaxial compression experiments: (a) Compaction of unsaturated specimen in a hollow cylinder, (b) free-standing specimen after lowering of hollow cylinder, (c) photograph of unsaturated sand specimen

After preparation, the unsaturated soil specimens, standing on a base plate, can be quickly placed in the uniaxial compression apparatus where they are fixed on the loading plate with the help of double sided tape in order to prevent movement during CT scanning.

For each material three different initial degree of saturation levels are investigated. The initial macroscopic specimen properties reached after preparation are summarised in Ta-

ble 5.2. The initial water contents w_0 are obtained from careful balancing of the real amount of water inside the free-standing granular columns. All sources of water loss occurring during specimen preparation, *e. g.*, resulting from evaporation and water adhering to the ceramic cup for mixing of grains and water and to the hollow cylinder, are thus considered to capture the true initial water content. Regarding the initial specimen volume for the calculation of initial void ratio e_0 and initial degree of saturation S_{r0}, the specimen height is derived from the number of CT slices in order to get a more accurate result compared to a measurement with a ruler. To account for evaporation during CT scanning, the gravimetric water content is measured at the end of the experiments.

Table 5.2: Initial macroscopic specimen properties

Hamburg Sand				
Test [-]	m_d [g]	e_0 [-]	w_0 [-]	S_{r0} [-]
1	2.1710	0.6308	0.0508	0.2124
2	2.1711	0.6383	0.1004	0.4153
3	2.1717	0.6152	0.1468	0.6302
Glass beads				
Test [-]	m_d [g]	e_0 [-]	w_0 [-]	S_{r0} [-]
1	2.1013	0.5674	0.0738	0.3252
2	2.1015	0.5673	0.1044	0.4601
3	2.1015	0.5777	0.1374	0.5945

m_d: dry mass

After a manual docking procedure, the unsaturated specimens are sheared with displacement control in different shear steps. After the initial docking and in between shear steps, CT images are acquired (with loading halted) resulting in a time series of uniaxial compression. Two of three test series on each material are run with 7 CT images and six shear steps at a strain increment $\Delta\varepsilon = 0.025$ resulting in a total strain of *ca.* 0.15 (depending on the individual initial specimen heights). One series is run with a finer strain resolution of $\Delta\varepsilon = 0.01$, resulting in 16 CT images during the shearing process (including the scan of the initial specimen configuration).

The time schedule of CT imaging and uniaxial compression steps and evolution of specimen water content, derived from CT data as well as the initial and final water content, are given in Figure 5.3. The good agreement of water content from CT data and measured water content indicates the linear effect of evaporation reducing the water content over time. This quantification of the inevitable effect of evaporation helps to evaluate the change in pore water clusters due to shearing, one of the research objectives.

The relationships between axial stress and strain as well as volume strain and axial strain, normally not measured in a uniaxial compression test, are derived from measured macroscopic data, *i. e.*, from the measured axial force and the displacement of the loading plate

as well as from specimen cross sectional area and total specimen volume. The specimen cross sectional area and total volume are measured from the CT data following an image analysis approach proposed by Andò (2013) which fills the inner pores of the voxelised specimen by a dilation algorithm and finally restores the outer shape of the specimen by erosion. These steps are applied to the CT data sets in the commercial image analysis software *Avizo* by using the implemented erosion and dilation algorithms. The modified specimen with all inner pores filled is finally used to calculate the cross sectional area and the total volume.

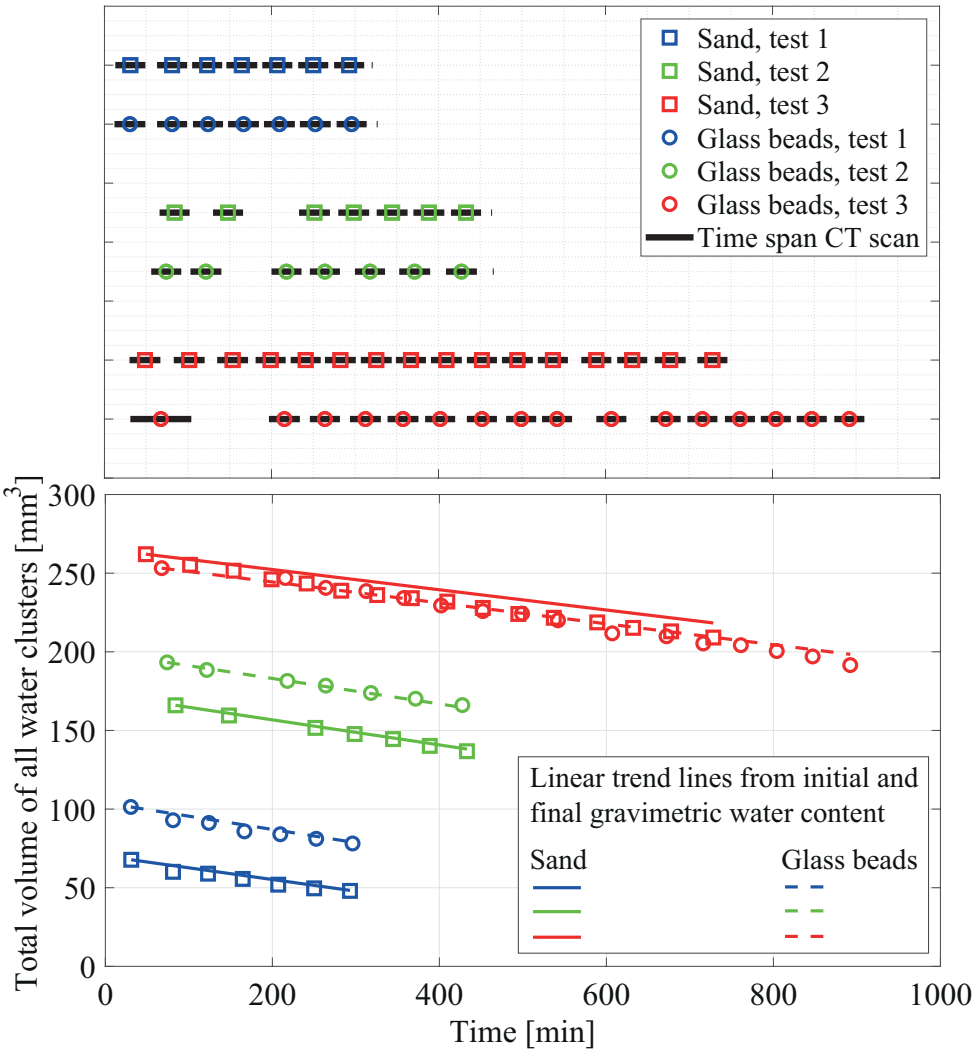


Figure 5.3: Timing of all CT scans during uniaxial compression (top) and development of pore water volume during the whole experiment based on voxel data and compared to trend lines derived from initial and final gravimetric water content (bottom) from Milatz *et al.* (2021b)

5.2.3 Evaluation of macroscopic hydro-mechanical behaviour

On a macroscopic level, the shear stress and volumetric strain have been measured as shown in Figure 5.4. The shear stress is calculated from the measured axial force per specimen cross sectional area from CT data and the volumetric strain is derived from the total volume change measured by a voxel count with all inner pores filled as described in Milatz *et al.* (2021b).

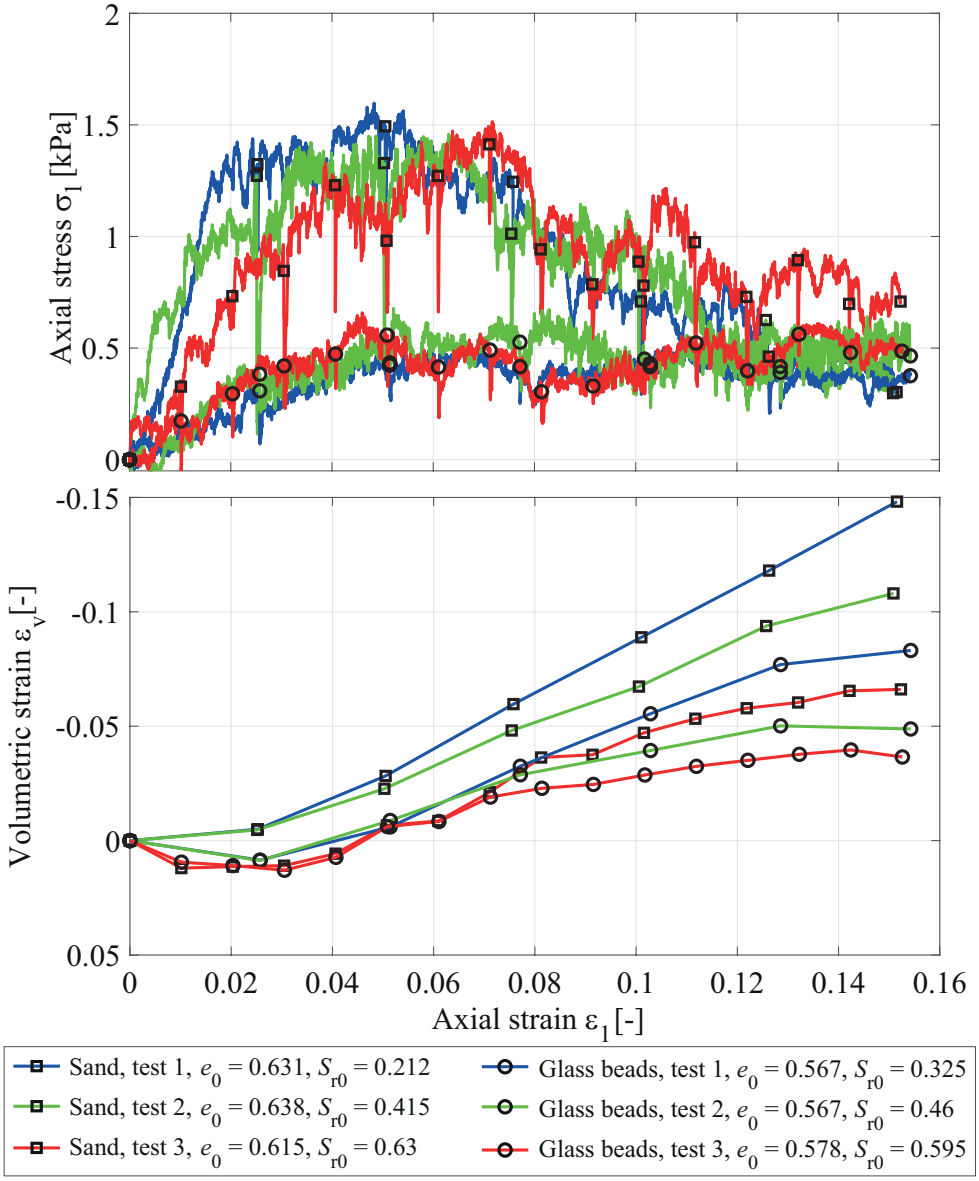


Figure 5.4: Axial stress (top) and volumetric strain (bottom) *vs.* axial strain measured on a macroscopic level during incremental uniaxial compression with CT imaging from Milatz *et al.* (2021b). Following the soil mechanics sign convention, dilatancy is expressed by negative volumetric strain

The results clearly indicate a higher shear strength of the Hamburg Sand specimens as compared to the glass beads. Although no clear dependence of maximum shear strength on varied degree of saturation is found, the volume change results exhibit a clear saturation-dependence with dryer specimens being more dilatant. While the sand specimens show a clear peak of axial stress with following softening phase, the glass bead specimens seem to shear in a more plastic mode with no clear peak encountered even for large axial strains up to $\varepsilon = 0.15$. The differences in the measured shear strengths to results from experiments under lab conditions, as shown in Figure 4.5 in Chapter 4, might be due to the incremental and rather long-time testing with parallel CT imaging, *e. g.*, leading to stress relaxation during CT scans with displacement controlled loading halted.

5.2.4 Evaluation and analysis of CT data

16-bit tiff greyscale images are obtained after image reconstruction using the software *X-act* by RX Solutions at Laboratoire 3SR. These raw image data are further processed using a combination of the open-source software *ImageJ/Fiji* and the commercial image analysis software *Avizo*. Based on different image filtering steps illustrated in Figure 5.5 the raw greyscale images are prepared for a following segmentation process where the different phases are separated.

In the filtering process, the greyscale values are firstly normalised in all images to increase the contrast, then they are median filtered and finally non-local means filtered based on Gastal and Oliveira (2012) using different *Avizo* modules. In all filtering steps, the settings are chosen such that the grain edges are preserved. The combination of filters allows to smooth greylevel differences in grains and in the liquid phase caused by noise as shown in Figure 5.5.

For the segmentation process, the 2D-histogram segmentation module in *Avizo* based on the approach by Jones *et al.* (2007) is applied. Different phases are identified using their greyscale value and a gradient of greyscale value in a stepwise semi-automatic procedure. Firstly, markers for seeding or labelling of the phases are calculated based on the greylevel gradient in the image. Then, a markers-based water shed algorithm is applied to assign the remaining unlabelled pixels to a corresponding material phase.

This kind of segmentation has been proven to be useful in the case of overlapping peaks in the greyvalue histograms of multiphase materials scanned with CT. This overlap of greylevels in some pixels does not allow to clearly derive a threshold to separate the phases thus leading to the so-called partial volume effect if a standard threshold-based segmentation is used. In the case of a granular material mixed with water, the partial volume effect would lead to ill-segmentation of the water phase at phase boundaries. With the help of the segmentation algorithm selected here, the partial volume effect can be minimised.

In order to obtain insights into the microscopic behaviour of the sheared specimens on the pore scale and to quantify capillary effects, the CT data are further analysed after segmentation. Firstly, macroscopic state variables, such as void ratio and degree of saturation, can be derived by a count of phase-separated voxels in a subvolume acting as a

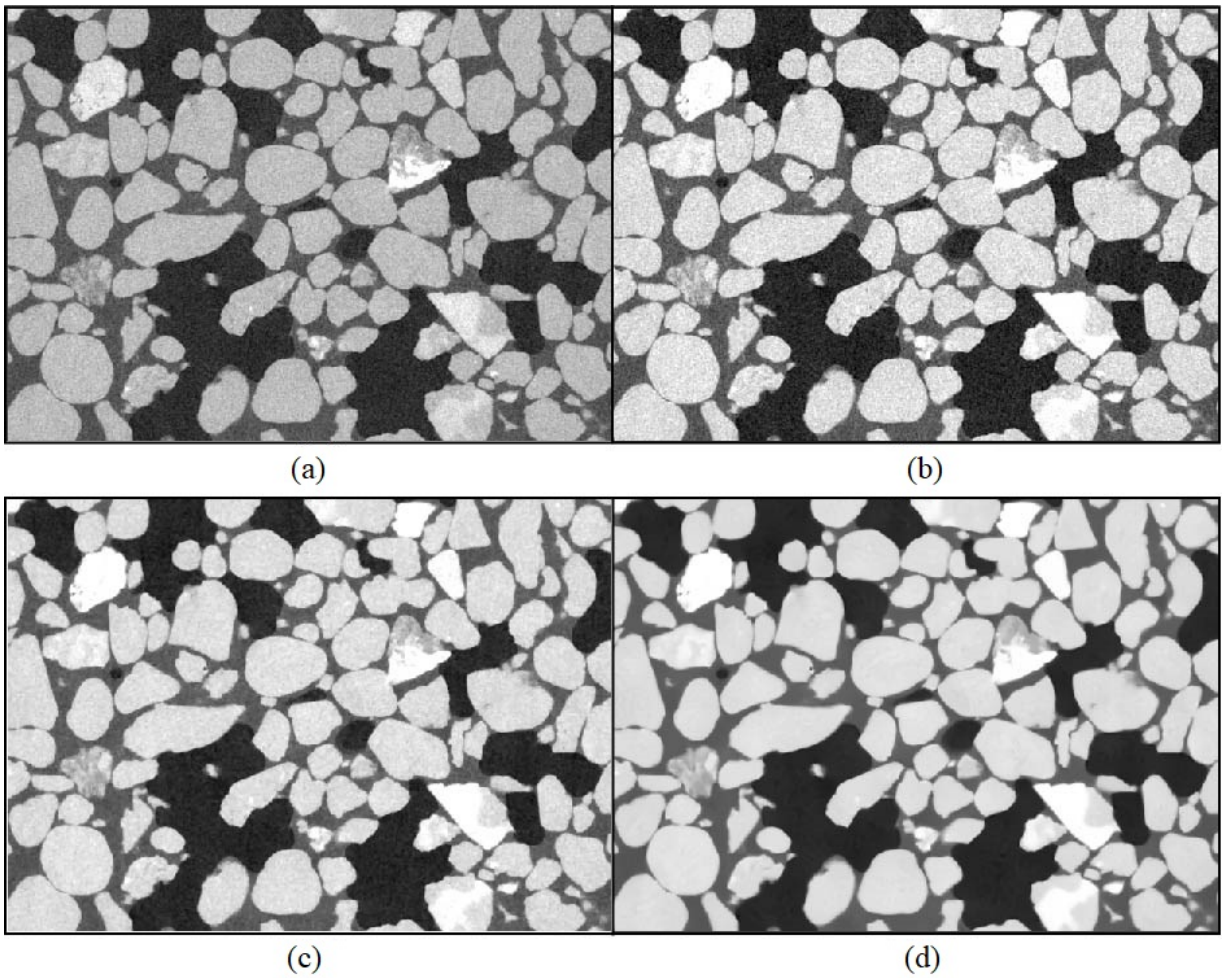
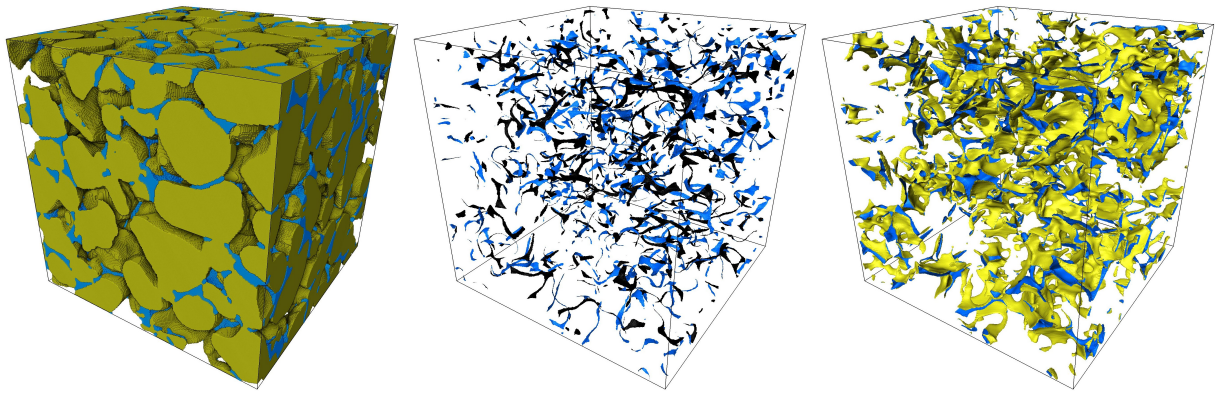


Figure 5.5: Steps of image improvement by different operations: (a) Raw image data, (b) greyscale normalisation, (c) median filter, (d) non-local means filter from Milatz *et al.* (2021b)

representative elementary volume (REV). The state variables are then calculated by averaging over the REV according to standard soil mechanical approaches. Besides a voxel count, also phase interfacial areas can be extracted from the CT data and related to the corresponding measurement volume yielding the specific interfacial areas between air and water and water and solid phase. Figure 5.6 shows a central cubic subvolume with edge lengths of 300 px extracted from a scanned unsaturated Hamburg Sand specimen with the sand grains shown in yellow and the water phase in blue colour. The air phase is not shown. Furthermore, the extracted air-water and solid-water interfacial areas are shown for the same subvolume. The interfaces are approximated by a surface triangulation using *Avizo* which allows to measure the specific interfacial areas per unit volume.

Averaging of voxel counts can also be achieved slice-wise and *vs.* specimen height, *i. e.*, allowing to analyse the distribution of state variables with scanned specimen height. The principle of subvolume-based local analysis of soil state variables is illustrated in Figure 5.7.



(a) (b) (c)

Figure 5.6: Solid and water phase in a central cubic subvolume with edge lengths of 300 px extracted from 3D CT data of a free-standing unsaturated Hamburg Sand column (a) as well as air-water interfacial areas (b) and solid-water interfacial areas (c) measured in the same subvolume

Usually, subvolumes are selected in a representative position inside the scanned specimen in order to avoid boundary effects. Furthermore, a specimen can be divided into several subvolumes to obtain information about local soil properties and their distribution inside a scanned specimen, which allows to evaluate homogeneity.

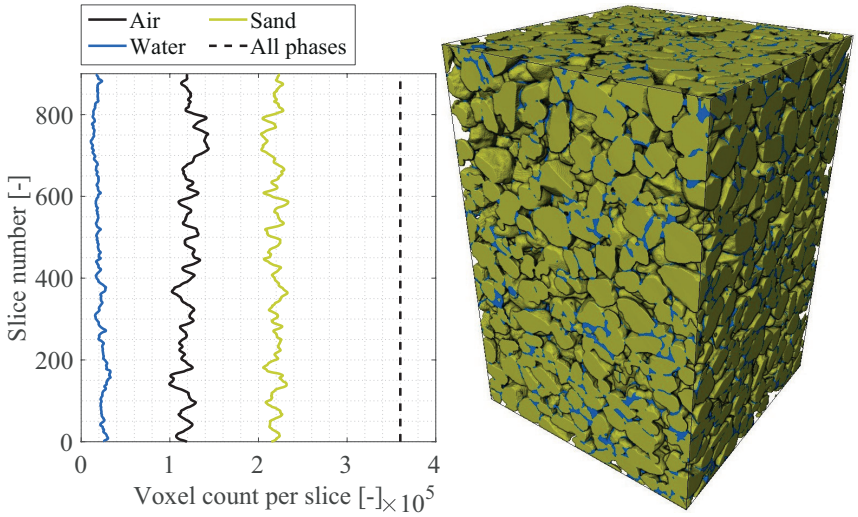
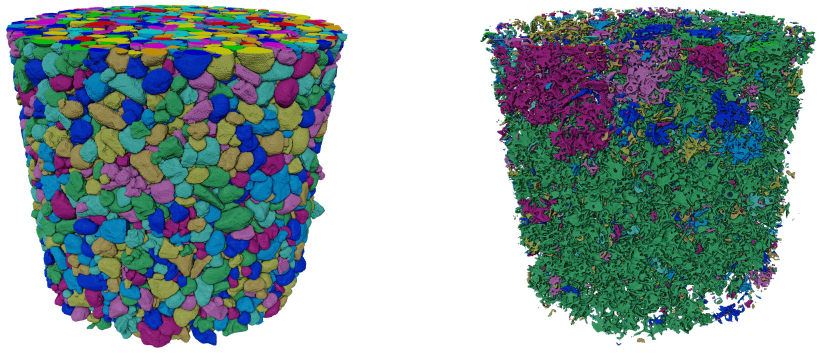


Figure 5.7: Analysis of segmented voxel-based CT data in a subvolume of Hamburg Sand: Voxel count *vs.* slice number (height) and 3D visualisation of the centred subvolume of $600 \times 600 \times 900$ px ($6.6 \times 6.6 \times 9.9$ mm) from Milatz *et al.* (2021b)

Secondly, also discrete properties of the multiphase system can be extracted from the CT data for quantitative analysis. After segmentation, individual grains as well as air and water clusters are firstly separated and then labelled, allowing to analyse the grain or cluster

collective statistically. Following this approach, grain and cluster volumes as well as shapes and morphologies can be studied, *e. g.*, regarding their distributions. Figure 5.8 shows the labelled sand grains and separated water clusters in an unsaturated sand specimen for uniaxial compression tests.



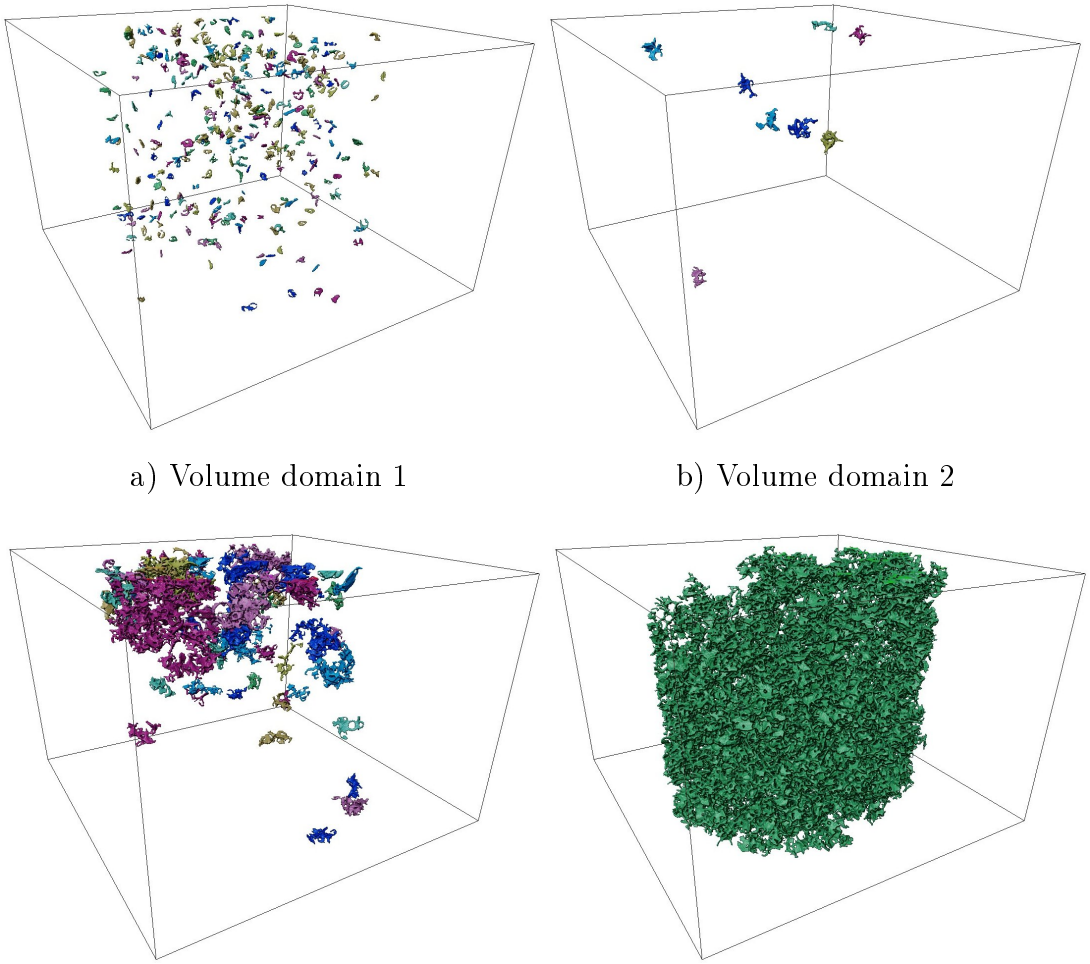
a) b)

Figure 5.8: 3D CT data of a free-standing unsaturated Hamburg Sand column. Independent grains and water clusters are labelled and distinguished by different colours. a) Sand grains, b) water clusters

For every CT data set, the liquid morphology of separate water clusters can be analysed as shown in Figure 5.9 for the initial state of a specimen of Hamburg Sand. Here, liquid clusters from the specimen shown in Figure 5.8 have been separated based on their volume, thus creating different volume domains 0–4. Volume domain 0 containing the smallest identified water volumes is not shown as it mainly covers noise and small fragments of capillary bridges. While volume domain 1 contains visible capillary bridges, volume domain 2 shows conglomerates of single capillary bridges. Volume domain 3 includes larger connected water clusters up to the second largest water volume, and volume domain 4 consists of a single cluster forming the largest portion of the water volume in the specimen. The development of the water clusters in both sand and glass bead specimens under uniaxial compression is analysed over time to investigate their behaviour in a dilating soil skeleton. Further results will be given in Chapter 6.

A discrete analysis of the grains during shearing is run using the open-source image analysis software *spam* "Software for Practical Analysis of Materials" (Stamati *et al.*, 2020). Based on a time series of greyscale images measured in an *in situ* CT experiment as well as on a labelled image of the initial grain configuration, the 3D discrete digital image correlation (DDIC) script in *spam* is applied to track grains and follow their labels during mechanical loading. Based on the known grain positions in every time step of an experiment, a regular Delaunay triangulation can be computed (Chareyre *et al.*, 2012), linking the grain centres and creating a mesh of tetrahedral finite elements for a further computation of strain fields from nodal displacements.

The regular Delaunay triangulation can be furthermore used in combination with the labelled phase-segmented images to analyse capillary effects on the pore level by defining



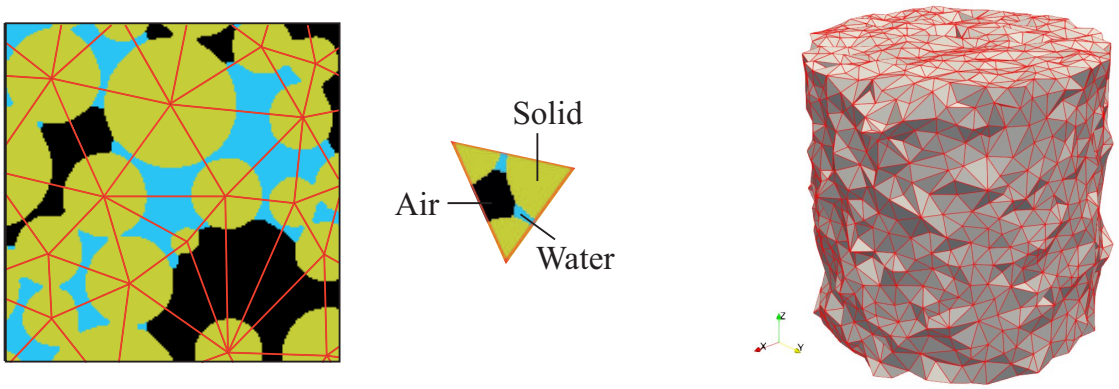
a) Volume domain 1 b) Volume domain 2

c) Volume domain 3 d) Volume domain 4

Figure 5.9: 3D representation of water clusters in unsaturated Hamburg Sand separated by their volume V: a) Domain 1: 2,618,500 $< V \leq$ 5,237,000 μm^3, b) Domain 2: 23,567,000 $< V \leq$ 26,185,000 μm^3, c) Domain 3: 26,185,000 $< V \leq 1.06637 \cdot 10^9$ μm^3, d) Domain 4: $V > 1.06637 \cdot 10^9$ μm^3 (Domain 0: $V <$ 2,618,500 μm^3 is not shown)

the tetrahedron in between four grain centres as a reference volume for which a pore-based degree of saturation can be calculated from the amount of segmented air and water voxels inside. This procedure is illustrated in Figure 5.10 showing an exemplary Delaunay triangulation on top of a 2D slice from a CT scan on a packing of glass beads together with an extracted triangle. The triangle includes voxels of all three phases. Over time, the development of "pore saturation" and local strains can be correlated to evaluate the mechanical effect of capillarity and its change during shearing of the grain skeleton of sand and glass beads.

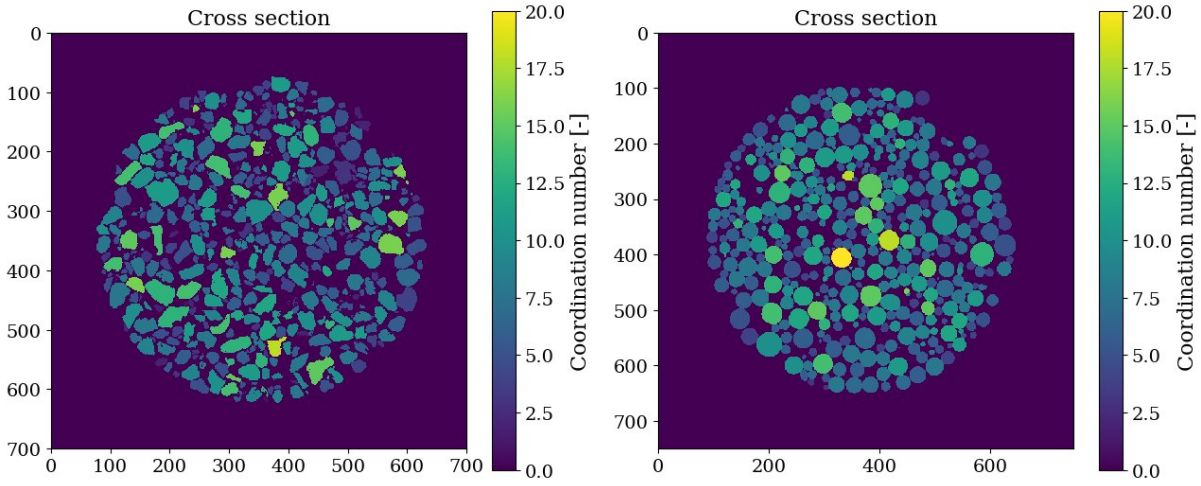
Grain contacts, represented by the coordination number, *i. e.*, the number of contact partners per grain, can be detected and calculated based on the work presented in Wiebicke *et al.* (2017b) and Wiebicke *et al.* (2019). For the calculation of coordination numbers in



(a) (b)

Figure 5.10: (a) Exemplary regular Delaunay triangulation for a 2D slice of a packing of glass beads together with an extracted triangle containing the solid, water, and air phase. The real analysis is run in 3D and results in tetrahedral volume elements in between grain centres (b)

spam, the greyscale and labelled images of the grain skeleton after a discrete image correlation analysis are needed. The evolution of grain contacts for the unsaturated glass bead and sand specimens is analysed following these approaches to study the change in grain fabric under the effect of matric suction. For this purpose, grain contacts can be mapped onto the corresponding grains to visualise their changes during shearing as shown in Figure 5.11.



a) Hamburg Sand b) Glass beads

Figure 5.11: Cross sectional middle slices of unsaturated free-standing soil columns of a) Hamburg Sand and b) glass beads with all particles labelled by their coordination number from Milatz *et al.* (2021b)

5.3 4D water retention experiments on sand and glass beads

With the help of *in situ* CT experiments during cyclic drainage and imbibition of granular media, microscopic hydraulic and capillary processes on the pore level are supposed to be uncovered leading to a more profound understanding of the macroscopic water retention behaviour of soils. The 4D data obtained from two experiments on Hamburg Sand is thus analysed in order to answer the following research questions:

1) Can the theories of microscopic origin of hysteresis be confirmed?
2) Which phase distributions and fluid structures develop during cyclic drainage and imbibition?
3) How do microscopic *capillary state variables*, such as fluid clusters, the interfacial areas, the length of the contact line or contact angles as potential ingredients of effective stress, develop upon different hydraulic paths?

In order to answer the research questions, the miniaturised flow cell apparatus for automated measurement of hydraulic paths of the WRC described in Section 4.3 of Chapter 4 has been applied in the X-ray tomograph at Laboratoire 3SR and at the Neutron and X-ray Tomograph (NeXT) at Institut Laue-Langevin (ILL) in Grenoble. In the framework of experiment UGA-73 at the ILL, reported in Milatz *et al.* (2019), a beamtime slot of 24 h could be used to run a transient water retention experiment with parallel X-ray and neutron CT imaging.

5.3.1 Experimental set-up at Laboratoire 3SR

For an experimental campaign at Laboratoire 3SR, the UNSAT-*Pi* 2 flow cell apparatus for WRC measurements is slightly adapted to account for CT imaging in between consecutive hydraulic experimental steps as shown in Figure 5.12. While the Raspberry Pi single-board computer is attached to the floor of the scanning cabin, all further hardware of the UNSAT-*Pi* 2 system, such as the miniaturised syringe pump, the pore water pressure sensors, and the specimen inside its flow cell are placed on the rotation stage to avoid relative movements of water tubes and data cables. The system on the rotation stage is connected to the single-board computer by a D-sub 25 cable which can curl up during rotation of the set-up.

5.3.2 Experimental set-up at Institut Laue-Langevin

For combined X-ray and neutron tomography imaging at the NeXT experimental facility, located at the Institut Laue-Langevin in Grenoble (Tengattini *et al.*, 2020), the previously described set-up using the UNSAT-*Pi* 2 system had to be further adjusted. As before, the

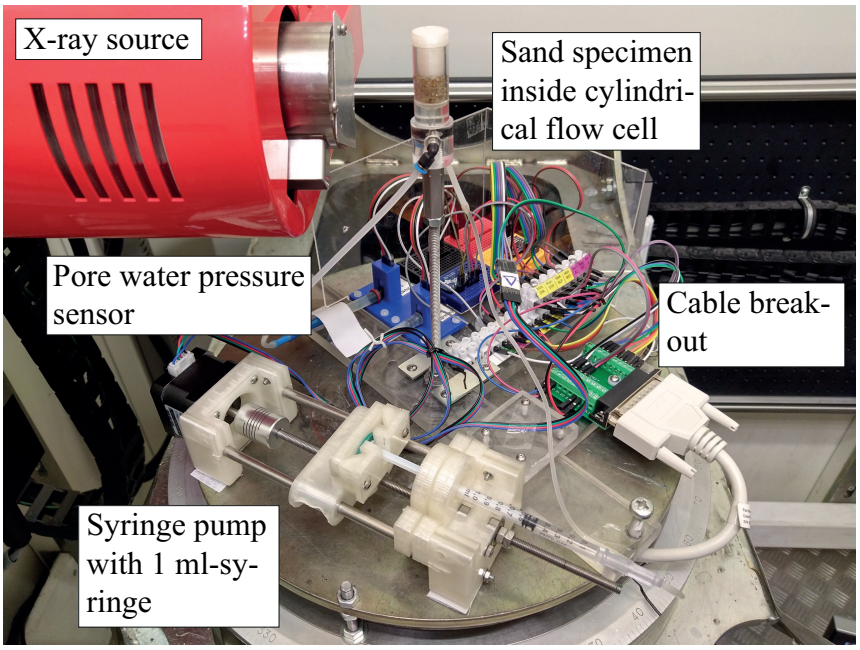


Figure 5.12: Detail of the experimental set-up for *in situ* CT imaging during a transient water retention experiment on Hamburg Sand on the rotation stage of the Laboratoire 3SR X-ray tomograph

hardware is placed on the rotation stage of the imaging instrument D50 T at ILL, with the Raspberry Pi being placed on the floor and connected to the set-up on the rotation stage by a D-sub 25 cable. The imaging beamline at NeXT is located inside a bunker for radiation protection constructed with heavy leaden concrete slabs. With the help of long cable connections, the Raspberry Pi for experimental control is connected to a screen, keyboard, and mouse outside of the bunker, enabling a manual control and monitoring of the experiments in the radioactive environment.

For the requirements of neutron imaging, the flow cell is made of aluminium, which is translucent for neutrons, with 1 mm thin walls to reduce the absorption of X-rays. In order to position the flow cell very closely to the neutron detector system, a lifting table is fixed on the rotation stage. Prior to the experiment, boron plates for radiation protection of sensitive hardware components, such as the Raspberry Pi and different circuit boards of the UNSAT-*Pi* 2 system, are placed around those components in the experimental bunker.

While the X-ray CT scanner is similar to the system at Laboratoire 3SR, the unique neutron imaging set-up, fully described in Tengattini *et al.* (2020), mainly consists of the ILL research reactor, representing the source of the neutron beam which is collimated to the desired rectangular field of view by an adjustable slit system, and of a neutron detector including a scintillator, a mirror, and a CCD camera with a mounted high quality lens for data acquisition. The whole set-up for combined X-ray and neutron tomography imaging of a transient water retention experiment with all technical components in place is shown in Figure 5.13. Further details on the experimental set-up are given in the technical report published in Milatz *et al.* (2019).

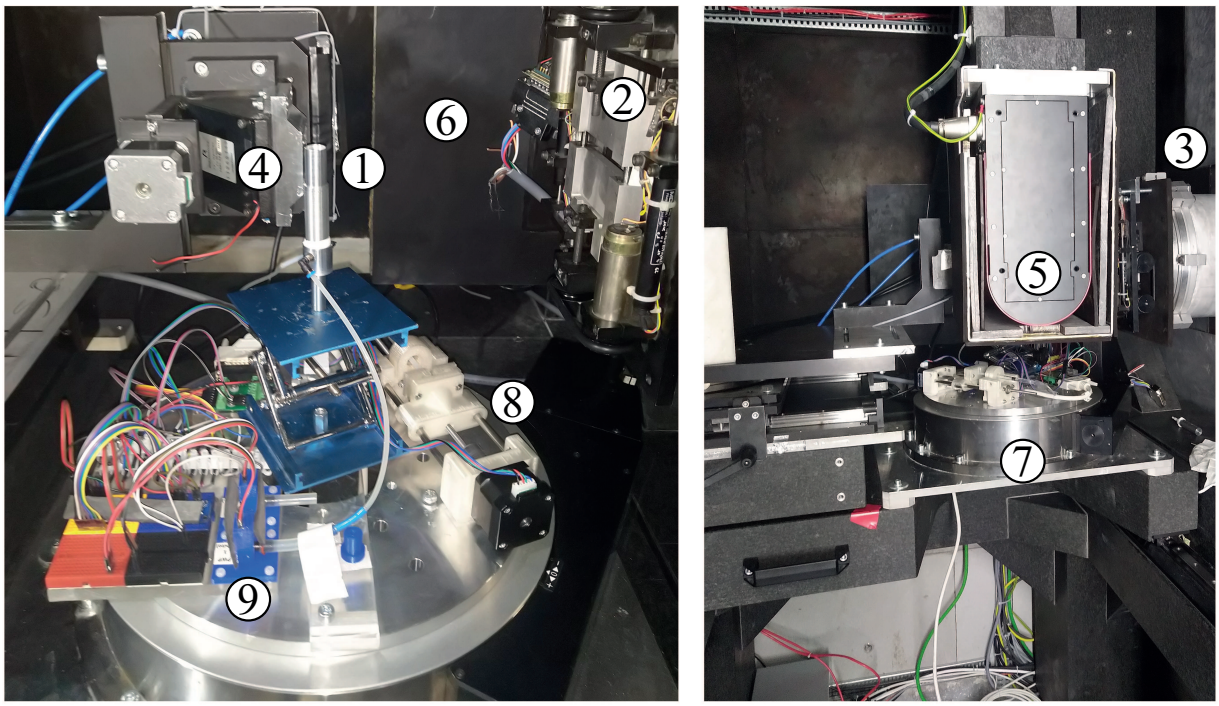


Figure 5.13: Experimental set-up in the NeXT research hutch using instrument D50 T at the ILL. Left: Water retention experiment placed on the rotation stage. Right: Same set-up centred in between neutron and X-ray source ready for the imaging experiments. ① Sand specimen in aluminium tube, ② Collimator slits of neutron source, ③ Neutron source, ④ Neutron detector with CCD camera, ⑤ X-ray tube, ⑥ X-ray detector, ⑦ Rotation stage, ⑧ Syringe pump, ⑨ Pore water pressure sensor

5.3.3 Testing procedure

In all water retention experiments with CT imaging reported here, initially water saturated specimens of Hamburg Sand are submitted to hydraulic cycles of drainage and imbibition. Initially and in between hydraulic steps, tomographies of the whole specimen volume are taken. In hydraulic steps, the same flow rate of $\frac{\partial V_w}{\partial t} = 0.0597\ \frac{mm^3}{s}$, corresponding to $\frac{\partial S_r}{\partial t} \approx 0.000112\ \frac{1}{s}$, as previously used in lab experiments is applied.

Specimens are prepared as described in Section 4.3.3 of Chapter 4 by pluviating the dry granular material in the water-filled flow cell. The initial macroscopic specimen properties in the two reported experiments at Laboratoire 3SR and at the ILL are summarised in Table 5.3.

Table 5.3: Initial macroscopic specimen properties in the water retention experiments

Test [-]	m_d [g]	e_0 [-]	w_0 [-]	S_{r0} [-]
1 (Lab. 3SR)	2.1711	0.650	0.2462	1.0
2 (ILL)	2.1711	0.650	0.2462	1.0

In the experiments run at Laboratoire 3SR, the Raspberry Pi used for the control of the experiment is connected to a secondary lab PC by an ethernet cable. This PC is connected to the control PC of the CT scanner. Via this network, a control loop is created that can automatically start CT scans from the main Python program on the Raspberry Pi. In this procedure, a second Python script is running on the auxiliary PC, checking the presence of control files written by the main Python script. If the file is written, a CT scan is started. This enhanced set-up leads to automated imaging experiments with CT scans initiated after all hydraulic steps in a regular pattern. At the ILL, no automated testing procedure is available. Therefore, hydraulic steps are started by a Python script in regular intervals with imaging steps in between. During imaging steps, combined X-ray and neutron tomography scans are started manually by the experimentalist.

While the available experimental time and automated testing procedure at Laboratoire 3SR nearly imposes no limitation on the experiment, leading to a test with 20 CT scans and 19 hydraulic steps, the limited beamtime at the ILL only allows to run a single experiment consisting of 10 CT scans and 9 hydraulic steps. Figure 5.14 illustrates the experimental procedure of the transient water retention test with parallel CT imaging run at Laboratoire 3SR. The sand specimen is subjected to an incremental primary drainage and main imbibition path, followed by further five incremental drainage and imbibition paths. The forced change of degree of saturation leads to a measured response of matric suction *vs.* time.

The settings of the X-ray source used in the experiments at Laboratoire 3SR and at the ILL are summarised in Table 5.4. Here, the scan settings of the ILL X-ray tomograph have been selected in accordance with the parallel neutron tomographies to achieve temporally simultaneous scans.

Table 5.4: Settings of X-ray CT scans at Laboratoire 3SR and at the ILL

Property	Laboratoire 3SR	ILL
X-ray tube voltage	120 kV	100 kV
X-ray tube current	83 μA	60 μA
Projections/360° revolution	1120	900
Isotropic voxel size	10 μm	22.8 μm
Binning	1	1
Averaging	4	6
Acquisition time per scan	$\approx$ 40 min	$\approx$ 46 min
Acquisition mode	Continuous rotation	Continuous rotation

Regarding the neutron beam characteristics at the time of the experiment, a neutron flux of $1.4{\cdot}10^{10}$ neutrons/cm^2/s reaches the experimental hutch at NeXT and is further reduced before hitting the specimen in its tomography position (Tengattini *et al.*, 2020). In the water retention experiment run at the ILL, neutron tomographies are measured in parallel to the X-ray tomographies at a voxel size of 15.2μm with 3$\times$ averaging and binning 2 (Milatz *et al.*, 2019).

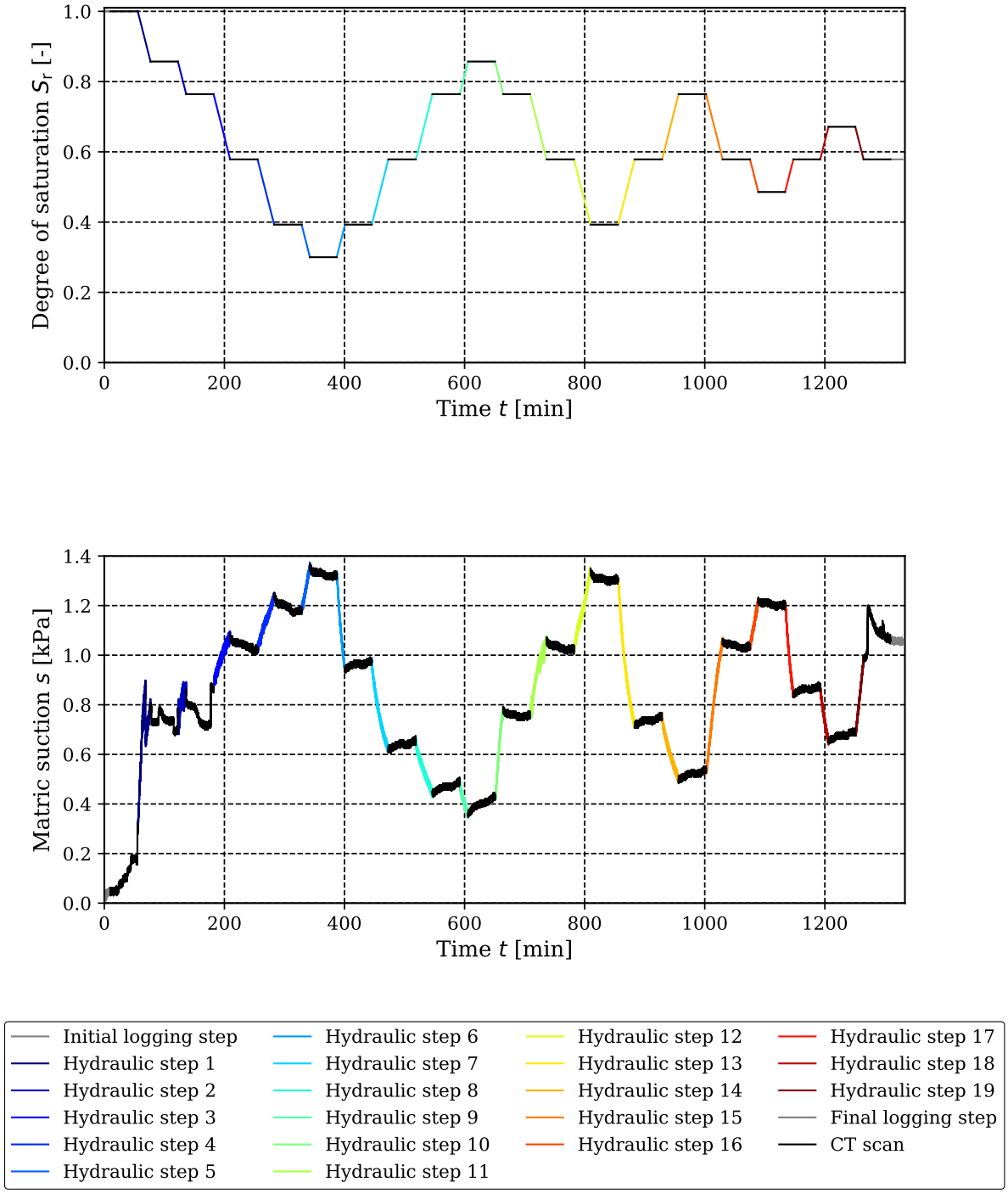


Figure 5.14: Change of degree of saturation (top) and measured response of matric suction (bottom) during a cyclic water retention experiment on a specimen of Hamburg Sand ($e_0 = 0.65$) with parallel CT imaging. Each colour represents a different hydraulic step. CT imaging steps are highlighted in black colour

5.3.4 Evaluation of macroscopic water retention behaviour

The combination of measured matric suction and degree of saturation prescribed in the transient hydraulic experiment with CT imaging and shown in Figure 5.14 results in a water retention curve reflecting the macroscopic hydraulic behaviour. As matric suction is continuously measured during CT scans with the prescribed pore water flow stopped, its change due to relaxation processes inside the specimen can be assessed. The WRC with all its consecutive 19 hydraulic steps, CT imaging steps (printed in black colour), and "just-log steps" (printed in grey colour), where matric suction is logged prior to and at the end of the experiment, is shown in Figure 5.15.

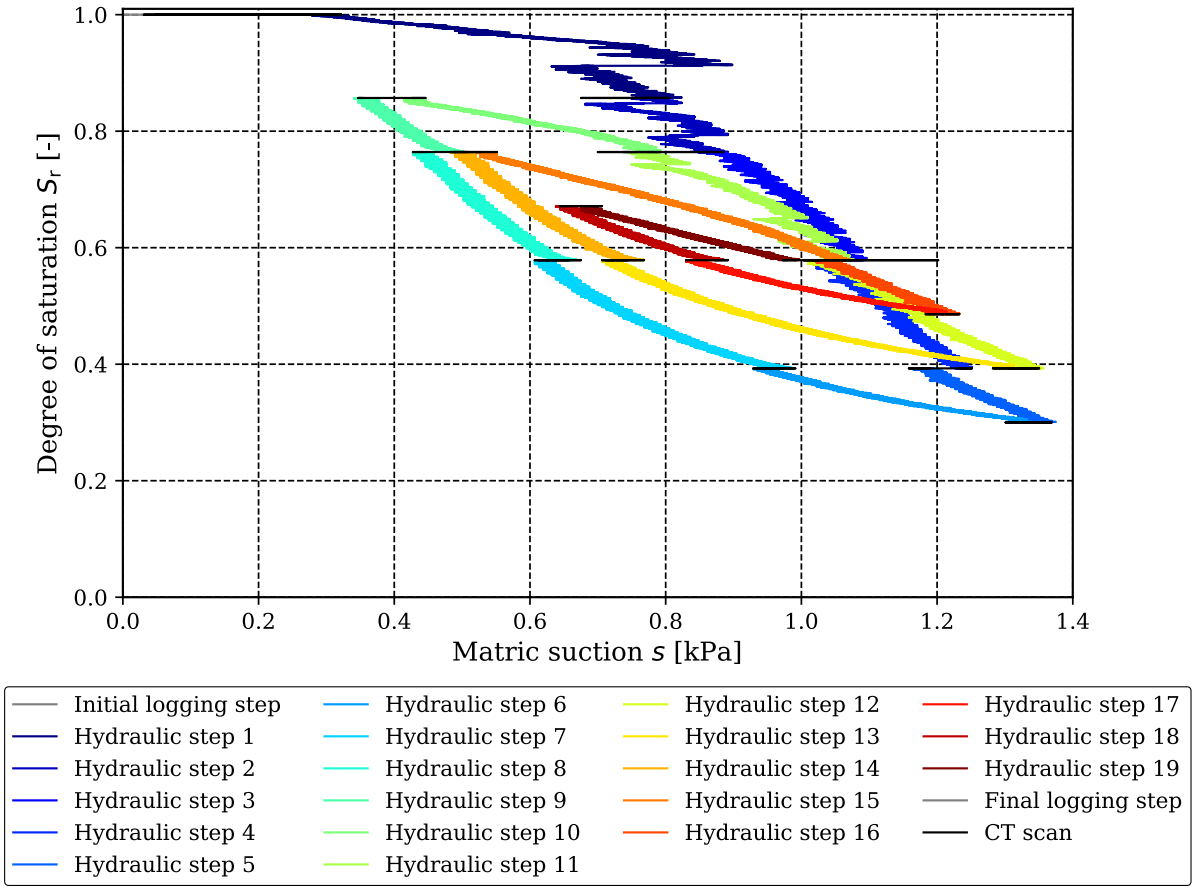


Figure 5.15: Transient water retention curve with 19 hydraulic steps measured during a cyclic water retention experiment on a specimen of Hamburg Sand ($e_0 = 0.65$) with parallel CT imaging. Each colour represents a different hydraulic step. CT imaging steps are highlighted in black colour

The WRC shows the typical hysteretic behaviour. Upon reversal of the flow direction, hydraulic scanning paths of elliptical shape returning to the bounding primary drainage and main imbibition paths are measured. There are many theoretical explanations for the hysteresis phenomenon originating from the microscale which will be discussed in the

detailled analysis of CT data in Chapter 6. The shape of the WRC measured during the CT experiment is very similar to the WRC shown in Figure 4.10 which is measured in transient mode under lab conditions without stops for CT scanning. However, in the *in situ* CT experiment a stop of water flow for CT imaging seems to lead to a decrease in measured matric suction on drainage paths and to an increase of matric suction on imbibition paths. This behaviour is encountered during all hydraulic steps, including higher-order scanning paths and might indicate slight non-equilibrium flow effects during transient pumping of pore water and a return to steady-state or equilibrium conditions during CT scanning with halted flow.

When drainage and imbibition paths are compared, pronounced differences in the smoothness of the curves with strong oscillations of matric suction occurring on drainage paths are revealed. However, these oscillations seem to rather occur during primary drainage and main drainage and are less pronounced on higher-order drainage scanning paths. Especially on the primary drainage path, a marked decrease and oscillation of matric suction after the air entry value around $s \approx 0.9$ kPa can be noticed. This decrease is partially recovered with increase of matric suction during further primary drainage. A reason for the discovered behaviour might be the invasion of air fingers upon primary drainage. This behaviour has been observed by eye in other experiments under lab conditions and is known to lead to heavy oscillations of matric suction measured through the porous plate at the bottom of the sand specimen. The phase distribution tracked by the available CT data will be checked to verify this assumption.

Besides hysteresis, air entrapment represents a macroscopic characteristic of the WRC. Air entrapment is based on microscopic hydraulic processes in a pore space with heterogeneous geometries. Although the main imbibition path shown in Figure 5.15 is changed to drainage prior to reaching $s = 0$ without showing evidence for air entrapment, other WRCs, *e. g.*, the one presented in Figure 4.10, hint at an entrapped air saturation of $S_{\mathrm{a}} \approx 0.1$. The air entrapment phenomenon will also be addressed by means of pore scale analyses in the following Chapter 6.

5.3.5 Evaluation and analysis of CT data

The evaluation procedure of reconstructed 16-bit greyscale images obtained in all CT scans is similar to the procedure described in Section 5.2.4. For image improvement, the greyscale images are firstly median filtered and then non-local means filtered before the phases are segmented with the 2D-histogram segmentation module in *Avizo*.

Due to the different attenuation mechanisms of neutrons as compared to X-rays, the highest absorption contrast of all present phases in neutron tomographies is obtained for the water phase, whereas air and the solid phase only cause little contrast in the images. This must be considered in the image processing and segmentation process of the neutron tomography data. A comparison of complementary greyscale images showing the multiphase system of Hamburg Sand during primary drainage as visualised by neutrons and X-rays is given in Figure 5.16 highlighting the benefits of combined neutron and X-ray imaging at NeXT.

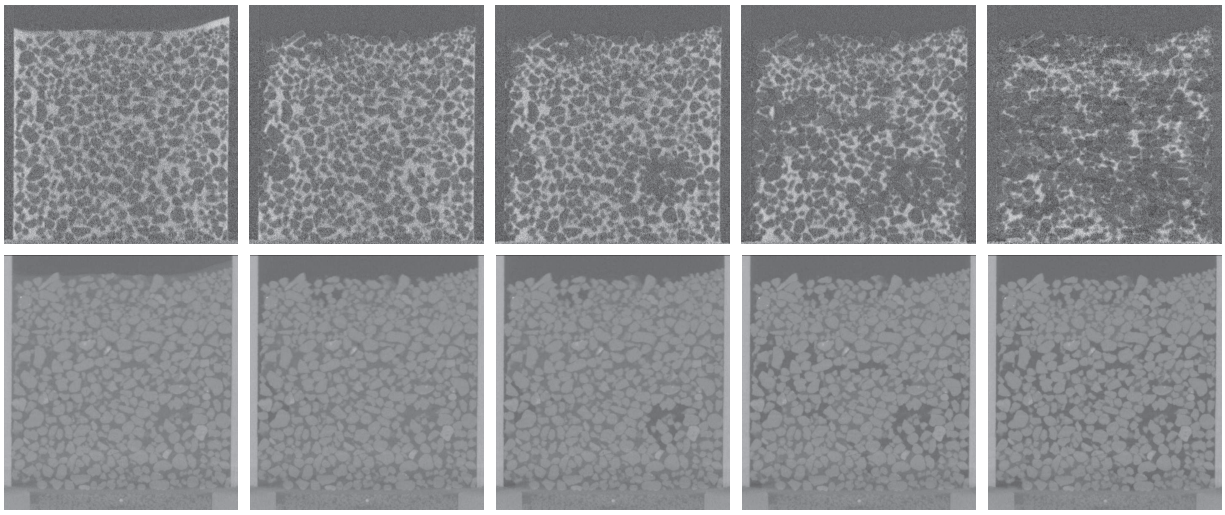


Figure 5.16: Greyscale images of vertical slices through a Hamburg Sand specimen during primary drainage as "seen" by neutrons (top row) and X-rays (bottom row) measured in the combined neutron and X-ray tomography experiment at the ILL. Scan 0 represents the initial water saturated state, while the following images in scans 1–4 are obtained after incremental drainage steps

For an analysis of soil properties *vs.* specimen height, such as void ratio and degree of saturation, a centred subvolume with edge lengths of 800 px × 800 px × 1145 px is cut out of the segmented specimen from the *in situ* water retention CT experiment at Laboratoire 3SR. In order to study local soil mechanical properties and capillary state variables, another cubic subvolume with edge lengths of 800 px × 800 px × 800 px is extracted. Both subvolumes are illustrated in Figure 5.17 inside the scanned specimen volume.

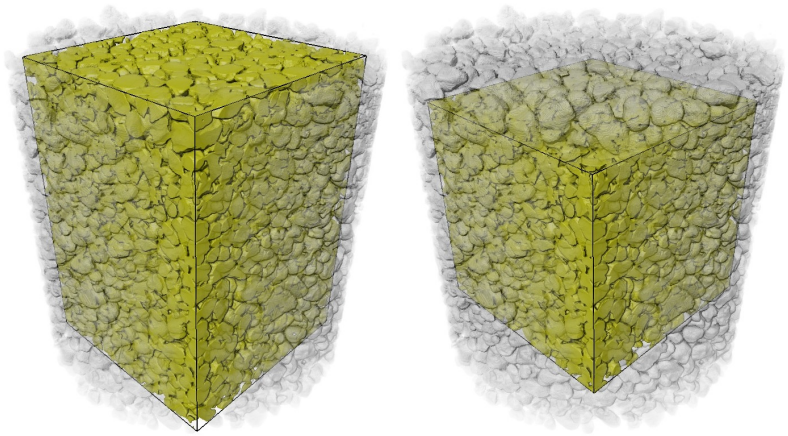


Figure 5.17: Embedded subvolumes within the grain skeleton of a Hamburg Sand specimen for further analysis of CT data measured at Laboratoire 3SR. Left: Subvolume of 800 px × 800 px × 1145 px. Right: Subvolume of 800 px × 800 px × 800 px (Milatz *et al.*, 2022b)

A systematic basis for the assessment of a sufficient subvolume size for yielding representative continuum results is given by a so-called REV analysis. In this analysis, the influence of the edge length of the Representative Elementary Volume (REV) on the corresponding state variables inside the REV is assessed. Such an analysis has been run on the cubic subvolume in Figure 5.17 with focus on the void ratio and degree of saturation. In order to consider all phases, the data after hydraulic step 5 with the lowest degree of saturation has been selected for the REV analysis. The results of the analysis in which subvolumes with edge lengths between 2 and 800 px are inflated centrally inside the cubic subvolume at an increment of 2 px are shown in Figure 5.18. The results indicate that the void ratio reaches a relatively stable plateau for a subvolume edge length of *ca.* 500 px. Regarding degree of saturation, a slightly larger subvolume size of *ca.* 700 px seems to be required to approach a constant degree of saturation. The homogeneity of the distributions of the state variables will be further discussed in Chapter 6.

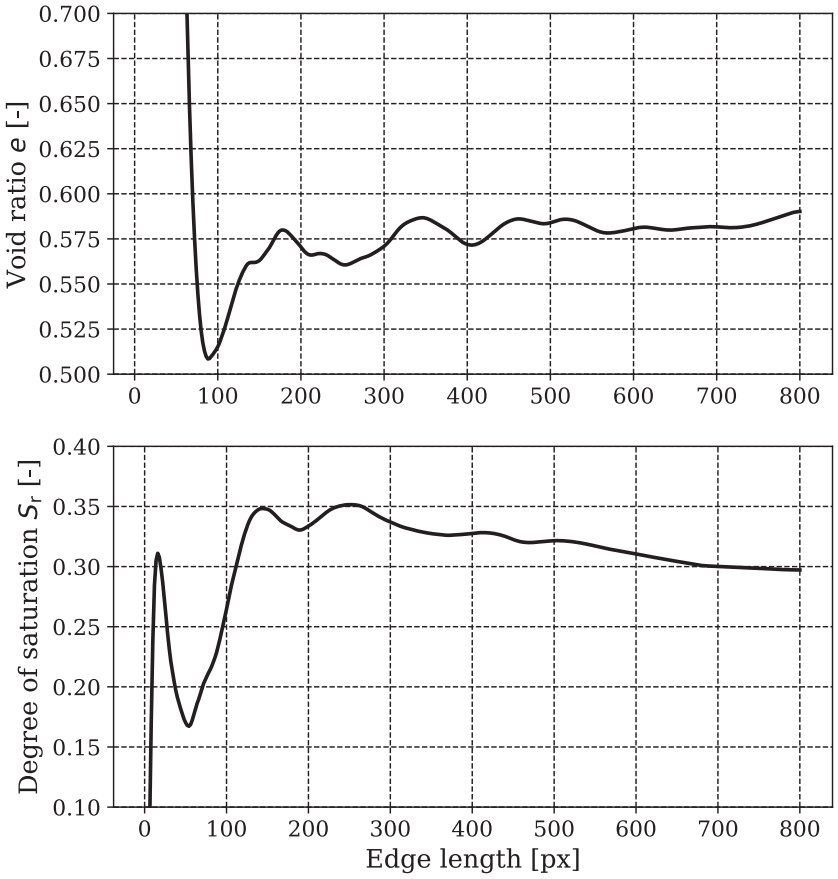


Figure 5.18: Subvolume-averaged void ratio (top) and degree of saturation (bottom) *vs.* edge length of the subvolume, calculated in a REV analysis of a subvolume of 800 px × 800 px × 800 px

Besides the interfacial areas, also the water and air clusters developing upon cyclic drainage and imbibition are investigated as described in Section 5.2.4. The connected air and water volumes can be classified by their volume distributions inside a reference subvolume. An

example of the distribution of individual air volumes evolving on a primary drainage path in Hamburg Sand is given in Figure 5.19.

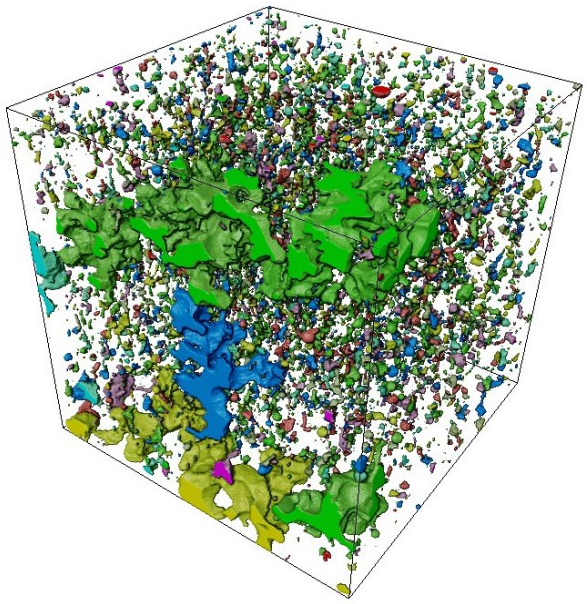


Figure 5.19: Separate air clusters in a subvolume of 800 px × 800 px × 800 px during primary drainage of a Hamburg Sand specimen measured in an *in situ* water retention CT experiment at Laboratoire 3SR. Individual air clusters are labelled by different colours (Milatz *et al.*, 2022b)

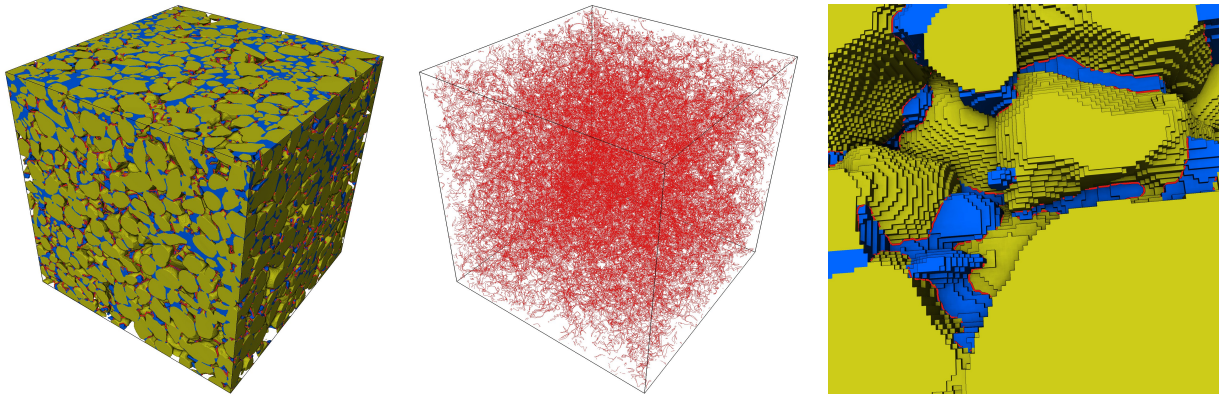
In order to characterise the shape of water and air clusters and especially to analyse the formation of air bubbles with the help of a single parameter, Wadell's sphericity ψ as defined by

$$\psi = \frac{\pi^{\frac{1}{3}}(6V)^{\frac{2}{3}}}{A} \tag{5.1}$$

is proposed. ψ relates the surface area of a sphere with the same volume as the considered volume V to its surface area A yielding $\psi = 1$ for exactly spherical volumes and lower values if the considered volume deviates from a sphere. With the help of sphericity, the regularity of the changing cluster distributions can be described. Furthermore, the occurrence of air bubbles and their entrapment in the pores can be investigated.

In addition to fluid volumes and interfacial areas, also the contact line representing the reference geometry for the action of surface tension in 3D space can be measured. Using the same triangulated surfaces as for the interfacial areas, the common line shared by all three present phases inside the cubic subvolume with edge length of 800 px is calculated using the *Avizo* software. The calculation procedure uses the *Avizo* module "Create Surface Geodesic Path" to extract the surface contours of all touching phases (a segmentation with 0: background, 1: air, 2: water, 3: solid is used here) which are then split into nodes and line segments and finally filtered by bounding box contact to remove contact line segments touching the bounding box to the exterior of the reference subvolume. If the total length

of all calculated line segments is normalised by the reference subvolume, the specific length of contact line per unit volume l_c is obtained that can act as another quantitative *capillary state variable* characterising the magnitude of mechanical capillary action due to surface tension in unsaturated granular soils. Figure 5.20 shows the 3D contact line and its extraction from the cubic subvolume for the lowest degree of saturation of the Hamburg Sand specimen after primary drainage.



(a) (b) (c)

Figure 5.20: Visualisation of the 3D contact line in a cubic subvolume containing Hamburg Sand and water at the lowest degree of saturation after primary drainage with the contact lines highlighted in red colour. The air phase is not shown. (a) Sand, water and highlighted contact line, (b) extracted contact line, and (c) zoom into a pore. Note that contact line segments touching the bounding box to exterior of the subvolume are not considered

The available CT data from the transient water retention experiment on Hamburg Sand is further analysed with focus on the radii of curvature and contact angles of individual capillary menisci. For this purpose, separate 2D slices parallel to the edges of the cubic subvolume and oriented in all three space directions are extracted from the subvolume. In these slices, different capillary menisci are identified and traced over time to obtain measurements of radii of curvature and contact angles for the same menisci on different hydraulic paths. Radii of curvature and contact angles are measured manually in extracted images of 120 × 120 px by using the radius of an inscribed circle and the "angle tool" in the software *ImageJ/Fiji* as illustrated in Figure 5.21. The measurements are based on the filtered images. Furthermore, the raw greyscale images and Sobel filtered images have been considered to facilitate the manual measurements. For regular menisci, one radius of curvature and two contact angles are extracted. However, not all menisci could be traced through all time steps due to irregular formation of menisci or image noise making the full measurement of all meniscus data impossible in some cases. The measured data, discussed in this work, consists of 182 drainage contact angles and 141 imbibition contact angles which might be representative to reflect the averaged macroscopic soil behaviour. However, more measurements are desirable in further studies for which an automatic detection procedure would be helpful. The procedure of manual measurement of radii of curvature and contact angles is illustrated in Figure 5.21.

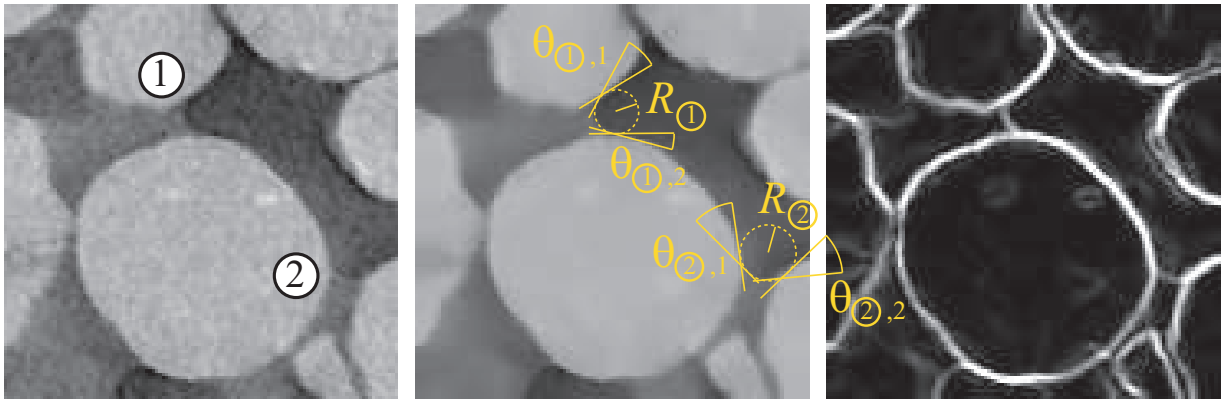


Figure 5.21: Manual measurement of radii of curvature and contact angles of selected capillary menisci in Hamburg Sand from 2D images with 120 × 120 px. (a) Identification of two menisci (labelled 1 and 2) in greyscale image, (b) measurement using inscribed circles and an angle tool in a filtered image and (c) Sobel filtered image for edge detection as a further help (Milatz *et al.*, 2022b)

In analogy to the DDIC analysis presented in Section 5.2.4 for the uniaxial compression tests, the grain displacements are tracked over time for the primary drainage path of the water retention experiment. Although rather no significant displacements are expected in an experiment with fixed grain skeleton and with focus on the hydraulic behaviour, the analysis is required as the grain positions in labelled images are needed for a pore-based analysis of the drainage process. This analysis is based on pores represented by tetrahedral elements linking the grain centres from a Delaunay triangulation as shown in Figure 5.10. Based on the obtained statistical information of pore volumes and pore-based degrees of saturation as well as linked grain displacements and strain calculated for every tetrahedron and for every drainage step, many insights into hydro-mechanical coupling and pore level drainage processes are brought to the light and described in detail in the following Chapter 6.

Chapter 6

Microscopic insights into the behaviour of unsaturated granular media

The quantitative analysis of three-dimensional and temporal data from imaging experiments opens the door to investigate possible links between macroscopic soil behaviour and microscopic capillary effects. In this chapter, selected results from the hydraulic and mechanical imaging experiments on unsaturated granular media described in the previous chapters are presented and discussed.

6.1 Hydro-mechanical behaviour during uniaxial compression

With the help of the miniaturised uniaxial compression tests on unsaturated granular media, the hydro-mechanical behaviour on the grain or pore scale can be investigated by analysing the phase distribution as well as further *capillary state variables*. This analysis is applied to answer the main questions from section 5.2 which are related to the link between macroscopic shear strength as well as volume change and the change of the microscale state variables due to shearing.

6.1.1 Evolution of phase distributions and discrete water clusters

Based on the reconstructed and segmented CT data during uniaxial compression, in a first analysis step, the overall behaviour of the solid and water phase is evaluated as shown in Figure 6.1. The image series captures the heavy bulging of the sand and glass bead grain skeletons as well as the deformation of the water phase which consists of water clusters of different volume size domains as described in Section 5.2.4 of Chapter 5.

Not a single grain is observed to fall out of the granular assemblies kept together by visible water clusters and capillary bridges during the experiment. However, movements of grain chains linked by water bridges along the sides of the bottom loading plate can be noticed

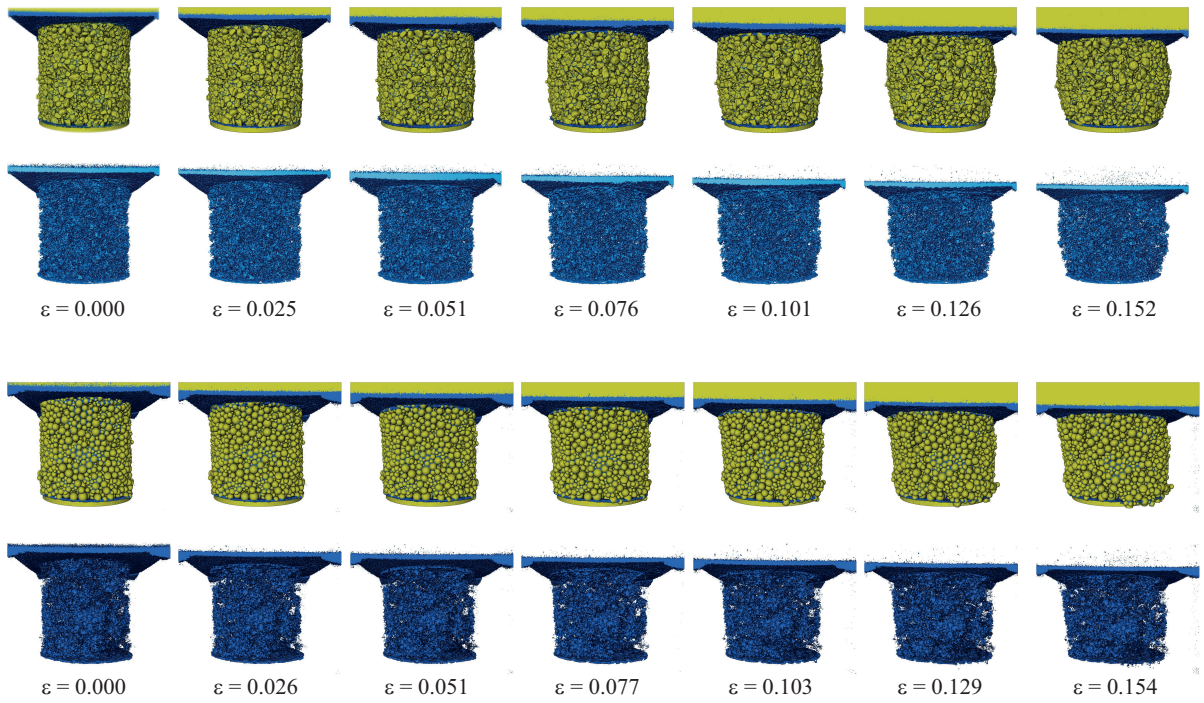


Figure 6.1: 3D rendering of segmented volumes (non-air phases) acquired during uniaxial compression of sand specimen (test 1) and glass bead specimen (test 1) from Milatz *et al.* (2021b). The initial macroscopic degrees of saturation are $S_{r0} = 0.2124$ for the sand specimen and $S_{r0} = 0.3252$ for the glass bead specimen (compare Table 5.2 in section 5.2)

particularly for the glass beads. From the second shear step onwards, both specimens show bulging due to the strong dilatancy discussed above. If only the water phase is observed, a large deformation of the water clusters due to the dilatant behaviour of the grain skeleton can be noticed.

Based on the analysis of subvolumes inside the sheared grain skeleton as shown in Figure 5.7, the evolution of state variables *vs.* specimen height is studied to evaluate their change and interaction. The state variables, such as void ratio or degree of saturation, are calculated on a local basis for every slice and are shown in Figure 6.2 and in Figure 6.3 for the driest sand and glass bead specimen, respectively. For all experiments, the measured state variables are compared to the macroscopic values and to the initial trend. In the case of void ratio, also the bounds given by the minimum and maximum void ratios e_{min} and e_{max} are plotted.

In most of the experiments, the trend of initial void ratio indicates a slightly denser specimen at the bottom which might be due to specimen preparation by compaction in layers. Especially for the specimens with lower initial macroscopic degrees of saturation, the initial void ratio is bounded by the minimum and maximum void ratios. The agreement of initial macroscopic and trend of void ratio is better for the sand specimens as compared to the glass beads. In all specimens, the void ratio is increasing in the middle of the specimen height in accordance with the observed macroscopic bulging which is likely due

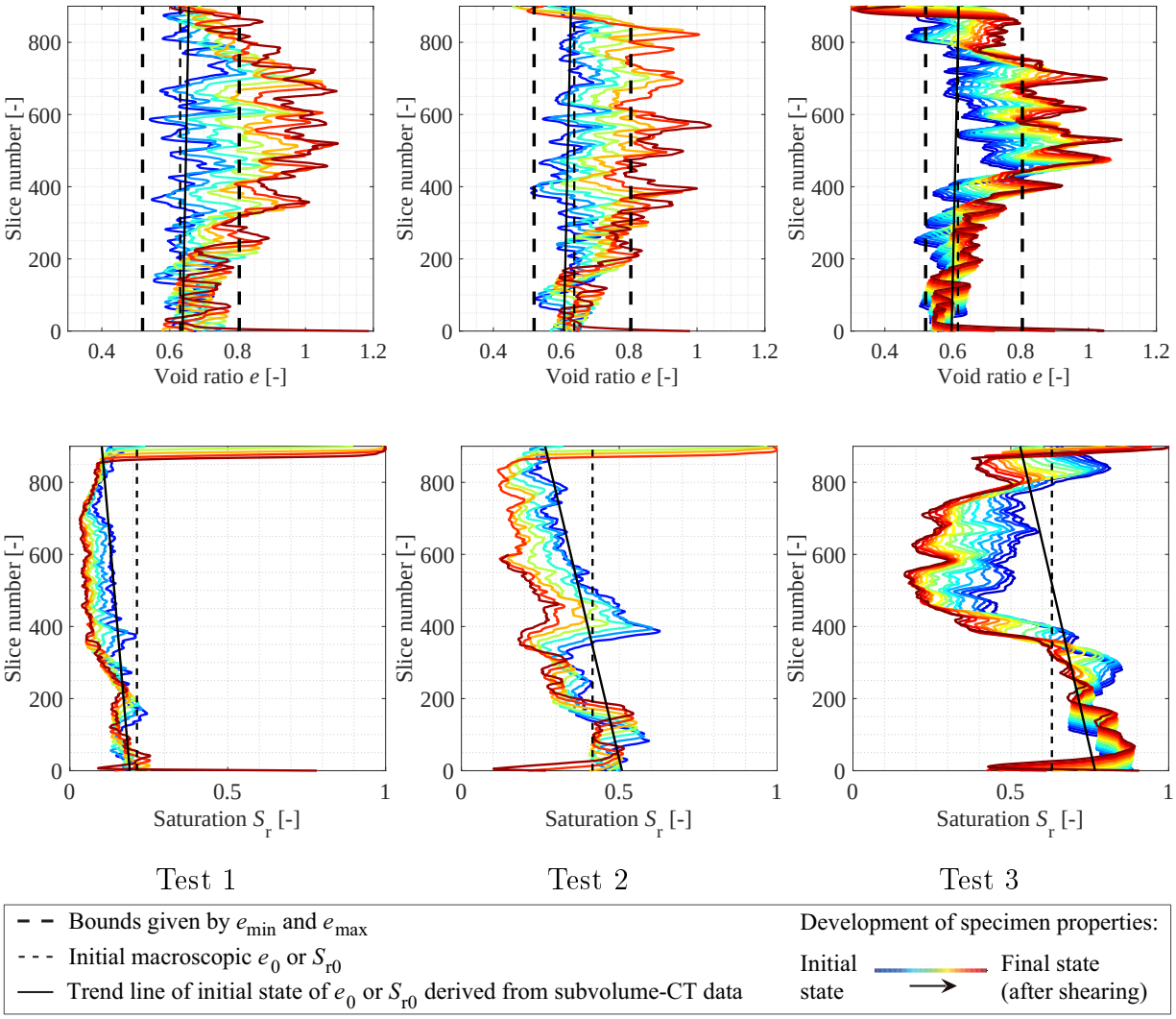


Figure 6.2: Slice-wise specimen properties derived from a subvolume of $600 \times 600 \times 900$ px for Hamburg Sand from Milatz *et al.* (2021b)

to friction at the top and bottom loading plate. The dilation is most pronounced for the driest specimens which confirms the macroscopic volume change results in Figure 5.4. It is noteworthy that in all specimens void ratios larger than e_{max} are reached after a few shear steps. This is only possible due to the reinforcing effect of water clusters and liquid bridges.

Despite the small specimen height, the local degrees of saturation reveal a gradient due to gravity with increased water content at the specimen bottom. The gradient is generally higher with increasing macroscopic water content and more pronounced in the glass bead specimens, probably due to their lower water retention capacity. Due to shearing, the degree of saturation is generally decreasing with the most pronounced reduction of degree of saturation in the zones of maximum dilation, highlighting the relationship of pore volume change and water content. Evidence for hydro-mechanical coupling and the strengthening effect of matric suction at elevated degrees of saturation is given by the observation that

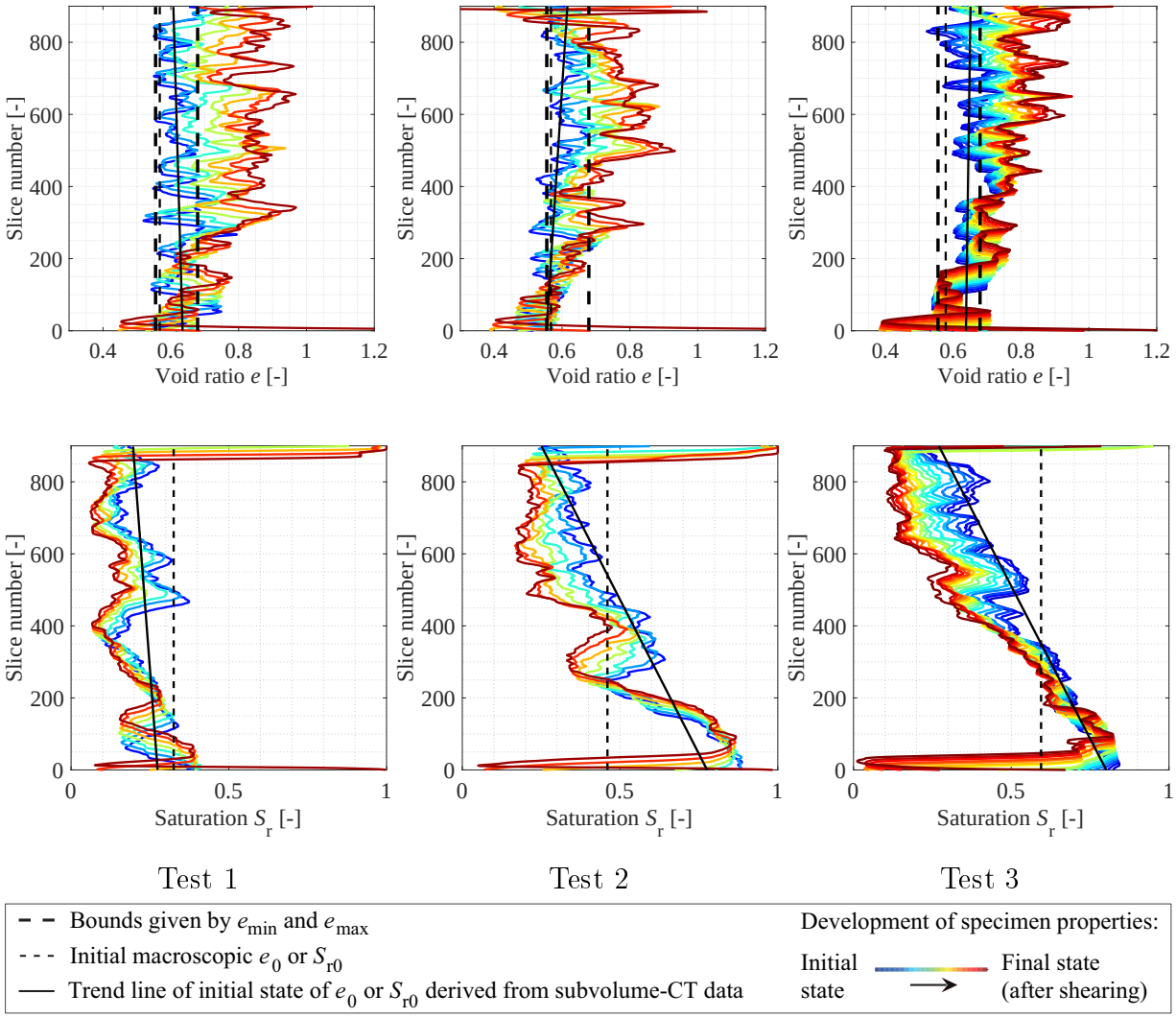


Figure 6.3: Slice-wise specimen properties derived from a subvolume of $600 \times 600 \times 900$ px for glass beads from Milatz *et al.* (2021b)

the dilation is more pronounced in dryer zones.

At the upper and lower boundaries which approach into the considered spatially fixed subvolume, always centred at specimen mid height with increasing number of shear steps, the image data is influenced by noise which is partially detected as the water phase in the segmentation process. This leads to the pronounced change of degree of saturation for the lower and upper slices in the discussed subvolume.

Besides the subvolume-based analysis of homogenised state variables, an analysis of discrete water clusters is of interest to evaluate the influence of shearing and dilation on the cluster distribution and its mechanical stability. For this purpose, different water cluster domains have been defined in an image series as illustrated in Figure 5.9. All water clusters are labelled based on their volume. The cluster volume size distribution *vs.* shear step as shown in Figure 6.4 for two tests on Hamburg Sand and glass beads allows to evaluate the change of clusters under the combined effect of shearing and evaporation.

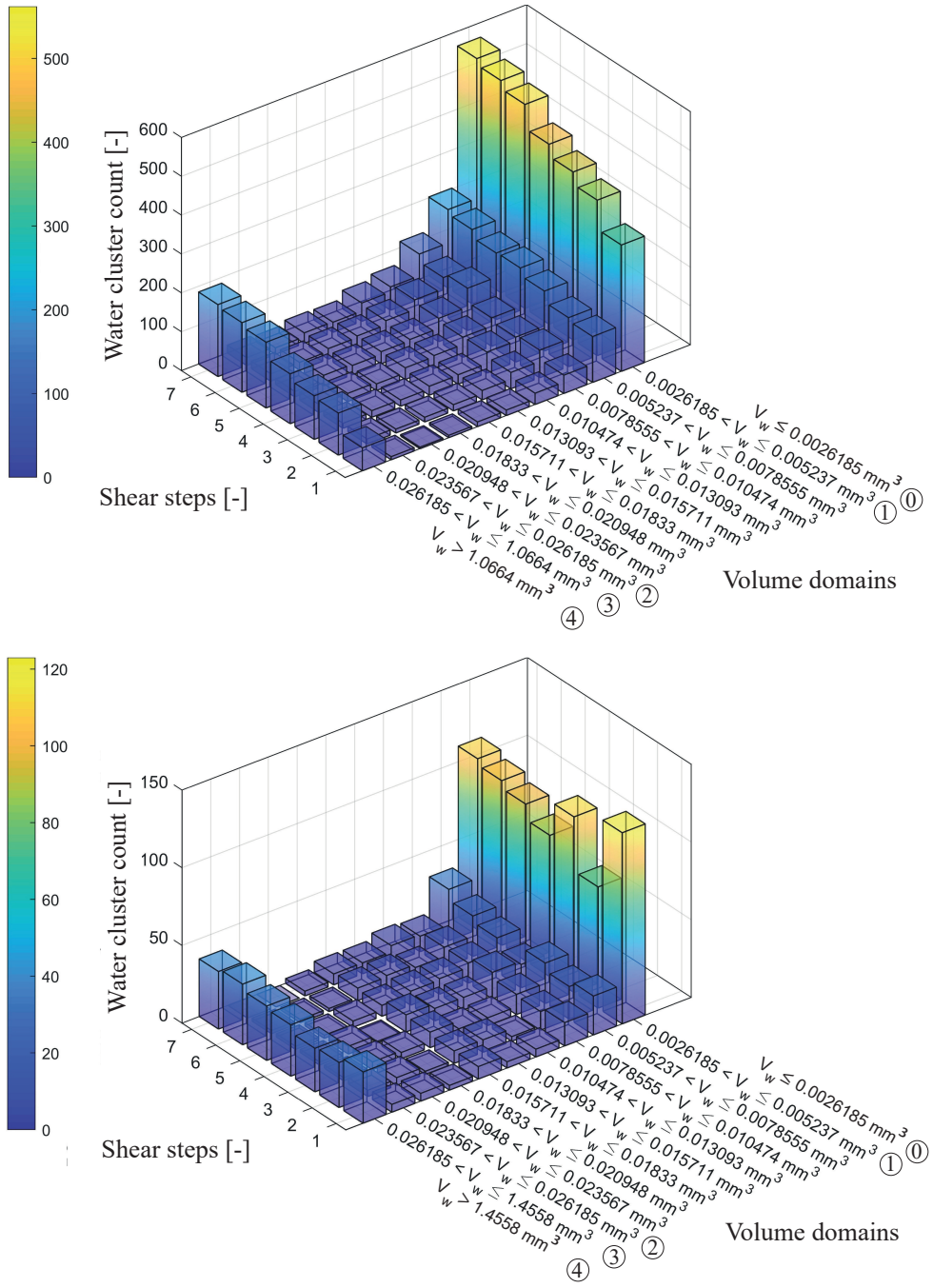


Figure 6.4: Histograms of water cluster volumes during shearing of the driest sand specimen (top) and driest glass bead specimen (bottom) from Milatz *et al.* (2021b). Volume domains according to Figure 5.9 in Chapter 5. Shear step 1 represents the initial specimen state

The analysis of water clusters reveals a dominance of smaller water clusters in both granular materials, however, with an increased amount of clusters in the larger volume domain 3

also present. During shearing, especially an increase in smaller clusters can be noticed in both materials. Being related to image noise, the smallest volume domain is not shown. Similarly, the largest volume domain, only containing a single cluster or very few clusters, is not plotted. When both materials are compared, it must be noticed that more clusters are present in the sand.

When the deformation of the labelled water clusters is tracked over time, their breakage behaviour can be visualised and studied. However, it must be mentioned that also evaporation is acting on all water volumes as further discussed in Milatz *et al.* (2021b). In both materials, a decay of larger water clusters into smaller ones can be noticed in Figure 6.5 and Figure 6.6. Especially, the break-up of the largest cluster into smaller clusters to be found in smaller volume domains, *e. g.*, in domain 3, can be observed in both materials. The rupture of the largest cluster in volume domain 4 and degradation into smaller clusters happens earlier, *i. e.*, at a smaller axial strain, in the sand as compared to the glass beads. Furthermore,the number of liquid bridges in volume domain 1 is also increasing in both materials. This increase is more pronounced in the sand specimen.

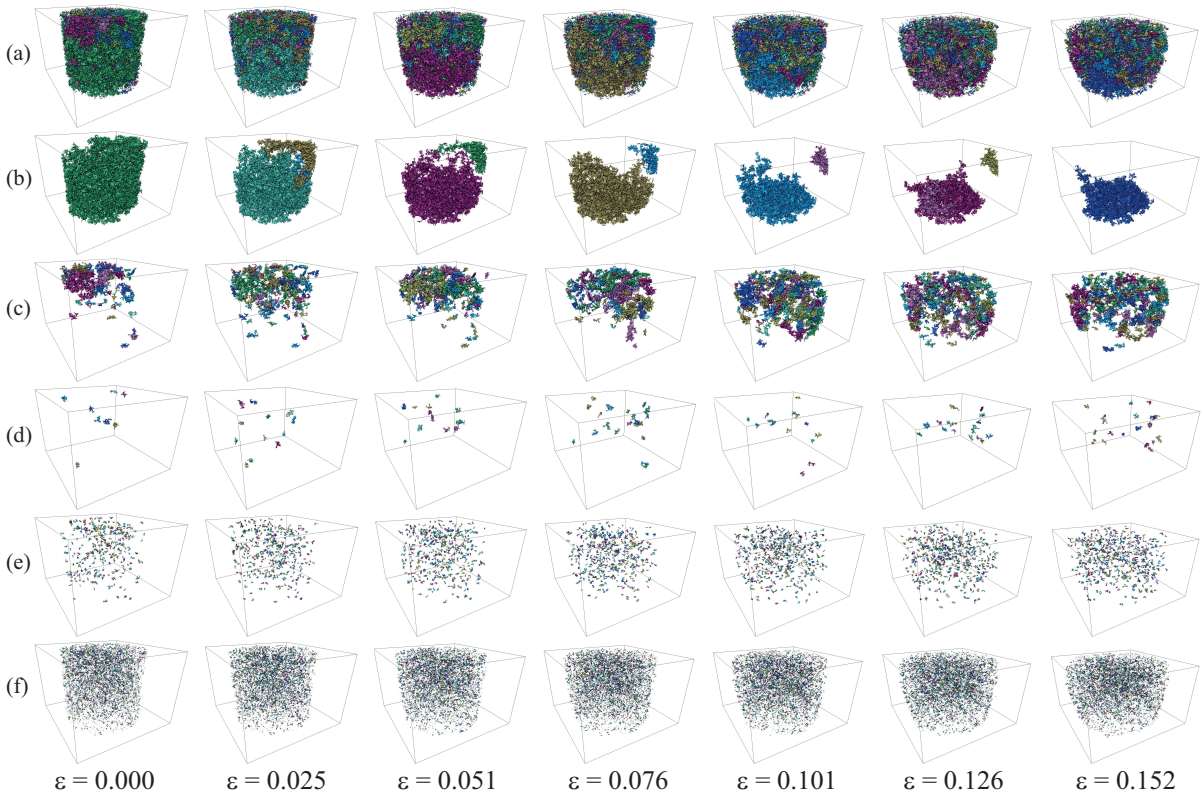


Figure 6.5: Visualisation of independent water clusters during shearing of the driest sand specimen: (a) All clusters, (b) domain 4, (c) domain 3, (d) domain 2, (e) domain 1, (f) domain 0 from Milatz *et al.* (2021b)

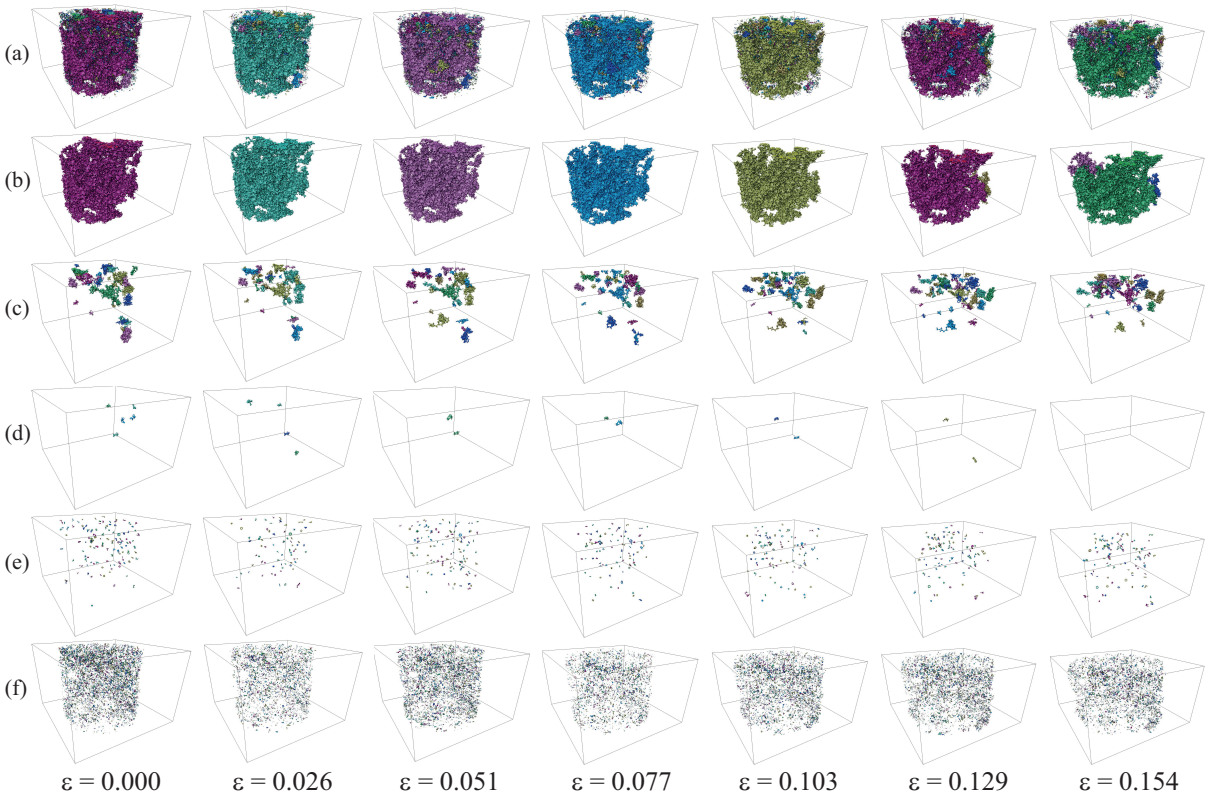


Figure 6.6: Visualisation of independent water clusters during shearing of the driest glass bead specimen: (a) All clusters, (b) domain 4, (c) domain 3, (d) domain 2, (e) domain 1, (f) domain 0 from Milatz *et al.* (2021b)

6.1.2 Evolution of interfacial areas

Besides the specimen void ratio and degree of saturation, also the specific interfacial areas are measured inside a central cubic subvolume and analysed with focus on their change during uniaxial compression. Plotting the air-water interfacial area a^{nw} and the solid-water interfacial area a^{sw} *vs.* degree of saturation in Figure 6.7, seems to yield a characteristic relationship for both granular materials.

Due to the different initial saturation levels of the six specimens and the change of degree of saturation during shearing and parallel evaporation, a large range of saturation is covered by the available data. While the air-water interfacial area shows a maximum in the range of the occurring saturation, the solid-water interfacial area data form a monotonic curve with a maximum apparently reached for the highest degree of saturation and with a theoretical value of $a^{\mathrm{sw}} = 0$ for $S_{\mathrm{r}} = 0$. Due to the combined effect of shearing leading to a decrease of saturation because of dilation and because of evaporation, the air-water interfacial area either increases or decreases depending on the initial degree of saturation during the experiments. The solid-water interfacial area, on the contrary, only shows a monotonic decrease during the combined effect of shearing and evaporation. These combined effects are included in the evolution of the interfacial areas with axial strain shown in Figure 6.8.

The change of the interfacial areas due to shearing is an important observation as both

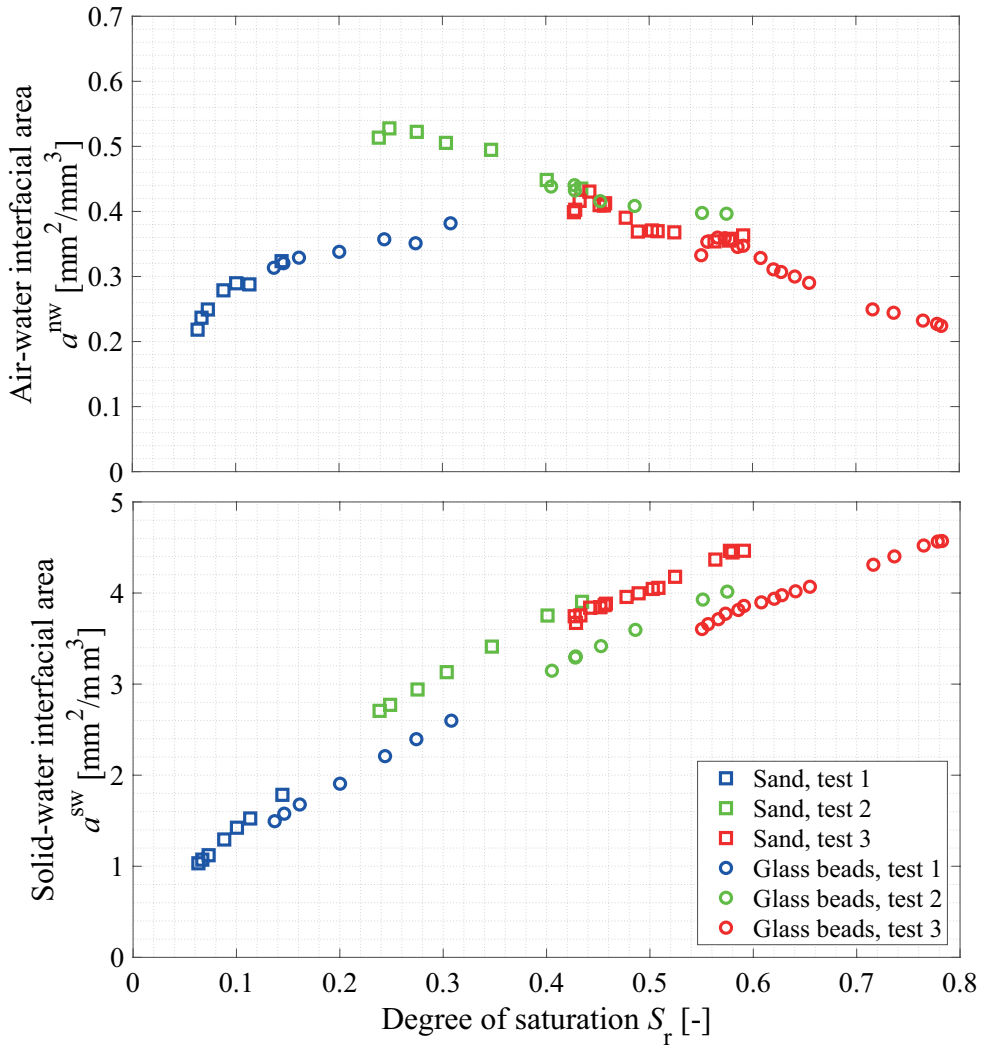


Figure 6.7: Development of air-water interfacial area (top) and solid-water interfacial area (bottom) *vs.* local degree of saturation in a centred subvolume of $300 \times 300 \times 300$ px during uniaxial compression of the sand and glass bead specimens from Milatz *et al.* (2021b)

capillary state variables can be seen as ingredients of suction stress which represents the contribution of capillarity to the effective stress as outlined in Chapter 2. Further measurements of characteristic relationships of the interfacial areas are presented and discussed in section 6.3 in the framework of the water retention experiments.

6.1.3 Discrete grain motion, strain fields, and coupling to pore saturation

The analysis of 4D data by means of discrete digital image correlation opens the door to further insights into the hydro-mechanical behaviour of unsaturated granular media on the grain scale. Based on the discrete grain movements and the discretisation by tetra-

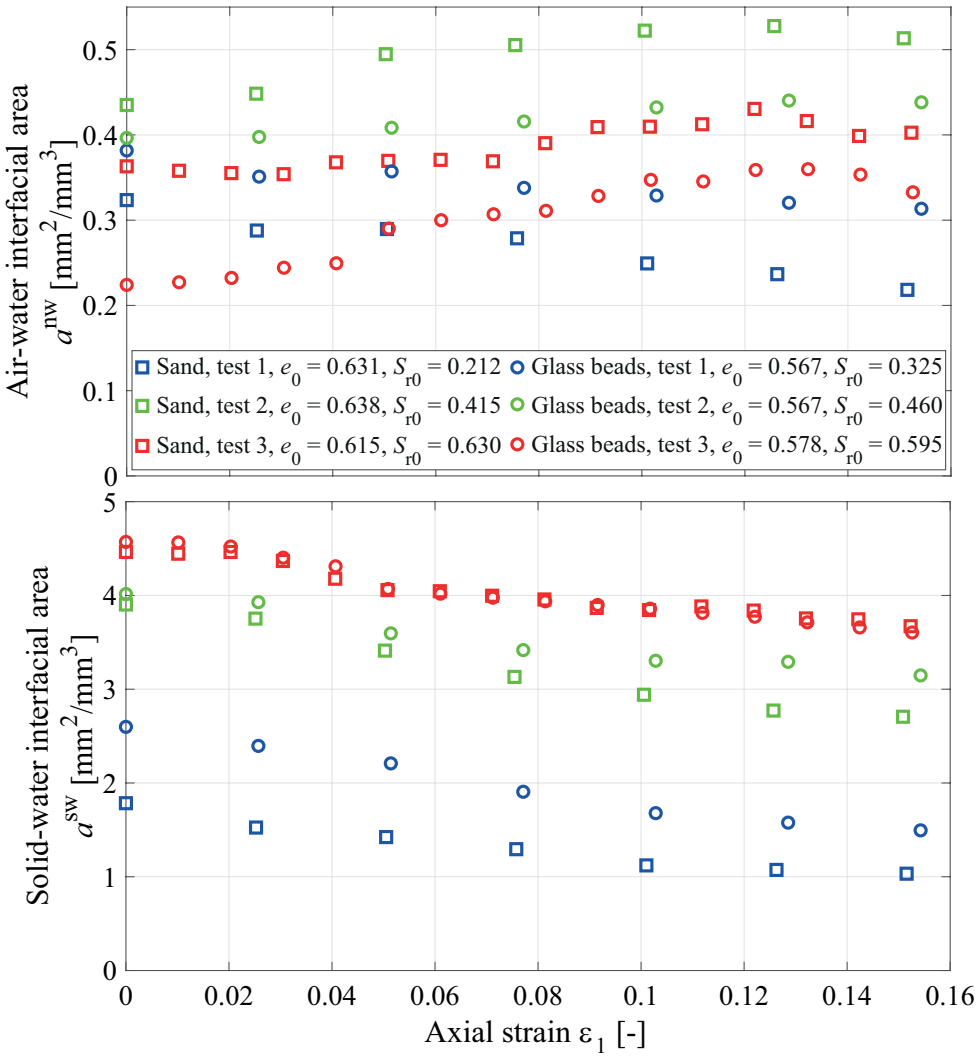


Figure 6.8: Development of air-water interfacial area (top) and solid-water interfacial area (bottom) *vs.* axial strain in a centred subvolume of 300 × 300 × 300 px during uniaxial compression of the sand and glass bead specimens from Milatz *et al.* (2021b)

hedral elements linking the grain centres, strain fields are computed tracking volumetric and deviatoric strain through time. The distributions of deviatoric strain in the driest specimens of Hamburg Sand and glass beads are shown in Figure B.1 and Figure B.2 in the Appendix. In both materials, local shear zones develop early during the experiments and result in distinguished shear planes which are more pronounced in the glass bead specimen. Outside of the shear zones, friction cones with nearly no strain become visible. An analogue time series of the development of calculated volumetric strains is given for both investigated specimens in Figure B.3 and Figure B.4 in the Appendix. The negative volumetric strains indicating dilative behaviour are occurring especially around the shear zones in both materials, but seem to be more concentrated in the glass beads.

Besides the strains, also other pore-based state variables, such as degree of saturation, are

computed for every tetrahedron. The state variables are then evaluated together with the strains to investigate the hydro-mechanical coupling based on the multitude of available data points. If pores are characterised by their pore-based degree of saturation as described in Chapter 5 and then are binned in different saturation groups, the relationship between local pore saturation and volumetric or deviatoric strain can be studied. Such an analysis is illustrated in Figure 6.9 showing the relationship between saturation in 10 bins *vs.* the median of volumetric and deviatoric strain for all shear steps in the uniaxial compression tests on the driest specimens of Hamburg Sand and glass beads. The median is calculated from all strain values in the corresponding bins in order to remove the spread in the available data point cloud.

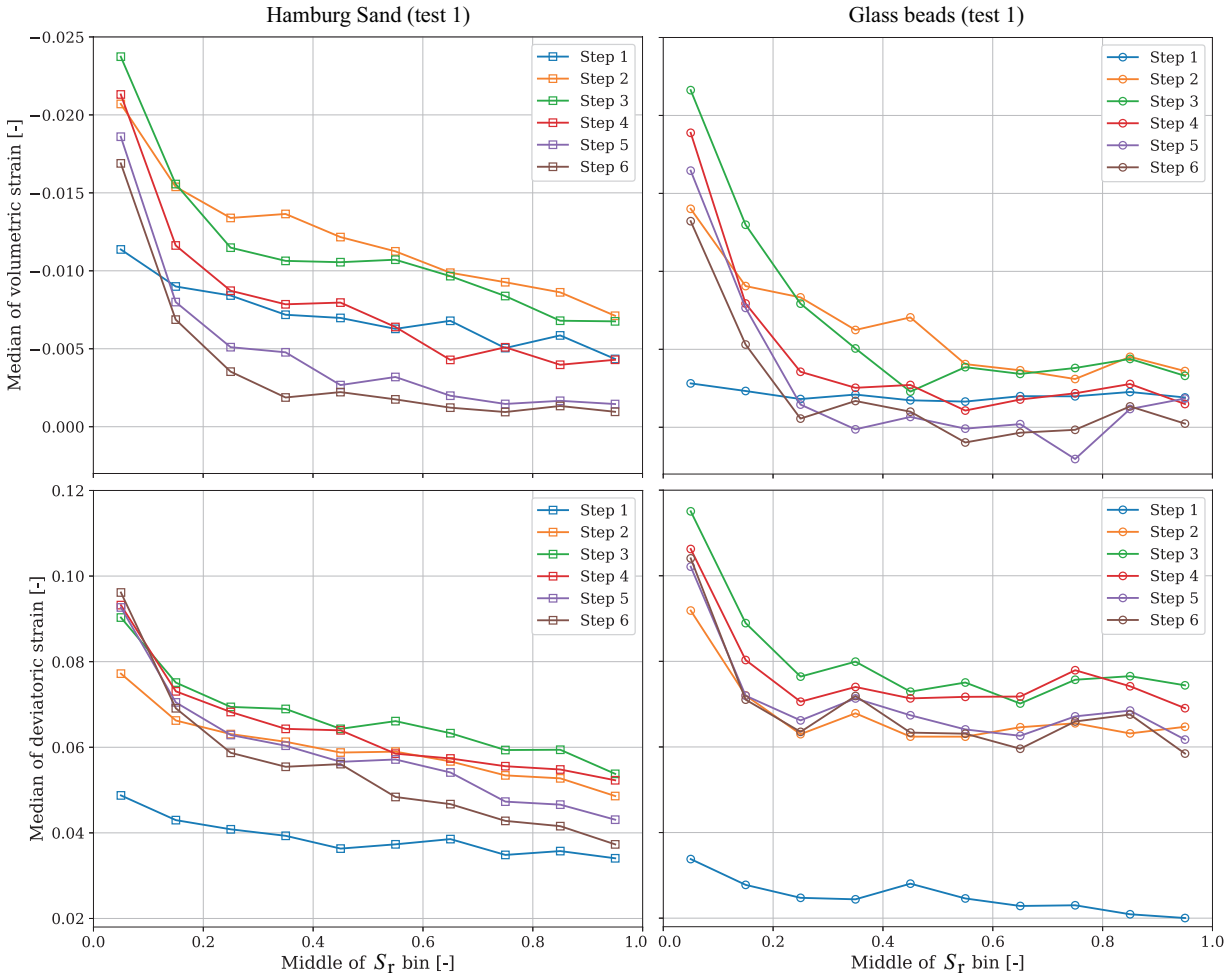


Figure 6.9: Median of volumetric (negative = dilation) strain (top) and median of deviatoric strain (bottom) computed for pores classified by degree of saturation presented for each shear step where a strain increment takes place of the driest specimens of Hamburg Sand (left column) and glass beads (right column) from Milatz *et al.* (2021b)

The pore-based analysis generally reveals an increase of median volumetric and deviatoric strain with decreasing degree of saturation, *i. e.*, obviously, the strain is limited in pores with higher local degree of saturation, whereas pores with lower degree of saturation dilate

and shear more. This could be evidence for the increase in stiffness and shear strength in pores with higher suction stress level given by the combination of higher degrees of saturation and the corresponding negative pore water pressure acting inside larger water clusters in the capillary domain. Comparing the behaviour of both materials, the change in median volumetric strain is more pronounced in the sand, whereas the median deviatoric strain is higher in the glass beads. The stronger dilative behaviour of the sand is confirmed by the macroscopic specimen response to shearing and might be due to the different grain shapes compared to the glass beads. Furthermore, the confining effect of suction stress seems to be more pronounced in the sand leading to the smaller and less local deviatoric strain responses as compared to the glass beads. If the strain responses for successive shear steps are focused on, an increase of median volumetric and deviatoric strain in both materials in the first two to three shear steps, especially for higher degrees of saturation, can be observed, followed by a decrease of strains. The decrease might be due to the effect of increasing shear localisation on the calculated median values leading to an emphasis of the less-sheared part inside the specimens.

6.1.4 Evolution of grain contacts

Another measure of mechanical integrity and force transfer inside of grain assemblies is given by coordination number indicating the count of contact partners per grain. Based on the analysis presented in Milatz *et al.* (2021b), the total number of grain contacts and mean coordination numbers during the shearing of the driest specimens of Hamburg Sand and glass beads are shown in Figure 6.10 revealing a decrease of grain contacts due to the dilating grain skeletons. The number of grain contacts is initially higher in the sand specimen, likely due to grain shape effects and interlocking because of elevated friction as compared to the spherical and smooth glass beads. However, during the shear process, the decrease of grain contacts is more pronounced in the sand specimen in agreement with the stronger dilatancy as compared to the glass beads. Likely also related to grain shape and to the increased tendency to compaction of the glass beads, they show a higher initial mean coordination number and its less pronounced reduction during shearing which might also be linked to the stronger localisation of shear planes observed for the glass beads. For the sand specimen, a low mean coordination number of *ca.* 3 is reached after the applied shear steps, which highlights the strong dilation in combination with capillary effects enabling the stability of a rather loose grain skeleton at a much reduced number of nearest neighbour grain contacts.

A histogram-based analysis of coordination number highlighting the evolution of the actual number of grains with different coordination numbers between 1 and 20 in the initial and final post-shear grain configurations is given in Figure B.5 in the Appendix. For both materials, distributions skewed to the left, *i. e.*, with a dominance of lower coordination numbers, are obtained. Due to the shearing and resulting dilatancy, the distributions move towards a lower mean coordination number. Likely related to their packing properties leading to a better compactibility, more grains with higher coordination number are found in the glass beads both in the initial and post-shear state. A further comparison of coordination numbers of the initial and final CT scans during uniaxial compression of

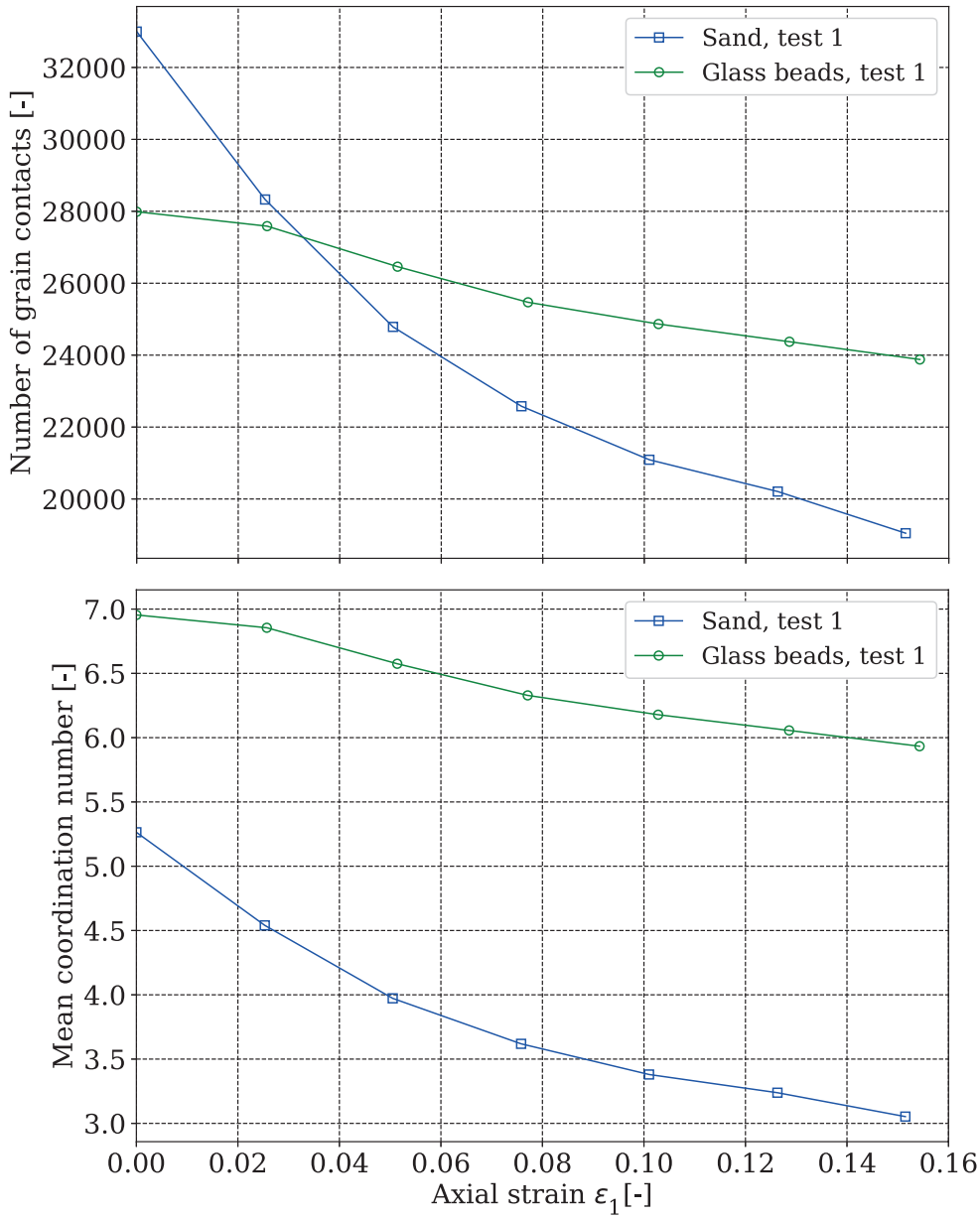


Figure 6.10: Evolution of the number of grain contacts (top) and of coordination number (bottom) *vs.* axial strain for the driest specimen of Hamburg Sand and glass beads from Milatz *et al.* (2021b)

Hamburg Sand and glass beads in selected slices is given in Figure B.6 and Figure B.7 in the Appendix. The contour plots with every grain coloured according to its coordination number clearly demonstrate the decrease of coordination numbers as pores open due to dilatancy.

6.2 Capillary bridge mechanics

As observed in the uniaxial compression tests, water clusters and liquid bridges are changing due to the combined action of shearing and evaporation. According to Hueckel *et al.* (2020) who studied the microscopic force evolution during evaporation of water clusters and liquid bridges in assemblies of discrete numbers of spherical particles, the change in water clusters and liquid bridges leads to changes in the interparticle forces which are accompanied by sudden jumps as the liquid suddenly rearranges during air entry events. Due to mechanical loading leading to the separation of grains, also the water clusters and liquid bridges are strained which might also modify their mechanical contribution to effective stress. Based on the literature study in Section 2.1.2, the impact of particle separation is studied by means of particle separation experiments and their evaluation as presented in section 4.5. In order to quantify the mechanical effect of capillary bridges on the materials investigated in this work, the stress-strain and rupture behaviour during monotonic straining of liquid bridges in between pairs of glass beads and Hamburg Sand grains are studied. Furthermore, the effect of cyclic straining of a liquid bridge is focused on.

6.2.1 Monotonic straining of capillary bridges

In three experiments, capillary bridges in between glass beads with $d \approx 2$ mm are strained until rupture at a constant separation velocity of *ca.* 0.09 mm/s. The capillary bridges are formed by different liquid volumes V_{liq} that are calculated from image data based on the assumption of a body of revolution. At a chosen frame rate of 10 frames/s, the displacement resolution per image for assessing the rupture length is 0.009 mm/frame. The rupture process is found to be very fast, so that capillary bridges vanish in between two images. Therefore, the measurement accuracy for measuring the rupture length is around 0.009 mm and the measurements represent lower bounds of the true rupture lengths. For a better temporal and displacement resolution of the detailed rupture process, a higher frame rate is required. The evolution of the studied capillary bridge geometries is shown as a time series of images in Figure B.8 in the Appendix.

Figure 6.11 shows the evolution of main radii of curvature R_1 and R_2 measured from each image *vs.* separation distance l. Depending on the tested liquid volume, characteristic curves for the radii of curvature are measured reflecting the size and geometry of the capillary bridge. The last data point is derived from the last image with still intact capillary bridge marking the rupture length l_{r} which can be resolved with the selected methodology. While the outer radii of curvature R_1 show a saddle-shaped curve *vs.* separation distance, the absolute values of the inner radii of curvature R_2 at the neck of the capillary bridge are reduced indicating a thinning of the neck until rupture.

From both radii of curvature the mean curvature H is calculated which can be either positive or negative based on the individual sign and magnitude of R_1 and R_2 yielding either positive (suction) or negative capillary pressure (excess pore water pressure) as shown in Figure 6.12. Interestingly, small capillary bridges initially show positive capillary

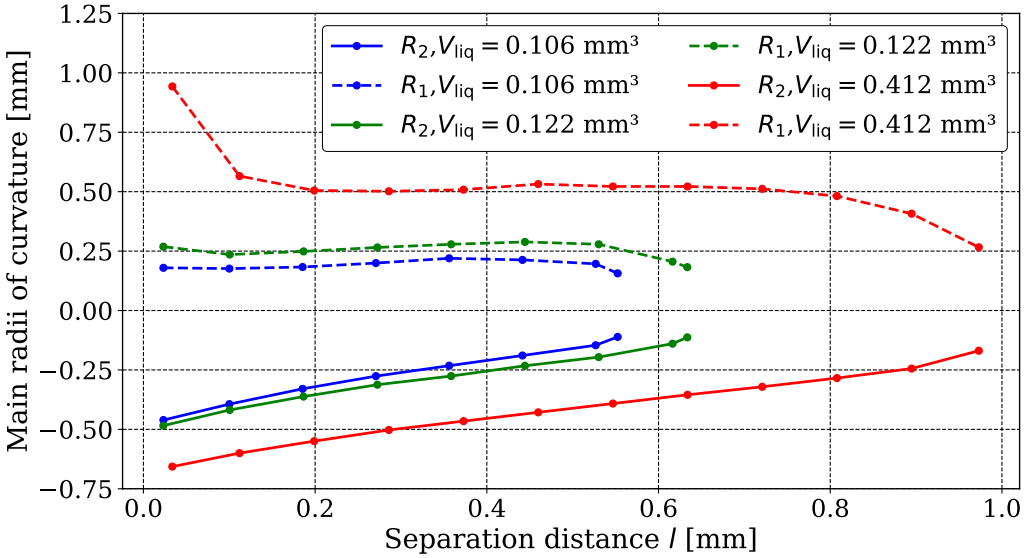


Figure 6.11: Evolution of radii of curvature *vs.* separation distance l during monotonic straining of capillary bridges with different initial liquid volumes V_{liq} in between glass beads with $d \approx 2$ mm

pressure, while larger ones are initially characterised by a negative capillary pressure. During the straining of the capillary bridges, the capillary pressure is reduced in all cases which is also reported by Mielniczuk *et al.* (2015).

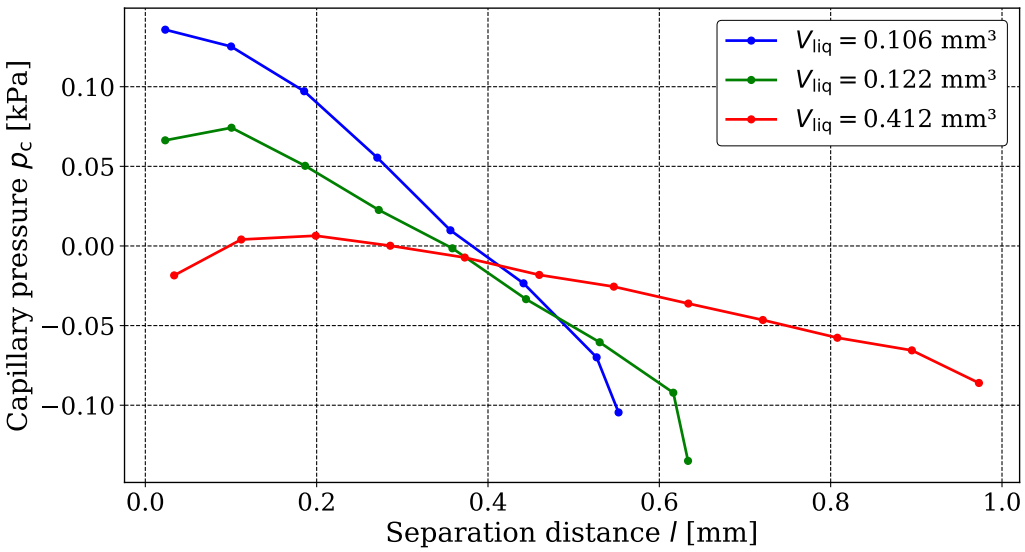


Figure 6.12: Evolution of capillary pressure p_c *vs.* separation distance l during monotonic straining of capillary bridges with different initial liquid volumes V_{liq} in between glass beads with $d \approx 2$ mm. Note that positive p_c equals a positive matric suction, while negative p_c corresponds to excess pore water pressure inside the capillary bridge

The dimensionless (normalised) capillary force and its components *vs.* dimensionless separation distance l^* are plotted in Figure 6.13. A reason for the normalisation of force components is the uncertain surface tension of the water and its sensitivity towards contained substances as outlined in Chapter 3. Mielniczuk *et al.* (2015) report a large deviation of the surface tension of their "lab water" from the nominal value of pure water of $\gamma = 0.07275$ N/m with a measured value of only $\gamma = 0.0496$ N/m. This low surface tension is confirmed by the own measurements presented in Chapter 3 yielding a nominal value of our de-ionised "lab water" of $\gamma = 0.05435$ N/m. The issue of reduced surface tension will be further addressed in the evaluation of the cyclic capillary bridge separation experiment.

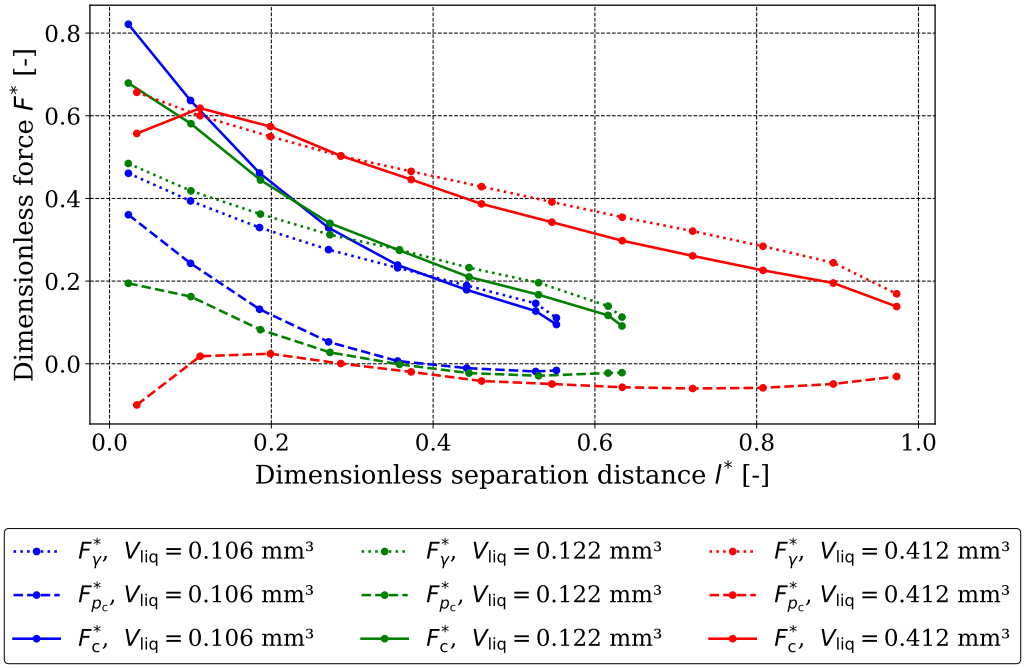


Figure 6.13: Evolution of dimensionless capillary force components F^* *vs.* dimensionless separation distance l^* during monotonic straining of capillary bridges with different initial liquid volumes V_{liq} in between glass beads with $d \approx 2$ mm

All experiments show a reduction of normalised capillary force F_c^* with increasing separation distance. However, for the highest liquid volume, initially, the capillary force increases because the initial excess pore water pressure inside the liquid bridge is shortly changing to suction. As shown previously, during further straining of the capillary bridges, capillary pressure is decreasing and strongly reducing the force component $F_{p_c}^*$. A principal finding of the experiments is an increase of capillary force with reduction of the liquid volume, *i. e.*, small capillary bridges at close particle distances show the highest action of force. However, the range of capillary forces in smaller capillary bridges is limited as the force magnitude decays stronger with increasing particle separation as compared to larger capillary bridges which feature an increased range until rupture occurs.

As indicated by Equation 2.8 proposed by Lian *et al.* (1993), the rupture length l_r of a liquid bridge grows with the cubic root of the liquid volume V_{liq}. Despite a thin data

basis, this relationship is generally confirmed by the measured rupture lengths as shown in Figure 6.14 in comparison to the empirical rupture length based on a measured average contact angle at rupture $\theta = 21.02°$.

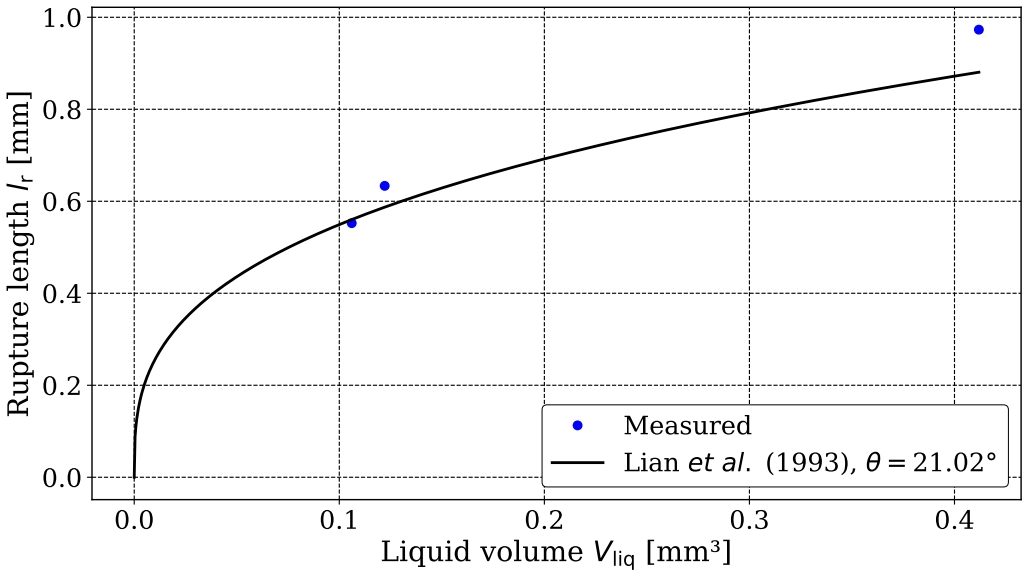


Figure 6.14: Rupture lengths l_r measured during monotonic straining of capillary bridges with different initial liquid volumes V_{liq} in between glass beads with $d \approx 2$ mm compared to the calculated rupture lengths according to Lian *et al.* (1993) *vs.* liquid volume

Besides the particle separation experiments on glass beads, also capillary bridges in between pairs of selected Hamburg Sand grains consisting of quartz have been tested. As compared to the glass beads, the capillary bridges are less symmetrical, especially in the initial configuration, due to irregular and probably also rougher grain surfaces. The image sequence of a selected experiment reported here is shown in Figure B.9 in the Appendix. The experiment is run with a separation velocity of *ca.* 0.09 mm/s and with an initial liquid volume of $V_{liq} \approx 0.451$ mm^3.

The mechanical behaviour of the liquid bridge in between the Hamburg Sand grains is also characterised by a plot of dimensionless force *vs.* dimensionless separation distance in Figure 6.15 showing the total capillary force F_c^* and its components from surface tension and capillary pressure. As the sand grains are rounded, but not spherical, the force components have been normalised according to Equation 4.2 using a reference sphere radius of $R = 1.0$ mm.

The evolution of capillary force with increasing particle distance in the experiment on Hamburg Sand is similar as compared to the glass beads. Due to the higher liquid volume, the normalised force is initially higher as in the experiments on glass beads. Furthermore, a relatively high repulsive force contribution $F_{p_c}^*$ due to negative capillary pressure is found when the sand grains are at the closest separation distance. The measured rupture length is $l_r \approx 1.016$ mm which is not so far from the theoretical rupture length of $l_r = 0.934$ mm

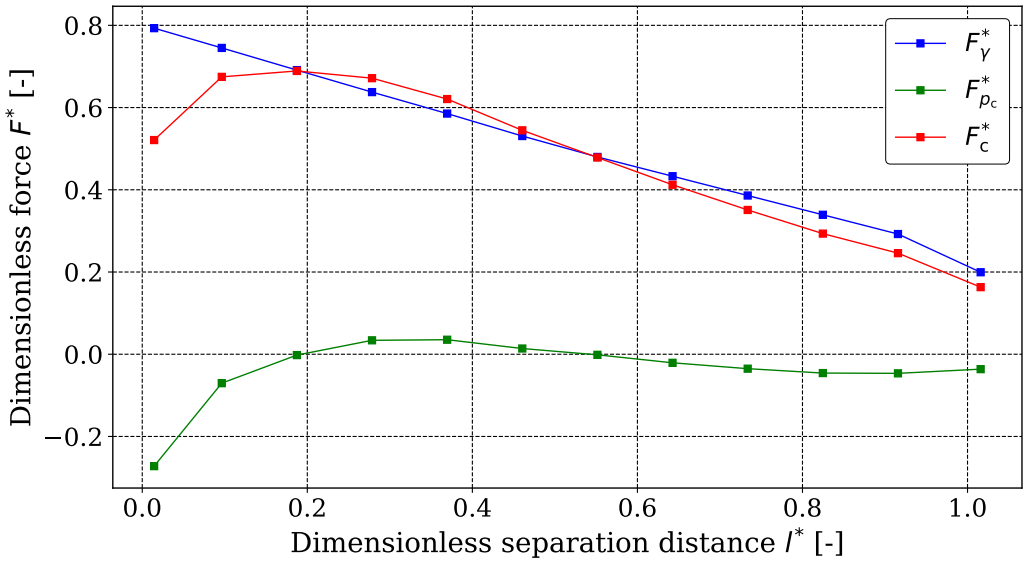


Figure 6.15: Evolution of dimensionless capillary force components F^* *vs.* dimensionless separation distance l^* during monotonic straining of a capillary bridge with an initial liquid volume $V_{\text{liq}} \approx 0.451$ mm^3 in between Hamburg Sand grains

according to the equation proposed by Lian *et al.* (1993) which is, strictly speaking, only valid for liquid bridges in between equally-sized spheres.

6.2.2 Cyclic straining and compression of a capillary bridge

Finally, a cyclic particle separation experiment with parallel measurement of force using a lab balance as described in section 4.5 is discussed. In the experiment, a capillary bridge with a liquid volume of $V_{\text{liq}} \approx 0.523$ mm^3 in between two glass beads with a diameter of *ca.* 2 mm is stretched and compressed in two cycles at a constant velocity of *ca.* 0.06 mm/s. In the image-based analysis, also the contact angles are measured manually as illustrated in Figure 4.15. Image-based results highlighting the evolution of capillary bridge geometry and contact angles during straining and compression are given in Figure 6.16 and Figure 6.17, respectively.

As before, smooth measurements of the radii of curvature are obtained which indicate a repeatable pattern during cyclic particle separation. The outer radius of curvature R_1 strongly increases when the particles approach each other. In the reported experiment, the mean curvature calculated from R_1 and R_2 corresponds to a negative capillary pressure with a permanent repulsive contribution to total capillary force. The contact angles measured in four locations and averaged as shown in Figure 4.15 show relatively strong deviations with a mean spread of *ca.* 7.8°. The deviation in the measurements is most likely due to asymmetries in the liquid bridge as well as measurement errors due to limited image resolution at the contact line. Starting from its initial value, the mean contact angle is remaining rather constant at a value around 15° during straining and compression

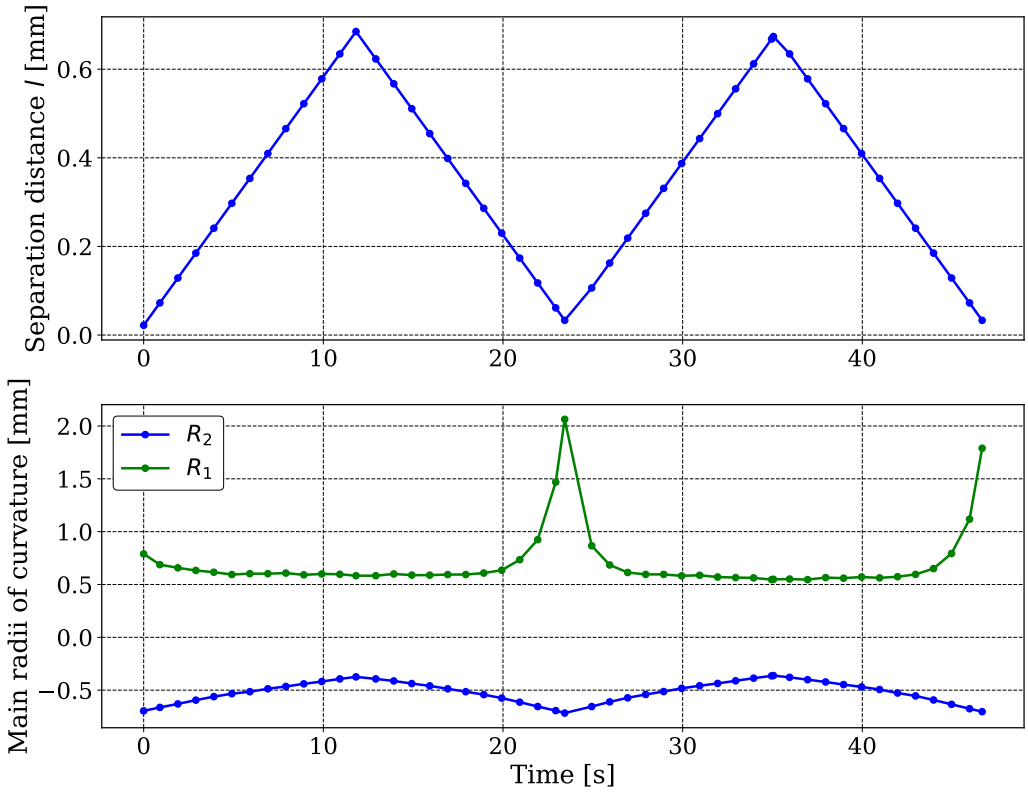


Figure 6.16: Temporal evolution of separation distance (top) and radii of curvature (bottom) during cyclic straining and compression of a capillary bridge with an initial liquid volume $V_{\text{liq}} \approx 0.523$ mm^3 in between glass beads with $d \approx 2$ mm

of the liquid bridge. However, when the particles approach each other closely, the mean contact angle increases to *ca.* 35°. This pattern is repeated after the second cycle and corresponds to the strong increase of the outer radius of curvature R_1. With focus on the two reported cycles, the change in contact angles seems to be reversible. The strong increase of the outer radius of curvature and of the contact angle seems to be due to pinning of the contact line when the particle separation is minimal. The pinning forces the contact angle to increase at this point of particle separation, while the contact angle can relax again to its initial value as the grains separate again allowing the contact line to move and adjust without further pinning. Due to the oscillations in the measured contact angles, no clear evidence for contact angle hysteresis, *i. e.*, for a path-dependence of mean contact angle upon reversal of separation direction, can be detected. However, this is reported by some authors, *e. g.*, Willett *et al.* (2007). Furthermore, there might be an influence of the separation velocity on the contact angles and capillary forces due to additional viscous effects of the liquid as investigated for instance by Shi *et al.* (2018).

The measured geometric changes in the capillary bridge during cyclic separation lead to the theoretical dimensionless capillary force and its components plotted *vs.* time in Figure 6.18. As the particles approach each other, the repulsive contribution of negative capillary pressure leads to a visible reduction of dimensionless capillary force.

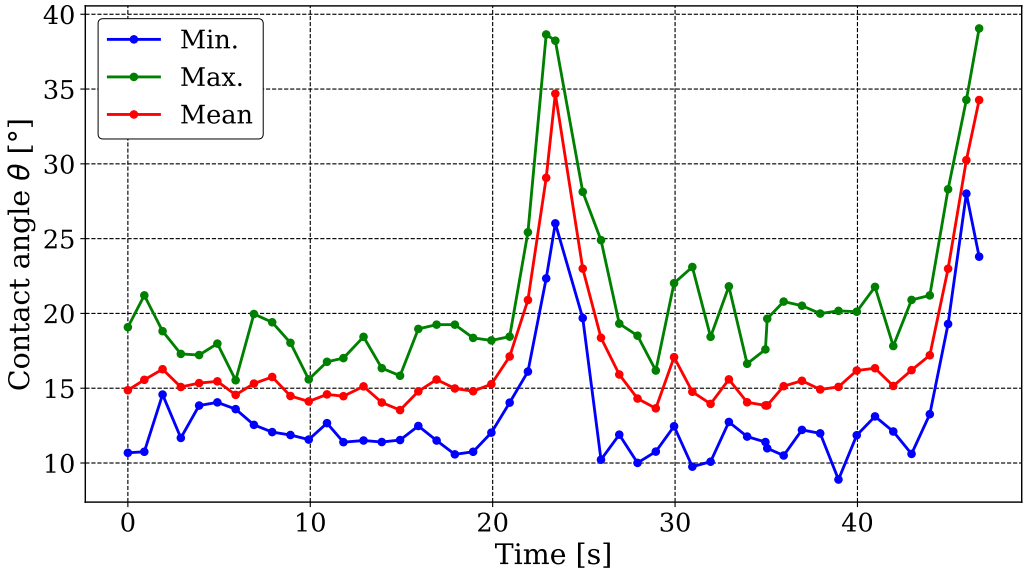


Figure 6.17: Temporal evolution of minimum, maximum, and mean contact angle during cyclic straining and compression of a capillary bridge with an initial liquid volume $V_{\text{liq}} \approx 0.523\ \text{mm}^3$ in between glass beads with $d \approx 2$ mm

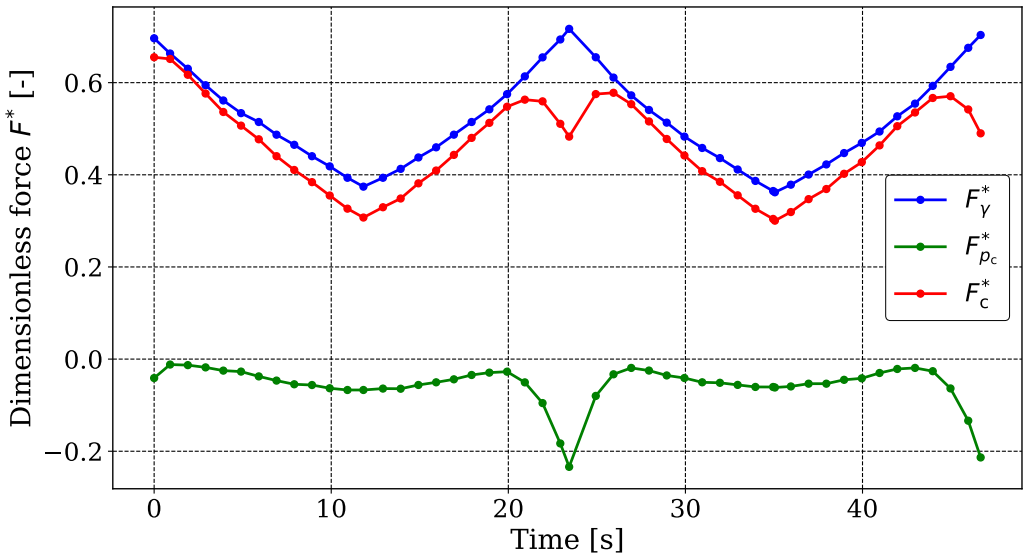


Figure 6.18: Temporal evolution of dimensionless capillary force and its components during cyclic straining and compression of a capillary bridge with an initial liquid volume $V_{\text{liq}} \approx 0.523\ \text{mm}^3$ in between glass beads with $d \approx 2$ mm

In order to check this behaviour, the theoretical image data-based capillary force is compared to the measured capillary force. For this purpose, the actual physical force is computed from the dimensionless force using the surface tension γ and particle radius R.

In all measurements done, the measured capillary force is much lower than expected if the nominal value of surface tension of pure water $\gamma = 0.07275$ N/m is assumed to calculate the actual physical force from dimensionless force based on the imaging experiments. Considering a reduced surface tension $\gamma = 0.05435$ N/m based on the Wilhelmy plate measurement of de-ionised water presented in Chapter 3, yields the image-based capillary force plotted in Figure 6.19 *vs.* measured force and time. Although the image-based capillary force is still larger than the measured one, it reflects the characteristic change of measured capillary force quite closely.

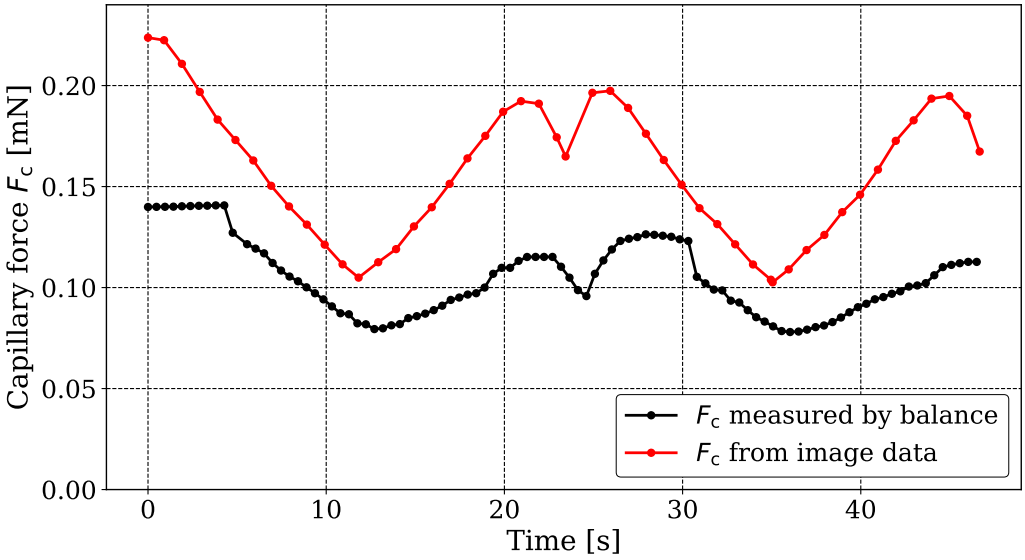


Figure 6.19: Temporal evolution of measured and image-based (calculated) capillary force during cyclic straining and compression of a capillary bridge with an initial liquid volume $V_{liq} \approx 0.523$ mm^3 in between glass beads with $d \approx 2$ mm. The calculation of the capillary force from image data is based on a measured surface tension of de-ionised "lab water" $\gamma = 0.05435$ N/m

If systematic experimental errors, such as bad balance measurements at very low absolute weights, asymmetries in the liquid bridge, differences between the 2D image analysis and the 3D reality as well as measurement errors in the image analysis are excluded, only a much reduced surface tension can be the reason for the measured low capillary forces. This could be explained by the sensitivity of water to impurities as also reported by Mielniczuk *et al.* (2015). As outlined in Chapter 3, a much reduced surface tension is very likely encountered in the utilised de-ionised water which possibly also includes other unknown chemical solutes. Additionally, the tested granular materials might influence the water chemistry inside the very small amount of water inside the capillary bridge leading to further changes of surface tension which are hard to quantify. Nevertheless, the measured capillary force confirms the general history of the calculated force with its pronounced sudden reduction at minimum separation distance due to the occurrence of excess pore water pressure (negative capillary pressure) in the capillary bridge. However, unlike the calculated image-based capillary force, the measured capillary force shows clear evidence of

hysteresis as its slope varies for straining and compression of the capillary bridge. Besides this observation, the measured capillary force might also include viscous effects due to the selected separation velocity which is relatively high in the presented experiments as compared to typical soil mechanical conditions, *e. g.*, the slow shearing of sand in a triaxial test. Viscosity could also be the reason for the lagging of the measured force, especially in the beginning and after reversal of separation direction. Finally, the order of magnitude of the measured forces seems to be correct as it is similar to the weight of a single soda-lime glass bead with $d = 2$ mm which is equivalent to a force of *ca.* 0.1 mN. This is also confirmed by the observation that a glass bead can be lifted by a capillary bridge similar to those in the presented measurements. To further study the behaviour of individual liquid bridges, the described experimental set-up could be improved, *e. g.*, by implementation of an integrated very fine load cell to replace the laboratory balance.

6.3 Water retention behaviour

In the literature, there is consent that the macroscopic water retention behaviour obviously reflects hydraulic phenomena occurring on the pore scale. Based on the *in situ* CT experiments during cyclic drainage and imbibition as described in section 5.3, many insights can be obtained to evaluate the link between micro- and macroscale. In this section, the results from the hydraulic experiment on Hamburg Sand using the Laboratoire 3SR X-ray tomograph in Grenoble (Milatz *et al.*, 2022b) are presented and discussed.

6.3.1 Phase distributions during cyclic drainage and imbibition

The visualisation of separated phases allows to obtain insights into microscopic hydraulic processes during cyclic drainage and imbibition. The 3D rendering of the water phase inside the grain skeleton for a cuboid-shaped subvolume of 800 px × 800 px × 1145 px (8 mm × 8 mm × 11.45 mm) is shown in Figure 6.20 for all experimental time frames. The complementary distributions of separated air phase and water phase are shown in Figure B.10 and in Figure B.11 in the Appendix.

The visualisation of the fluid phases confirms the pronounced invasion of the pore space by air fingers early on the primary drainage path. The air entries the pores from the top in vertical direction and then starts to branch horizontally close to the specimen bottom. During this process, the liquid phase separates into clusters and becomes disconnected. This represents a probable explanation for the strong oscillation of measured matric suction because its measurement depends on a continuous water phase between the pore system and the water underneath the filter system in the bottom of the flow cell.

The temporal evolution of water and air degree of saturation as well as of void ratio is analysed *vs.* specimen height in Figure 6.21 by means of slice-wise averaged data in a central cubic subvolume as shown in Figure 5.17. Besides the macroscopic initial void ratio, also the average void ratio from CT data as well as the bounds given by e_{min} and e_{max} are plotted.

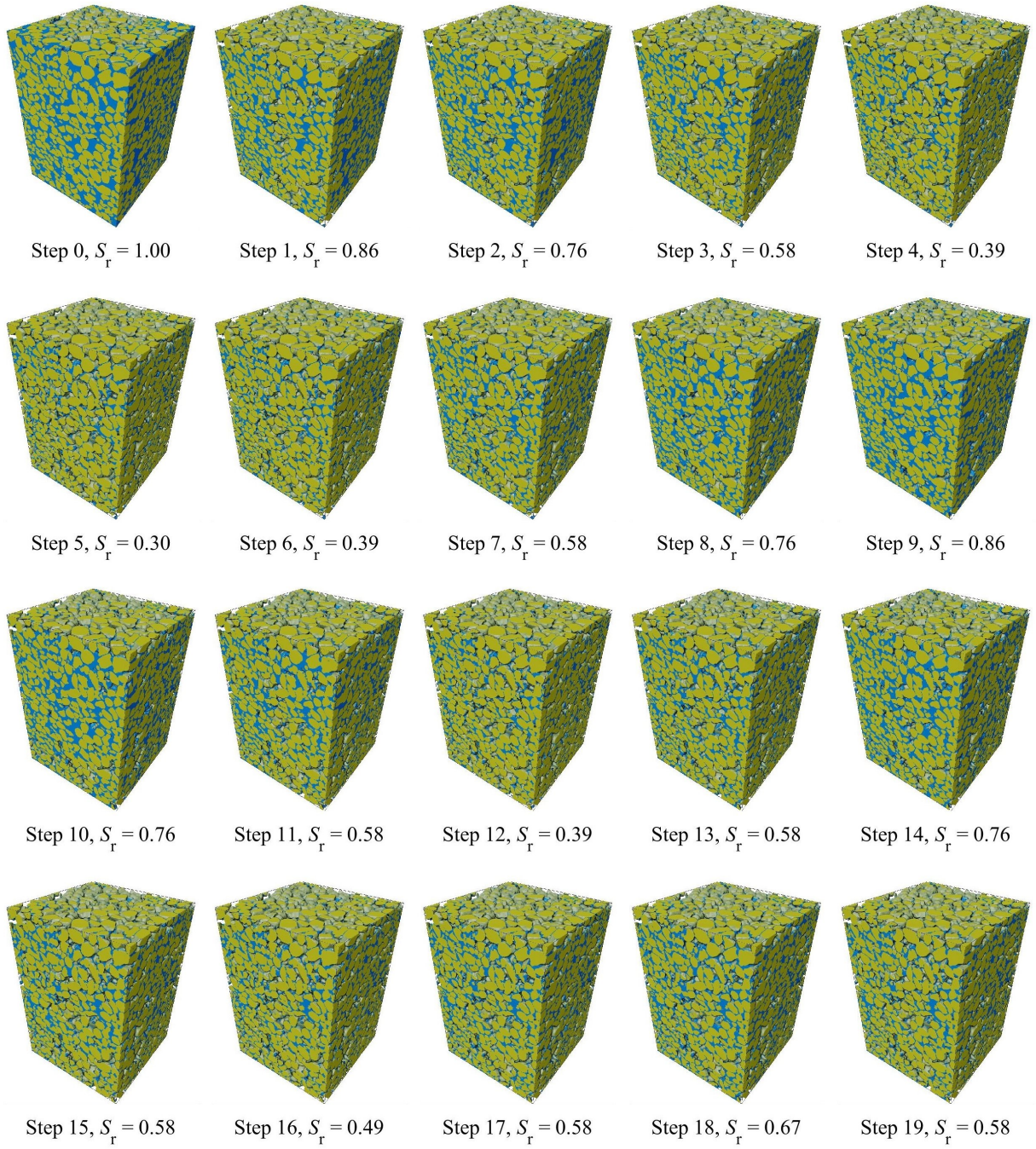


Figure 6.20: 3D visualisation of segmented sand and water phase shown for all 20 time steps in a cyclic drainage and imbibition experiment on a subvolume of 800 px × 800 px × 1145 px (8 mm × 8 mm × 11.45 mm). Reconstructed sand and water volumes are shown in yellow and blue, respectively. Air volumes are not shown. Step 0 indicates the water saturated initial specimen state. Hydraulic steps and macroscopic degree of saturation according to Figure 5.14 (Milatz *et al.*, 2022b)

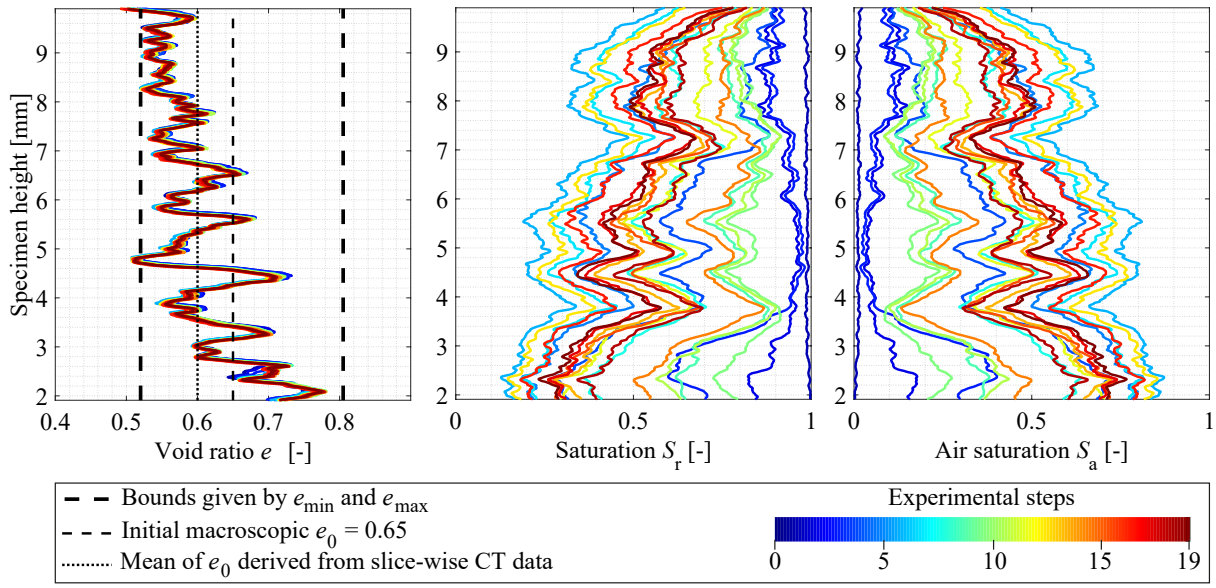


Figure 6.21: Void ratio e, water degree of saturation S_r, and air saturation S_a shown *vs.* specimen height in a central cubic subvolume of 800 px × 800 px × 800 px (8 mm × 8 mm × 8 mm) for all experimental steps including the initial state (Milatz *et al.*, 2022b)

The average void ratio in the selected subvolume is lower than the macroscopic one as calculated from the amount of sand and available volume of the whole specimen. Furthermore, the void ratio distribution, bounded by the minimum void ratio, shows a trend towards larger values at the bottom. During cyclic drainage and imbibition, small changes in local void ratio can be observed with zones of compaction and loosening of the grain skeleton. The initial distributions of S_r and S_a indicate that the specimen is not fully saturated in the beginning with local S_a in between 0.1 and 0.15 especially at the bottom and at the top of the considered subvolume. The 3D visualisation of the air phase in Figure B.10 in the Appendix reveals that initially many small air bubbles are present with larger air clusters at the bottom and at the top most likely originating from the specimen preparation. The temporal evolution of water and air saturation confirms the air invasion by fingering and the horizontal branching of air in the lower parts of the specimen correlating with higher void ratios which facilitate the air flow. This relationship is also confirmed at other specimen heights inside the subvolume. Higher air saturations prevail in zones with higher void ratio, while higher water saturation occurs in zones with lower void ratio. These observed trends seem to remain unchanged during all applied cycling of macroscopic degree of saturation, *i. e.*, the void ratio distribution obviously dictates the local phase distribution.

If degree of saturation is averaged over the whole cubic subvolume, it can be compared to the macroscopic degree of saturation which is changed by the syringe pump. Such an evaluation together with the calculated void ratio in the same subvolume is shown in Figure 6.22.

Generally, a very good agreement of local and macroscopic degree of saturation is obtained despite the local variations of degree of saturation *vs.* specimen height. The differences in

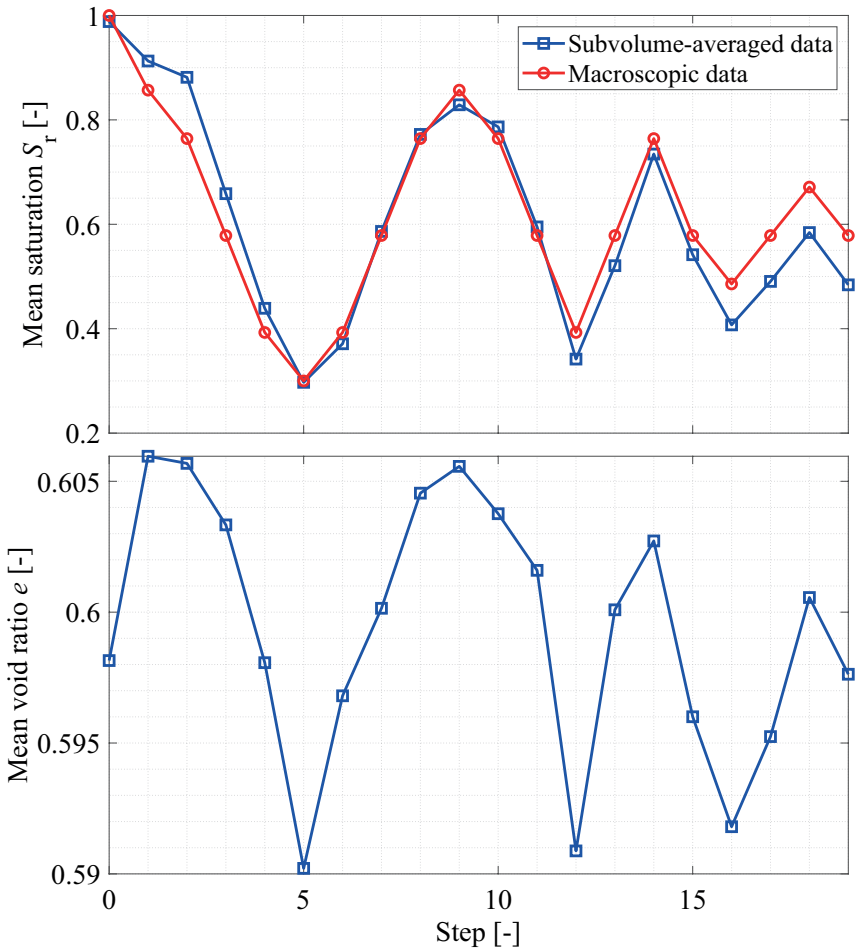


Figure 6.22: Change of local subvolume-averaged degree of saturation compared to macroscopic degree of saturation (top) and change of local subvolume-averaged void ratio (bottom) for all experimental steps including the initial step

the first primary drainage steps might be due to the pronounced local fingering of the air phase invading the pore space and branching at lower parts of the specimen. The selected subvolume is obviously only partially influenced by these local flow effects.

The visualisation of local void ratio in Figure 6.22 calculated from the subvolume-averaged data indicates its cyclic change with void ratio decreasing on drainage paths and increasing on imbibition paths. If the sudden increase of void ratio after the first drainage step, which could be due to local settlements, is ignored, a coupling of local void ratio and degree of saturation is discovered. This might represent evidence for hydro-mechanical coupling as governed by changing suction stress. This possible coupling will be addressed in further evaluations of the strains.

6.3.2 Analysis of discrete fluid clusters

A count of air and water clusters and their classification in different volume groups similar to the evaluation presented in section 6.1 reveals relationships between the cluster distribution and degree of saturation and matric suction, respectively. In Figure 6.23, the number of air and water clusters in the central cubic subvolume with edge lengths of 800 px is shown *vs.* local degree of saturation and measured matric suction before and after the corresponding CT scan in which the evaluated phase distribution was captured. The data is shown for all hydraulic steps which are distinguished by different colours.

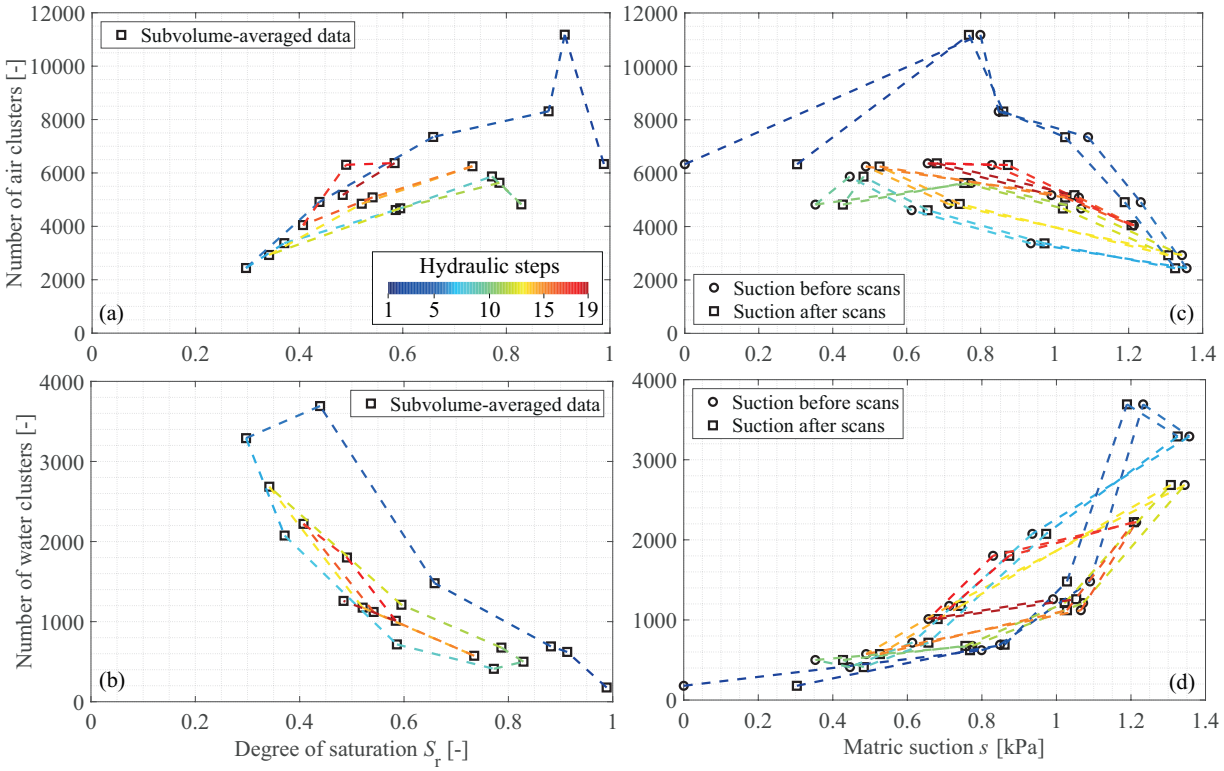


Figure 6.23: Evolution of (a) air cluster count, (b) water cluster count *vs.* degree of saturation, (c) air cluster count, and (d) water cluster count *vs.* matric suction for all hydraulic steps (Milatz *et al.*, 2022b)

The considered subvolume contains more air clusters than water clusters. Initially, many air clusters are present which can be attributed to the presence of occluded air bubbles after specimen preparation as well as to image noise. Furthermore, air represents the nonwetting phase and therefore tends to form isolated volumes or bubbles inside the pore space, whereas water as the wetting phase rather forms connected clusters.

Both air and water cluster count show hysteresis when plotted *vs.* degree of saturation and matric suction. However, the hysteresis is more pronounced when the cluster counts are shown *vs.* matric suction in Figure 6.23 (c) and (d). This important finding highlights that the hysteresis phenomenon is obviously characterised by different phase and cluster size distributions on the pore scale.

Further quantitative insights regarding the response of the cluster size distribution to cyclic drainage and imbibition can be derived from Figure B.12 and Figure B.13 in the Appendix. Both cluster size distributions are strongly skewed towards smaller clusters. During drainage, an increase in water clusters and a decrease in air clusters can be noticed as larger water clusters are drained and separated and air clusters merge, while this trend is reversed on imbibition paths. The effect of cyclic drainage and imbibition seems to affect all considered volume groups so that the cluster size distribution seems to maintain a similar skewed shape through all hydraulic steps indicating a dominance of the smallest clusters. The skewness of the distribution most likely reflects the pore size distribution which is also characterised by a dominance of smaller pores as will be shown in the pore-based analysis in this chapter.

As another way to classify and characterise clusters, Wadell's sphericity according to Equation 5.1 is proposed to analyse phase distribution and morphologies on different hydraulic paths. Here, separate air clusters are classified by sphericity in order to study the complexity of their shape as well as the occurrence of true bubbles with very high sphericity during cyclic drainage and imbibition. The selected sphericity groups used for classification are illustrated in Figure B.14 in the Appendix. At low sphericity, typically large connected air clusters form as ganglia with a complex shape, while more regular, but separate air cluster shapes are characterised by increasing sphericity up to nearly spherical clusters, *i. e.*, air bubbles, for sphericities close to 1. The evolution of air cluster count in the different sphericity groups *vs.* experimental steps is shown in Figure 6.24.

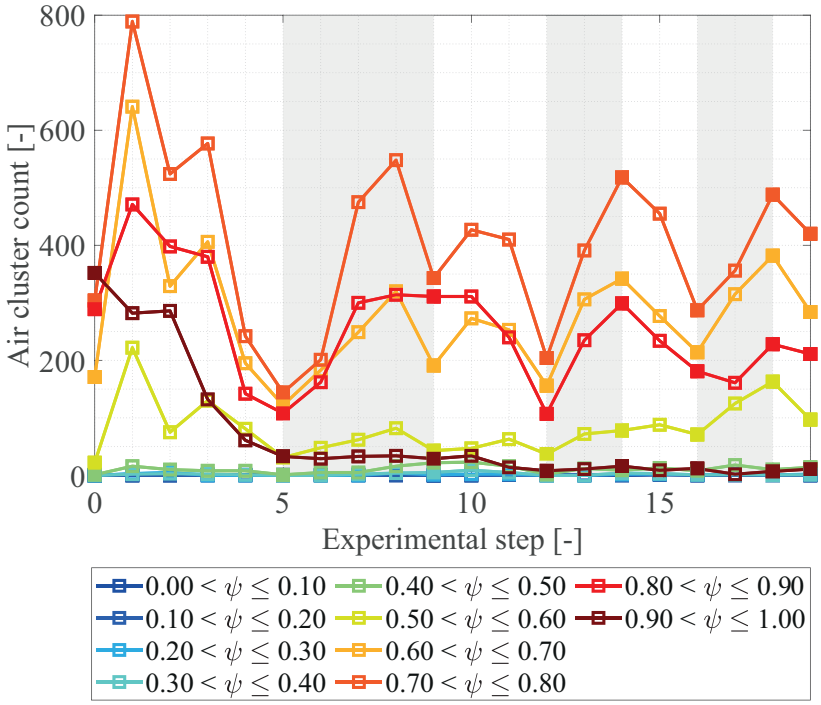


Figure 6.24: Evolution of air cluster count in different sphericity groups contained in the cubic subvolume shown for all hydraulic steps. Imbibition steps are highlighted by a grey background (Milatz *et al.*, 2022b)

Interestingly, the initially present air bubbles in the sphericity group with $0.90 < \psi \leq 1.00$ are strongly reduced during primary drainage and are further diminishing until a residual amount during cyclic flow in the consecutive hydraulic steps. However, the air clusters in the neighbouring sphericity groups, indicating a yet high roundness, strongly respond to cyclic drainage and imbibition with air clusters vanishing during drainage and emerging during imbibition. For air clusters with lower sphericity as in the group with $0.50 < \psi \leq 0.60$ only slight variations can be noticed as these contain the very few large and largest connected water clusters with complex shapes which remain stable during cyclic flow.

If the mean as well as bounding minimum and maximum sphericities are considered as shown in Figure 6.25, a slight trend towards lower mean sphericity indicating an increase in complexity of cluster shapes becomes visible. Also the maximum sphericity is decreasing, while the minimum sphericity shows a downward trend with the strongest response to drainage and imbibition.

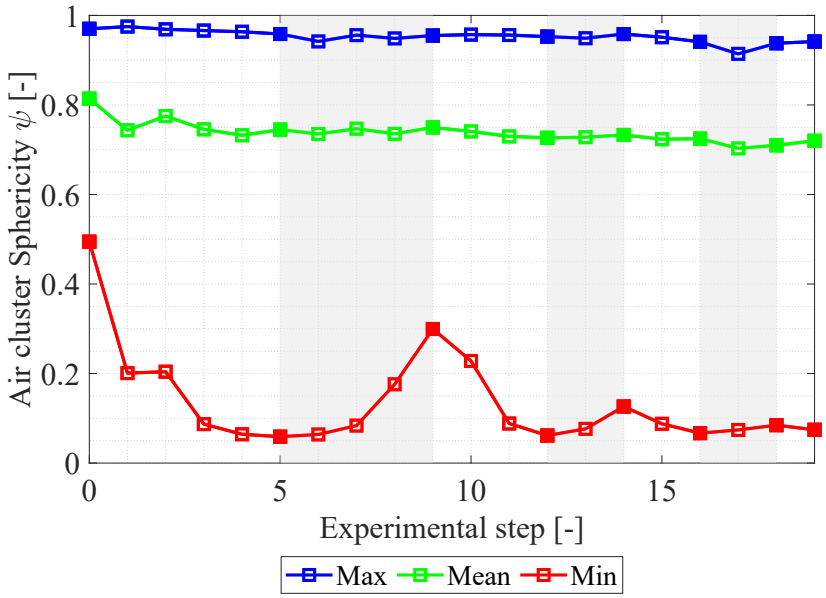


Figure 6.25: Evolution of maximum, mean and minimum sphericity of all air clusters contained in the cubic subvolume for all hydraulic steps. Imbibition steps are highlighted by a grey background (Milatz *et al.*, 2022b)

The analysis of air cluster morphology based on sphericity also indicates a change in the shape distributions of the clusters, especially when multiple hydraulic steps are included. This is further evidence for different phase distributions occurring on drainage and imbibition steps underlining their potential role for hysteresis.

The presented findings based on the fluid cluster analysis are not in agreement with the results and especially the interpretation from Kido *et al.* (2020) who find that no significant difference between the morphologies of pore air and pore water clusters seems to exist at similar degrees of saturation on consecutive drainage and imbibition paths of Toyoura sand which is, however, finer than Hamburg Sand. In their study, drainage and imbibition is applied by suction control with a hanging water column. Morphology is characterised by a

count of clusters and by an analysis of phase continuity based on connected volumes. Kido *et al.* (2020) argue that instead of different cluster morphologies, different curvatures of capillary menisci on drainage and imbibition paths could be responsible for the hysteresis phenomenon. In the end, based on the available experimental data, it remains unclear, if the observed different fluid distributions and changes in morphology on cyclic drainage and imbibition paths represent a result of or a reason for hysteresis. Further experimental research is needed to clarify this.

6.3.3 Analysis of interfacial areas and contact lines

For every CT data set of the initial state and after all hydraulic steps, the specific air-water and solid-water interfacial areas are calculated based on the procedure described in Chapter 5. The visualisation of both capillary state variables *vs.* degree of saturation and matric suction in Figure 6.26 reveals characteristic relationships similar to the WRC.

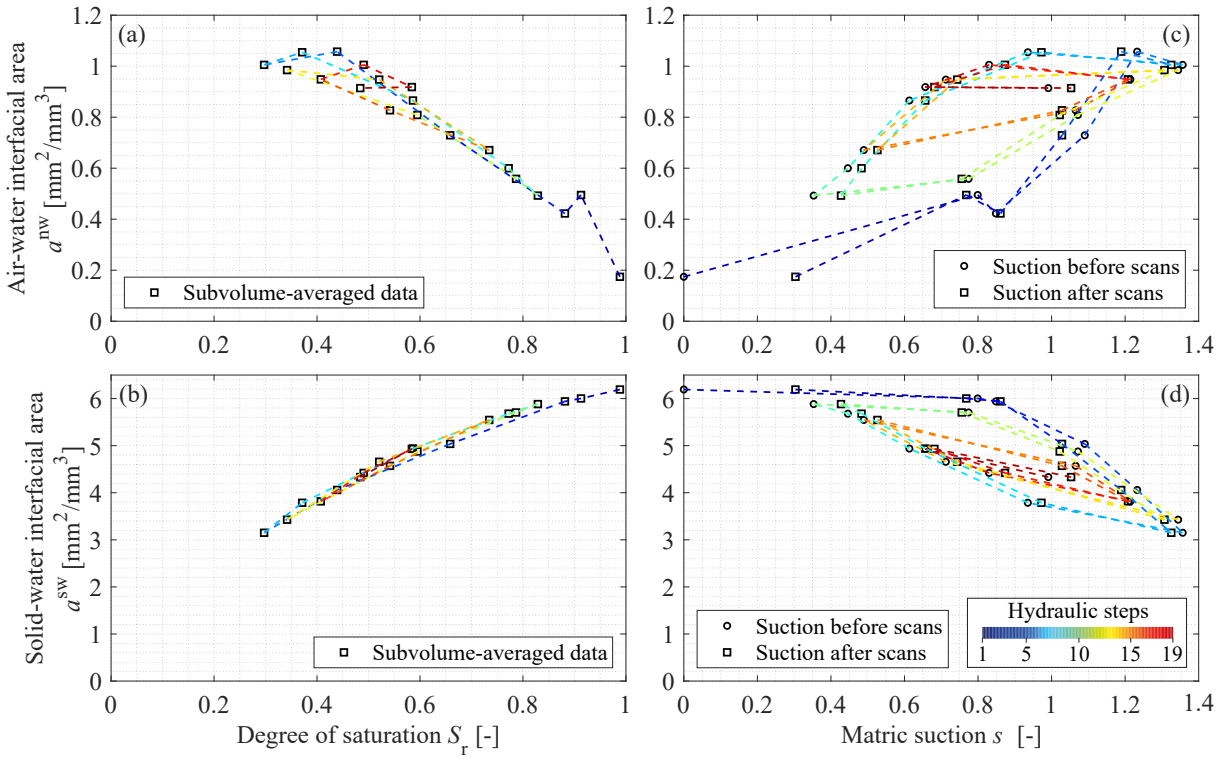


Figure 6.26: Evolution of (a) air-water interfacial area and (b) solid-water interfacial area *vs.* degree of saturation, (c) air-water interfacial area and (d) solid-water interfacial area *vs.* matric suction for all hydraulic steps (Milatz *et al.*, 2022b)

While the air-water interfacial area *vs.* S_r seems to show a peak for a medium saturation of $S_r \approx 0.4$ with $a^{nw} = 0$ for $S_r = 0$ and $S_r = 1$, the solid-water interfacial area *vs.* S_r shows a non-linear and monotonic curve with $a^{sw} = 0$ for $S_r = 0$ and apparently a maximum value of $a^{sw} \approx 6.2$ mm^2/mm^3 for $S_r = 1$. Very similar results have been measured in the uniaxial compression test on Hamburg Sand presented in section 6.1. The maximum of the specific

solid-water interfacial area a^{sw} should theoretically be identical to the specific surface area a^{s} of the corresponding porous medium which has been measured from the grain surfaces inside the discussed subvolume as $a^{s} = 6.28\ mm^2/mm^3$. This is very close to the maximum of solid-water interfacial area and reveals the solid-water interfacial area as the wetted portion of the specific surface area which is characteristic of every porous medium and which can be measured either by CT or other methods, such as gas adsorption. However, the characteristic relationship of a^{sw} *vs.* S_r might depend on other flow and surface properties as well as microscopic effects, such as flow rate, surface wettability, and air entrapment, which should be addressed in further studies.

Both measured interfacial areas show pronounced hysteresis when plotted *vs.* matric suction in Figure 6.26 (c) and (d), but only slight hysteresis or rather a drift when shown *vs.* degree of saturation in Figure 6.26 (a) and (b). Based on the characteristic properties of the measured curves, it might not be too daring to postulate the existence of "soil-water-air-interfacial area characteristic curves" which describe the evolution of the multiphase interfaces inside a porous medium upon different hydraulic paths. Both described interfacial areas have a strong physical meaning. While the specific air-water interfacial area describes the amount of interfaces per unit volume which form a minimal surface where surface tension is acting, storing surface energy, the specific solid-water interfacial area represents the interface of wetted solid surface per unit volume where capillary pressure or matric suction is acting normally to the solid surface. Therefore, both interfacial capillary state variables can be considered as ingredients of effective stress in unsaturated soils. Furthermore, the air-water interfacial area represents a flow surface important for surfactant transport.

The specific length of contact line l_c is much related to the interfacial areas as similar trends can be observed when it is plotted *vs.* degree of saturation and matric suction in Figure 6.27. When plotted *vs.* matric suction, l_c shows pronounced hysteresis, whereas rather a cyclic drift is encountered when it is plotted *vs.* degree of saturation. The specific length of contact line seems to reach a maximum for some lower degree of saturation with nearly 60 mm of contact line length being included in one cubic millimetre of Hamburg Sand. Representing a quantitative measure of the action length of surface tension in a granular medium, the specific length of contact line could reflect its impact on effective stress. Furthermore, similar to the interfacial areas, the relationship between degree of saturation or matric suction and the specific length of contact line might be characteristic of the tested material, which needs more verification by further experiments on other granular materials.

6.3.4 Pore scale analysis of contact angles and radii of curvature

As described in Chapter 5 and outlined in Figure 5.21, a multitude of radii of curvature and contact angles are measured in various 2D images from different time steps of the *in situ* water retention experiment on Hamburg Sand. Where possible, the measurements are taken for the same capillary menisci in order to include the temporal evolution of wettability of the same phase interfaces in the same pore. Based on these data, the differences of contact angles and radii of curvature on drainage and imbibition paths as

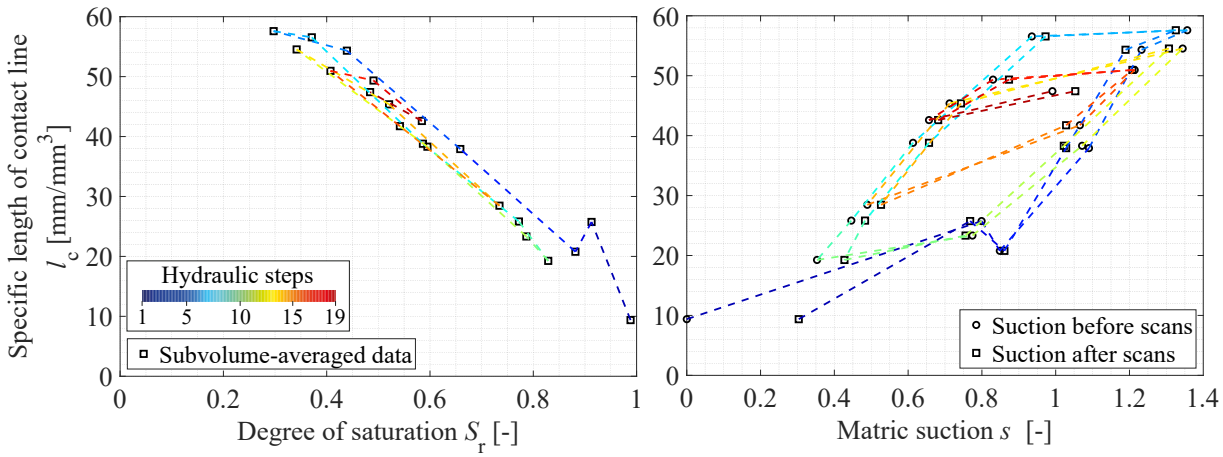
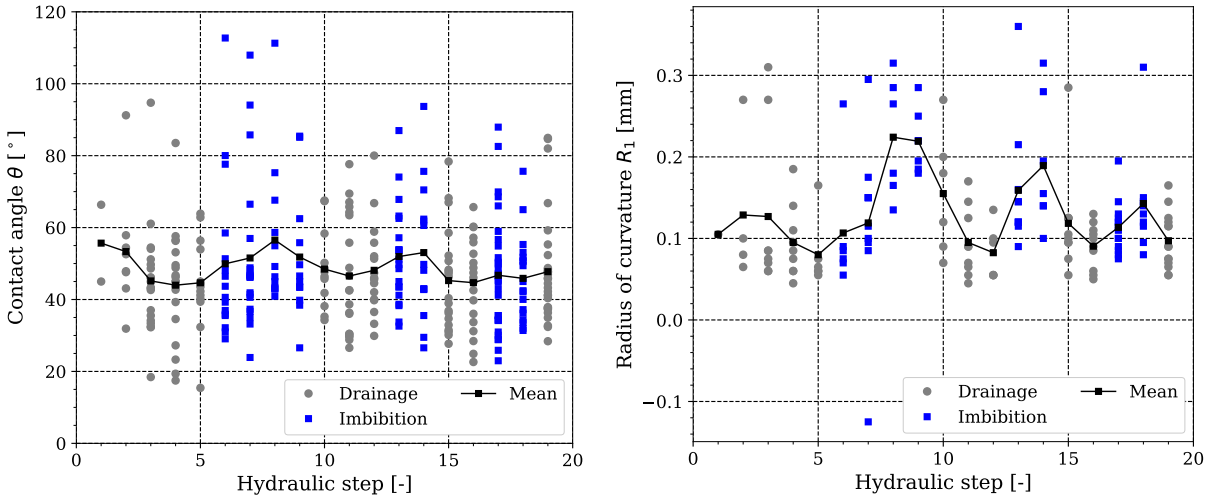


Figure 6.27: Evolution of specific length of contact line *vs.* degree of saturation (left) and *vs.* matric suction (right) for all hydraulic steps

well as their temporal evolution are studied. The measured contact angles and radii of curvature as well as their mean values are shown *vs.* hydraulic steps 1–19 in Figure 6.28.



(a) (b)

Figure 6.28: Evolution of measured contact angles (a) and radii of curvature (b) for all drainage and imbibition steps in the water retention experiment on Hamburg Sand

It must be noted that the data density varies from step to step. Furthermore, especially the measured contact angles show a lot of spread, *i. e.*, many different contact angles are measured in every hydraulic step. However, the mean of both state variables shows a trend with mean of contact angle and mean of radius of curvature decreasing during drainage steps and increasing during imbibition steps. This finding indicates a smooth transition of the shape of menisci upon reversal of the flow direction. Besides this, larger contact

angles are formed on imbibition paths compared to drainage paths which is confirmed by the distribution of contact angles illustrated as a histogram for the contact angles on drainage and imbibition paths in Figure 6.29.

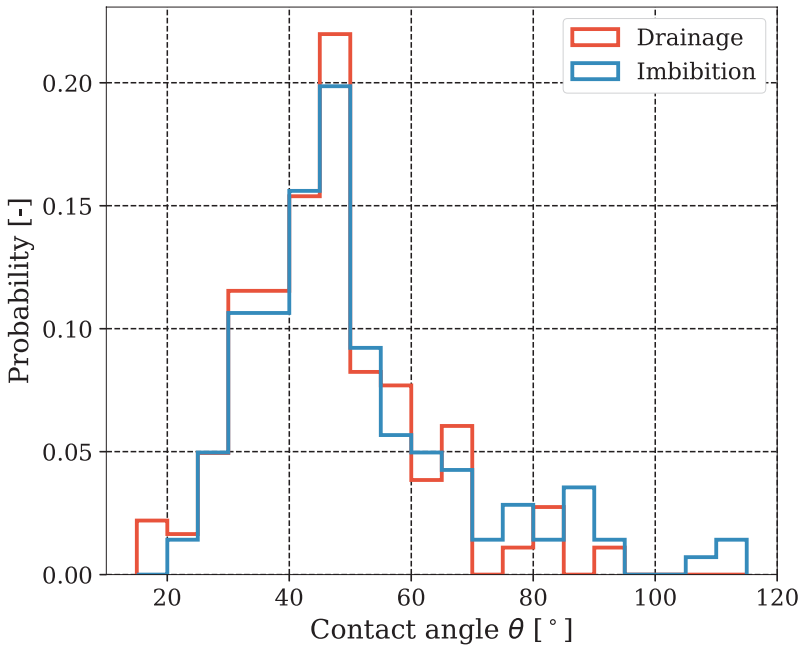


Figure 6.29: Probability distribution of contact angles measured on drainage and imbibition paths

The histograms reveal a contact angle distribution which might originate from varying microscopic wettability of the sand grains which is governed by their mineralogical compounds mostly represented by quartz, but also by portions of other minerals, such as feldspar. Furthermore, contact angles are influenced by microscopic surface roughness which can lead to pinning effects. The pinning leads to forced contact angles at microscopic solid boundaries where the contact line gets stuck as could be observed in some CT images.

In the histogram, the larger contact angles prevail on imbibition paths. Despite a similar shape of the histograms with leftward skewness towards smaller contact angles both for drainage and imbibition, the mean imbibition contact angle of 50.307° is slightly higher than the mean drainage contact angle of 46.478° confirming the presence of contact angle hysteresis in the studied soil.

Using the relationship between capillary pressure and the mean curvature H given in Equation 2.6 based on the Young-Laplace law, the theoretical capillary pressure can be calculated and compared to the macroscopic capillary pressure or matric suction measured in the sand specimen. This evaluation is based on the assumption that the radii of curvature R_1 measured in 2D images represent the mean curvature H according to Equation 2.5 with the contribution of the second radius of curvature R_2 in the view direction of the 2D images being neglected. Thus, capillary pressure is calculated from a 2D mean curvature given by $1/R_1$. Figure 6.30 shows a comparison of theoretical capillary pressure calculated

from this measured 2D mean curvature for a surface tension of $\gamma = 0.07275$ N/m and matric suction measured at the start and at the end of each CT scan.

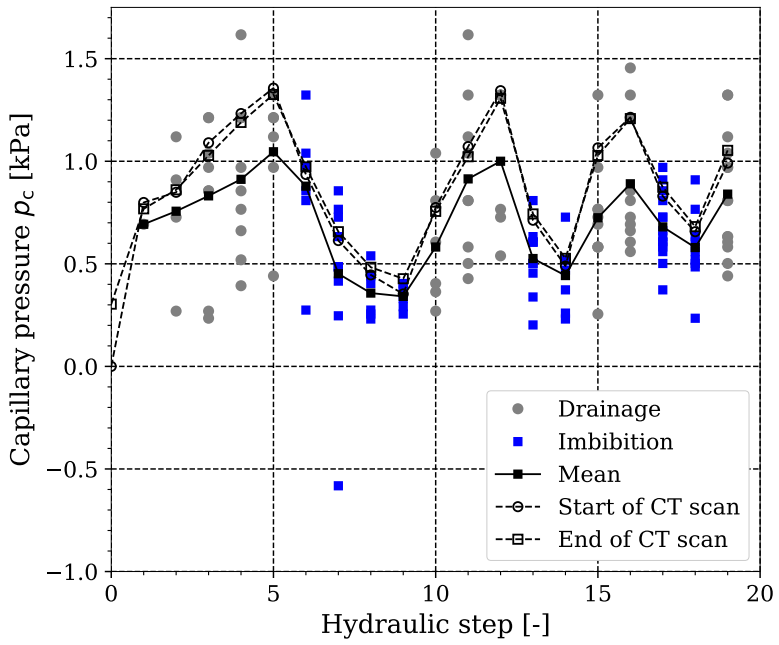


Figure 6.30: Evolution of capillary pressure calculated from surface tension γ and 2D mean curvature $1/R_1$ compared to matric suction measured on a macroscopic level for all drainage and imbibition steps before and after a CT scan

Interestingly, a good agreement of measured matric suction and mean capillary pressure based on measured mean curvature is found during all hydraulic steps. However, the measured matric suction is slightly higher which could be explained by the limited resolution in measuring radii of curvature from images as imposed by the pixel size of 10 μm. The good agreement between measured and theoretical suction confirms that the macroscopic matric suction is obviously the averaged result of the capillary effects in the multitude of different pores on the pore level.

6.3.5 Discrete analysis of grain motion and pore-based hydraulic effects

In order to study hydraulic processes governed by capillarity on the pore level, a pore-based analysis in analogy to the evaluation of the CT data from the uniaxial compression experiments in Section 6.1 is run. For this purpose, discrete grain movements are tracked for the first time steps on the primary drainage path in a DDIC analysis in *spam*. Based on the particle positions in all time frames, a Delaunay triangulation is again applied to generate tetrahedral elements whose corners are defined by the grain centres with every 3D tetrahedron minus the included solid voxels representing a discrete pore. This pore definition is then applied to characterise the specimen by pore size distribution and to

study the emptying of pores. This drainage process is described by pore saturation derived from the amount of water voxels inside each pore. Furthermore, finite volumetric strain is calculated based on the deformation of every tetrahedral element in order to evaluate the hydro-mechanical effect of drainage.

As a result of the discrete digital image correlation, the displacements of all solid grains are measured and illustrated for central vertical slices in Figure B.15 and in Figure B.16 in the Appendix together with the corresponding phase distributions. The drainage of pore water leads to a slight vertical displacement of the main part of the grains, however, locally at the bottom of the specimen a larger settlement occurs early during drainage leading to a cone-shaped region of settled grains. This increased, but locally restrained settlement that remains constant in the rest of the experiment is most likely due to a vertical adjustment and settlement of the filter membrane on top of the porous filter stone at the beginning of pore water outflow.

As often, at a closer view, nature is more complicated as would have been expected from the first view from a macroscopic perspective. Besides this local settlement, several individual grains attract attention due to their unexpected upward vertical movements characterised by positive displacements. These "grain jumps" are obviously induced by emerging air-water interfaces or capillary menisci which attract those grains and lift them up against gravity. A visual inspection of a series of greyscale images confirms the observed upward grain movements in the viscinity of occurring liquid bridges. This observation proofs an interesting effect of capillary action and the mechanical work that can be done by changing surface energy upon drainage. A quantification of the lifted particles is given by Figure 6.31 comparing the evolution of particles with downward and upward movement in the first 5 hydraulic steps of primary drainage.

The main downward grain movements already occur after the first drainage step probably due to the movement of the filter membrane and slightly increase in the following steps. The number of grains with upward displacement increases gradually with the first two drainage steps and afterwards decreases to a relatively constant value. If the local settlement at the bottom of the specimen is neglected, the measured grain movements are an indicator for hydro-mechanical coupling which can apparently lead to complex changes in the local grain skeleton.

The mechanisms of pore scale drainage are analysed based on Figure 6.32 in which the pore size distribution is juxtaposed to the median values of pore-based degree of saturation and resulting median of volumetric strains plotted *vs.* different corresponding pore sizes for all hydraulic steps on the primary drainage path. The occurring pore volumes are binned in 25 bins which are used to study the emptying and straining of different pore sizes.

The pore size distribution in Figure 6.32 (a) shows a strong dominance of smaller pore volumes in the investigated sand specimen. During primary drainage, slight changes in the pore size distribution, which is measured for every hydraulic step and therefore accounts for grain rearrangements, can be noticed.

The visualisation of median of pore-based saturation in Figure 6.32 (b) represents an important finding as it reveals clear evidence for a drainage sequence. Accordingly, larger

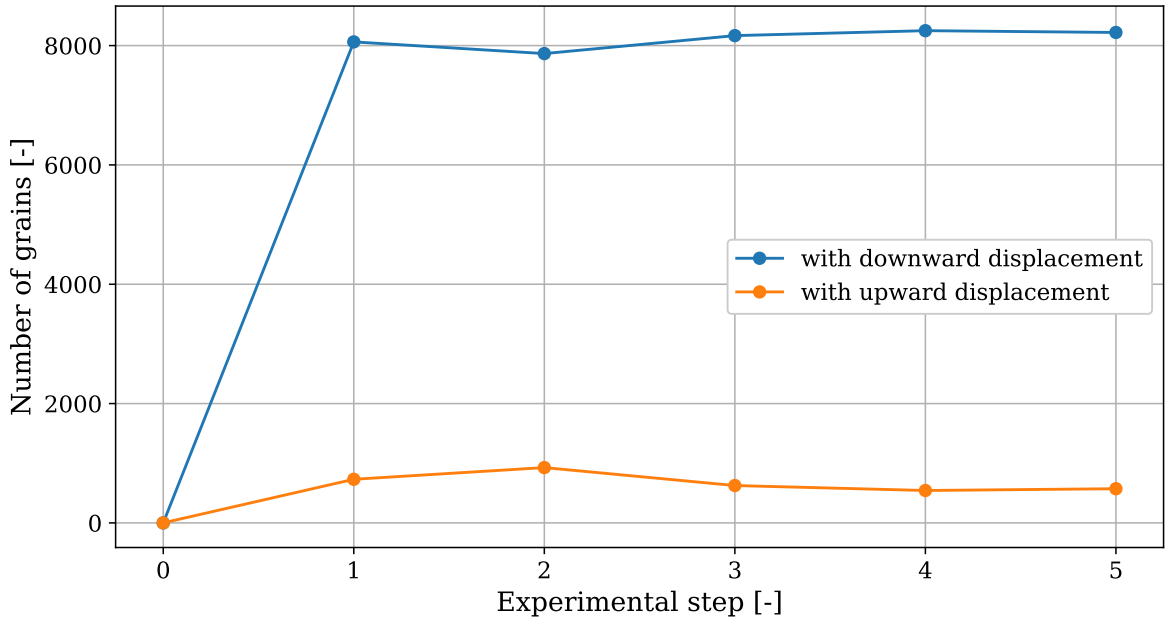


Figure 6.31: Number of grains moving downwards or upwards extracted from the results of a DDIC analysis during primary drainage of Hamburg Sand

pores empty before smaller ones which is absolutely in agreement with theory. After hydraulic step 2, a strongly varying median of degree of saturation can be noticed for the pores larger than 0.0045 mm^3, while smaller pores remain fully saturated. This irregular emptying of larger pores could be the consequence of the air fingering observed in the other evaluations. In the following hydraulic steps 3 to 5, a smooth relationship between pore volume and median of saturation evolves reflecting the trend of higher saturation with smaller pore volume. Furthermore, the distributions grow steeper during drainage leading to a more "binary" distribution with pores being either fully saturated or fully dry depending on their size.

The hydro-mechanical effect of pore drainage can be analysed based on Figure 6.32 (c) showing the median of volumetric strain calculated from the deformation of the tetrahedra which enclose a pore *vs.* the pore volume bins as used in the subplots discussed before. The findings must be interpreted based on the fact that there are many small pores, but much fewer larger pores included in the sand specimen. The distribution of median volumetric strain indicates an increasing positive volumetric strain for the many smaller pores during drainage which corresponds to mechanical contractancy. The fewer larger pores, however, show an irregular build-up of negative median volumetric strain, *i. e.*, mechanical dilation. This observation might be evidence for the effect of suction stress in different saturation and pore size domains. According to this interpretation, the change of suction stress leads to an increase in effective stress in the many saturated or close-to-saturated small pores with the result of contractancy and to a decrease in the fewer larger emptied pores which react by dilative volumetric behaviour to the release of effective stress and emerging capillary bridges. These observations and interpretations of the effective stress could also

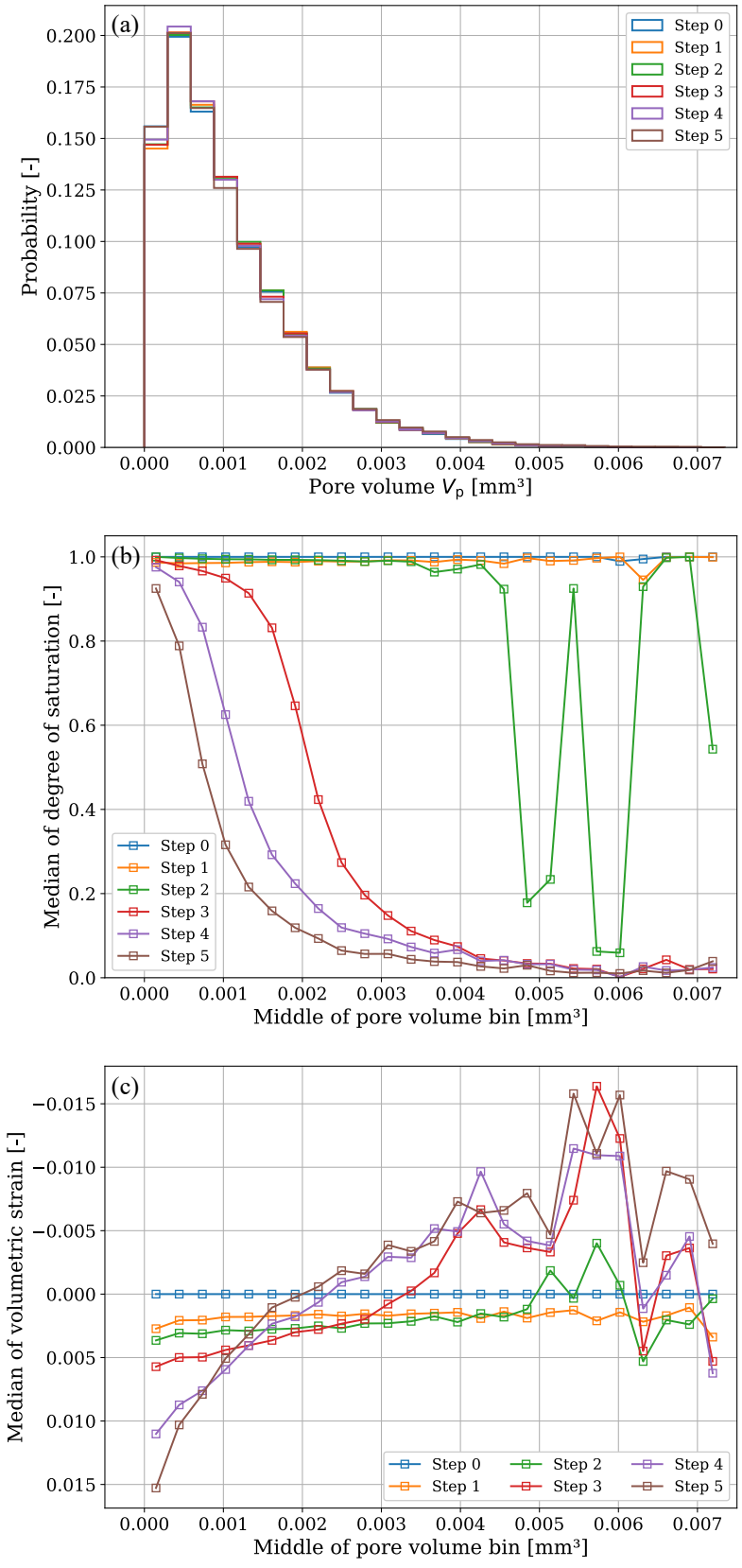


Figure 6.32: (a) Evolution of pore size distribution, (b) median of pore saturation, and (c) median of volumetric strain in pores classified by pore size for primary drainage (Milatz *et al.*, 2022b)

explain the cyclic change in void ratio presented in Figure 6.22. This "breathing" of the pore volume measured on the subvolume-scale could also be the result of microscopic grain rearrangements as response to a cyclically changing suction stress.

6.4 Links between microscopic and macroscopic soil behaviour

With the help of the described imaging and *in situ* CT experiments, many physical processes occurring on the pore or grain scale could be studied on a qualitative and quantitative level to relate the microscale to the macroscale soil behaviour. The insights from the experiments help to answer some of the guiding research questions, but also open new ones. In the following, these findings are further summarised and structured into their meaning for the hydraulic and mechanical behaviour of unsaturated granular soils.

6.4.1 Water retention behaviour

Based on the results from the water retention experiments with *in situ* CT imaging, it can be shown that the microscopic phase distribution as well as flow effects on the pore scale influence the macroscopic water retention curve measured on a representative specimen volume. By means of imaging, discrete microscopic structures and continuum soil properties can be measured and quantified. The statistical distribution of microscopic structures, *e. g.*, pore sizes, contact angles or capillary radii of curvature, seems to be characteristic of the investigated porous material, *i. e.*, it depends on the grain shape and density. Knowledge of the distributions as measured by CT imaging represents the key to a better understanding of the macroscopic soil properties and soil behaviour, such as the water retention curve.

As an example, it could be shown that the temporal evolution of mean radius of curvature from a measured contact angle distribution allows to calculate a capillary pressure based on the Young-Laplace equation which is close to the matric suction measured on a macroscopic level. The measured data also include evidence for contact angle hysteresis and related hysteresis of radii of curvature leading to higher capillary pressures on drainage paths as compared to imbibition paths. Another quantitative finding based on a pore-based analysis on multiphase CT data reveals a drainage sequence much in agreement with theory with larger pores emptying prior to smaller pores during drainage. Furthermore, local events on the pore scale trigger the evolution of macroscopic matric suction during drainage. This is for example reflected by the oscillations of matric suction during primary drainage when the sudden emptying of larger pores due to the entering of air fingers into the pore space occurs as seen in the CT data.

All these results from the hydraulic experiments indicate that the macroscopic matric suction is obviously the averaged result of the capillary effects in the multitude of different pores on the pore level.

6.4.2 Mechanical behaviour

As a link to the mechanical behaviour, the analysed CT data from the water retention experiment on sand have revealed interesting insights into hydro-mechanical coupling with cyclic drainage and imbibition apparently leading to changes in void ratio but also to local reordering of grains. Especially the latter observation, with small grains being moved or even lifted against gravity by reconfiguring air-water interfaces or capillary bridges, is a new aspect of discrete hydro-mechanical coupling that needs further studies. While the "breathing" of void ratio might be a measurable volumetric effect of changing suction stress, the local movement of grains is of a rather discrete nature. These findings highlight the importance of the WRC regarding the mechanical behaviour of a soil. Also the role of the interfacial areas as potential ingredients for the formulation of suction stress needs to be further addressed. Based on the findings of this work, a soil-water-air interfacial area characteristic curve might exist besides the WRC which could be used as the basis for new models of effective stress in unsaturated soils.

The uniaxial compression tests with *in situ* CT imaging supplement the insights from the water retention experiment concerning hydro-mechanical coupling. During the shearing of unsaturated soils, discrete water clusters and capillary bridges are found to change with larger clusters being generally degraded into smaller ones. The studies on the mechanical straining of individual capillary bridges due to particle motion confirm the observed behaviour with the rupture length of capillary bridges mainly depending on their liquid volume. Larger liquid bridges corresponding to a higher local degree of saturation can transfer higher forces and have a longer range until rupture, whereas smaller capillary bridges rupture after shorter separation distances in the order of magnitude of shear displacements reached under uniaxial compression.

A further insight from the uniaxial compression tests is represented by the quantitative evidence of the impact of pore scale capillary effects on the volumetric shear behaviour. On the macroscopic level, the tendency to dilation increases with decreasing degree of saturation. In agreement with this macroscopic observation, pores with lower degree of saturation dilate more based on the analysis of pore saturation and its relationship to local strain. The higher the pore-based saturation, the smaller the suction, but the higher the effect of suction transferred at the wetted interface between water and solid phase, thus contributing stronger to effective stress holding the grains together. On the other hand, the lower the pore-based saturation, the higher the suction, but the lower the effect of suction due to a reduced solid-water interface. However, the effect of surface tension should theoretically prevail at lower saturation due to the presence of menisci which are characterised by the air-water interfaces. The contribution of suction as well as surface tension to the total capillary force is also analysed in the straining experiments on individual liquid bridges. In the case of the tested capillary bridges, the contribution of surface tension is generally higher compared to the contribution of suction which theoretically can take negative values depending on the capillary bridge geometry.

As outlined earlier, macroscopic suction stress proposed by Lu and Likos (2006) and Lu *et al.* (2010) based on Bishop's effective stress could represent a link between the microscopic unsaturated state and the macroscopic stress state in unsaturated soils if it is defined

based on "micro variables". With the help of powerful imaging techniques and suitable *in situ* experiments, such *capillary state variables* can be measured as shown in this work. Therefore, besides the use of degree of saturation or effective degree of saturation as the weight χ of suction in the effective stress equation as discussed in Section 2.4, also the interfacial areas could provide a basis for the definition of effective stress in unsaturated soils as proposed by different authors and highlighted in Section 2.4.1.

While most authors propose the calculation of χ based on only one of the interfacial area terms combined with effective degree of saturation, it is proposed here to define χ based on both interfacial areas in mechanical agreement to the capillary force contributions in a capillary bridge. According to this proposition, the solid-water interfacial area, following a monotonic curve in between $S_\mathrm{r} = 0$ and $S_\mathrm{r} = 1$, would represent the contribution of suction, whereas the air-water interfacial area, showing a peak at a medium saturation, could provide the contribution of surface tension to effective stress. Based on the proposed soil-water-air-interfacial area characteristic curves, *i. e.*, the set of functions describing $a^\mathrm{sw}(s)$ or $a^\mathrm{sw}(S_\mathrm{r})$ and $a^\mathrm{nw}(s)$ or $a^\mathrm{nw}(S_\mathrm{r})$, as measured from the CT data in this work, characteristic relationships for effective stress *vs.* degree of saturation or suction including hysteresis can be derived according to the proposed equation

$$\sigma_\mathrm{s} = \chi_\mathrm{sw}\, s + \gamma\, a^\mathrm{nw} = \frac{a^\mathrm{sw}}{a^\mathrm{s}}\, \gamma\, H + \gamma\, a^\mathrm{nw} \quad . \tag{6.1}$$

As the specific solid-water interfacial area a^sw would take the role of degree of saturation, reflecting the wetted amount of total solid surface area (transferring suction) when normalised by specific solid surface area a^s, degree of saturation would not be needed in this effective stress formulation. This approach represents a combination of the suction stress definitions according to Equations 2.17 and 2.21 which either include the air-water interfacial area a^nw or the solid-water interfacial area a^sw, but which share the contribution of degree of saturation. In order to also avoid the macroscopic measurement of suction s, this kind of micro-macro model could be even extended by incorporation of a characteristic radius of curvature and corresponding mean curvature H from measurements allowing to calculate suction based on the Young-Laplace equation as also indicated in Equation 6.1.

The proposed suction stress formulation based on both interfacial areas in Equation 6.1 is evaluated using the data measured in the water retention test on Hamburg Sand with parallel CT imaging presented in Section 6.3. Figure 6.33 shows the contributions of solid-water interfacial area and air-water interfacial area to total suction stress *vs.* matric suction and degree of saturation. In the calculation according to Equation 6.1, a specific solid surface area per unit volume of $a^\mathrm{s} = 6.28$ 1/mm as well as a surface tension of $\gamma = 0.07275$ N/m are assumed. Furthermore, the measured matric suction after a CT scan and degree of saturation as calculated in the centred cubic subvolume are used. The calculated suction stress reflects the hysteresis already encountered in the interfacial areas. The contribution of the air-water interfacial area and the surface tension is small as compared to the contribution of the solid-water interfacial area and suction. However, the ratio of the contributions might change in the case of finer grained soils. Generally, a suction-stress characteristic curve with a similar shape as presented by Lu *et al.* (2010) is obtained. Interestingly, hysteresis leads to a path-dependence of suction stress, which should be

further verified in dedicated hydro-mechanical experiments. This path-dependence would practically mean a higher capillary cohesion or shear strength of soils on a drainage path as compared to soils on an imbibition path.

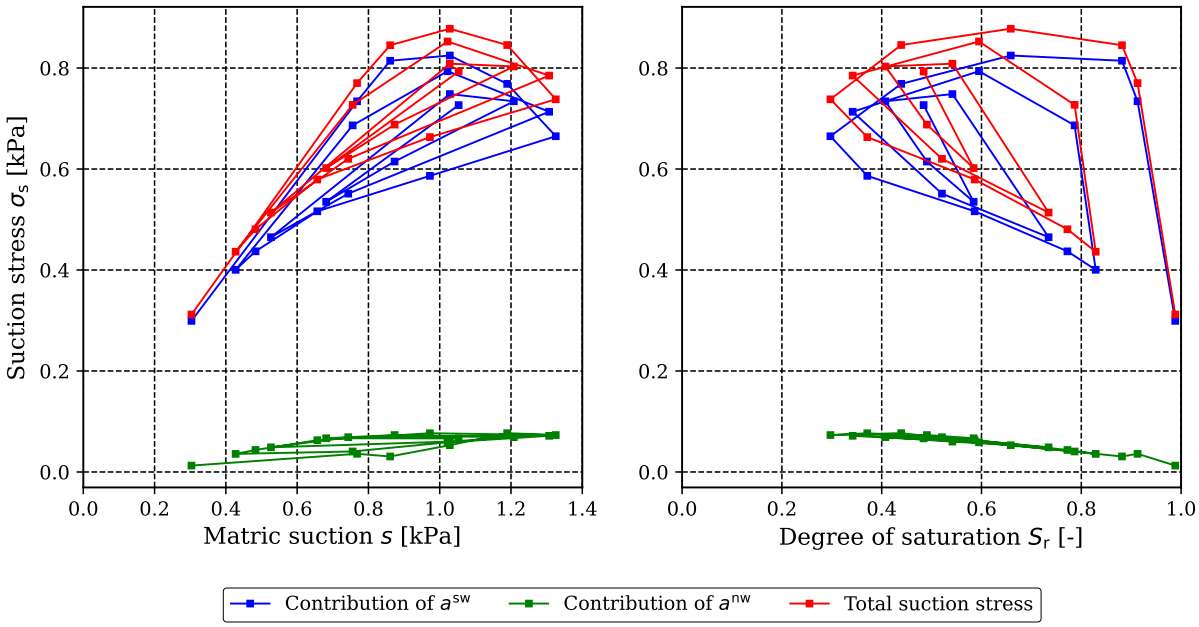


Figure 6.33: Suction stress according to Equation 6.1 calculated for the interfacial areas measured in CT data from the water retention test on Hamburg Sand and plotted *vs.* measured matric suction (left) and subvolume-based degree of saturation (right) assuming $\gamma = 0.07275$ N/m and $a^s = 6.28$ 1/mm

The relationship between suction stress and capillary cohesion

$$c_c = \sigma_s \tan \varphi' \tag{6.2}$$

can be applied to calculate the corresponding capillary cohesion. It is directly obtained from the Mohr-Coulomb failure criterion including capillary cohesion if suction stress is interpreted as the maximum tensile stress needed to overcome the isotropic capillary stress state as given by suction stress (neglecting a tension cutoff). A comparison of calculated capillary cohesion based on suction stress to values from the uniaxial compression tests presented in Section 4.2 is shown in Figure 6.34. The capillary cohesion based on the interfacial areas is in the same order of magnitude as the values from uniaxial compression tests, and it reflects the non-linear curve between $S_r = 0$ and $S_r = 1$ with a peak closer to higher degrees of saturation.

In order to better understand the observed hydro-mechanical effects, to support the outlined theoretical model based on interfaces, and to include them in micro models, such as DEM or in continuum-based engineering models, *e. g.*, FEM, more specialised (imaging) experiments also including different granular materials and corresponding evaluations will be needed. Due to their partially discrete and dispersed nature, the microscopic effects can probably only be included on a statistical basis, which requires many measurements.

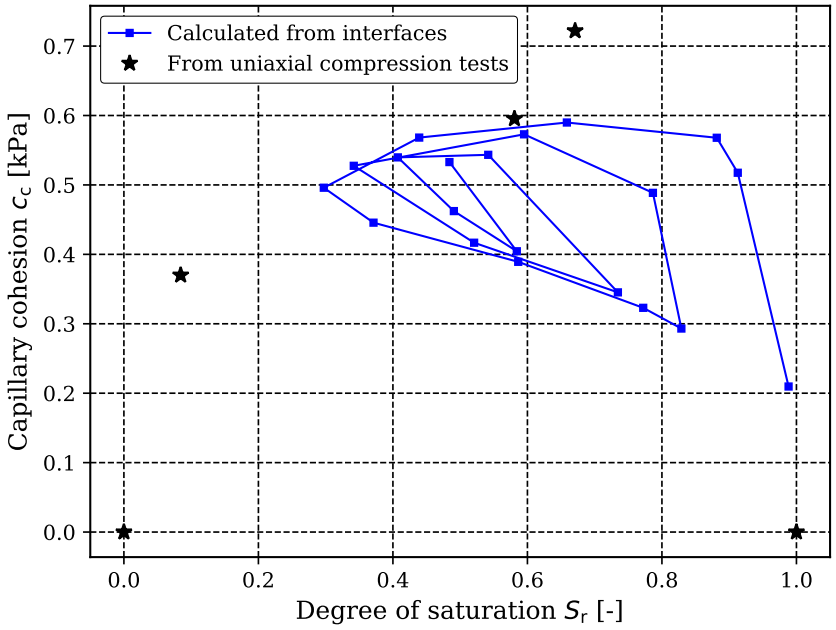


Figure 6.34: Capillary cohesion derived from suction stress calculated according to Equation 6.1 using the interfacial areas measured in CT data from the water retention test on Hamburg Sand compared to capillary cohesion measured in uniaxial compression tests plotted *vs.* degree of saturation

Chapter 7

Outlook on further applications of imaging experiments

In this chapter, an outlook on current and future applications of imaging experiments in soil mechanical and geotechnical research as well as in teaching will be given. The presented examples from ongoing research and research ideas may inspire to set up further future research projects, but also student projects with an educational background.

7.1 Synchrotron-based CT imaging of direct shear tests

In the framework of the 96 h beamtime I-20210425 "Synchrotron-based tomography of changing pore scale capillary effects during transient water retention experiments on granular media", water retention tests with parallel synchrotron-based CT imaging have been run at the P07 High Energy Materials Science Beamline operated by Helmholtz-Zentrum hereon at DESY. Besides these main experiments, which will be reported elsewhere, also two direct shear tests with the set-up presented in Section 4.4 could be run. Within the scope of this work, the miniaturised direct shear tests and the potential of the images acquired with the help of synchrotron radiation will be briefly discussed.

In the experiment discussed here, a cylindrical specimen of unsaturated Hamburg Sand with a diameter of 16 mm and height of 10 mm at an initial macroscopic void ratio of $e = 0.65$ and initial macroscopic degree of saturation of $S_\mathrm{r} = 0.3$ is sheared incrementally with a shear velocity of 0.004 mm/s at increments of 0.2 mm in between image acquisitions up to a maximum shear displacement of 2 mm. The specimen is sheared at a total vertical stress of $\sigma = 2$ kPa caused by a dead weight. After each shear step, three minutes for equilibration of the water phase inside the specimen are scheduled before the next CT scan is started.

Figure 7.1 shows the general geometry of the scanned domain of the specimen relative to the synchrotron beam with a rectangular cross section. The beam width and beam height are fixed at *ca.* 6.57 mm and 2.6 mm, respectively. In order to obtain a larger field of view, two stacks of the specimen are scanned successively with a vertical overlap of the

beam of *ca.* 0.18 mm height as illustrated in Figure 7.1 a). The energy of the X-rays is 47 keV. Each scan took about 7.7 min, *i. e.*, the total tomography volumes consisting of two stacks are captured in *ca.* 15.4 min. Accordingly, it must be noted that, strictly speaking, there is a temporal shift in between each two imaged stacks.

The CT data is reconstructed with phase retrieval according to the work described in Moosmann *et al.* (2014) using the ASTRA toolbox (van Aarle *et al.*, 2016). The two scanned tomography volumes for each experimental step at different shear displacements are stitched after reconstruction yielding a scanned volume of 2565 px×2565 px×1961 px (6.57 mm×6.57 mm×5.02 mm) at a voxel size of 2.56 μm with the shear plane located nearly in the middle.

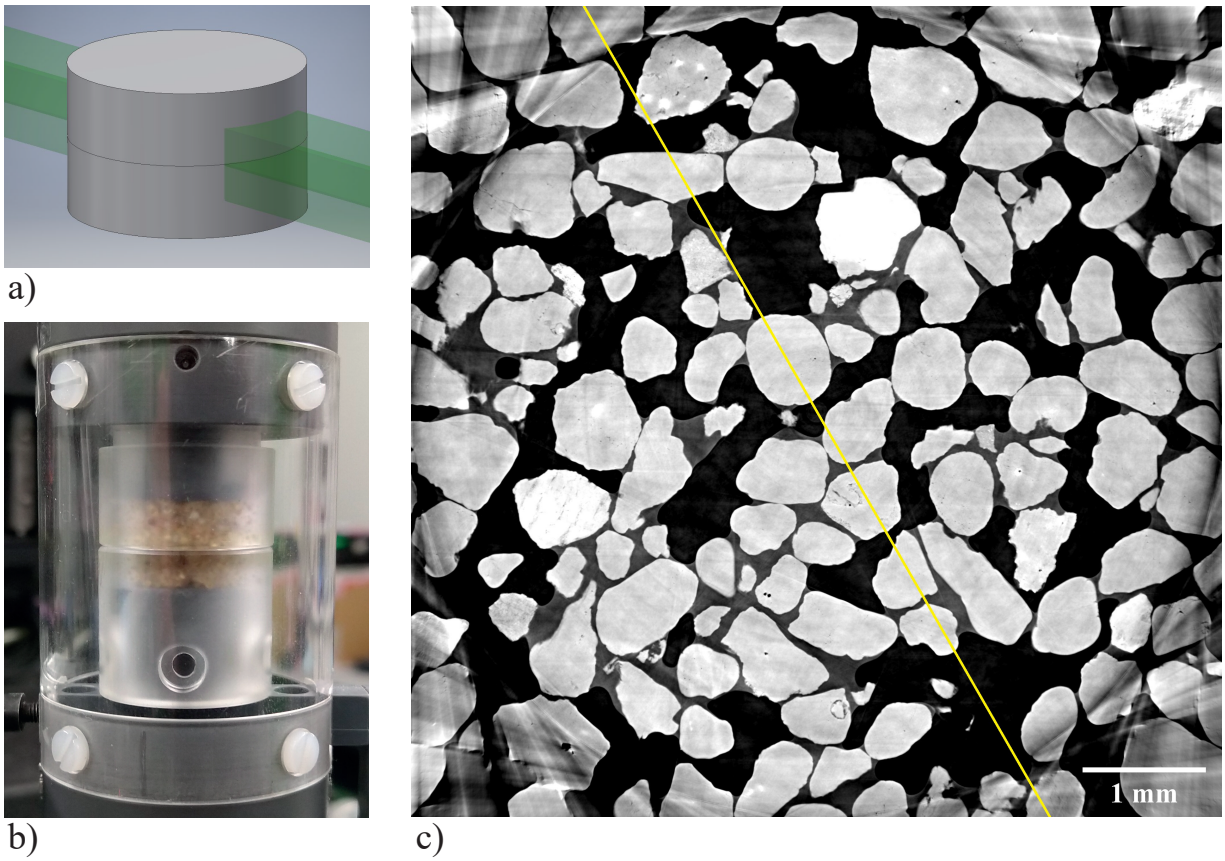


Figure 7.1: Overview of the scanned specimen volume and synchrotron beam location a), photograph of the specimen prior to shearing b), and reconstructed CT slice in the shear plane c) from an *in situ* direct shear test on Hamburg Sand with synchrotron-based CT imaging. The yellow line in figure c) indicates the shear direction

The macroscopic shear stress *vs.* shear displacement is plotted in Figure 7.2. The force measurements are only slightly disturbed by the specimen rotation. Only during the fourth CT scan after the third shear step, pronounced jumps in the force measurement occur, one of which needed to be corrected by subtracting the jump in the force data. Generally, the measured force slightly decays during CT imaging which is also noticed in the uniaxial

compression tests on Hamburg Sand presented in Section 5.2. After a shear displacement of *ca.* 0.155 mm, the load cell connects to the shear sledge leading to an increase in shear stress with further shearing. In the first four shear steps, the shear stress continues to increase until a plateau is reached slightly above a shear stress of 5 kPa. Besides a slight further increase in the 7th shear step, the stress level is rather maintained up to the 8th shear step from which a decrease until the end of the experiment is noticed. As compared to the experiments on dry Hamburg Sand discussed in Section 4.4, the evolution of shear stress of the unsaturated specimen shows no peak behaviour with the stress level being rather constant, probably due to the strengthening capillary effects.

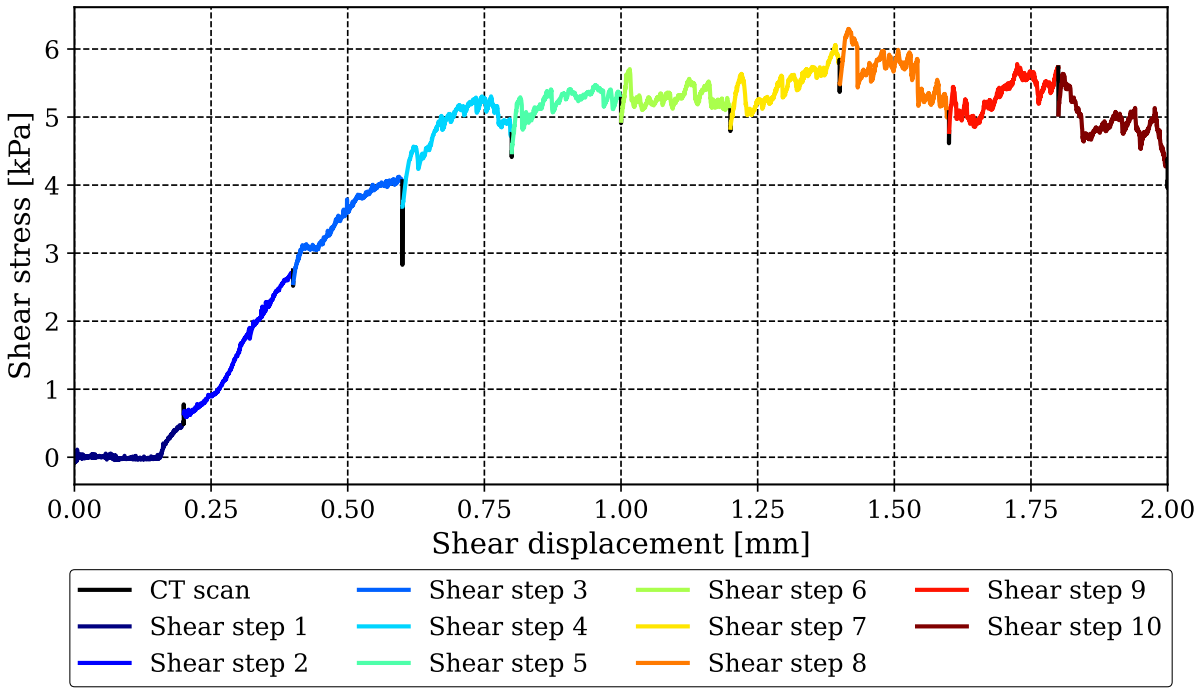


Figure 7.2: Shear stress *vs.* shear displacement measured in an *in situ* direct shear test on unsaturated Hamburg Sand with synchrotron-based CT imaging

In order to investigate the particle movement as well as the behaviour of capillary bridges and water clusters under direct shearing, 2D images are derived by reslicing the tomography volume vertically along the yellow path in Figure 7.1 c) which indicates the shear direction in the horizontal plane. Such a resliced image is shown in Figure 7.3 with horizontal artefact-like traces of the slit and the shear plane in between in the middle of the image well visible.

If the particle movement is studied simply based on the image sequence as shown in Figure B.17 in the Appendix, some basic observations can be made. Firstly, the sand grains below the shear plane rather move horizontally with slight rotations visible, whereas particles above the shear plane show horizontal motion combined with vertical upward movement. With increasing vertical distance from the shear plane, the upward movement of the sand grains starts to prevail leading to the strong dilatancy of the specimen as

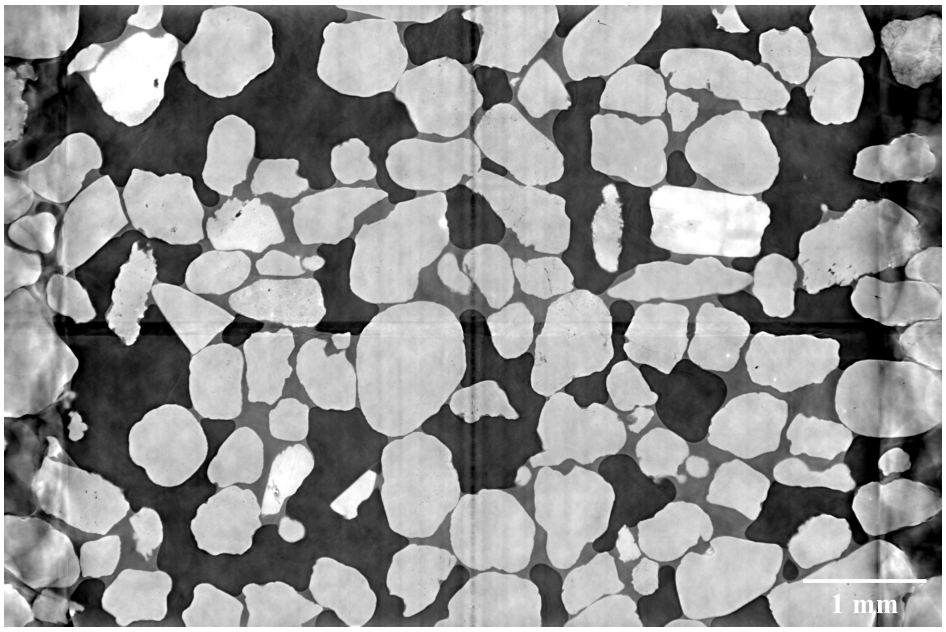


Figure 7.3: Vertical CT image resliced through the tomography volume of the initial scan prior to shearing in parallel to the shear direction (from left to right) showing the horizontal shear plane in the middle

observed on the macroscopic level. A second important observation is the behaviour of capillary bridges and water clusters. Locally, repeated evidence of rupture events of capillary bridges as well as fusion of water clusters is found as particles change their contact partners during displacement and rotation. These qualitative findings need to be further quantified by means of more elaborated analysis in the future. Based on the analysis tools developed and applied in this work, the local shear behaviour characterised by shear strain and grain contacts as well as the evolution of water clusters inside and outside of the shear zone could be quantified. Furthermore, local changes in pore-based degree of saturation as well as contact angles could be studied which will help to better understand the hydro-mechanical coupling during the shear process. As compared to images acquired with laboratory X-ray sources, the images show a low signal-to-noise ratio and high phase contrast which will facilitate the segmentation process. Due to the high spatial resolution, the surface morphology of sand grains as well as inner structures, such as ruptures or different enclosed minerals or pores can be resolved. The quality of the acquired images combined with their spatial and temporal resolution will open the door to new possible analyses and insights.

7.2 Investigation of soil-structure interaction on the microscale

The approach to investigate soil mechanical processes on the microscale by means of imaging experiments as outlined in this work can be extended to study different processes with relevance to geotechnical applications from a new point of view. In geotechnical engineering, many open questions on the field of soil-structure interaction still exist. Suitable imaging experiments could be applied to better understand the evolution of friction at the boundary of geotechnical structures, such as sheet pile walls or piles, during installation or over time. This would help to better understand the microscopic origins of friction, leading to the macroscopic resulting bearing capacity of foundation structures. Here, it is also unknown how temporal processes lead to a change of bearing capacity over time, *e. g.*, due to ageing of the structures and their interference with the soil microstructure.

Another example is given by the set of problems due to soil clogging in the field of mechanised tunneling. Here, the build-up of soil masses adhering to the cutting wheel, its cutting tools or clogging the excavation openings and discharge lines is still problematic in engineering practice. In the eyes of the author, this is due to the fact that clogging and soil adhesion are still not well understood on the microscale. Being also related to unsaturated soil mechanics, the development of soil clogging could also be studied with the help of CT in miniaturised *in situ* experiments based on the experience written down in this work. Figure 7.4 outlines the idea and potential of such miniaturised clogging-experiments based on a prototype set-up that was already tested in a CT scanner to study the development of clogging soil underneath a loading plate. In the experiment, the loading plate is initially driven 1 mm into the clay specimen and then extracted in three steps. After all experimental steps, CT images are acquired to study the soil-structure interaction as well as the adhering soil.

Besides the macroscopic stress-strain response to derive the evolution of adhesion, the CT data can be analysed quantitatively, *e. g.*, by measurement of the adhering soil volume as well as by analysis of changing soil density and the occurrence of rupture zones as further outlined in Schröder *et al.* (2022).

7.3 Soil mechanical experiments with CT imaging

In addition to the different soil mechanical experiments that have been implemented in miniaturised versions for *in situ* CT experiments within the scope of this work, but also by other authors, further related experiments could be focused on in future research. The investigation of the different loading mechanisms and the local soil response by means of full-field CT images in other experiments, such as the oedometer or simple shear test, could help to better understand the chances and limits of the element test philosophy. Furthermore, the microscopic mechanical response, especially, but not exclusively, of granular soils under different loading conditions could be studied on the grain or pore scale, *e. g.*, focusing on grain displacements, rotations, the evolution of grain fabric, grain crushing or the

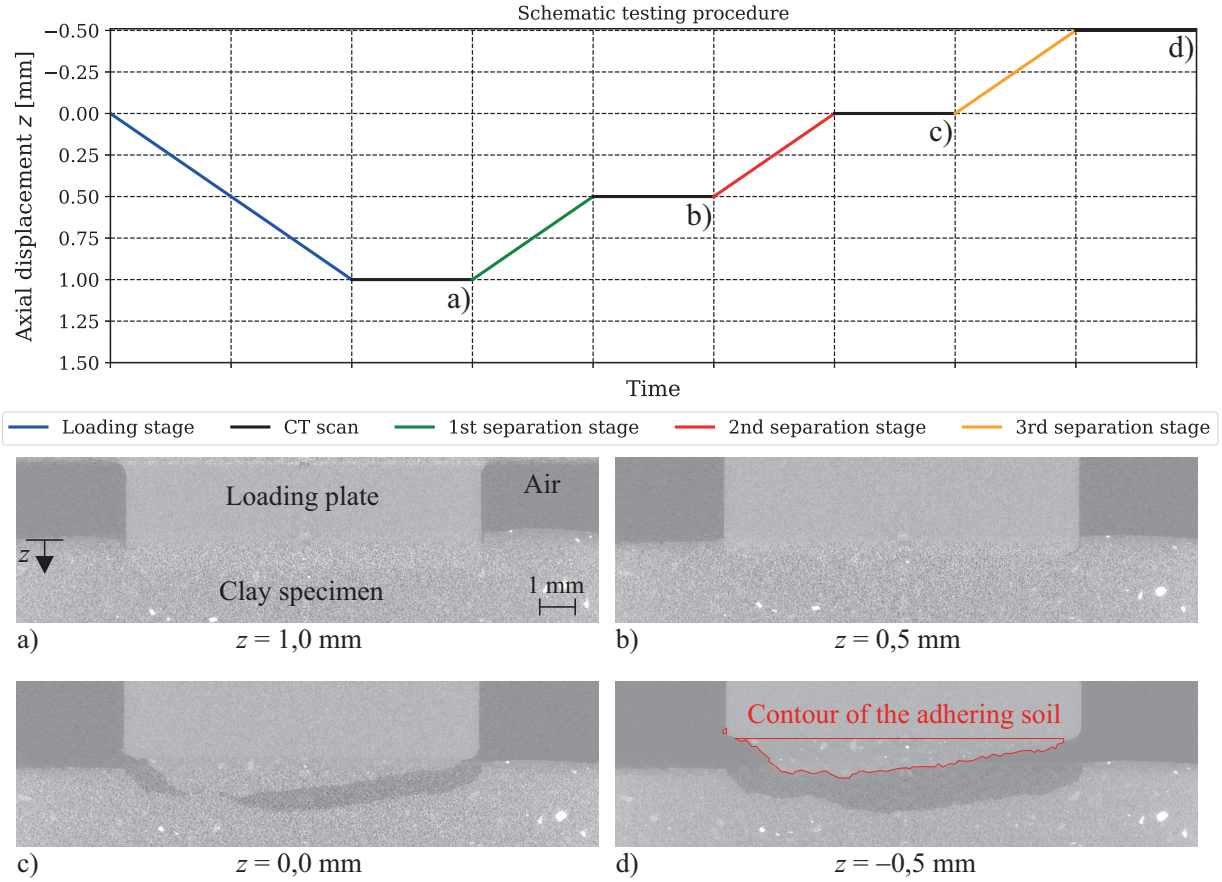


Figure 7.4: Schematic testing procedure (top) and greyscale CT images (bottom) showing the vertical cross section of the loading plate and underlying soil for different time steps a) to d) during a clogging experiment

local changes of the unsaturated state. A special challenge on this research field is always found in the miniaturisation of the testing devices and the accessibility of the specimens for the imaging radiation.

7.4 Physical computing and its experimental applications in teaching

With respect to contemporary teaching applications, driven by digitalisation, some of the presented experimental procedures seem to be suitable to be included in engineering education. Under the term "physical computing", students can get in contact with programming languages in an illustrative way as programming is applied to drive practical experiments and their technical components, such as actuators and sensors, frequently with the aim to study real-world problems. Based on only a few hardware components, *e. g.*, a single-board computer, a set of motors with their motor driver boards, and maybe

a simple sensor, such as an accelerometer, students can quickly develop experimental environments, of course under some supervision, to study research questions in the field of geotechnical engineering. As an example, students built a mini-vibrator to study the penetration of a miniaturised model pile in sand using different vibration settings in a geotechnical project course at TUHH. Besides some 3D-printed components, which could easily be designed in a CAD program and fabricated by a FabLab, and some screws and cables, only the named hardware components were needed. In the course of a semester, it was great to observe the development of specialists in each student team closely working together with great motivation and interest to get their experiment running for the final demonstration.

Besides this example, some of the developed experimental set-ups for research presented in this work have been used in student research projects in the framework of Master's theses. By own experience, students with natural interest in experimental work quickly understand the set-ups as well as the provided software to tackle complicated research questions, for instance about the investigation of unsaturated soils by means of CT imaging. On this field, different preliminary uniaxial compression tests to study unsaturated shear strength and water retention tests focussing on air entrapment have been run in a CT scanner available at TUHH within the scope of Master's theses supervised by the author.

Chapter 8

On the way to a virtual soil lab for simulations on the grain scale

In this chapter, the idea of a virtual soil lab is outlined and discussed based on different modelling approaches and practical examples of numerical simulations on the grain or pore scale focussing on unsaturated granular soils. The presented simulations aim at a better understanding of the micromechanics and microhydraulics by combination of CT experiments and numerical models which might represent one aspect of a possible future virtual soil lab.

8.1 Introduction

Based on the possible microscopic insights from CT experiments, micromechanical or microhydraulic models can be derived in order to simulate the microscopic soil behaviour. This could lead to a better understanding of microscopic processes and of the macroscopic hydro-mechanical behaviour which can then be modelled by better constitutive models taking account of the microscale. An example of the development of a mechanical constitutive model based on a (theoretical) micro model of relative particle movements and straining is the concept of "Intergranular Strains" as presented by Niemunis and Herle (1997) and the successor model called "Intergranular Strain Anisotropy" (Fuentes and Triantafyllidis, 2015). Similarly, also hydraulic models, *e. g.*, for the modelling of hysteretic water retention curves, apply knowledge of filling and emptying mechanisms occurring on the pore level.

Besides the constitutive behaviour that can be designed according to microscopic insights from CT experiments, CT data can be used to directly derive the geometries of particles and pores for numerical simulations as detailed spatial information about particle size, shape, and positions over time is captured. Segmented volumes which are represented by voxels can act as input for numerical domains discretised by finite elements or for discrete particles in a DEM approach.

These two aspects, the direct measurement of geometric information *vs.* time as well as the possibility to design and calibrate constitutive models based on CT experiments,

can open the door to new numerical modelling techniques and applications which can be summarised by the term "virtual soil lab". This idea, partially already existing in the form of "simulation environments" inside of numerical software packages, can be figured out more deeply. The idea becomes visionary when a whole virtual or digital lab is imagined where all kinds of soil mechanical experiments can be performed on a purely virtual basis using "digital soil" from a data base bringing statistical variation into play.

In the following sections, different steps on the way to a virtual soil lab will be illustrated based on practical examples which consider the collected CT data discussed in previous chapters.

8.2 Generation of numerical models based on CT data

8.2.1 Meshing study of a single grain of sand

The voxelised output of CT scans can be directly used for the generation of numerical models either following a continuum-based or a discrete approach. While the Finite Cell Method (FCM) can directly exploit the voxelised nature of CT data by discretising solid volumes by cell-like finite elements (Parvizian *et al.*, 2007; Düster *et al.*, 2008), the standard FEM approximates scanned volume domains by finite elements. For this purpose, FE meshes, *e. g.*, on individual particles, have to be extracted from voxelised CT data. In this approach, named the Combined Finite-Discrete Element Method (FDEM), every particle in a larger model is approximated by an individual FE mesh (Munjiza, 2004). Examples with soil mechanical background exist in the form of the works presented by Turner *et al.* (2016) and Nadimi and Fonseca (2019) who consider the effect of microscopic grain morphology in particle-based FE simulations.

Figure 8.1 shows a meshing study on a CT scanned Hamburg Sand grain where the volume mesh coarseness has been varied according to Table 8.1. The volume meshes are generated using *Avizo*. Based on the initial voxelised volume, the grain surface is approximated with different accuracy. For highly accurate surfaces which capture the surface roughness of individual grains, rather fine meshes are required leading to a large amount of finite elements and correspondingly, the required numerical effort is highly increased.

Table 8.1: Meshing parameters applied in the meshing study

Meshing option	Number of nodes	Number of tetrahedra
0 (very coarse)	140	353
1 (coarse)	411	1160
2 (medium)	1611	5106
3 (fine)	17,567	59,022
4 (very fine)	62,170	248,781

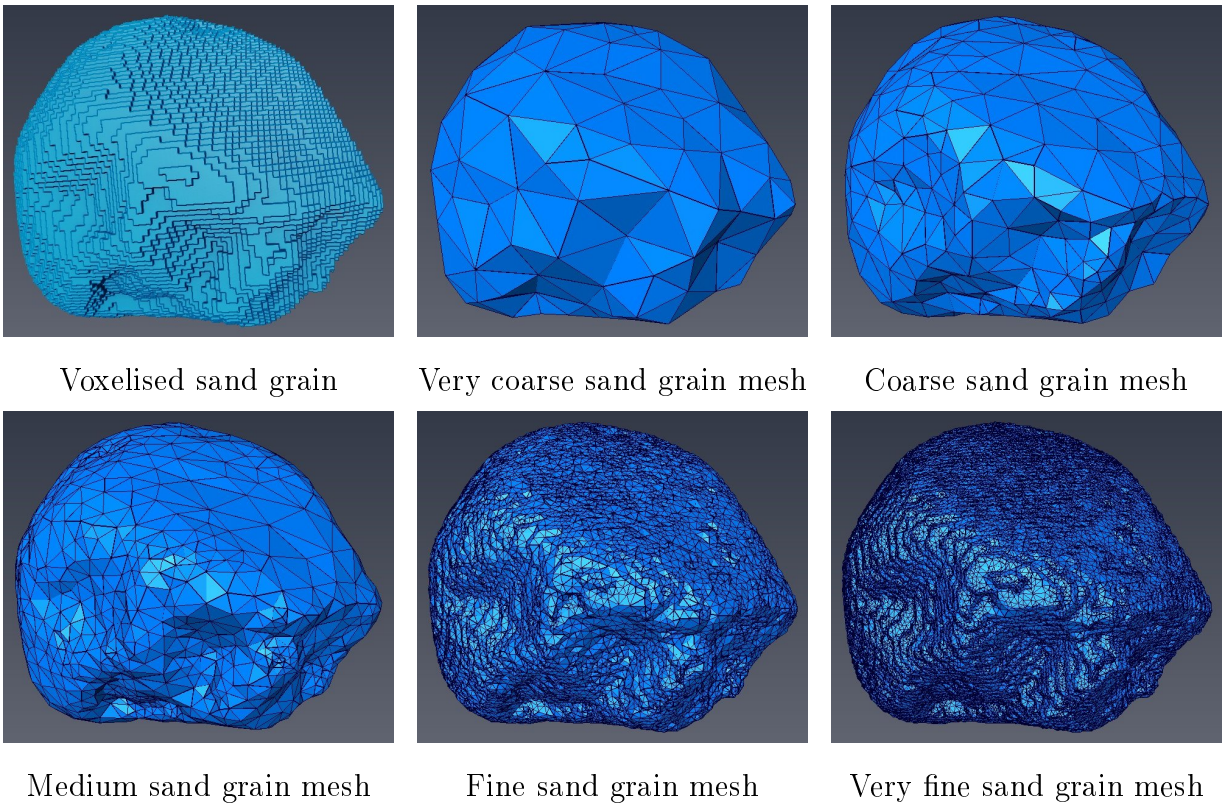


Figure 8.1: Meshing study on a CT scanned single grain of Hamburg Sand at a voxel size of 10 μm. The volume of the voxelised grain is *ca.* 0.21 mm^3. Meshing parameters according to Table 8.1

8.2.2 Pore scale meshes for CFD simulations

In addition to a geometric modelling of single grains and grain skeletons, CT data can be used for CFD simulations on the pore scale. In this approach, microhydraulic effects can be investigated by simulating the flow of single phases, such as liquids or gases, or the multiphase flow of mixed fluids in the pore space which can also be directly derived from CT data. As an example, CFD-based flow analyses allow to calculate the permeability of CT image-based digital porous media. Single- or multiphase flow problems can be addressed with the help of the Lattice Boltzmann Method which can simulate complex flow in restricted geometries and resolve capillary interfaces on the pore level. Following this approach, the common voxel-based nature of CT data and LBM computation cells or nodes is used to directly define fluid or solid cells based on segmented CT data.

For the extraction of LBM simulation models, CT images are trinarised (segmented) and then labelled. Frequently, a stack of TIFF-files is used. For a multiphase simulation, consisting of the solid grain phase acting as boundary and of the pore space where the fluid phase flow is simulated, binary images are sufficient with *e. g.*, the grains labelled as 1 and the pore space labelled as 0. An extracted region of interest can be efficiently stored in a 3-dimensional matrix consisting of ones and zeros. In order to reduce the numeri-

cal computation efforts, the number of lattice cells/nodes can be reduced by "binning", *i. e.*, the reduction of model size and coarsening of discretisation or resolution by pooling of pixels with a binning factor. The extraction of a 3D simulation domain from CT data of segmented Hamburg Sand and glass beads is illustrated in Figure 8.2. The cubic subvolumes from CT data with an edge length of 400 px are transferred and binned into LBM simulation domains with an edge length of 200 px. The void ratio of the Hamburg Sand model is $e = 0.632$. For the glass beads, a simulation domain with a similar void ratio of $e = 0.637$ is selected. The solid phase and pore space in the LBM simulation domains are visualised using *ParaView* (Ahrens *et al.*, 2005).

8.3 Combined FDEM simulation of particle interaction

8.3.1 Free fall study of a meshed sand grain

For a particle-based FE simulation, meshed sand grains can be imported into FE models which allow to simulate multi-body systems. Here, the commercial FE code Abaqus/Explicit is applied for a dynamic deformation analysis with direct explicit time integration. The single particle from the meshing study is imported and a free fall from a height of 4.461 mm into an open container discretised by shell elements is simulated as shown in Figure 8.3.The general contact algorithm for mechanical contacts with finite-sliding is used which allows all surfaces to contact each other. The mechanical contact is modelled as a "hard contact" in normal direction, *i. e.*, during contact detection, the penetration of contacting surfaces is minimised. For sliding contact in tangential direction, a friction coefficient of 0.3 is assumed. In the simulations, only the mesh coarseness of the sand grain as summarised in Table 8.1 is varied in order to study the effect of different surface resolutions on the dynamic behaviour. Except for a "dummy element" with elastic material properties for controlling the critical time step in the explicit dynamic analysis, the sand grain and the container are modelled as rigid bodies, *i. e.*, their dynamic behaviour is governed by a single reference point in their centre of mass. While the container is fixed in space, the particle can move freely in a gravitational field.

As shown in Figure 8.4, the mesh coarseness influences the contact behaviour in the FDEM simulations. The results indicate very different trajectories of the grain centre of mass after the first impact at the bottom of the container. After some similar initial rebounds, the grains are following very different directions. During their motion, the grains also collide with the walls of the container before coming to rest. This finding also highlights the role of grain discretisation for multi-body simulations, *e. g.*, in the case of the particle-based simulation of soil mechanical experiments in a virtual soil lab, as the discretisation strongly influences the contact behaviour.

8.3.2 Simulation of a sand column collapse

The developed procedure to extract discretised particles from CT data for particle-based FE simulations also works for larger grain assemblies as shown in Figure 8.5. Here, the

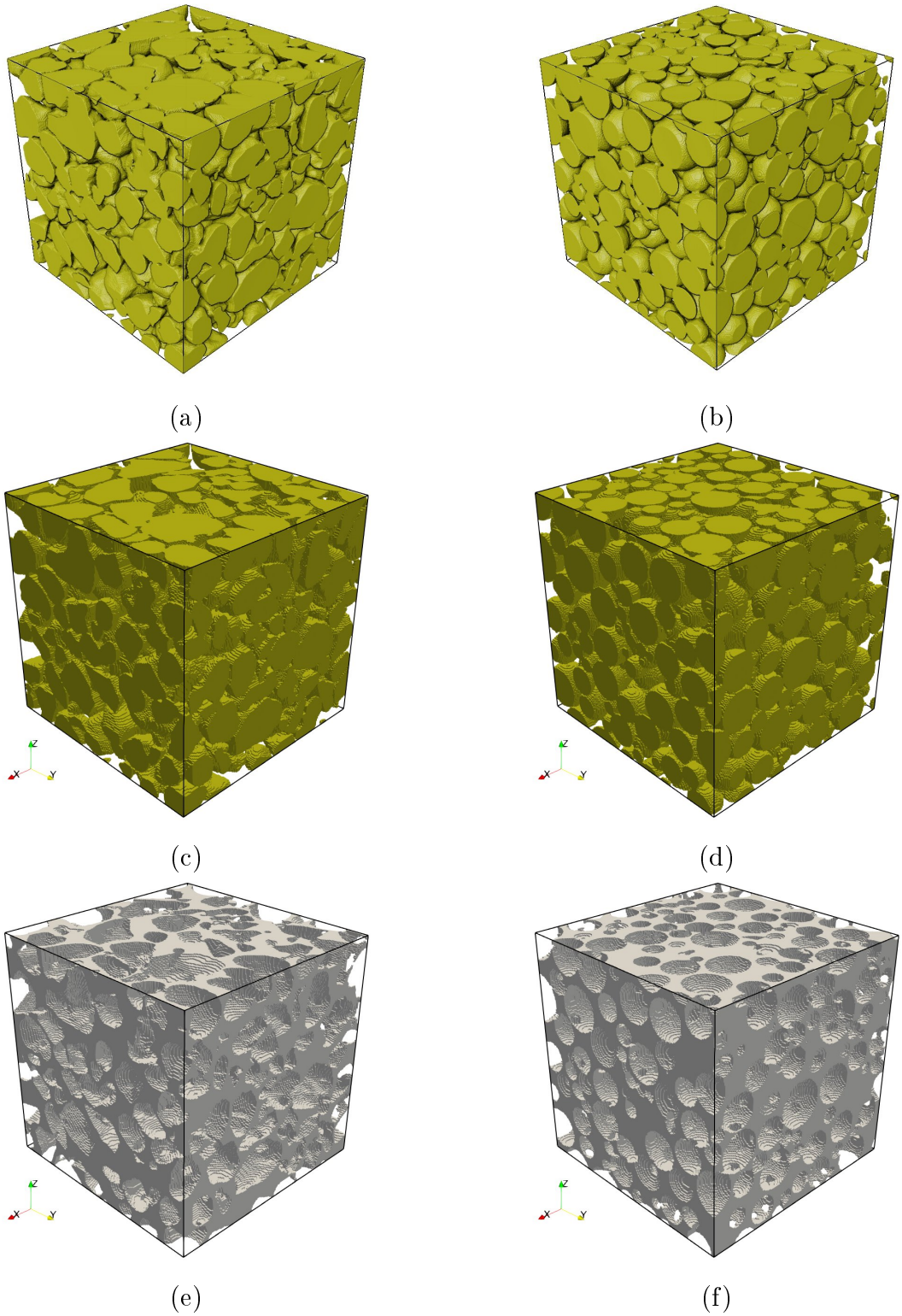


Figure 8.2: Extraction of solid phase and pore space models for LBM simulations from voxelised CT data: Subvolumes with edge lengths of 400×400×400 voxels of CT scanned Hamburg Sand (a) and glass beads (b), LBM solid computation cells of Hamburg Sand (c) and glass beads (d) derived from (a) and (b) with binning 2 (200×200×200 cells) and corresponding LBM pore computation cells of Hamburg Sand (e) and glass beads (f)

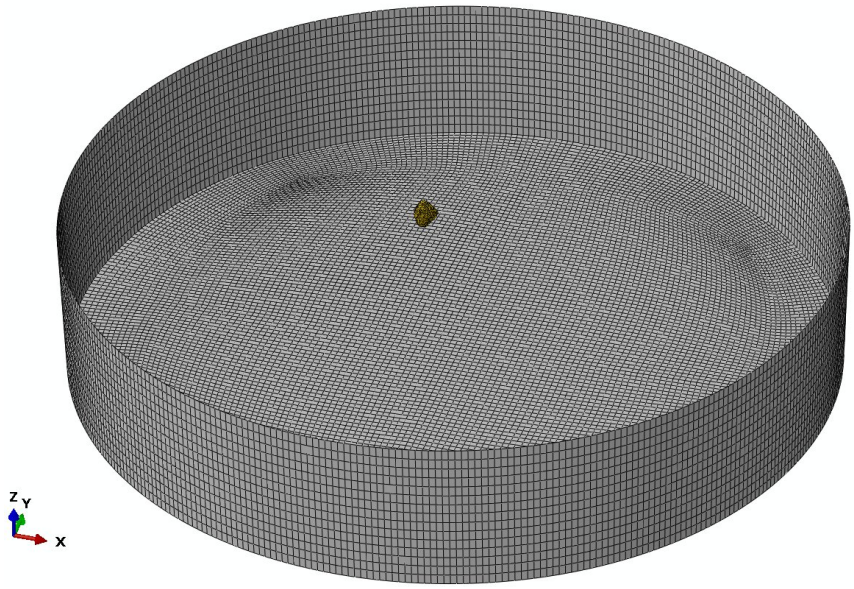


Figure 8.3: Numerical study on the free fall behaviour of a single sand grain into a cylindrical container

collapse of 1999 individual CT scanned rigid Hamburg Sand grains in a rigid cylindrical container is shown for the initial state and after a simulated time of 0.35 s. After this time, the particles have come to rest forming a heap in the middle of the container. Due to CPU-based parallelisation, the simulation can be run in a reasonable time. In this case, the computational time of a simulation with parallelisation with 10 threads and double precision on a desktop computer with an Intel(R) Xeon(R) W-2133 CPU @3.60 GHz and with 256 GB RAM was 6 hours and 45 minutes for a simulated time of 0.5 s. The simulation was found to be RAM-intensive, with the amount of required RAM increasing with the simulated number of particles. Furthermore, the size of output files can become problematic if the location of all nodes is of interest for many time steps.

In order to also investigate quasi-static and especially the intergranular contact behaviour, further "numerical experiments" similar to the studies by Turner *et al.* (2016), Nadimi and Fonseca (2019), and Thakur and Penumadu (2020) should be run in the future. With slight modifications, simple geotechnical experiments which include rigid boundary conditions, such as an oedometer or a direct shear test, but also a triaxial test with more complex pressure boundary conditions, on dry granular material could be simulated using the presented FDEM approach. For the simulation of capillary effects, the model needs to be enhanced. Potential is seen in user-defined contact models which could model adhesive effects of liquid bridges and water clusters by means of distance-dependent tensile contact forces. Another option would be discrete distance-dependent capillary force models which simulate capillary bridges by linking the centres of mass of neighbouring grains with beam elements.

This section is concluded with some final thoughts on further future modelling efforts. In order to obtain physically correct behaviour, the dynamic simulation settings, such as

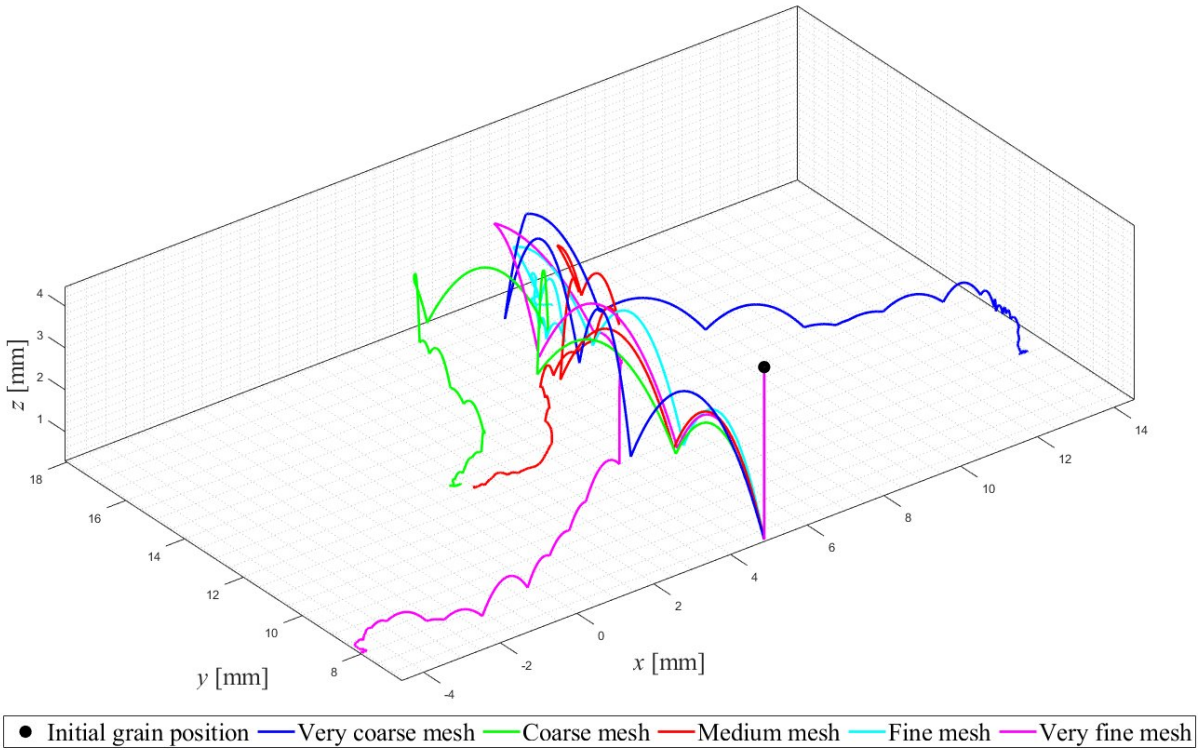


Figure 8.4: Simulated 3D trajectories of the centre of mass of the same sand particle with different mesh coarseness during free fall and repeated bounce back

damping and contact modelling, must be verified. Simulation settings need to be adjusted to achieve realistic contact behaviour. If grain deformations are of interest, elastic or inelastic properties can be assigned to all involved materials, however, at the probable expense of higher computation time. If Abaqus is used for FDEM simulations, additional software might be needed to extract grain contacts, contact directions, and contact force chains. On the way to a virtual soil lab, a software for generation of particle packings from a database of CT scanned particles along with rigid geometries for the modelling of soil mechanical tests and their boundary conditions could be designed and applied in the FDEM approach.

8.4 Multiphase LBM simulation of capillary phenomena on the pore scale

Inspired by the work of Hosseini *et al.* (2021), a single-component multiphase LBM formulation based on Huang *et al.* (2015) is implemented in C++ and applied to model the hysteretic water retention behaviour in different granular media. The applied LBM formulation is fully described in Appendix C. The focus of the numerical studies presented here lies on the model response to cyclic drainage and imbibition following the *in situ* CT experiment discussed in Chapter 5.

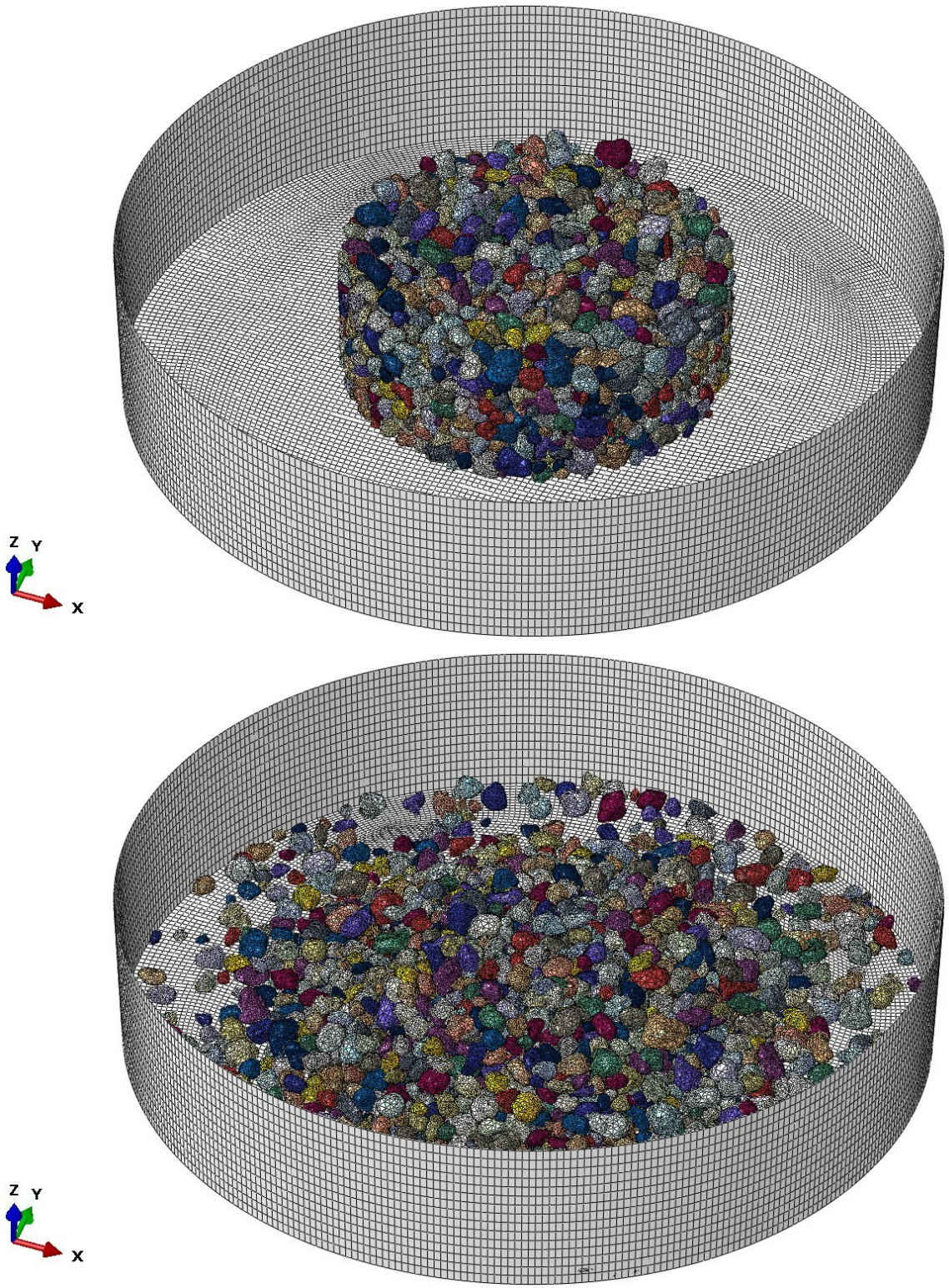
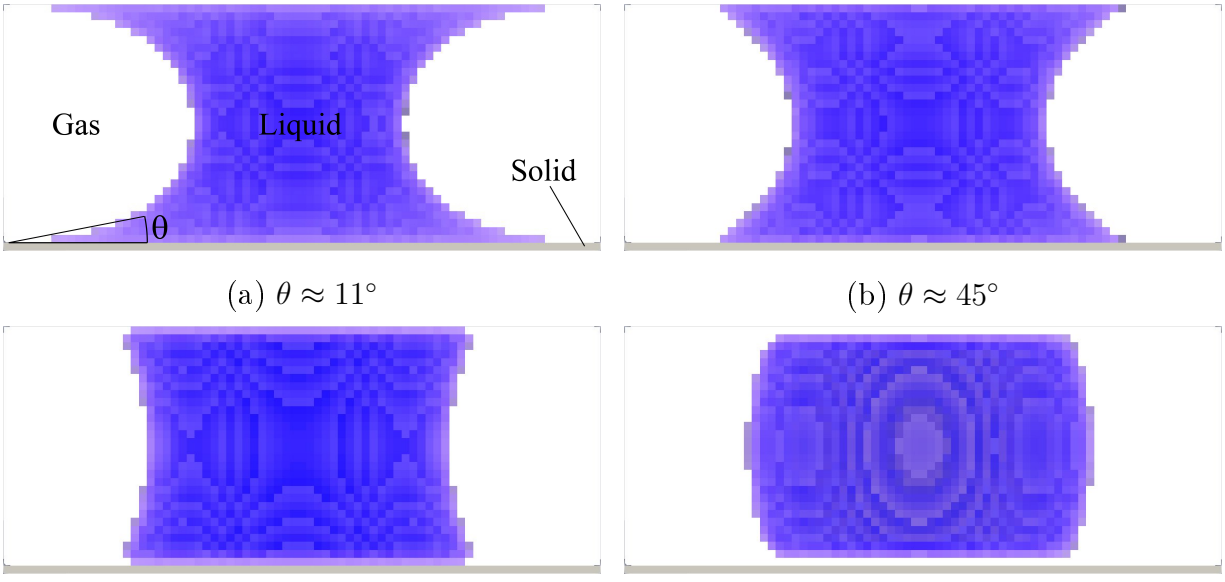


Figure 8.5: Simulation of a dry granular column collapse in a rigid cylindrical container with 1999 CT scanned rigid Hamburg Sand particles involved: Initial grain column (top) and heap of collapsed grains after a simulated time of 0.35 s (bottom)

8.4.1 Capillary bridges and contact angles

In the applied multiphase LBM formulation, the equilibrium contact angle between solid and liquid phase can be modelled with the help of the wall density ρ_{wall}. Based on the results of preliminary simulations which include the numerical study of the formation of a liquid bridge between two solid plates as shown in Figure 8.6, a wall density $\rho_{\text{wall}} = 0.35084$ mu/lu^3 has been selected to model nearly full hydrophilic behaviour of the solid surfaces, *i. e.*, a high wettability. The 3D models in the study with a domain size of $l_x \times l_y \times l_z = 75 \times 75 \times 31 = 174{,}375$ computation cells are initialised with a random field of fluid density representing a mixture of gas and vapour. A subdomain in the shape of a sphere with a radius of 15 lu is placed at a height of 16 lu above the middle of the lower plate. This subdomain is initialised with the coexisting density of the liquid. Based on this initial state, the density distribution inside the computation domain is subjected to phase separation to form an equilibrium liquid bridge adhering to both plates over time. Periodic boundaries are applied in the simulations. The results in Figure 8.6 showing the segmented equilibrium liquid phase distributions indicate that nearly complete hydrophilic behaviour at high values of ρ_{wall} and hydrophobic behaviour at low values of ρ_{wall} with convex shaped liquid bridges can be modelled.



(a) $\theta \approx 11°$ (b) $\theta \approx 45°$

(c) $\theta \approx 72°$ (d) $\theta \approx 135°$

Figure 8.6: Vertical cross sectional visualisation of the liquid phase density domains with $\rho > 0.2726$ mu/lu^3 in a study on equilibrium contact angles θ developing between two plates in 3D multiphase LBM simulations at different wall densities ρ_{wall}: (a) $\rho_{\text{wall}} = 0.35084$ mu/lu^3, (b) $\rho_{\text{wall}} = 0.26850$ mu/lu^3, (c) $\rho_{\text{wall}} = 0.17900$ mu/lu^3, (d) $\rho_{\text{wall}} = 0.08950$ mu/lu^3. Note that every pixel represents a computation cell

The further model parameters used in all LBM simulations presented here are summarised in Table 8.2 and explained in Appendix C.

Table 8.2: Model parameters used in the multiphase LBM simulations

ρ_{wall} [mu/lu^3]	$\tau/\Delta t$ [-]	T/T_{c} [-]	$\rho_{\text{boundary, g}}$ [mu/lu^3]	$\rho_{\text{boundary, l}}$ [mu/lu^3]
0.35084	1.0	0.7	0.0484	0.2726

ρ_{wall}: Wall density
τ: Relaxation time
T/T_{c}: Temperature ratio (EOS)
$\rho_{\text{boundary, g}}$ and $\rho_{\text{boundary, l}}$: Boundary densities of gas and liquid

8.4.2 Water retention behaviour

The lattice models for the simulation of water retention behaviour are directly derived from CT data of a cubic subvolume inside a 3D data set of Hamburg Sand and glass beads as illustrated in Section 8.2. The discrete Lattice Boltzmann equation is solved over time on a $200\times200\times200$ lattice, *i. e.*, for 8 million computation cells, following the experimental pattern of change of liquid degree of saturation which is idealised numerically by transient density injection.

Starting from an initial perturbation with randomised density distribution, phase separation is modelled until an equilibrium state with stable phase distribution is reached. This is generally the case after 5000 ts. Afterwards, the density is transiently changed by increasing or decreasing the fluid density in liquid cells only until fixed bounds of liquid degree of saturation as derived from the experiments are reached. The fluid density is changed by injecting or subtracting a density increment of ±0.005 mu/lu^3 every 1000 ts leading to imbibition or drainage of pore computation cells, respectively. The flow direction is changed when a prescribed bound is hit by the current degree of liquid saturation. Starting with an initial imbibition phase up to $S_{\text{r}} = 0.98$ after phase separation, the degree of saturation is then cycled between the bounds $S_{\text{r}} = [0.3, 0.857, 0.393, 0.764, 0.486, 0.671, 0.579]$ which are based on the experimental data from Chapter 5.

Similar to the physical reality of the experiments, macroscopic, *i. e.*, averaged, values of liquid degree of saturation S_{r} and capillary pressure p_{c} are computed as follows.

$$S_{\text{r}} = \frac{N_{\text{cells, l}}}{N_{\text{cells, f}}} \quad , \tag{8.1}$$

where $N_{\text{cells, l}}$ represents the number of computation cells (or nodes) with a density corresponding to the liquid phase and where $N_{\text{cells, f}}$ is the number of computation cells representing the pore space occupied by the fluid phase.

$$p_{\text{c}} = \bar{p}(N_{\text{cells, g}}) - \bar{p}(N_{\text{cells, l}}) \quad , \tag{8.2}$$

with $\bar{p}$ indicating the mean gas or liquid pressure and $N_{\text{cells, g}}$ representing the number of computation cells which are filled by gas.

In the simulations of the water retention behaviour, the macroscopic state variables p, p_{c}, and S_{r} as well as the number of gas and liquid cells are calculated and stored in a results

file every time step, while the density, pressure, and velocity fields in all computation cells are written every 5000 ts only in order to reduce the amount of output data to be stored.

In the following, we discuss two simulations using the 200×200×200 lattice models based on CT scanned Hamburg Sand and glass beads as presented in Figure 8.2. The simulations on these models with 8 million computation cells are run on the High-Performance Computing (HPC)-Cluster Bombus at Hamburg University of Technology using thread-based parallelisation with OpenMP (Open Multi-Processing) with 28 threads. The simulations were performed on computation nodes g164 and g191, each equipped with 2×14 cores, two E5-2680v4 CPUs, and a RAM of 128 GB. Despite the parallelisation, runtimes of *ca.* 276 h and 272.2 h are required for the simulations on the Hamburg Sand and glass bead model, respectively.

The calculated results of S_r and p_c *vs.* time steps are shown in Figure 8.7 for Hamburg Sand and in Figure 8.8 for the glass beads. In both figures, every hydraulic step with changed flow direction is plotted in a different colour. After initial phase separation for 5000 ts and a primary imbibition step up to $S_r \approx 0.98$, cyclic drainage and imbibition paths are followed according to the hydraulic experiment presented in Chapter 5.

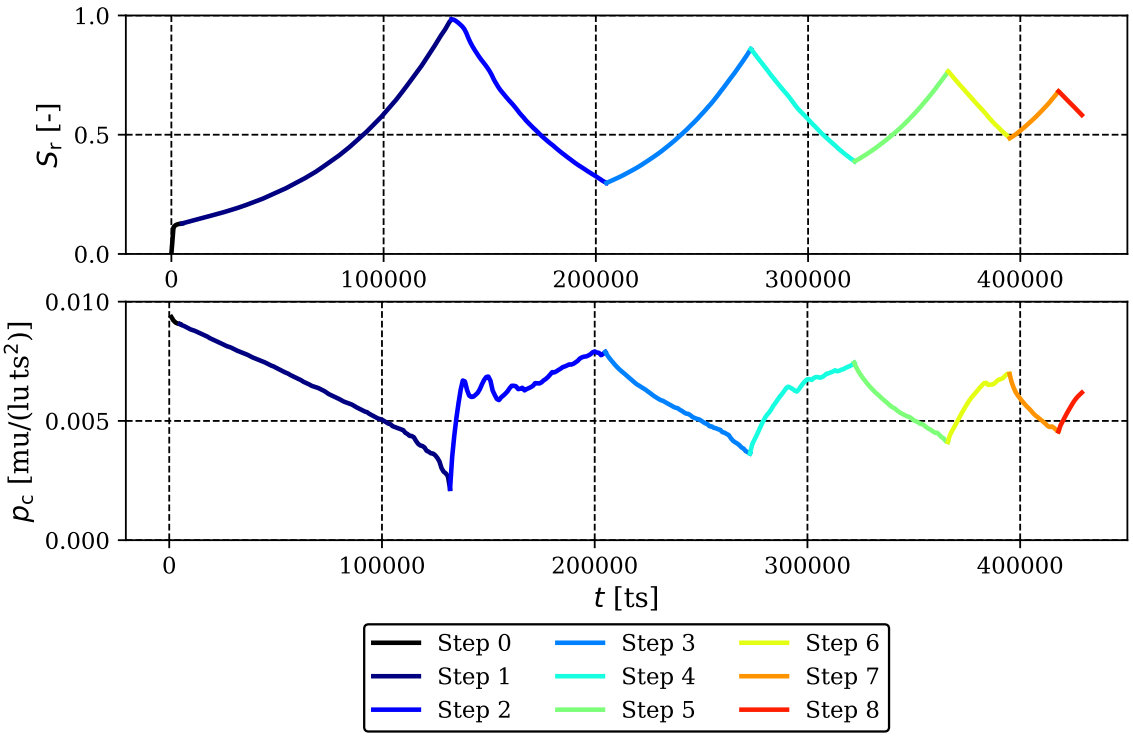


Figure 8.7: Calculated degree of saturation S_r (top) and capillary pressure p_c (bottom) *vs.* time steps from a multiphase LBM simulation on a 3D lattice model derived from CT scanned Hamburg Sand with 200×200×200 computation cells

Very similar to the experiments, oscillations of capillary pressure occur after air entry on the primary drainage path, while rather smooth curves of capillary pressure are obtained

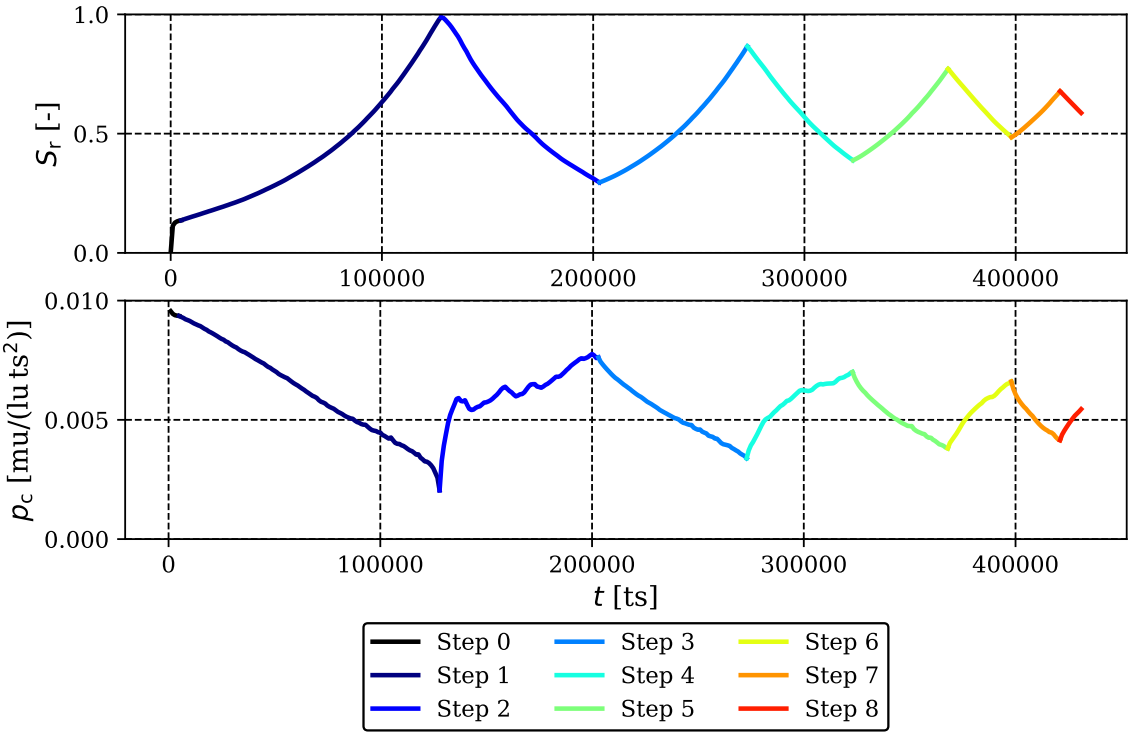


Figure 8.8: Calculated degree of saturation S_r (top) and capillary pressure p_c (bottom) *vs.* time steps from a multiphase LBM simulation on a 3D lattice model derived from CT scanned glass beads with 200×200×200 computation cells

on imbibition paths. In the case of Hamburg Sand, slightly higher capillary pressures as compared to the glass beads can be noticed which is probably due to the slightly lower void ratio in the sand model. As already shown by Hosseini *et al.* (2021), the multiphase LBM captures the void ratio dependence of the WRC with higher capillary pressures obtained for lower void ratios at constant discretisations. As the change in degree of saturation is modelled by means of a simple density injection into liquid cells whose number varies over time, the simulations show a non-linear change of degree of saturation. In the figures presented here, only equilibrium data are plotted, *i. e.*, the results are shown for every 1000 ts at the end of an injection step where S_r and p_c have been relaxed over the previous 1000 ts approaching a steady state in most cases.

When the temporal results of degree of saturation and capillary pressure are combined, the simulated WRCs are obtained similarly to the measured WRC presented in Section 5.3.4. As shown in Figure 8.9, the hysteresis effect with closed elliptical hydraulic loops is reproduced by the multiphase LBM. The WRCs of the "digital" Hamburg Sand and glass beads look similar. However, a higher capillary pressure is reached at the air entry value upon primary drainage and more pronounced oscillations of capillary pressure occur in the simulation of Hamburg Sand.

Similar to the CT experiments, the simulation results allow to link the macroscopic water retention behaviour to hydraulic events on the pore level. In agreement with the theoretical

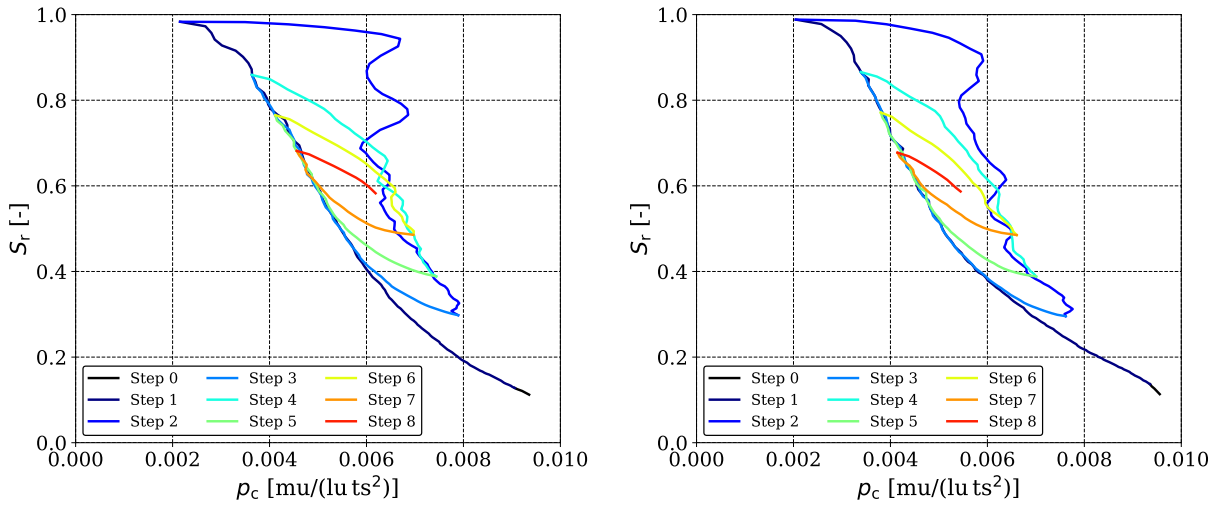


Figure 8.9: Calculated WRCs of Hamburg Sand (left) and glass beads (right) from multiphase LBM simulations on 3D lattice models derived from CT scans with 200×200×200 computation cells

capillary domains, the evolution of the phases during primary imbibition in Figure 8.10 and Figure 8.11 shows the growth of liquid clusters which move into initially gas-filled pores, apparently filling the smaller pores first, while the gas-phase is expelled and its initial interconnected ganglia are changed into occluded bubbles at high degrees of liquid saturation. This behaviour is observed both in the sand and in the glass bead model. If different hydraulic states are compared for nearly the same degrees of liquid saturation as shown in Figure 8.12 and Figure 8.13 (the 3D output is written for fixed time steps, not for fixed saturation levels), slight differences in the volumetric liquid and gas distributions can be noticed between the imbibition and drainage paths. These differences in the simulated phase distributions might correspond to the hysteresis of capillary pressures on imbibition and drainage paths which is also captured by the multiphase LBM.

A full quantitative comparison of experimental and numerical results is not directly possible due to the incomplete similarity between the physical experiment and the LBM simulation which will be discussed in Section 8.4.3. Furthermore, the LBM simulation is run on a subdomain of the CT scanned specimen volume for which the experimental WRC was measured. Although the simulated degree of saturation levels correspond to the experiment, the suction or capillary pressure in LBM units cannot be compared directly to the physical suction. However, a scaling approach might be followed to compare dimensionless capillary pressures from experiments and simulations or to transform the capillary pressure from LBM into a physical capillary pressure as presented in Pan *et al.* (2004) and Schaap *et al.* (2007). This scaling should be investigated in further numerical studies, including the effect of discretisation on the obtained numerical results.

In further studies, the evaluation tools developed in the analysis of the CT data in the previous chapters should also be applied to the artificial LBM data, *e. g.*, to extract and analyse further capillary state variables, such as the interfacial areas or the cluster count.

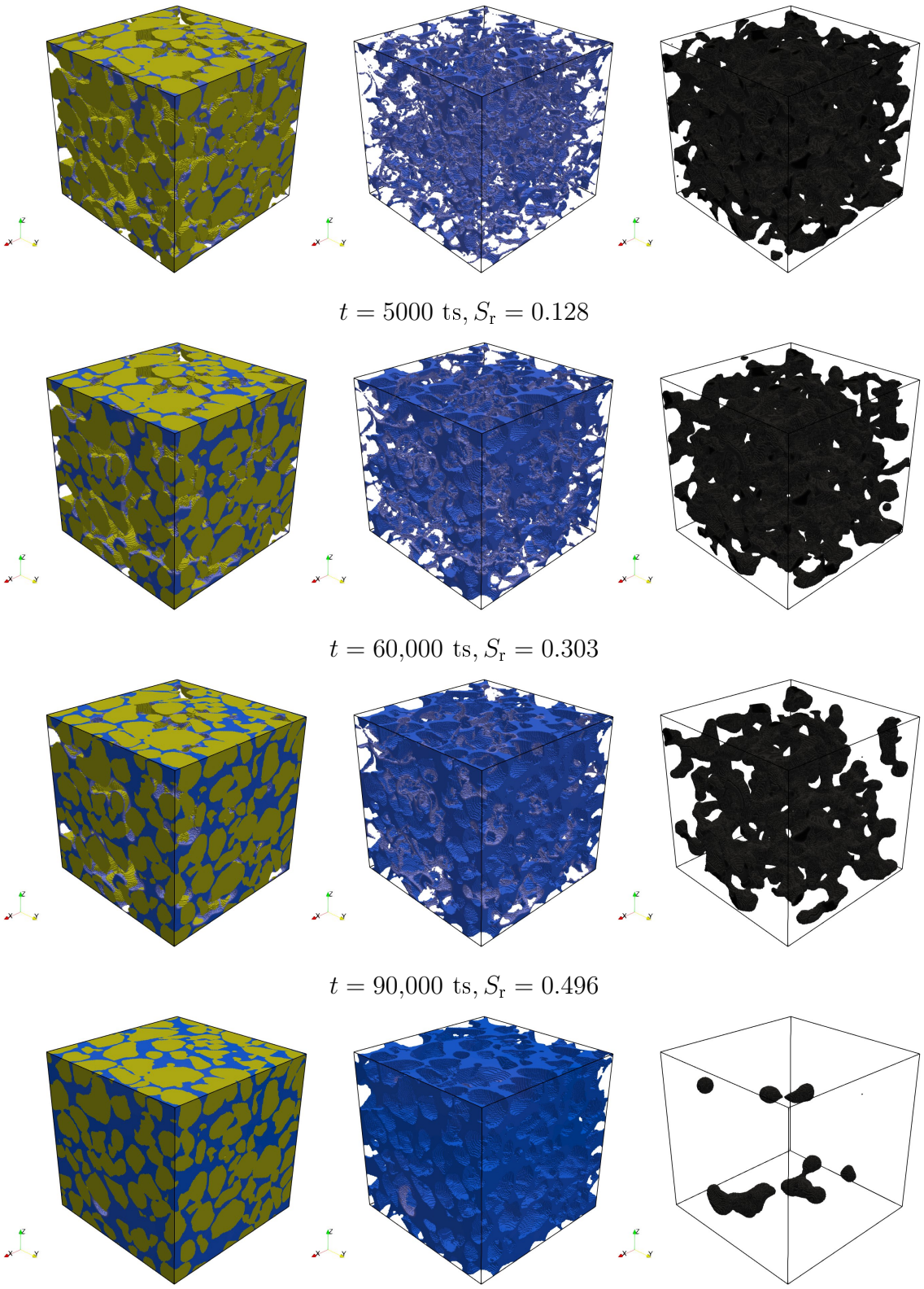


Figure 8.10: Phase distributions from LBM simulations on a 3D lattice model of Hamburg Sand during primary imbibition. Left: sand and liquid, middle: liquid, right: gas

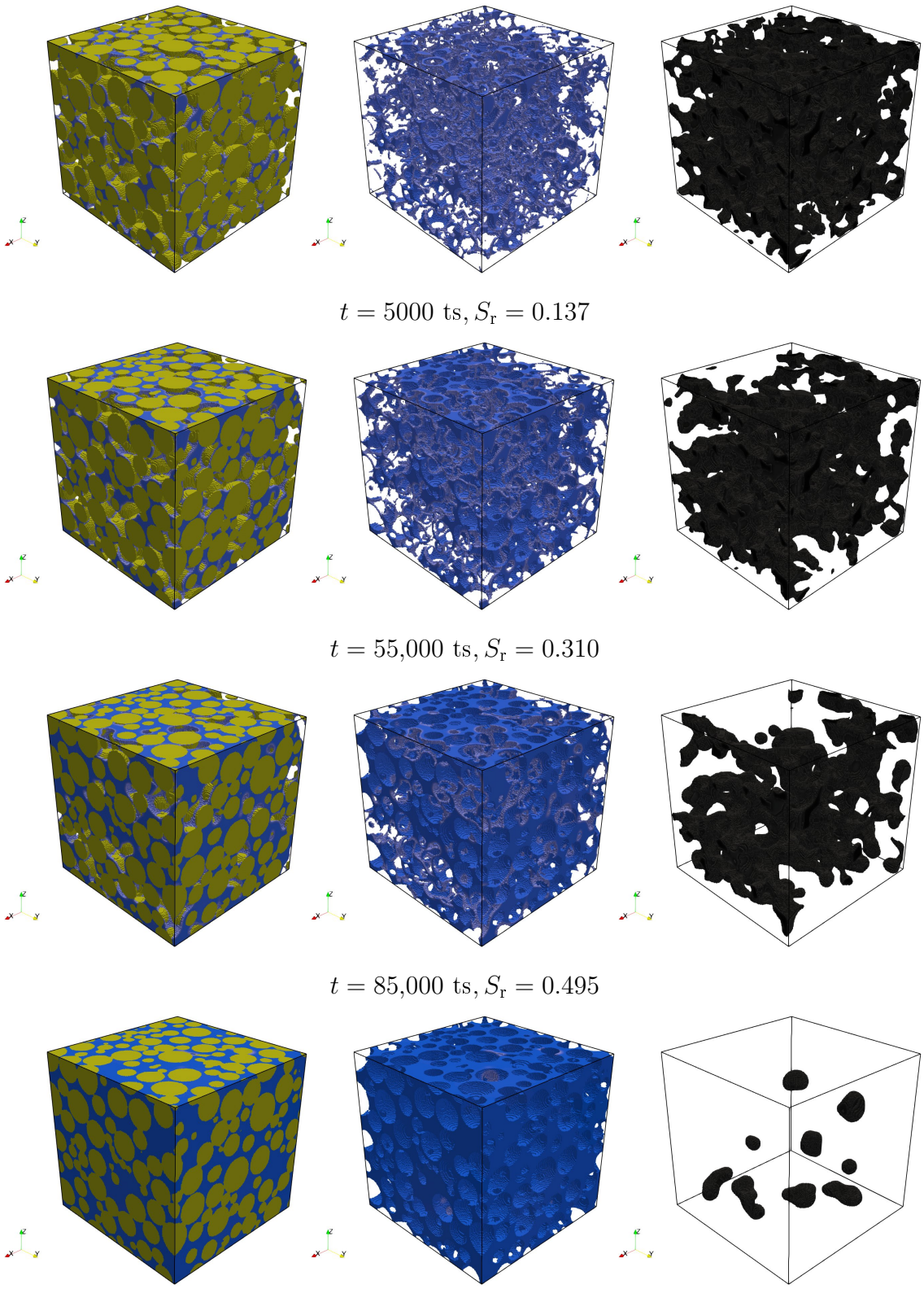


Figure 8.11: Phase distributions from LBM simulations on a 3D lattice model of glass beads during primary imbibition. Left: glass beads and liquid, middle: liquid, right: gas

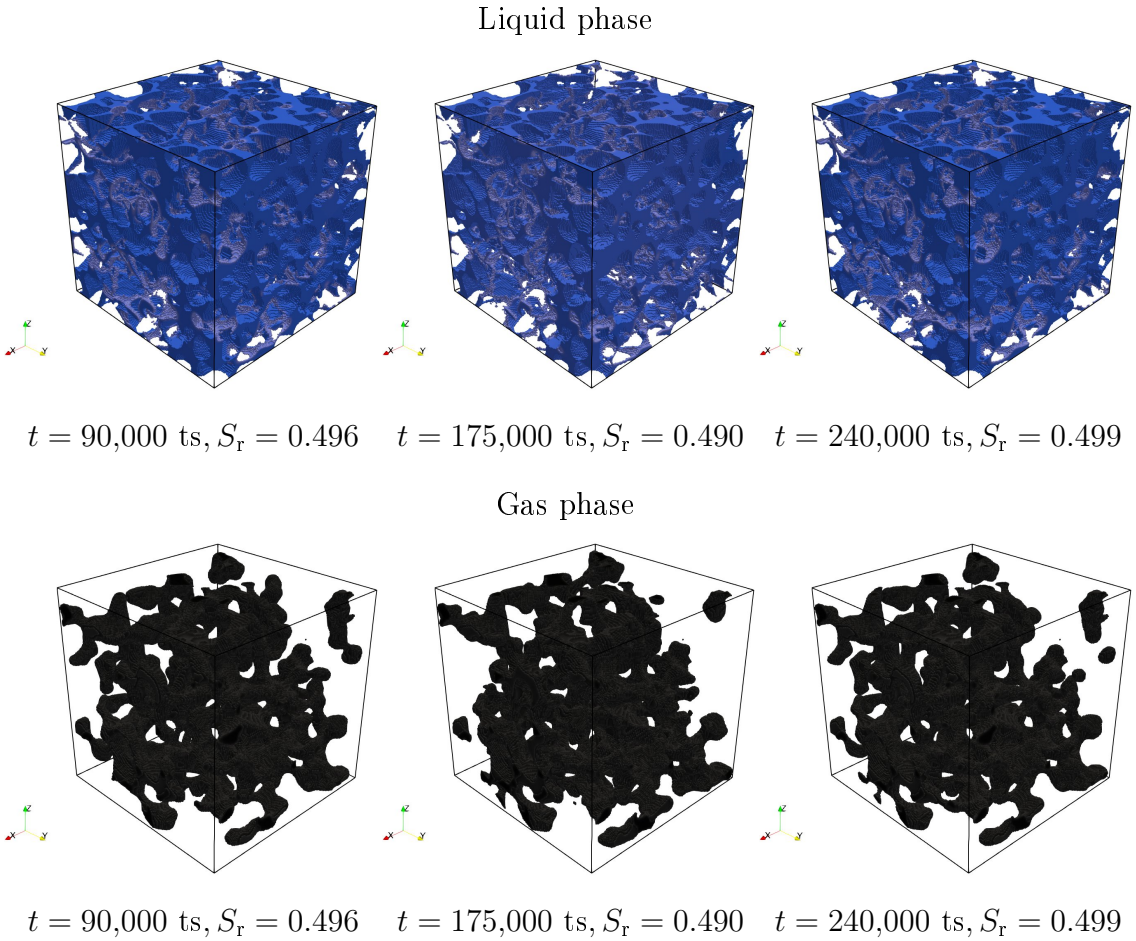


Figure 8.12: Liquid and gas phase distributions from LBM simulations on a 3D lattice model of Hamburg Sand on different hydraulic paths at nearly the same liquid saturation. Left: primary imbibition, middle: main drainage, right: main imbibition

8.4.3 Comments on similarity between LBM model and physical "reality"

The dimensionless quantities Bo and Ca as described in Section 2.3.2 are usually considered to achieve similarity between the physical "reality" and the LBM simulation. Furthermore, the dynamic viscosity ratio of both fluids is considered (Huang *et al.*, 2015). Analogy between the physical reality and the LBM model is achieved by equating the dimensionless quantities and accordingly setting the LBM parameters. Due to restrictions given by the selected multiphase LBM model, this is however not always a simple task, as further outlined by Huang *et al.* (2015) and Krüger *et al.* (2017).

Here, it is tried to characterise the microscopic flow conditions in the reported water retention test on Hamburg Sand by Bond number Bo and capillary number Ca. In addition, the flow conditions in the presented LBM simulation will be studied, compared and discussed. The material properties in the experiment and in the LBM simulations are juxtaposed in

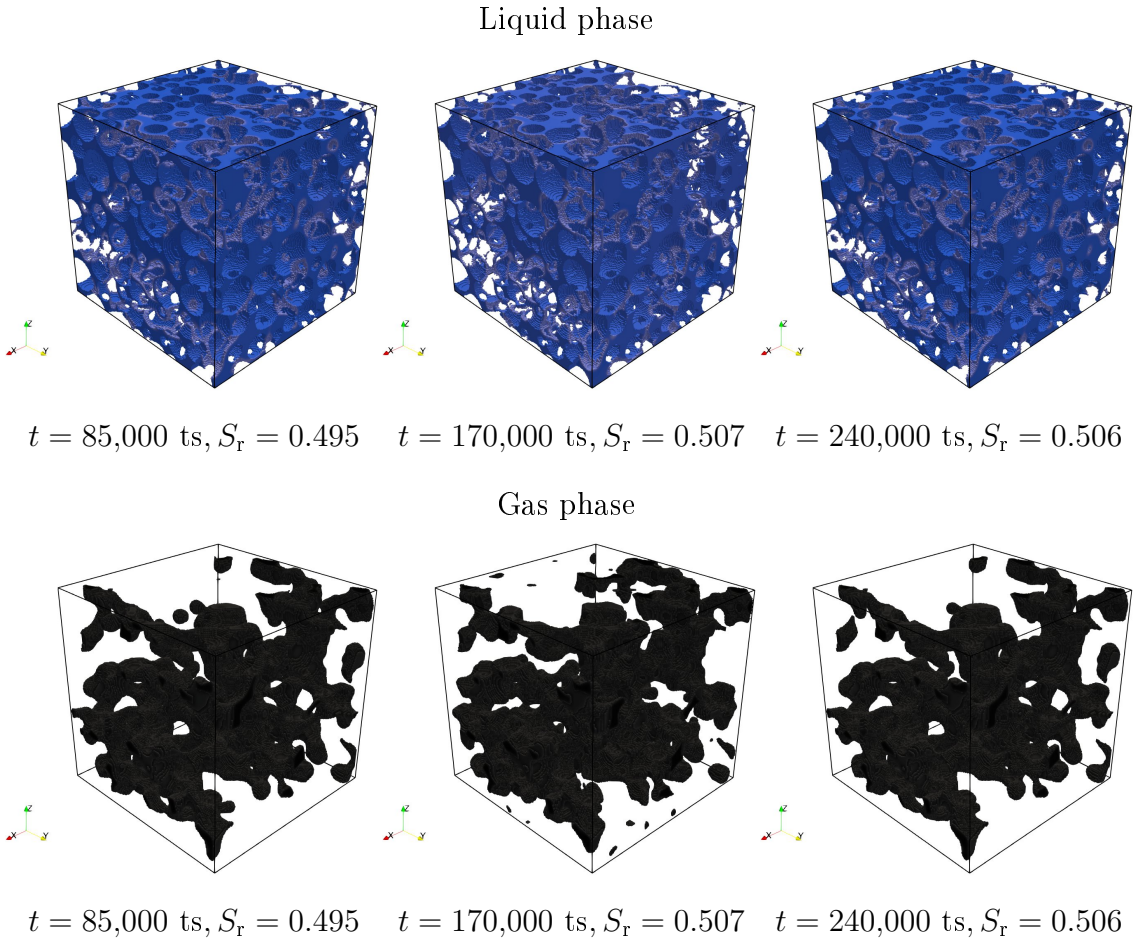


Figure 8.13: Liquid and gas phase distributions from LBM simulations on a 3D lattice model of glass beads on different hydraulic paths at nearly the same liquid saturation. Left: primary imbibition, middle: main drainage, right: main imbibition

Table 8.3. The physical fluid properties are collected from literature for a temperature of 20 °C or are calculated from CT data of the water retention experiment on Hamburg Sand. The material properties in the LBM model are derived from the simulation model in agreement to the selected multiphase formulation. All material properties with relevance to the calculation of Bo and Ca will be explained in the following.

The physical mean pore radius needed to determine the Bond number Bo is derived from the mean pore volume obtained from the pore-based analysis of CT data as presented in Section 6.3.5. For the mean pore volume of 0.0011 mm^3, a mean pore radius $R_p = 0.064$ mm is calculated assuming a spherical pore shape.

The phase densities in the LBM simulations correspond to the coexisting wetting and nonwetting phase densities according to the Carnahan-Starling EOS at the selected $T/T_c = 0.7$. Note that the density ratio is much different as compared to the physical reality. The dynamic viscosities of the two fluids are calculated as

$$\eta_i = \rho_i \, c_s^2 \, (\tau_i - 0.5 \, \Delta t) \quad , \tag{8.3}$$

Table 8.3: Physical and model parameters in the water retention test and LBM simulations

Parameter	Experiment	LBM model
Wetting phase density ρ_w	1000.0 kg/m^3	0.358 mu/lu^3
Nonwetting phase density ρ_n	1.2041 kg/m^3	0.009 mu/lu^3
Wetting phase dyn. viscosity η_w	$1.0016{\cdot}10^{-3}$ Ns/m^2	0.0597 mu/(lu ts)
Nonwetting phase dyn. viscosity η_n	$1.8210{\cdot}10^{-5}$ Ns/m^2	0.0015 mu/(lu ts)
Surface tension γ_w	0.07275 N/m	*ca.* $13.5{\cdot}10^{-3}$ mu/ts^2
Gravitational acceleration g	9.81 m/s^2	-
Mean pore radius R_p	0.064 mm	3.2 lu

with i = w indicating the wetting fluid, i = n indicating the nonwetting fluid, and the relaxation time $\tau_w = \tau_n = \tau = 1.0\ \Delta t$. The time step $\Delta t = 1.0$ ts is constant. The speed of sound c_s is defined in Appendix C.

The surface tension in the LBM simulations is picked as the numerical value from comparative 2D simulations of a droplet, presented in Huang *et al.* (2015, p. 52).

Using the parameters collected in Table 8.3, the physical flow conditions can be characterised. The physical Bond number is calculated as $Bo = 0.000552$ according to Equation 2.11 with the characteristic length $L = R_p$. Generally, $Bo << 1$ indicates that the surface tension dominates the flow, while the effect of gravity can be neglected. In the case of the LBM simulations, no gravity is considered. Therefore, the capillary effects caused by surface tension also stand out against gravity in the LBM simulations.

In order to calculate the physical capillary number, a characteristic pore scale flow velocity, such as the average velocity of the gas-liquid interface, is required. Here, we assume a local flow velocity of the gas-liquid interface calculated based on the injected constant flow rate of $Q = 0.0597$ mm^3/s and the specimen cross sectional area A corresponding to a diameter of $d = 12$ mm. The actual pore-based flow velocity v, to be plugged into Equation 2.12 for the calculation of Ca, is finally calculated from the filter velocity v_f from Darcy's law divided by the mean porosity of $n = 0.375$ from CT data according to

$$v = \frac{v_f}{n} = \frac{Q}{A\,n}, \text{ with } A = \frac{\pi\, d^2}{4} \quad . \tag{8.4}$$

Following this approach, a physical capillary number of $Ca = 1.938 \cdot 10^{-8}$ is calculated. As it is much lower than 10^{-5}, the capillary effects due to surface tension are stronger than the viscous effects. To sum up, based on both Bo and Ca, the physical flow is dominated by capillarity in the considered experiment on Hamburg Sand.

The capillary number in the LBM simulation will be estimated based on local pore scale flow by assuming the movement of liquid in a local saturated pore with mean pore radius $R_p = 3.2$ lu considering a voxel size of 10 μm and the applied binning. Density injection is applied to apply flow in all liquid cells which vary during drainage and imbibition. Therefore, the simulated macroscopic flow rate is not constant as compared to the experiment.

To determine the required pore-based flow velocity, the local numerical mass flow rate is firstly calculated as $Q_\mathrm{m} = 0.005$ mu/1000 ts according to the applied density injection. In the next step, the volume flow rate Q in a pore is calculated by dividing Q_m by ρ_w. The pore scale flow velocity v required for Ca is finally computed by dividing Q by the cross sectional area $A = \pi\, R_\mathrm{p}^2$ of a single pore in lattice units. The calculation of the capillary number from all parameters in lattice units results in $Ca = 1.917 \cdot 10^{-6}$ which is *ca.* a hundred times larger than the capillary number in the experiment, but which also reflects a dominance of capillary effects over viscous effects similar to the physical reality.

A possible way to exactly fit the capillary number in the LBM model to reality would be to change the flow conditions, *e. g.*, by implementation of true flow boundary conditions to mimic a liquid in- and outflow from the bottom with constant flow rate as applied in the experiments. Furthermore, the numerical surface tension could be adjusted which is, however, not possible without limitations in the selected LBM formulation where the surface tension depends on the relaxation time τ as outlined in closer detail by Huang *et al.* (2015).

Chapter 9

Summary and outlook

9.1 Summary of results

9.1.1 *In situ* imaging experiments

The combination of the currently available plethora of imaging techniques with custom-built experiments to be run *in situ* opens the door to study different multiphysical processes on different length scales. Although the design and construction of specialised experimental set-ups requires time and frequently needs further adaptation to special needs of imaging environments, very individual experiments as outlined in Chapters 4 and 5 can be realised in order to observe various processes and to record quantitative data in four dimensions.

Within the scope of this work, very different experimental set-ups as summarised in Table 9.1 have been presented which can be applied to study the hydro-mechanical behaviour of soils either under lab conditions or *in situ* in a CT imaging environment for applications in research but also in university teaching. Besides the originally intended functions, also extended applications are described in Table 9.1.

Table 9.1: Applications of miniaturised set-ups for *in situ* imaging experiments

Set-up	Main and extended applications
Uniaxial compression apparatus	Compression of unsaturated granular specimens, adhesion testing
Flow cell apparatus	Measurement of the transient WRC, investigation of air entrapment, suffusion and related flow phenomena
Direct shear apparatus	Direct shear tests on unsaturated granular material, interface shear tests
Particle separation test	Monotonic and cyclic straining of capillary bridges

As shown in Chapter 7, the existing set-ups can easily be enhanced or adapted to other research questions which shows the versatility of the followed approach of *in situ* imaging experiments.

9.1.2 Hydraulic and mechanical behaviour of unsaturated soils

The experimental data from the different imaging experiments, such as the uniaxial compression and water retention tests, have led to a variety of insights into the hydro-mechanical behaviour of unsaturated granular soils. The findings allow to answer some of the guiding research questions from Chapter 5 which will be summarised with focus on the water retention behaviour and hydro-mechanical coupling in this section.

Hydraulic water retention behaviour

Focusing on the water retention behaviour which is key to the hydraulic and mechanical behaviour of unsaturated soils, the guiding research questions can be answered as follows.

Microscopic origin of hydraulic hysteresis The rich 4D data from the water retention experiments with emphasis on the cyclic hydraulic behaviour and resulting hysteresis reveal different pore scale phenomena that can lead to hysteresis: Firstly, different phase distributions and morphologies are encountered on different hydraulic paths with initially present air bubbles and discrete air fingers occurring during primary drainage as shown in Section 6.3.1. Further cycling of the degree of saturation yields a shift to more complex shaped air ganglia and a further reduction of spherical air bubbles which can be derived from the fluid cluster analysis in Section 6.3.2. As a further reason for hydraulic hysteresis, the measured contact angles confirm the presence of contact angle hysteresis in the investigated sand as discussed in Section 6.3.4. A pore-based study of emptying events presented in Section 6.3.5 reveals clear evidence for a drainage sequence with larger pores being emptied prior to smaller ones during primary drainage due to different corresponding capillary pressures. To sum up, the hysteresis phenomenon is obviously induced by different phase distributions on drainage and imbibition paths, by the pore size distribution, and by local flow and wetting phenomena on the pore scale.

Phase distributions and fluid structures during cyclic drainage and imbibition On different cyclic hydraulic paths, water and air clusters evolve in opposite directions with the cluster counts being hysteretic both *vs.* degree of saturation and matric suction as shown in Sections 6.3.1 and 6.3.2. This means that varying cluster size distributions must also be present on different hydraulic paths for the same degree of saturation. Based on image data, the capillary regimes as well as different flow events can be quantified. During air entry on a primary drainage path, a concentrated relatively local propagation of air fingers is observed entering through larger connected pores. Consecutive cyclic drainage and imbibition changes this rather local effect to a more homogeneous distribution of water and air clusters with the air cluster shape analysis revealing a transition to the presence of

more and more air ganglia with complex 3D geometry, whereas the initially present small air bubbles vanish.

Evolution of microscopic *capillary state variables* as potential ingredients of effective stress on different hydraulic paths Based on unsaturated granular media studied on the microscale, a framework of the proposed *capillary state variables* can be established that allows a hierarchical and multidimensional quantitative description of capillary action. This description includes fluid clusters (volumes), interfacial areas and the contact line (surfaces and lines) as well as contact angles, radii of curvature, and resulting mean curvature which represent the wetting properties at the solid-liquid interface and reflect capillary pressure, respectively. An overview of the named capillary state variables, their geometric dimension, and physical meaning is given in Table 9.2. Besides these state variables, also their (statistical) distribution might be of importance which is so far only measured in the case of the discrete clusters as well as contact angles and radii of curvature. The concept of capillary state variables combines continuum measures, such as the degree of saturation linked to the distribution of liquid volumes, the specific interfacial areas, and specific length of contact line (both given per unit volume), with discrete measures, such as individual clusters with their size and shape and the contact angles and radii of curvature. Regarding the continuum measures, also distributions could be analysed by defining and quantifying them inside representative elementary volumes inside a larger specimen volume. However, this generally requires highly resolved data for large specimens.

Table 9.2: Hierarchical capillary state variables and their physical meaning

Capillary state variable	Geometry type	Physical meaning
Fluid clusters	Volume	Phase distribution, related to degree of saturation, hydraulic connectivity and conductivity, and soil moist density
Air-water interfacial area	Surface area	Surface area of menisci, transfer of surface tension, interfacial energy, surfactant transport
Solid-water interfacial area	Surface area	Contact surface of water and solid, transfer of capillary pressure to solid phase
Contact line	Line length	Common line of air, water, and solid, transfer of surface tension to solid phase
Contact angle	Angle	Wetting phase angle at the contact line, reflecting wetting properties
Radii of curvature	Radius (length)	Radii describing the curvature of air-water interface, governed by capillary pressure

During hydraulic drainage and imbibition cycles, the fluid clusters, interfacial areas, and length of contact line show hysteresis, especially, when plotted *vs.* matric suction. All

named capillary state variables seem to yield characteristic relationships, when shown *vs.* degree of saturation or matric suction in Section 6.3.3. Further research on different granular materials might proof their dependence on basic granulometric properties and other soil state variables, such as pore size and grain size distribution or void ratio.

While the radii of curvature can be applied to calculate capillary pressure based on the Young-Laplace law with the calculated mean capillary pressure reflecting the matric suction measured on the macroscopic level with good agreement as outlined in Section 6.3.4, the specific interfacial areas and specific length of contact line represent state variables with direct relationship to the mechanical action of capillarity leading to its contribution to suction stress or effective stress. While the solid-water interfacial area acts as the reference surface for the transfer of capillary pressure from the liquid to the solid phase, the air-water interfacial area represents the surfaces of capillary menisci which are spanned by surface tension. Finally, the contribution of surface tension to effective stress is transferred along the interfacial contact line to the solid phase. These micro-mechanical considerations lead to the idea that the interfacial capillary state variables could be applied as ingredients of suction stress or effective stress in unsaturated soils as outlined and discussed in section 6.4. Due to their hysteresis, also suction stress should theoretically be hysteretic for different hydraulic histories of the same soil specimen.

Hydro-mechanical behaviour

The previously summarised findings regarding water retention are relevant to the hydro-mechanical behaviour which has been studied in the uniaxial compression tests and also in the particle separation tests for individual capillary bridges on the grain scale. Based on the principal results, the guiding questions with regard to the hydro-mechanical behaviour can be answered and summarised in the following.

Influence of capillarity on macroscopic effective stress In addition to the theoretical considerations from the water retention experiments, especially the uniaxial compression experiments reveal strong quantitative evidence for the impact of capillarity on effective stress. Under lab conditions, an increasing capillary cohesion and resulting shear strength for higher degrees of saturation can be shown for the tested granular materials as presented in Section 4.2.4. As the capillary cohesion must vanish for the dry and fully saturated case, a maximum shear strength exists for some elevated degree of saturation which has been impressively elaborated by further uniaxial compression tests on various granular media within the scope of DFG funded project "Microscale investigations of the hydro-mechanical behaviour of unsaturated granular soils with computed tomography"[1]. The related findings will be published elsewhere. Based on the pore-based strain analysis in Section 6.1.3 run on the 3D image data during uniaxial compression of sand and glass beads, it is discovered that pores with higher degree of saturation show reduced volumetric and shear strain which indirectly underlines the impact of matric suction on local effective stress.

[1] https://gepris.dfg.de/gepris/projekt/401096010?language=en

Relationship between the microscopic capillary system, described by air-water distribution and degree of saturation, and measured shear strength and volumetric response on a macroscopic level Based on the uniaxial compression tests under lab conditions as well as in *in situ* CT experiments, a robust dependence of dilative behaviour on the degree of saturation can be established. Both on the macroscopic and microscopic, *i. e.*, pore-based, level, the tendency to dilation is more pronounced for lower degrees of saturation in Hamburg Sand and in glass beads as presented in Sections 5.2.3 and 6.1.3. This highlights the obviously higher effective stress and accordingly higher shear strength at elevated degrees of saturation when capillary pressure can be transferred to grain surfaces in rather saturated pores as compared to drier pores which are strained more. This influence of pore saturation on volumetric and deviatoric strain could also be shown in the pore-based strain analysis based on the image data acquired during the water retention experiment as discussed above.

Evolution of grain scale quantities, such as number and size of water clusters, location of capillary bridges, and interfacial areas, during macroscopic shearing Due to the high spatial resolution of the acquired image data during uniaxial compression, different kinds of water clusters, so-called "liquid morphologies" as coined by Scheel *et al.* (2008), can be identified and measured by volume. The different volumes account for very large water volumes, medium-sized to small clusters and individual capillary bridges as illustrated in Section 6.1.1. Water clusters link grains and obviously influence the shear behaviour. Vice versa, also the clusters themselves are changed as they are strained due to the translation of grain assemblies upon shearing and the occurrence of shear planes.

If the straining experiments on individual capillary bridges as presented in section 6.2 are considered, the capillary forces are reduced until rupture at a finite rupture length that essentially depends on the involved water volume. This also highlights the impact of local pore-based degree of saturation, *i. e.*, the water contained in the form of clusters in pores, on the stress-strain behaviour on the pore scale as quantitatively measured in the uniaxial compression and water retention tests. In both investigated granular materials, Hamburg Sand and glass beads, the number of water clusters is increasing during shearing as discussed in Section 6.1.1. Based on cluster size distributions, larger clusters seem to disintegrate into smaller water clusters. However, it must be noted that this effect might partially be due to evaporation, acting simultaneously on the unsaturated soil specimens.

The capillary state variables mentioned above are influenced by the shearing process. For example, the interfacial areas are found to change which is due to the reduction of degree of saturation and the microscopic reordering of water clusters in a dilating grain skeleton as shown in Section 6.1.2. The mechanical effect of capillary cohesion also seems to be reflected by the coordination number as interpreted in Section 6.1.4. The presented analysis and interpretation of results indicate a dominance of grains with low coordination number, especially in the sand, after shearing. In this post-shear state, characterised by dilation, large stable pores leading to a low coordination number can still exist as the neighbouring grains are held in position by capillary forces. To sum up, these findings highlight the hydro-mechanically coupled effects occurring on the pore or grain scale during shearing with capillary state variables influencing the shear process and, vice versa, local

shear zones also changing the microscopic capillary state.

9.2 Outlook, open questions, and work ahead

The insights from the experiments help to answer some of the guiding research questions, but also open new ones.

The experimental findings reveal that "soil-water-air-interfacial property characteristic curves" can be measured. The question is, if these relationships can really be labelled as "characteristic", such as the soil-water characteristic curve. The relationship of the specific interfacial areas and specific length of contact line to degree of saturation and matric suction might depend on other flow and surface properties as well as microscopic effects, *e. g.*, flow rate, surface wettability, and air entrapment, which should be addressed in further experimental studies. Those experiments should also investigate how the capillary state variables discussed before depend on granulometric properties, such as grain shape (and its distribution), as well as grain size distribution and void ratio. This being said, further hydraulic and mechanical *in situ* CT experiments are needed to gather more detailed data and to validate effective stress formulations based on interfacial and other microscopic properties, such as radii of curvature, from which matric suction can be derived. Due to the advancing imaging techniques, certainly even better image data leading to more detailled insights will be available in the future.

The suction stress principle under consideration of a hysteretic WRC as well as the measured interfacial properties indicate that the effective stress in unsaturated soils is also hysteretic which essentially means a higher shear strength of soils with drainage history as compared to wetting for the same degree of saturation. This thesis should be further verified by suitable experiments, *e. g.*, by shear strength testing for specimens with different hydraulic histories.

The concepts of the presented experimental set-ups can be improved and should be adapted for a smoother and more user-friendly operation in imaging environments as well as synchrotron radiation facilities, such as DESY. A faster imaging at the synchrotron will allow to reach a better temporal resolution for the capturing of fast processes in geomaterials. Open questions regard transient or even dynamic flow effects on the pore level, such as relaxation processes of the liquid phase, *e. g.*, caused by viscosity and dynamic contact angle changes. As a vision, a geomechanical lab with many miniaturised experiments integrated in imaging environments could be established to study soils, rocks and other porous media and related multiphysics problems with relevance to current pressing research questions, such as the mitigation of climate change.

The rigorous application of imaging techniques comes at the cost of massive amounts of data and the question of how to effectively analyse them. Huge amounts of data are recorded, especially, when using synchrotron radiation with high spatial and temporal resolution of measurements. Therefore, automatic procedures for high quality segmentation and extraction of microscale information is needed, *e. g.*, automated detection and

extraction of interfacial geometry data or of contact angles, which requires smart and user-friendly image analysis software to be developed. First approaches to facilitate challenging image analysis tasks are already available based on machine learning.

Regarding the vast field of numerical methods and the idea of a "virtual soil lab" outlined in Chapter 8, it is worth discussing what would be the most promising numerical approaches to include the observed coupled hydro-mechanical processes on the pore or grain scale by microscale or mesoscale models and how the findings could be transferred back to macroscale models. A multiphase LBM-DEM with dynamic moving particle and liquid interaction and particles with arbitrary shape could be an interesting approach on the way to a virtual soil lab, however, very likely at high numerical costs. Many numerical developments including the named characteristics are already existent. However, the challenge would be to combine them in an efficient way. The practical development of such a virtual soil lab could be split in partial tasks, *e. g.*, the development of a soil data base, including geometry data of many virtual particles as well as 4D validation data and material properties from imaging experiments. In addition, several multiscale and multiphysics numerical methods could be included making use of the soil input data to simulate very different soil mechanical tests. Finally, a link could be established to derive the macroscopic constitutive soil behaviour based on microscopic or mesoscopic models in order to simulate geotechnical problems on the macroscopic level which is in the end relevant to geotechnical applications.

Beyond their application in research, how can the outlined experimental approaches and numerical tools be further integrated into teaching in geomechanics? Unified approaches to implement physical computing of experiments should be further applied in teaching, such as lab courses. For this purpose, technical layouts, *e. g.*, for mechanical actuators or sensors, could be standardised in a modular system to be easier accessible to students. Future curricula in engineering teaching could then include experimental environments where students can discover physical principles in geomaterials based on very illustrative and practical experiments, also boosting curiosity for further research. If this approach was also linked to a virtual soil lab, students could encounter the whole cycle of engineering research and practice including experiments and simulations.

Bibliography

ADS1115 analog-to-digital converter. https://cdn-learn.adafruit.com/downloads/pdf/adafruit-4-channel-adc-breakouts.pdf. Accessed: 2019-04-26.

Agarwal, P., R. M. Murdande, A. S. Kandaswamy, and M. S. Bobji (2019): Dynamic stretching of a liquid bridge. In: *International Journal of Advances in Engineering Sciences and Applied Mathematics* 11(4), pp. 238–243. DOI: 10.1007/s12572-020-00256-8.

Ahrens, J., B. Geveci, and C. Law (2005): ParaView: An End-User Tool for Large-Data Visualization. In: *The Visualization Handbook*. DOI: 10.1016/B978-012387582-2/50038-1.

Alonso, E. E., A. Gens, and A. Josa (1990): A constitutive model for partially saturated soils. In: *Géotechnique* 40(3), pp. 405–430.

Andò, E. (2013): Experimental investigation of microstructural changes in deforming granular media using x-ray tomography. PhD thesis. Mechanics [physics.med-ph]. Université de Grenoble.

Andò, E., G. Viggiani, S. A. Hall, and J. Desrues (2013): Experimental micro-mechanics of granular media studied by x-ray tomography: recent results and challenges. In: *Géotechnique Letters* 3(3), pp. 142–146. DOI: 10.1680/geolett.13.00036.

Andrew, M., B. Bijeljic, and M. J. Blunt (2014): Pore-scale contact angle measurements at reservoir conditions using X-ray microtomography. In: *Advances in Water Resources* 68, pp. 24–31. DOI: 10.1016/j.advwatres.2014.02.014.

Armstrong, R. T., M. L. Porter, and D. Wildenschild (2012): Linking pore-scale interfacial curvature to column-scale capillary pressure. In: *Advances in Water Resources* 46, pp. 55–62. DOI: 10.1016/j.advwatres.2012.05.009.

ASTMD6836-16 (2016): *Standard Test Methods for Determination of the Soil Water Characteristic Curve for Desorption Using Hanging Column, Pressure Extractor, Chilled Mirror Hygrometer, or Centrifuge.* ASTM International.

Aubertin, M., M. Mbonimpa, B. Bussière, and R. P. Chapuis (2003): A model to predict the water retention curve from basic geotechnical properties. In: *Canadian Geotechnical Journal* 40(6), pp. 1104–1122.

Avizo (2022). https://www.thermofisher.com/de/de/home/electron-microscopy/products/software-em-3d-vis/avizo-software.html. Accessed: 2022-03-11.

Bay, B., T. Smith, D. Fyhrie, and M. Saad (1999): Digital volume correlation: Three-dimensional strain mapping using X-ray tomography. In: *Experimental Mechanics* 39(3), pp. 217–226.

Bear, J. (1979): *Hydraulics of groundwater.* New York: Mc Graw-Hill (Mc Graw-Hill Series in Water Resources and Environmental Eng.)

Benzi, R., L. Biferale, M. Sbragaglia, S. Succi, and F. Toschi (2006): Mesoscopic modeling of a two-phase flow in the presence of boundaries: The contact angle. In: *Physical Review E* 74. DOI: 10.1103/PhysRevE.74.021509.

Bhatnagar, P. L., E. P. Gross, and M. Krook (1954): A Model for Collision Processes in Gases. I. Small Amplitude Processes in Charged and Neutral One-Component Systems. In: *Physical Review* 94(3). DOI: 10.1103/PhysRev.94.511.

Bircumshaw, L. L. (1922): The Surface Tension of Mixtures of Alcohol and Water at 25°. In: *Journal of the Chemical Society, Transactions* 121, pp. 887–891. DOI: 10.1039/CT9222100887.

Bishop, A. W. (1959): The principle of effective stress. In: *Teknisk Ukeblad* 106(39), pp. 859–863.

Bishop, A. W. (1961): The experimental study of partly saturated soil in the triaxial apparatus. In: *Proc. 5th International Conference on Soil Mechanics, Paris*, pp. 13–21.

Blunt, M. J. (2017): *Multiphase Flow in Permeable Media: A Pore-Scale Perspective.* Cambridge University Press. DOI: 10.1017/9781316145098.

Bozkurt, M., D. Fratta, and W. Likos (2017): Capillary forces between equally sized moving glass beads: an experimental study. In: *Canadian Geotechnical Journal* 54(9), pp. 1300–1309. DOI: 10.1139/cgj-2016-0213. URL: https://doi.org/10.1139/cgj-2016-0213.

Brooks, R. H. and A. T. Corey (1964): Hydraulic properties of porous medium. In: *Hydrology Paper No. 3*, Civil Engineering Department, Colorado State Univ., Fort Collins, Colorado.

Bruchon, J.-F., J.-M. Pereira, M. Vandamme, N. Lenoir, P. Delage, and M. Bornert (2013): Full 3D investigation and characterisation of capillary collapse of a loose unsaturated sand using X-ray CT. In: *Granular Matter* 15(6), pp. 783–800.

Buckingham, E. (1907): *Studies on the movement of soil moisture.* Bull 38 USDA, Bureau of Soils, Washington DC.

Burdine, N. T. (1953): Relative permeability calculations from pore size distribution data. In: *Journal of Petroleum Technology* 198, pp. 71–78.

Butt, H.-J., K. Graf, and M. Kappl (2003): *Physics and Chemistry of Interfaces.* Wiley-VCH Verlag & Co. KGaA.

Carnahan, N. F. and K. E. Starling (1969): Equation of State for Nonattracting Rigid Spheres. In: *Journal of Chemical Physics* 51(2). DOI: 10.1063/1.1672048.

Ceccato, F., A. Yerro, V. Girardi, and P. Simonini (2021): Two-phase dynamic MPM formulation for unsaturated soil. In: *Computers and Geotechnics* 129. DOI: 10.1016/j.compgeo.2020.103876.

Chareyre, B., A. Cortis, E. Catalano, and E. Barthélemy (2012): Pore-scale modeling of viscous flow and induced forces in dense sphere packings. In: *Transport in porous media* 94(2), pp. 595–615. DOI: 10.1007/s11242-011-9915-6.

Childs, E. C. and G. N. Collis-George (1950): The permeability of porous materials. In: *Proc. of The Royal Society, 210 A, London, U.K.* Pp. 392–405.

Cook, B. K., D. R. Noble, and J. R. Williams (2004): A direct simulation method for particle-fluid systems. In: *Engineering Computations: Int. J. for Computer-Aided Engineering* 21(2–3), pp. 151–168.

Craciun, O. and S.-C. R. Lo (2009): Matric suction measurement in stress path cyclic triaxial testing of unbound granular base materials. In: *Geotechnical Testing Journal* 33(1), pp. 33–45.

Culligan, K. A., D. Wildenschild, B. S. B. Christensen, W. G. Gray, M. L. Rivers, and A. F. B. Tompson (2004): Interfacial area measurements for unsaturated flow through a porous medium. In: *Water Resources Research* 40(W12413). DOI: 10.1029/2004WR003278.

Cundall, P. A. and O. D. Strack (1979): A discrete numerical model for granular assemblies. In: *Géotechnique* 29(1), pp. 47–65. DOI: 10.1680/geot.1979.29.1.47.

de Gennes, P.-G., F. Brochard-Wyart, and D. Quéré (2004): *Capillarity and Wetting Phenomena: Drops, Bubbles, Pearls, Waves.* Springer.

Debenedetti, P. G. (1997): *Metastable Liquids – Concepts and Principles.* Princeton University Press. DOI: 10.1515/9780691213941.

Delage, P., E. E. Romero, and A. Tarantino (2008): Recent developments in the techniques of controlling and measuring suction in unsaturated soils. In: *Proc. 1st European Conference on Unsaturated Soils, Durham*, pp. 33–52.

Desrues, J., R. Chambon, M. Mokni, and F. Mazerolle (1996): Void ratio evolution inside shear bands in triaxial sand specimens studied by computed tomography. In: *Géotechnique* 46(3), pp. 539–546. DOI: 10.1680/geot.1996.46.3.529.

DFG Research Training Group GRK 2462 "Processes in natural and technical Particle-Fluid-Systems" (PintPFS) (2022). https://gepris.dfg.de/gepris/projekt/390794421?language=en. Accessed: 2022-03-28.

Diamantopoulos, E. and W. Durner (2012): Dynamic nonequilibrium of water flow in porous media: A review. In: *Vadose Zone Journal* 11(3). DOI: 10.2136/vzj2011.0197.

DIN 18137-2:2011-04 (2011): *Baugrund, Untersuchung von Bodenproben – Bestimmung der Scherfestigkeit – Teil 2: Triaxialversuch.* Deutsches Institut für Normung e.V. (DIN).

DIN EN ISO 17892-10:2019-04 (2019): *Geotechnische Erkundung und Untersuchung – Laborversuche an Bodenproben – Teil 10: Direkte Scherversuche.* Deutsches Institut für Normung e.V. (DIN).

Donald, I. B. (1956): Shear strength measurements in unsaturated non-cohesive soils with negative pore pressures. In: *Proc. of 2nd Australia-New Zealand Conf. Soil Mech. Found. Eng. (Christchurch, New Zealand)*, pp. 200–205.

DRV8825 stepper motor controller board. http://www.ti.com/lit/ds/symlink/drv8825.pdf. Accessed: 2019-04-25.

Düster, A., J. Parvizian, and E. Rank (2008): The finite cell method for three-dimensional problems of solid mechanics. In: *Computer Methods in Applied Mechanics and Engineering* 197, pp. 3768–3782. DOI: 10.1016/j.cma.2008.02.036.

ffmpeg (2021). https://www.ffmpeg.org/. Accessed: 2021-05-31.

Flores, B. G. A. (2010): A Simplified Image Analysis Method To Evaluate LNAPL Saturation Under Fluctuating Groundwater Conditions. PhD Thesis. Kyoto University, Japan.

Fredlund, D. G. and N. R. Morgenstern (1977): Stress state variables for unsaturated soils. In: *ASCE J. Geotech. Eng. Div. GT5* 103, pp. 447–466.

Fredlund, D. G. and H. Rahardjo (1993): *Soil mechanics for unsaturated soils.* John Wiley & Sons.

Fredlund, D. G. and A. Xing (1994): Equations for soil-water characteristic curve. In: *Canadian Geotechnical Journal* 31, pp. 521–532. DOI: 10.1139/t94-061.

Fredlund, D. G., N. R. Morgenstern, and R. A. Widger (1978): The shear strength of unsaturated soils. In: *Canadian Geotechnical Journal* 15(3), pp. 313–321.

Fuentes, W. and T. Triantafyllidis (2013): Hydro-mechanical hypoplastic models for unsaturated soils under isotropic stress conditions. In: *Computers and Geotechnics* 51, pp. 72–82.

Fuentes, W. and T. Triantafyllidis (2015): ISA model: A constitutive model for soils with yield surface in the intergranular strain space. In: *International Journal for Numerical and Analytical Methods in Geomechanics* 39(11), pp. 1235–1254. DOI: 10.1002/nag.2370.

Gastal, E. S. L. and M. M. Oliveira (July 2012): Adaptive Manifolds for Real-Time High-Dimensional Filtering. In: *ACM Trans. Graph.* 31(4). DOI: 10.1145/2185520.2185529. URL: https://doi.org/10.1145/2185520.2185529.

Gray, W. G. and B. A. Schrefler (2001): Thermodynamic approach to effective stress in partially saturated porous media. In: *European Journal of Mechanics - A/Solids* 20(4), pp. 521–538. DOI: 10.1016/S0997-7538(01)01158-5.

Gray, W. G., B. A. Schrefler, and F. Pesavento (2009): The solid phase stress tensor in porous media mechanics and the Hill–Mandel condition. In: *Journal of the Mechanics and Physics of Solids* 57(3), pp. 539–554. DOI: 10.1016/j.jmps.2008.11.005.

Haines, W. B. (1930): Studies in the physical properties of soil: V. The hysteresis effect in capillary properties and the modes of moisture distribution associated therewith. In: *Journal of Agricultural Science* 20, pp. 97–116.

Hall, S., M. Bornert, J. Desrues, Y. Pannier, N. Lenoir, G. Viggiani, and P. Bésuelle (2010): Discrete and continuum experimental study of localised deformation in Hostun sand under triaxial compression using X-ray μCT and 3D digital image correlation. In: *Géotechnique* 60(5), pp. 315–322.

Hassanizadeh, S. M., M. A. Celia, and H. K. Dahle (2002): Dynamic Effect in the Capillary Pressure-Saturation Relationship and its Impacts on Unsaturated Flow. In: *Vadose Zone Journal* 1(1), pp. 38–57. DOI: 10.2136/vzj2002.3800.

He, X. and L.-S. Luo (1997): Theory of the lattice Boltzmann method: From the Boltzmann equation to the lattice Boltzmann equation. In: *Physical Review E* 56. DOI: 10.1103/PhysRevE.56.6811.

Higo, Y., F. Oka, T. Sato, Y. Matsushima, and S. Kimoto (2013): Investigation of localized deformation in partially saturated sand under triaxial compression using microfocus X-ray CT with digital image correlation. In: *Soils and Foundations* 53(2), pp. 181–198. DOI: 10.1016/j.sandf.2013.02.001.

Higo, Y., R. Morishita, R. Kido, G. Khaddour, and S. Salager (2015): Local water-retention behaviour of sand during drying and wetting process observed by micro x-ray tomography with trinarisation. In: *Japanese Geotechnical Society Special Publication* 2(16), pp. 635–638. DOI: 10.3208/jgssp.OTH-13.

Hilf, J. W. (1956): An investigation of pore-water pressure in compacted cohesive soils, Technical Memorandum No. 654. Dissertation. Denver, Colorado, USA: United State Department of the Interior Bureau of Reclamation, Design and Construction Devision.

Hosseini, R., K. Kumar, and J.-Y. Delenne (2021): Investigating the effect of porosity on the soil water retention curve using the multiphase Lattice Boltzmann Method. In: *Proc. of Powders & Grains 2021 – 9th International Conference on Micromechanics on Granular Media*. DOI: 10.1051/epjconf/202124909007.

Huang, H., M. C. Sukop, and X.-Y. Lu (2015): *Multiphase lattice Boltzmann methods: Theory and application*. Chichester: Wiley Blackwell.

Hueckel, T., B. Mielniczuk, and M. S. El Youssoufi (2020): Adhesion-force micro-scale study of desiccating granular material. In: *Géotechnique* 70(12). DOI: 10.1680/jgeot.18.P.298.

Iglberger, K., N. Thürey, and U. Rüde (2008): Simulation of moving particles in 3D with the Lattice Boltzmann method. In: *Computers and Mathematics with Applications* 55(7), pp. 1461–1468. DOI: 10.1016/j.camwa.2007.08.022.

ImageJ/Fiji (2021). https://imagej.net/Fiji. Accessed: 2021-05-31.

Iske, A. (2018): *Approximation*. Springer.

Jones, A. C., C. H. Arns, A. P. Sheppard, D. W. Hutmacher, B. K. Milthorpe, and M. A. Knackstedt (2007): Assessment of bone ingrowth into porous biomaterials using MICRO-CT. In: *Biomaterials* 28(15). DOI: 10.1016/j.biomaterials.2007.01.046.

Karatza, Z., J. Buckman, G. M. Medero, and C. T. S. Beckett (2020): Effect of wetting and drying on meniscus structures in hydrophobic sands. In: *4th European Conference on Unsaturated Soils (E-UNSAT 2020)*. Ed. by R. Cardoso, C. Jommi, and E. Romero. Lisboa, Portugal. DOI: 10.1051/e3sconf/202019503040. URL: https://www.e3s-conferences.org/articles/e3sconf/abs/2020/55/e3sconf_e-unsat2020_03040/e3sconf_e-unsat2020_03040.html.

Kawamoto, R., E. Andò, G. Viggiani, and J. E. Andrade (2016): Level set discrete element method for three-dimensional computations with triaxial case study. In: *Journal of the Mechanics and Physics of Solids* 91, pp. 1–13. DOI: 10.1016/j.jmps.2016.02.021.

Keen, B. (1963): Dr. W. B. Haines. In: *Nature* 198, p. 434.

Khaddour, G. (2015): Multi-scale characterisation of the hydro-mechanical behaviour of unsaturated sand: water retention and triaxial responses. Ph.D. thesis. Laboratoire 3SR, Université Grenoble Alpes.

Khaddour, G., I. Riedel, E. Andò, P. Charrier, P. Bésuelle, J. Desrues, G. Viggiani, and S. Salager (2018): Grain-scale characterization of water retention behaviour of sand using X-ray CT. In: *Acta Geotechnica* 13. DOI: 10.1007/s11440-018-0628-7.

Kido, R. and Y. Higo (2019): Distribution changes of grain contacts and menisci in shear band during triaxial compression test for unsaturated sand. In: *Proc. of 7th Asia-Pacific Conference on Unsaturated Soils (AP-UNSAT 2019)*. Nagoya, Japan. URL: https://www.jstage.jst.go.jp/article/jgssp/7/2/7_v07.096/_article.

Kido, R. and Y. Higo (2020): Microscopic characteristics of partially saturated dense sand and their link to macroscopic responses under triaxial compression conditions. In: *Acta Geotechnica*. DOI: 10.1007/s11440-020-01049-w.

Kido, R., Y. Higo, F. Takamura, R. Morishita, and G. Khaddour (2020): Morphological transitions for pore water and pore air during drying and wetting processes in partially

saturated sand. In: *Acta Geotechnica* 15, pp. 1745–1761. DOI: 10.1007/s11440-020-00939-3.

Krüger, T., H. Kusumaatmaja, A. Kuzmin, O. Shardt, G. Silva, and E. M. Viggen (2017): *The Lattice Boltzmann Method – Principles and Practice*. Springer. DOI: 10.1007/978-3-319-44649-3.

Levin, Y. and J. E. Flores-Mena (2001): Surface tension of strong electrolytes. In: *Europhysics Letters* 56(2), pp. 187–192. DOI: 10.1209/epl/i2001-00504-y.

Lewis, R. W. and B. A. Schrefler (1998): *The Finite Element Method in the Static and Dynamic Deformation and Consolidation of Porous Media*. John Wiley & Sons.

Li, S., M. Liu, D. Hanaor, and Y. Gan (2018): Dynamics of Viscous Entrapped Saturated Zones in Partially Wetted Porous Media. In: *Transport in Porous Media* 125, pp. 193–210. DOI: 10.1007/s11242-018-1113-3.

Li, X. S. (2005): Modelling of hysteresis response for arbitrary wetting/drying paths. In: *Computers and Geotechnics* 32, pp. 133–137.

Lian, G., C. Thornton, and M. J. Adams (1993): A Theoretical Study of the Liquid Bridge Forces between Two Rigid Spherical Bodies. In: *Journal of Colloid and Interface Science* 161(1), pp. 138–147. DOI: 10.1006/jcis.1993.1452.

Likos, W. J., A. Wayllace, J. Godt, and N. Lu (2010): Modified direct shear apparatus for unsaturated sands at low suction and stress. In: *Geotechnical Testing Journal* 33(4), pp. 286–298.

Lins, Y. (2009): Hydro-mechanical properties of partially saturated sand. Dissertation. Faculty of Civil Engineering, University Bochum.

Liu, X., A. Zhou, S.-l. Shen, J. Li, and D. Sheng (2020): A micro-mechanical model for unsaturated soils based on DEM. In: *Computer methods in applied mechanics and engineering* 368. DOI: 10.1016/j.cma.2020.113183.

Lu, N. and W. J. Likos (2006): Suction stress characteristic curve for unsaturated soil. In: *Journal of Geotechnical and Environmental Engineering* 132(2), pp. 131–142.

Lu, N., J. W. Godt, and D. T. Wu (2010): A closed-form equation for effective stress in unsaturated soil. In: *Water Resources Research* 46(5).

Luo, L.-S. (1998): Unified theory of lattice Boltzmann models for nonideal gases. In: *Physical Review Letters* 81(8), pp. 1618–1621. DOI: 10.1103/PhysRevLett.81.1618.

Mascini, A., V. Cnudde, and T. Bultreys (2020): Event-based contact angle measurements inside porous media using time-resolved micro-computed tomography. In: *Journal of Colloid and Interface Science* 572, pp. 354–363. DOI: 10.1016/j.jcis.2020.03.099.

MATLAB (2022). https://www.mathworks.com/products/matlab.html. Accessed: 2022-03-11.

Méheust, Y., G. Løvoll, K. Måløy, and J. Schmittbuhl (2002): Interface scaling in a two-dimensional porous medium under combined viscous, gravity and capillary effects. In: *Physical review. E, Statistical, nonlinear, and soft matter physics* 66, p. 051603. DOI: 10.1103/PhysRevE.66.051603.

Mielniczuk, B., T. Hueckel, and M. S. El Youssoufi (2015): Laplace pressure evolution and four instabilities in evaporating two-grain liquid bridges. In: *Powder Technology* 283, pp. 137–151. DOI: 10.1016/j.powtec.2015.05.024.

Milatz, M. (2015): An experimental method to study the drying-wetting behaviour of a sand. In: *Proc. of 6th Asia-Pacific Conference on Unsaturated Soils (AP-UNSAT 2015), Guilin, China*. Ed. by Z. Chen, C. Wei, D. Sun, and X. Xu, pp. 211–216.

Milatz, M. (2019): Zur Anwendung von Einplatinen-Computern in der bodenmechanischen Forschung und Lehre am Beispiel eines einaxialen Druckversuchs zur Untersuchung teilgesättigter granularer Böden (On the application of single-board computers in soil mechanical research and teaching using the example of an uniaxial compression test for the investigation of unsaturated granular soils). In: *Geotechnik* 42(1). (In German). DOI: 10.1002/gete.201800015.

Milatz, M. (2020a): An automated testing device for continuous measurement of the hysteretic water retention curve of granular media. In: *Acta Geotechnica* 15. DOI: 10.1007/s11440-020-00922-y.

Milatz, M. (2020b): Application of single-board computers in experimental research on unsaturated soils. In: *4th European Conference on Unsaturated Soils (E-UNSAT 2020)*. Ed. by R. Cardoso, C. Jommi, and E. Romero. Lisboa, Portugal. DOI: 10.1051/e3sconf/202019502022.

Milatz, M. (2022): *Implementation of a multiphase Lattice Boltzmann Method for the simulation of water retention behaviour of CT scanned granular media.* TUHH Open Research (TORE), Hamburg University of Technology. DOI: 10.15480/336.4364.

Milatz, M. and J. Grabe (2015): A new simple shear apparatus and testing method for unsaturated sands. In: *Geotechnical Testing Journal* 38(1), pp. 9–22. DOI: 10.1520/GTJ20140035.

Milatz, M. and J. Grabe (2019): Microscopic investigation of the hydro-mechanical behavior of unsaturated granular media with X-ray CT. In: *Proc. of 7th Asia-Pacific Conference on Unsaturated Soils (AP-UNSAT 2019)*. Nagoya, Japan. URL: https://www.jstage.jst.go.jp/article/jgssp/7/2/7_v07.095/_article.

Milatz, M., T. Törzs, and J. Grabe (2016): Settlements in unsaturated granular soils induced by changes in saturation and suction. In: *Proc. of 3rd European Conference on Unsaturated Soils (E-UNSAT 2016), Paris, France*. DOI: 10.1051/e3sconf/20160914009.

Milatz, M., T. Törzs, and J. Grabe (2018a): Investigation of transient effects on the soil-water characteristic curve of different granular soils. In: *Proc. of 7th International Conference on Unsaturated Soils (UNSAT 2018)*. Ed. by C. W. W. Ng, A. K. Leung, A. C. F. Chiu, and C. Zhou. Vol. 1. Hong Kong, pp. 355–360. URL: http://gcf-conf.ust.hk/unsat2018/paper/pdf/1b-6.UNSAT2018_038.pdf.

Milatz, M., T. Törzs, E. Nikooee, S. M. Hassanizadeh, and J. Grabe (2018b): Theoretical and experimental investigations on the role of transient effects in the water retention behaviour of unsaturated granular soils. In: *Geomechanics for Energy and the Environment* 15, pp. 54–64. DOI: 10.1016/j.gete.2018.02.003.

Milatz, M., E. Andò, L. Helfen, N. Hüsener, and A. Tengattini (2019): *Partial saturation in granular media.* Institut Laue-Langevin (ILL). DOI: 10.5291/ILL-DATA.UGA-73.

Milatz, M., N. Hüsener, E. Andò, G. Viggiani, and J. Grabe (2021a): *Data from in situ uniaxial compression experiments on unsaturated granular media with X-ray CT-imaging.* TUHH Open Research (TORE), Hamburg University of Technology. DOI: 10.15480/336.3291.

Milatz, M., N. Hüsener, E. Andò, G. Viggiani, and J. Grabe (2021b): Quantitative 3D imaging of partially saturated granular materials under uniaxial compression. In: *Acta Geotechnica* 16, pp. 3573–3600. DOI: 10.1007/s11440-021-01315-5.

Milatz, M., E. Andò, and G. Viggiani (2022a): *Data from in situ X-ray CT imaging of transient water retention experiments with cyclic drainage and imbibition.* TUHH Open Research (TORE), Hamburg University of Technology. DOI: 10.15480/336.4291.

Milatz, M., E. Andò, G. Viggiani, and S. Mora (2022b): In situ X-ray CT imaging of transient water retention experiments with cyclic drainage and imbibition. In: *Open Geomechanics* 3, 5. DOI: 10.5802/ogeo.13.

Mirzaei, M. and D. B. Das (2013): Experimental Investigation of Hysteretic Dynamic Effect in Capillary Pressure-Saturation Relationship for Two-Phase Flow in Porous Media. In: *AIChE Journal* 59(10), pp. 3958–3974. DOI: 10.1002/aic.14121.

Moosmann, J., A. Ershov, V. Weinhardt, T. Baumbach, M. S. Prasad, C. LaBonne, X. Xiao, J. Kashef, and R. Hofmann (2014): Time-lapse X-ray phase-contrast microtomography for *in vivo* imaging and analysis of morphogenesis. In: *Nature Protocols* 9, pp. 294–304. DOI: 10.1038/nprot.2014.033.

Moscariello, M., S. Cuomo, and S. Salager (2018): Capillary collapse of loose pyroclastic unsaturated sands characterized at grain scale. In: *Acta Geotechnica* 13, pp. 117–133.

Mualem, Y. (1976): A new model for predicting the hydraulic conductivity of unsaturated porous media. In: *Water Resources Research* 12, pp. 593–622.

Munjiza, A. (2004): *The Combined Finite-Discrete Element Method.* John Wiley & Sons, Ltd.

Myers, D. (2006): *Surfactant Science and Technology.* Wiley.

Nadimi, S. and J. Fonseca (2019): Image based simulation of one-dimensional compression tests on carbonate sands. In: *Meccanica* 54, pp. 697–706. DOI: 10.1007/s11012-018-0923-2.

Niemunis, A. and I. Herle (1997): Hypoplastic model for cohesionless soils with elastic strain range. In: *Mechanics of Frictional and Cohesive Materials* 2, pp. 279–299.

Nikooee, E., G. Habibagahi, S. M. Hassanizadeh, and A. Ghahramani (2013): Effective Stress in Unsaturated Soils: A Thermodynamic Approach Based on the Interfacial Energy and Hydromechanical Coupling. In: *Transport in Porous Media* 96, pp. 369–396. DOI: 10.1007/s11242-012-0093-y.

Nishimura, T., J. Koseki, D. G. Fredlund, and H. Rahardjo (2012): Microporous Membrane Technology for Measurement of Soil-Water Characteristic Curve. In: *Geotechnical Testing Journal* 35(1), pp. 1–8.

Otani, J., T. Mukunoki, and Y. Obara (2000): Application of X-ray CT method for characterization of failure in soils. In: *Soils and Foundations* 40(2), pp. 111–118. DOI: 10.3208/sandf.40.2_111.

Pan, C., M. Hilpert, and C. T. Miller (2004): Lattice-Boltzmann simulation of two-phase flow in porous media. In: *Water Resources Research* 40(W01501). DOI: 10.1029/2003WR002120.

Parera, F., N. Pinyol, and E. Alonso (2020): Image-based measurements of degree of saturation. In: *4th European Conference on Unsaturated Soils (E-UNSAT 2020).* Ed. by R. Cardoso, C. Jommi, and E. Romero. Lisboa, Portugal. DOI: 10.1051/e3sconf/202019503010.

Parvizian, J., A. Düster, and E. Rank (2007): Finite cell method – h- and p-extension for embedded domain problems in solid mechanics. In: *Computational Mechanics* 41, pp. 121–133. DOI: 10.1007/s00466-007-0173-y.

Pedroso, D. M. and D. J. Williams (2010): A novel approach for modelling soil-water characteristic curves with hysteresis. In: *Computers and Geotechnics* 37(3). DOI: 10.1016/j.compgeo.2009.12.004.

Peters, A. and W. Durner (2008): Simplified evaporation method for determining soil hydraulic properties. In: *Journal of Hydrology* 356, pp. 147–162.

Petrovic, A. M., J. E. Siebert, and P. E. Rieke (1982): Soil bulk density analysis in three dimensions by computed tomography scanning. In: *Soil Science Society of America Journal* 46(3), pp. 445–450. DOI: 10.2136/sssaj1982.03615995004600030001x.

Posner, A. M., J. R. Anderson, and A. E. Alexander (1952): The surface tension and surface potential of aqueous solutions of noral aliphatic alcohols. In: *Journal of Colloid Science* 7(6), pp. 623–644. DOI: 10.1016/0095-8522(52)90044-5.

Potyondy, D. O. (2015): The bonded-particle model as a tool for rock mechanics research and application: current trends and future directions. In: *Geosystem Engineering* 18(1), pp. 1–28. DOI: 10.1080/12269328.2014.998346.

Purwana, Y. M., P. Jitsangiam, H. Nikraz, and A. Jotisankasa (2011): Experimental studies of suction-monitored direct shear apparatus on Perth poorly graded sand. In: *Proc. of International Conference on Advances in Geotechnical Engineering (Perth, Australia)*, pp. 273–278.

Raspberry Pi (2022). https://www.raspberrypi.org/. Accessed: 2022-03-10.

Russo, J. W. and M. M. Hoffmann (2010): Influence of Typical Impurities on the Surface Tension Measurements of Binary Mixtures of Water and the Ionic Liquids 1-Butyl-3-Methylimidazolium Tetrafluoroborate and Chloride. In: *Journal of Chemical and Engineering Data* 55, pp. 5900–5905. DOI: 10.1021/je100949x.

Salvatore, E., E. Andò, G. Modoni, and G. Viggiani (2016): Micromechanical study of cyclically loaded sands with x-ray microtomography and digital image correlation. In: *Procedia Engineering* 158, pp. 92–97. DOI: 10.1016/j.proeng.2016.08.411.

Schaap, M. G., M. L. Porter, B. S. B. Christensen, and D. Wildenschild (2007): Comparison of pressure-saturation characteristics derived from computed tomography and lattice Boltzmann simulations. In: *Water Resources Research* 43(W12S06). DOI: 10.1029/2006WR005730.

Scheel, M., R. Seemann, M. Brinkmann, M. Di Michiel, A. Sheppard, B. Breidenbach, and S. Herminghaus (2008): Morphological clues to wet granular pile stability. In: *Nature Materials* 7. DOI: 10.1038/nmat2117.

Schindler, U., W. Durner, G. von Unold, L. Mueller, and R. Wieland (2010): The evaporation method: Extending the measurement range of soil hydraulic properties using the air-entry pressure of the ceramic cup. In: *Journal of Plant Nutrition and Soil Science* 173, pp. 563–572.

Schlüter, S., S. Berg, M. Rücker, R. T. Armstrong, H.-J. Vogel, R. Hilfer, and D. Wildenschild (2016): Pore-scale displacement mechanisms as a source of hysteresis for two-phase flow in porous media. In: *Water Resources Research* 52(3), pp. 2194–2205. DOI: 10.1002/2015WR018254.

Schröder, M., M. Milatz, and J. Grabe (2022): Investigation of soil clogging mechanisms at the cutting tool-soil interface with miniaturised separation tests and computed tomography. In: *Proc. of 10th International Conference on Physical Modelling in Geotechnics (ICPMG 2022)*. Daejeon, Korea, pp. 188–191.

Schubert, H. (1982): *Kapillarität in porösen Feststoffsystemen*. Springer Verlag.

Shan, X. and H. Chen (1993): Lattice Boltzmann model for simulating flows with multiple phases and components. In: *Physical Review E* 47(3), pp. 1815–1819. DOI: 10.1103/PhysRevE.47.1815.

Shi, Z., Y. Zhang, M. Liu, D. A. H. Hanaor, and Y. Gan (2018): Dynamic contact angle hysteresis in liquid bridges. In: *Colloids and Surfaces A* 555, pp. 365–371. DOI: 10.1016/j.colsurfa.2018.07.004.

Singh, K., H. Menke, M. Andrew, C. Rau, B Bijeljic, and M. J. Blunt (2018): Time-resolved synchrotron X-ray micro-tomography datasets of drainage and imbibition in carbonate rocks. In: *Scientific Data* 5. DOI: 10.1038/sdata.2018.265.

Singh, K., M. Jung, M. Brinkmann, and R. Seemann (2019): Capillary-Dominated Fluid Displacement in Porous Media. In: *Annual Review of Fluid Mechanics* 51, pp. 429–449. DOI: 10.1146/annurev-fluid-010518-040342.

Soundararajan, K. K. (2015): Multi-scale multiphase modelling of granular flows. Doctoral thesis. University of Cambridge. DOI: 10.17863/CAM.14130.

Stamati, O., E. Andò, E. Roubin, R. Cailletaud, M. Wiebicke, G. Pinzon, C. Couture, R. C. Hurley, R. Caulk, D. Caillerie, T. Matsushima, P. Bésuelle, F. Bertoni, T. Arnaud, A. O. Laborin, R. Rorato, Y. Sun, A. Tengattini, O. Okubadejo, J.-B. Colliat, M. Saadatfar, F. E. Garcia, C. Papazoglou, I. Vego, S. Brisard, J. Dijkstra, and G. Birmpilis (2020): 'spam': Software for Practical Analysis of Materials. In: *Journal of Open Source Software* 5(51), p. 2286. DOI: 10.21105/joss.02286. URL: https://doi.org/10.21105/joss.02286.

Sulsky, D., Z. Chen, and H. L. Schreyer (1994): A particle method for history-dependent materials. In: *Computer Methods in Applied Mechanics and Engineering* 118(1–2), pp. 179–196. DOI: 10.1016/0045-7825(94)90112-0.

Tani, K. (1997): X-ray computed tomography technique to observe shear banding in dense sands. In: *Proc. of Int. Symp. on Deformation and Progressive Failure in Geomechanics, Nagoya*, pp. 315–320.

Tengattini, A., N. Lenoir, E. Andò, B. Giroud, D. Atkins, J. Beaucour, and G. Viggiani (2020): NeXT-Grenoble, the Neutron and X-ray tomograph in Grenoble. In: *Nuclear Inst. and Methods in Physics Research, A* 968. DOI: 10.1016/j.nima.2020.163939.

Tengattini, A., N. Lenoir, E. Andò, and G. Viggiani (2021): Neutron imaging for geomechanics: A review. In: *Geomechanics for Energy and the Environment* 27. DOI: 10.1016/j.gete.2020.100206.

Thakur, M. M. and D. Penumadu (2020): Triaxial compression in sands using FDEM and micro-X-ray computed tomography. In: *Computers and Geotechnics* 124. DOI: 10.1016/j.compgeo.2020.103638.

Thakur, M. M., D. Penumadu, and C. Bauer (2020): Capillary suction measurements in granular materials and direct numerical simulations using X-ray computed tomography microstructure. In: *Journal of Geotechnical and Geoenvironmental Engineering* 146(1). DOI: 10.1061/(ASCE)GT.1943-5606.0002194.

Thomas, P. A. and J. D. Bray (1999): Capturing Nonspherical Shape of Granular Media with Disk Clusters. In: *Journal of Geotechnical and Geoenvironmental Engineering* 125(3). DOI: 10.1061/(ASCE)1090-0241(1999)125:3(169).

Tombolato, S., A. Tarantino, and L. Mongiovi (2008): A simple shear apparatus for testing unsaturated soils. In: *Unsaturated Soils. Advances in Geo-Engineering, Proc. 1st European Conference, E-Unsat 2008, Durham, United Kingdom*, pp. 89–95.

Tötzke, C. (2009): Untersuchungen über den Zustand tensilen Wassers in Bäumen. Dissertation. Fachbereich Biologie, Chemie, Pharmazie der Freien Universität Berlin.

Turner, A. K., F. H. Kim, D. Penumadu, and E. B. Herbold (2016): Meso-scale framework for modeling granular material using computed tomography. In: *Computers and Geotechnics* 76, pp. 140–146. DOI: 10.1016/j.compgeo.2016.02.019.

van Aarle, W., W. J. Palenstijn, J. Cant, E. Janssens, F. Bleichrodt, A. Dabravolski, J. De Beenhouwer, K. J. Batenburg, and J. Sijbers (2016): Fast and flexible X-ray tomography using the ASTRA toolbox. In: *Optics Express* 24(22), pp. 25129–25147. DOI: 10.1364/OE.24.025129.

van Genuchten, M. T. (1980): A closed-form equation for predicting the hydraulic conductivity of unsaturated soils. In: *Soil Science Society of America Journal* 44(5), pp. 892–898.

Vanapalli, S. K., M. V. Nicotera, and R. S. Sharma (2008): Axis translation and negative water column techniques for suction control. In: *Geotechnical and Geological Engineering* 26(6), pp. 645–660.

Viggiani, G., E. Andò, E. Takano, and J. C. Santamarina (2015): Laboratory X-ray Tomography: A Valuable Experimental Tool for Revealing Processes in Soils. In: *Geotechnical Testing Journal* 38(1). DOI: 10.1520/GTJ20140060.

Wang, J., P. Lambert, T. De Kock, V. Cnudde, and B. François (2019): Investigation of the effect of specific interfacial area on strength of unsaturated granular materials by X-ray tomography. In: *Acta Geotechnica* 14, pp. 1545–1559. DOI: 10.1007/s11440-019-00765-2.

Wang, X., C. Chen, K. Binder, U. Kuhn, U. Pöschl, H. Su, and Y. Cheng (2018): Molecular dynamics simulation of the surface tension of aqueous sodium chloride: from dilute to highly supersaturated solutions and molten salt. In: *Atmospheric Chemistry and Physics* 18, pp. 17077–17086. DOI: 10.5194/acp-18-17077-2018.

White, D. J., W. A. Take, and M. D. Bolton (2003): Soil deformation measurement using particle image velocimetry (PIV) and photogrammetry. In: *Géotechnique* 53(7), pp. 619–631. DOI: 10.1680/geot.2003.53.7.619.

White, D. J., M. Randolph, and B. Thompson (2005): An image-based deformation measurement system for the geotechnical centrifuge. In: *International Journal of Physical Modelling in Geotechnics* 5(3), pp. 1–12. DOI: 10.1680/ijpmg.2005.050301.

Wiebicke, M. (2020): Experimental analysis of the evolution of fabric in granular soils upon monotonic loading and load reversals. PhD thesis, TU Dresden University.

Wiebicke, M., E. Andò, E. Salvatore, G. Viggiani, and I. Herle (2017a): Experimental measurement of granular fabric and its evolution under shearing. In: *Proc. of Powders & Grains 2017, EPJ Web of Conferences 140, 02020.* DOI: 10.1051/epjconf/201714002020.

Wiebicke, M., E. Andò, I. Herle, and G. Viggiani (2017b): On the metrology of interparticle contacts in sand from x-ray tomography images. In: *Measurement Science and Technology* 28. DOI: 10.1088/1361-6501/aa8dbf.

Wiebicke, M., E. Andò, V. Šmilauer, I. Herle, and G. Viggiani (2019): A benchmark strategy for the experimental measurement of contact fabric. In: *Granular Matter* 21(3). DOI: 10.1007/s10035-019-0902-x.

Wijnen, B., E. J. Hunt, G. C. Anzalone, and J. M. Pearce (2014): Open-Source Syringe Pump Library. In: *PLoS ONE* 9(9). DOI: 10.1371/journal.pone.0107216.

Wildenschild, D., J. W. Hopmans, C. M. P. Vaz, M. L. Rivers, D. Rikard, and B. S. B. Christensen (2002): Using X-ray computed tomography in hydrology: systems, resolutions, and limitations. In: *Journal of Hydrology* 267, pp. 285–297. DOI: 10.1016/S0022-1694(02)00157-9.

Wildenschild, D., J. W. Hopmans, A. J. R. Kent, and M. L. Rivers (2005): Quantitative analysis of flow processes in a sand using synchrotron-based x-ray microtomography. In: *Vadose Zone Journal* 4(1), pp. 112–126. DOI: 10.2113/4.1.112.

Willett, C. D., S. A. Johnson, M. J. Adams, and J. P. K. Seville (2007): Pendular Capillary Bridges. In: *Handbook of Powder Technology*. Ed. by A. D. Salman, M. J. Hounslow, and J. P. K. Seville. Vol. 11. Elsevier Science B.V. Chap. 28, pp. 1317–1351. DOI: 10.1016/S0167-3785(07)80063-7.

Yan, W. M. and Y. Shi (2015): Visualisation of grain crushing using micro-focused X-ray CT scanning. In: *Proc. of the TC105 ISSMGE International Symposium on Geomechanics from Micro to Macro, Cambridge, UK*. Vol. 2, pp. 1131–1135.

Yerro, A., E. E. Alonso, and N. M. Pinyol (2015): The material point method for unsaturated soils. In: *Géotechnique* 65(3), pp. 201–217. DOI: 10.1680/geot.14.P.163.

Zhao, B. D., J. Wang, and M. R. Coop (2015): Investigation of the fracture behaviour of individual LBS particle using Nanofocus X-ray CT. In: *Proc. of the TC105 ISSMGE International Symposium on Geomechanics from Micro to Macro, Cambridge, UK*. Vol. 2, pp. 1125–1129.

Zhuang, L. (2017): Advanced Theories of Water Infiltration and Redistribution in Porous Media; Experimental Studies and Modeling. PhD thesis, Utrecht University, Utrecht, Netherlands.

Zienkiewicz, O. C., C. T. Chang, and P. Bettess (1980): Drained, undrained, consolidating dynamic behaviour assumptions in soils. In: *Géotechnique* 30, pp. 385–395.

Zienkiewicz, O. C., A. H. C. Chan, M. Pastor, B. A. Schrefler, and T. Shiomi (1999): *Computational Geomechanics with Special Reference to Earthquake Engineering*. John Wiley & Sons.

Symbols and units

Upper-case letters

A	Cross sectional area, page 162	[m^2]
A_i	Interfacial area per unit volume of phase couple i, page 25	[m^2/m^3]
Bo	Bond number, page 23	[-]
Ca	Capillary number, page 23	[-]
Eo	Eötvös number, page 23	[-]
F	Force, page 69	[N]
$\boldsymbol{F}_{ads}$	Vector of adhesive force (LBM), page 216	[mu/(lu^{2}ts^2)]
F_c	Capillary force, page 13	[N]
F_γ	Contribution of surface tension to capillary force, page 13	[N]
$\boldsymbol{F}_{int}$	Vector of inter-particle force (LBM), page 215	[mu/(lu^{2}ts^2)]
F_{p_c}	Contribution of capillary pressure to capillary force, page 13	[N]
F^*	Dimensionless force, page 69	[-]
G	Parameter for the strength of inter-particle force (LBM), page 215	[lu^3/(mu ts^2)]
H	Mean curvature, page 12	[1/m]
I	Intensity of radiation, page 30	[1/(m^2 s)]
I_0	Initial intensity of radiation, page 30	[1/(m^2 s)]
J_{sa}	Mean curvature of the solid-air interface, page 25	[1/m]
J_{sw}	Mean curvature of the solid-water interface, page 25	[1/m]
L	Characteristic length, page 23	[m]
M	Number of velocity directions (LBM), page 212	[-]

N Model dimension (LBM), page 212 . . . . . [-]

N Number of samples, page 45 . . . . . [-]

$N_{\text{cells, f}}$ Number of fluid cells/pore cells (LBM), page 154 . . . . . [-]

$N_{\text{cells, g}}$ Number of gas cells (LBM), page 154 . . . . . [-]

$N_{\text{cells, l}}$ Number of liquid cells (LBM), page 154 . . . . . [-]

Q Physical flow rate, page 162 . . . . . [m^3/s]

Q Volume flow rate (LBM), page 163 . . . . . [lu^3/ts]

Q_{m} Local mass flow rate (LBM), page 163 . . . . . [mu/ts]

R Particle radius, page 69 . . . . . [m]

R Radius of curvature, page 12 . . . . . [m]

R_1 1st main radius of curvature, page 12 . . . . . [m]

R_2 2nd main radius of curvature, page 12 . . . . . [m]

R Gas constant in the Carnahan-Starling EOS (LBM), page 215 . . . . . [$\text{lu}^2/(\text{ts}^2\ \text{tu})$]

R_{c} Radius of the contact line, page 14 . . . . . [m]

R_{p} Pore radius, page 161 . . . . . [m]

S_{a} Air degree of saturation, page 61 . . . . . [-]

S_{e} Effective/normalised degree of saturation, page 21 . . . . . [-]

S_{i} Source term (LBM), page 211 . . . . . [mu/lu^3]

S_{max} Maximum degree of saturation, page 21 . . . . . [-]

S_{r} Degree of saturation, page 16 . . . . . [-]

S_{res} Residual degree of saturation, page 17 . . . . . [-]

T Temperature in the Carnahan-Starling EOS (LBM), page 153 . . . . . [tu]

T_{c} Critical temperature in the Carnahan-Starling EOS (LBM), page 153 . . . . . [tu]

V Volume, page 25 . . . . . [m^3]

V_{liq} Liquid volume of capillary bridge, page 16 . . . . . [m^3]

V_{p} Pore volume, page 99 . . . . . [m^3]

V_{w} Water volume, page 60 . . . . . [m^3]

Lower-case letters

a	Parameter in the Carnahan-Starling EOS (LBM), page 215	[$lu^5/(mu\ ts^2)$]
a^{nw}	Specific nonwetting-wetting fluid (air-water) interfacial area, page 25	[m^2/m^3]
a^{s}	Specific solid surface area (specific surface), page 25	[m^2/m^3]
a^{sw}	Specific solid-wetting fluid (solid-water) interfacial area, page 25	[m^2/m^3]
b	Parameter in the Carnahan-Starling EOS (LBM), page 215	[lu^3/mu]
c	Lattice speed (LBM), page 212	[lu/ts]
c_c	Capillary cohesion, page 55	[N/m^2]
c_s	Speed of sound (LBM), page 162	[lu/ts]
d	Diameter, page 6	[m]
d_{10}	Grain diameter at 10% passing, page 41	[m]
d_{50}	Grain diameter at 50% passing, page 41	[m]
d_{max}	Maximum grain diameter, page 41	[m]
e	Void ratio, page 93	[-]
e_0	Initial void ratio, page 46	[-]
$\boldsymbol{e}_i$	Vector of discrete velocity directions (LBM), page 211	[lu/ts]
e_{max}	Maximum void ratio, page 41	[-]
e_{min}	Minimum void ratio, page 41	[-]
f_i	Density distribution function for velocity direction i (LBM), page 211	[mu/lu^3]
f_i^{eq}	Equilibrium density distribution function (LBM), page 211	[mu/lu^3]
g	Gravitational acceleration, page 12	[m/s^2]
h_c	Height of capillary rise, page 11	[m]
k^{nw}	Material parameter, page 25	[N/m]
l	Separation distance, page 69	[m]
l_c	Specific length of contact line, page 95	[m/m^3]
l_r	Rupture length of capillary bridge, page 16	[m]
l^*	Dimensionless separation distance, page 69	[-]

l_x Domain size in x-direction (LBM), page 153 ..... [lu]

l_y Domain size in y-direction (LBM), page 153 ..... [lu]

l_z Domain size in z-direction (LBM), page 153 ..... [lu]

m Empirical exponent in the van Genuchten (1980) model, page 21 ..... [-]

m_d Dry mass, page 76 ..... [kg]

n Empirical exponent in the van Genuchten (1980) model, page 21 ..... [-]

n Porosity, page 25 ..... [-]

p Pressure (LBM), page 215 ..... [mu/(lu ts^2)]

$\bar{p}$ Mean pressure (LBM), page 154 ..... [mu/(lu ts^2)]

r Radius of capillary, page 11 ..... [m]

s Matric suction, page 10 ..... [N/m^2]

t Radius or radial coordinate in polar coordinates (CT), page 33 ..... [m]

t Time, page 61 ..... [s]

t Time (LBM), page 211 ..... [ts]

$\boldsymbol{u}$ Displacement vector, page 38 ..... [m]

u_a Pore air pressure, page 11 ..... [N/m^2]

u_w Pore water pressure, page 11 ..... [N/m^2]

$\boldsymbol{v}$ Macroscopic fluid velocity vector (LBM), page 214 ..... [lu/ts]

v Average velocity of fluid interface, page 23 ..... [m/s]

v Pore-based flow velocity, page 162 ..... [m/s]

v_f Filter velocity, page 162 ..... [m/s]

v_{sep} Separation velocity, page 69 ..... [m/s]

w Gravimetric water content, page 54 ..... [-]

$\boldsymbol{x}$ Position vector (LBM), page 211 ..... [lu]

Greek symbols

α Empirical parameter in the van Genuchten (1980) model, page 21 ..... [1/kPa]

α Meniscus slope angle, page 14 ..... [°]

χ Bishop parameter/effective stress parameter, page 24 . . . . . [-]

χ_{sw} Fraction of wetted solid surface area per unit volume, page 25 . . . . . [-]

ΔS_{r} Difference in degree of saturation due to air entrapment, page 17 . . . . . [-]

Δt Time step (LBM), page 162 . . . . . [ts]

$\Delta\varepsilon$ Strain increment, page 76 . . . . . [-]

ε_1 Axial strain, page 55 . . . . . [-]

ε_{v} Volumetric strain, page 78 . . . . . [-]

η Dynamic viscosity, page 23 . . . . . [kg/(m s)]

η_{n} Nonwetting phase dynamic viscosity (LBM), page 161 . . . . . [mu/(lu ts)]

η_{w} Wetting phase dynamic viscosity (LBM), page 161 . . . . . [mu/(lu ts)]

γ Interfacial/surface tension, page 9 . . . . . [N/m]

Γ_{sa} Interfacial energy of the solid-air interface, page 25 . . . . . [N/m]

Γ_{sw} Interfacial energy of the solid-water interface, page 25 . . . . . [N/m]

γ_{w} Surface tension of the wetting phase (LBM), page 161 . . . . . [mu/ts^2]

κ Permeability, page 23 . . . . . [m^2]

μ Linear attenuation coefficient, page 30 . . . . . [1/m]

ν Kinematic fluid viscosity (LBM), page 213 . . . . . [lu^2/ts]

ω Numerical weight (LBM), page 214 . . . . . [-]

ψ Wadell's sphericity, page 94 . . . . . [-]

ψ Mean-field potential (LBM), page 215 . . . . . [mu/lu^3]

φ' Effective friction angle, page 46 . . . . . [°]

ρ Macroscopic density (LBM), page 153 . . . . . [mu/lu^3]

$\rho_{\mathrm{boundary,\,g}}$ Boundary density for gas (LBM), page 153 . . . . . [mu/lu^3]

$\rho_{\mathrm{boundary,\,l}}$ Boundary density for liquid (LBM), page 153 . . . . . [mu/lu^3]

ρ_{w} Density of water, page 12 . . . . . [kg/m^3]

ρ_{s} Grain density, page 41 . . . . . [kg/m^3]

ρ_{wall} Wall density (LBM), page 153 . . . . . [mu/lu^3]

σ	Total stress, page 24	$[\mathrm{N/m^2}]$
σ'	Effective stress, page 24	$[\mathrm{N/m^2}]$
σ_1	Total axial stress, page 55	$[\mathrm{N/m^2}]$
$\sigma_{\max}$	Uniaxial compression strength, page 55	$[\mathrm{N/m^2}]$
σ_s	Suction stress, page 24	$[\mathrm{N/m^2}]$
τ	Relaxation time (LBM), page 153	[ts]
Θ	Projection or polar angle in polar coordinates (CT), page 33	[°]
θ	Contact angle, page 9	[°]

Appendix A

List of abbreviations

ADC	Analog Digital Converter
AEV	Air Entry Value
BGK	Bhatnagar-Gross-Krook (LBM)
BPM	Bonded-Particle Model
CAD	Computer-Aided Design
CCD	Charge-Coupled Device
CFD	Computational Fluid Dynamics
CPU	Central Processing Unit
CT	Computed Tomography
DDIC	Discrete Digital Image Correlation
DEM	Discrete Element Method
DESY	Deutsches Elektronen-Synchrotron
DFG	Deutsche Forschungsgemeinschaft
DIN	Deutsches Institut für Normung e.V.
e. g.	*Exempli gratia* (for example)
EOS	Equation Of State
et al.	*Et alii* (and others)
etc.	*Et cetera* (and the rest)
FabLab	Fabrication Laboratory (MakerSpace)
FCM	Finite Cell Method
FDEM	Combined Finite-Discrete Element Method
FE	Finite Element
FEM	Finite Element Method
GB	Gigabyte
GHz	Gigahertz
GPIO	General Purpose Input/Output
GPU	Graphics Processing Unit
HD	High Definition
HPC	High-Performance Computing
i. e.	*Id est* (that is)
ILL	Institut Laue-Langevin

keV	Kilo electron volt
LBM	Lattice Boltzmann Method
LS-DEM	Level Set Discrete Element Method
lu	Lattice unit (LBM)
MRI	Magnetic Resonance Imaging
mu	Mass unit (LBM)
NASA	National Aeronautics and Space Administration
NeXT	Neutron and X-ray Tomography
OpenMP	Open Multi-Processing
PEEK	Polyether Ether Ketone
PintPFS	Processes in natural and technical Particle-Fluid-Systems
PIV	Particle Image Velocimetry
px	Pixel/s
RAM	Random-Access Memory
REV	Representative Elementary Volume
SEM	Scanning Electron Microscope
spam	Software for practical analysis of materials
SPM	Scanning Probe Microscope
SWCC	Soil-Water Characteristic Curve
TEM	Transmission Electron Microscope
TIFF	Tagged Image File Format
ts	Time step (LBM)
tu	Temperature unit (LBM)
TUHH	Hamburg University of Technology
vs.	*Versus* (against)
vx	Voxel/s
WRC	Water Retention Curve

Appendix B

Further selected results

B.1 Deviatoric strain during uniaxial compression

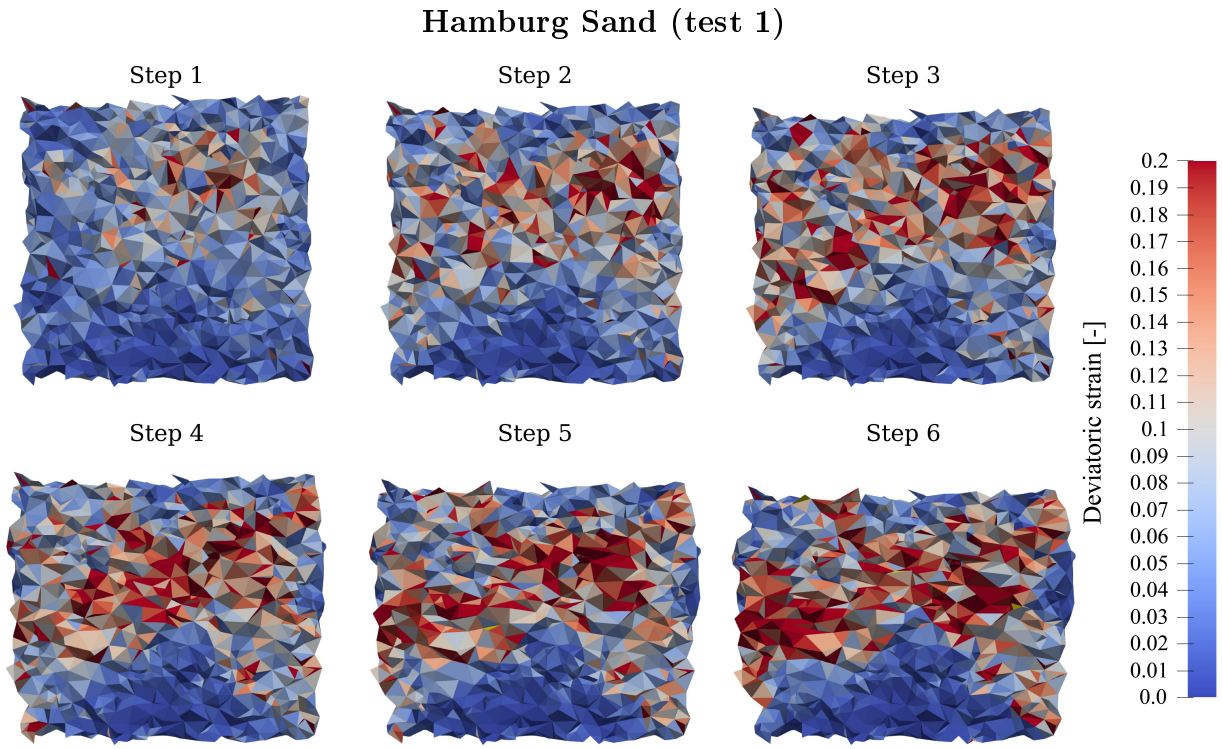


Figure B.1: Incremental deviatoric strain fields (second invariant of the strain tensor computed in finite strains on tetrahedra and shown in x-direction using a "crinkle clip" to cut around them rather than through them) in the middle of the driest specimen of Hamburg Sand from Milatz *et al.* (2021b)

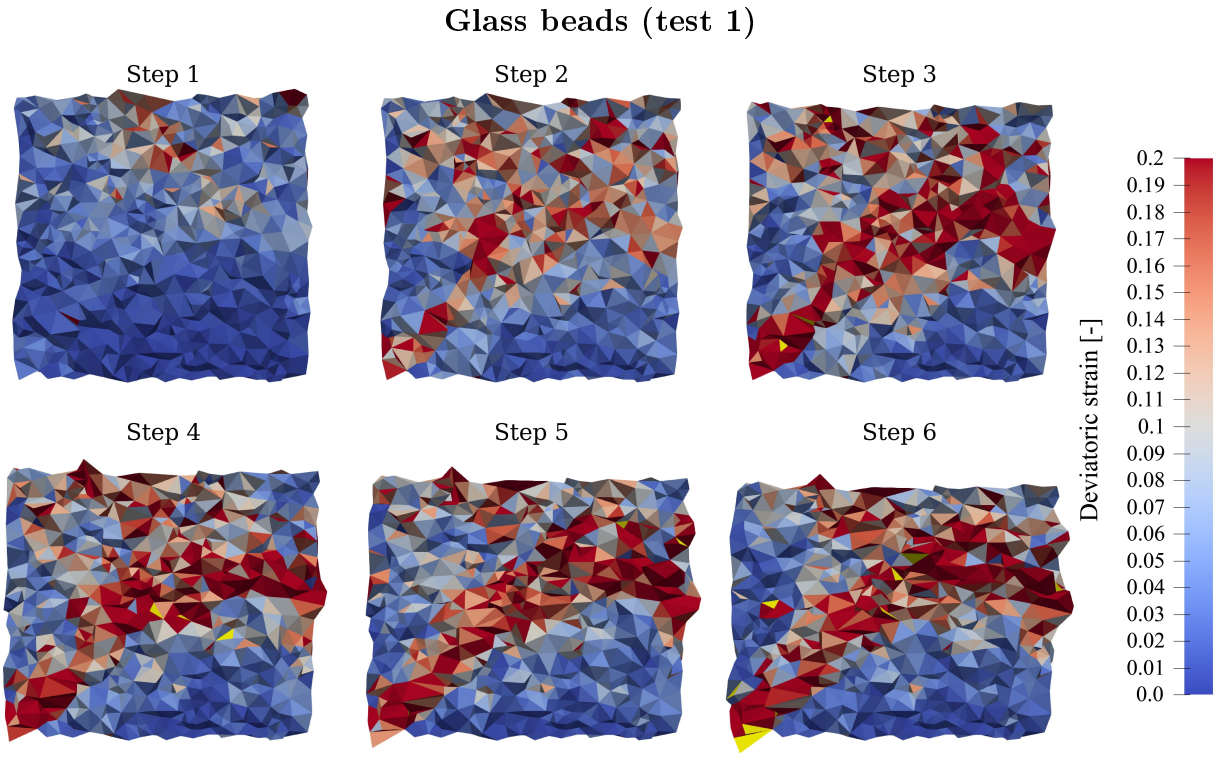


Figure B.2: Incremental deviatoric strain fields (second invariant of the strain tensor computed in finite strains on tetrahedra and shown in x-direction using a "crinkle clip" to cut around them rather than through them) in the middle of the driest specimen of glass beads from Milatz *et al.* (2021b)

B.2 Volumetric strain during uniaxial compression

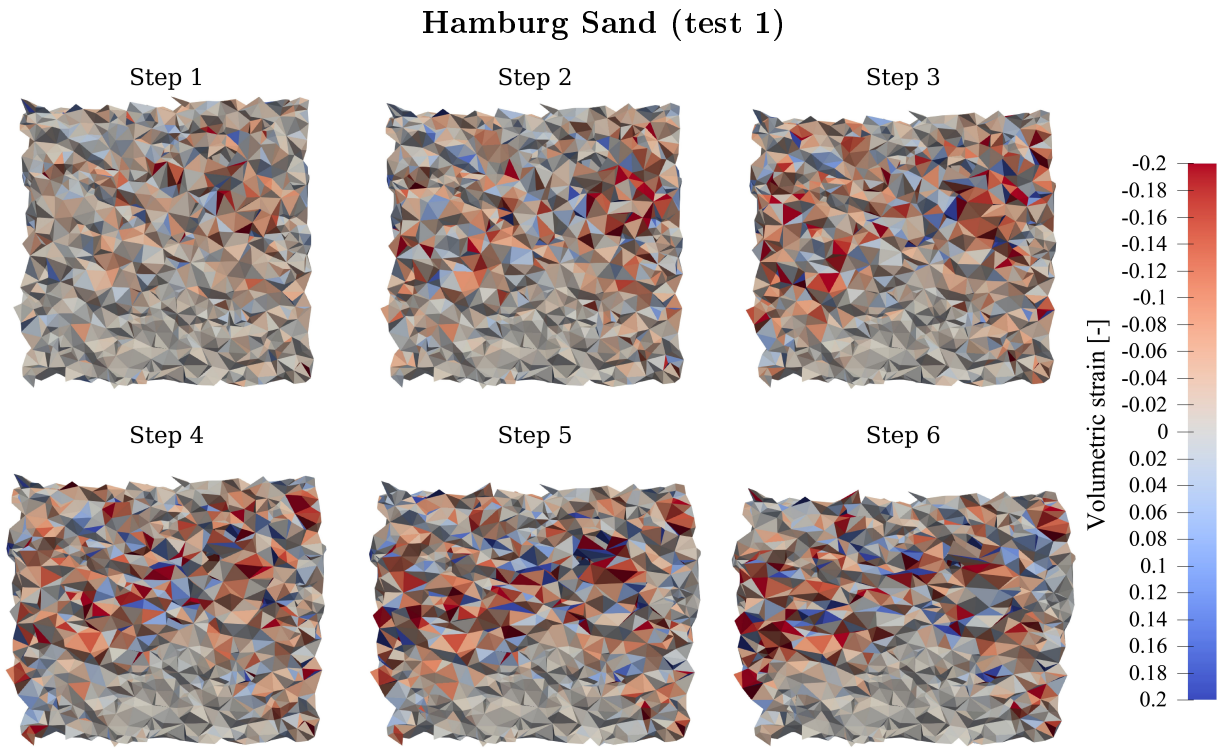


Figure B.3: Incremental volumetric strain fields (first invariant of the strain tensor computed in finite strains on tetrahedra and shown in x-direction using a "crinkle clip" to cut around them rather than through them) in the middle of the driest specimen of Hamburg Sand

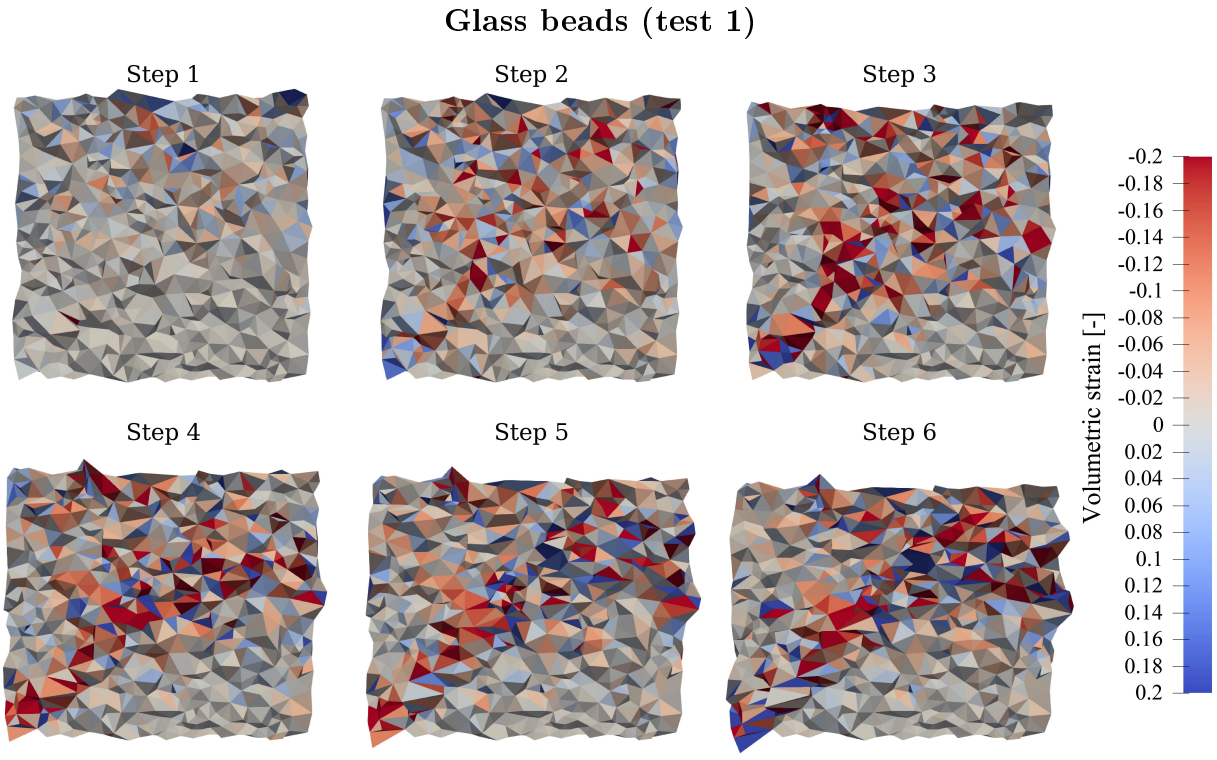


Figure B.4: Incremental volumetric strain fields (first invariant of the strain tensor computed in finite strains on tetrahedra and shown in x-direction using a "crinkle clip" to cut around them rather than through them) in the middle of the driest specimen of glass beads

B.3 Evolution of grain contacts during uniaxial compression

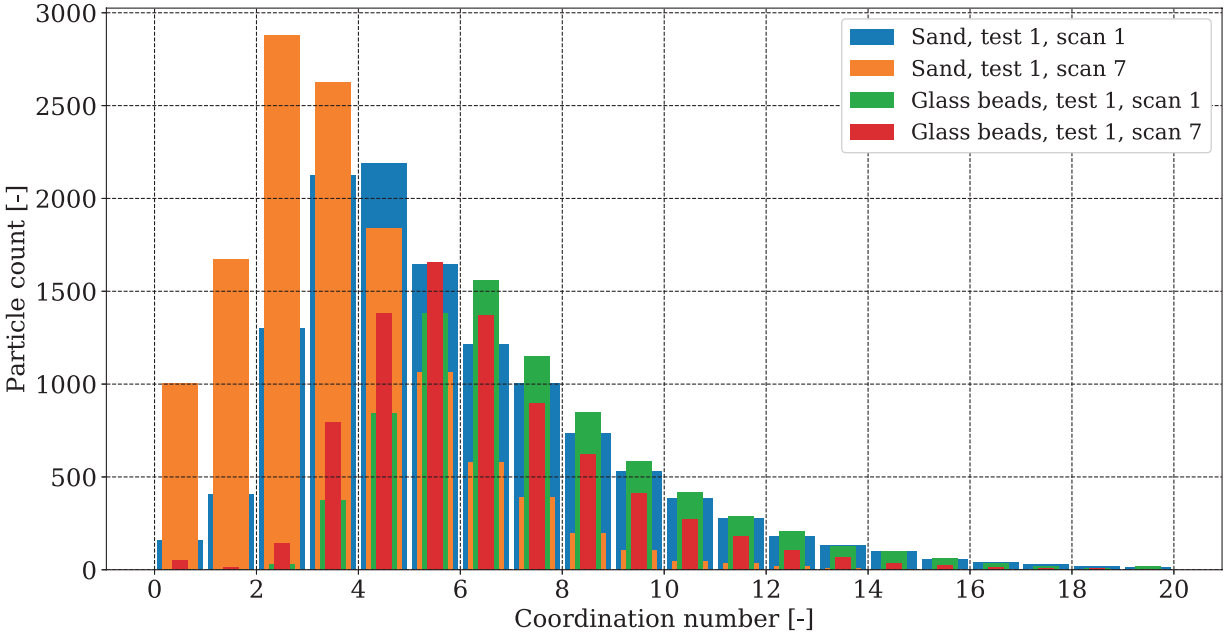
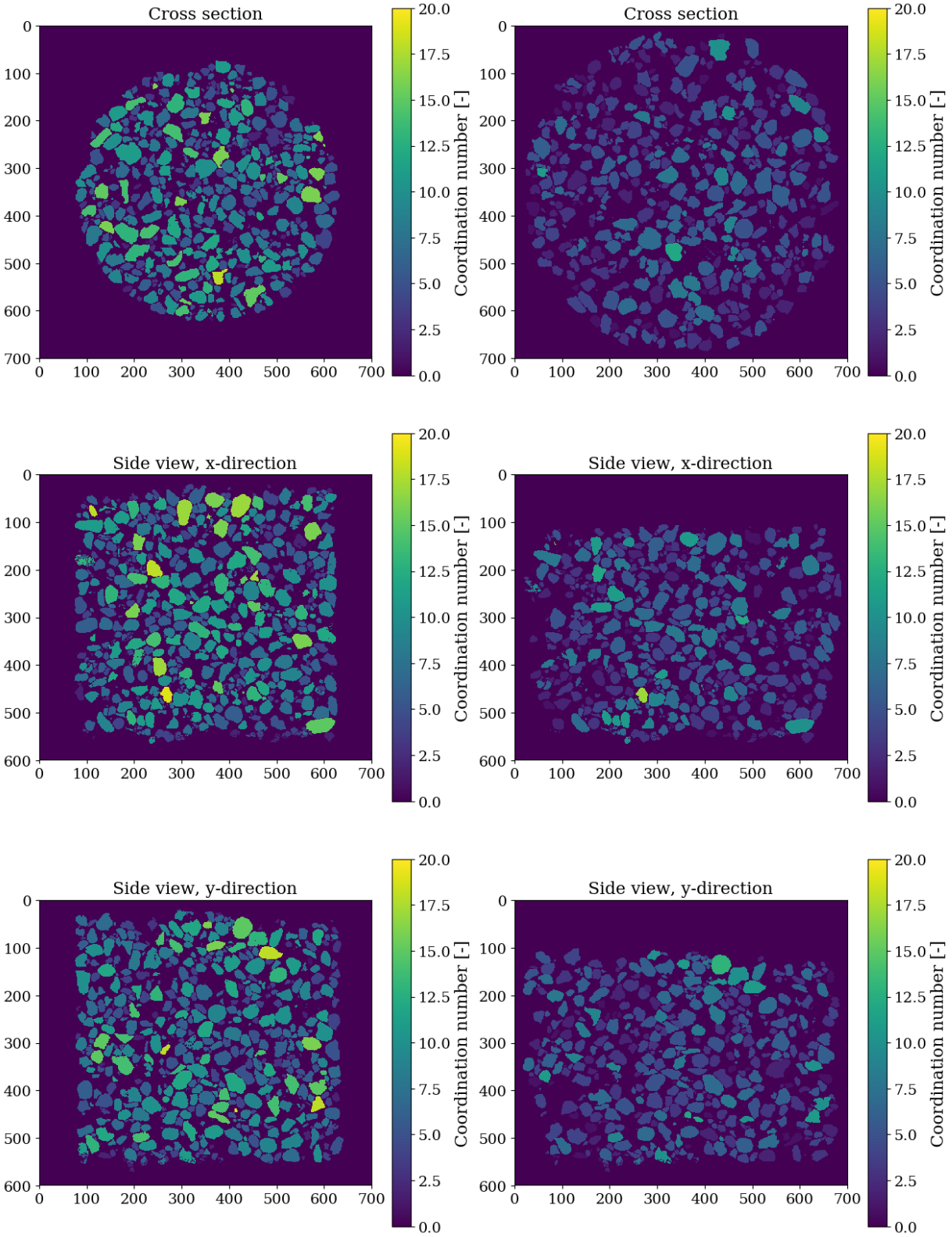
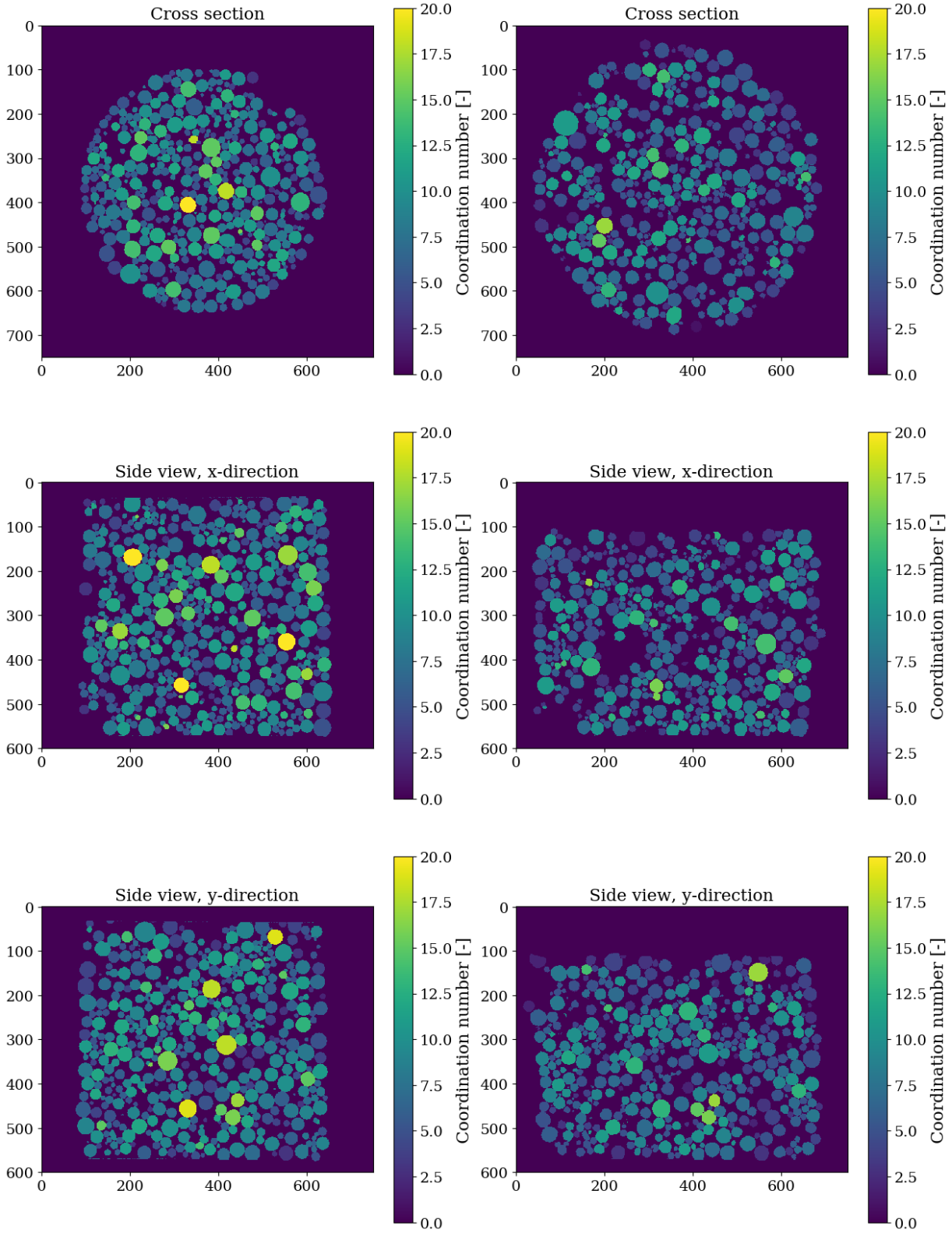


Figure B.5: Histogram-based comparison of the development of coordination numbers in a specimen of Hamburg Sand and glass beads (test 1) from Milatz *et al.* (2021b)



Sand, test 1, scan 1 Sand, test 1, scan 7

Figure B.6: Visualisation of coordination numbers for every grain in a specimen of Hamburg Sand (test 1) in middle slices of the cross section and viewed from both sides (Milatz *et al.*, 2021b)



Glass beads, test 1, scan 1 Glass beads, test 1, scan 7

Figure B.7: Visualisation of coordination numbers for every grain in a specimen of glass beads (test 1) in middle slices of the cross section and viewed from both sides (Milatz *et al.*, 2021b)

B.4 Monotonic straining of capillary bridges

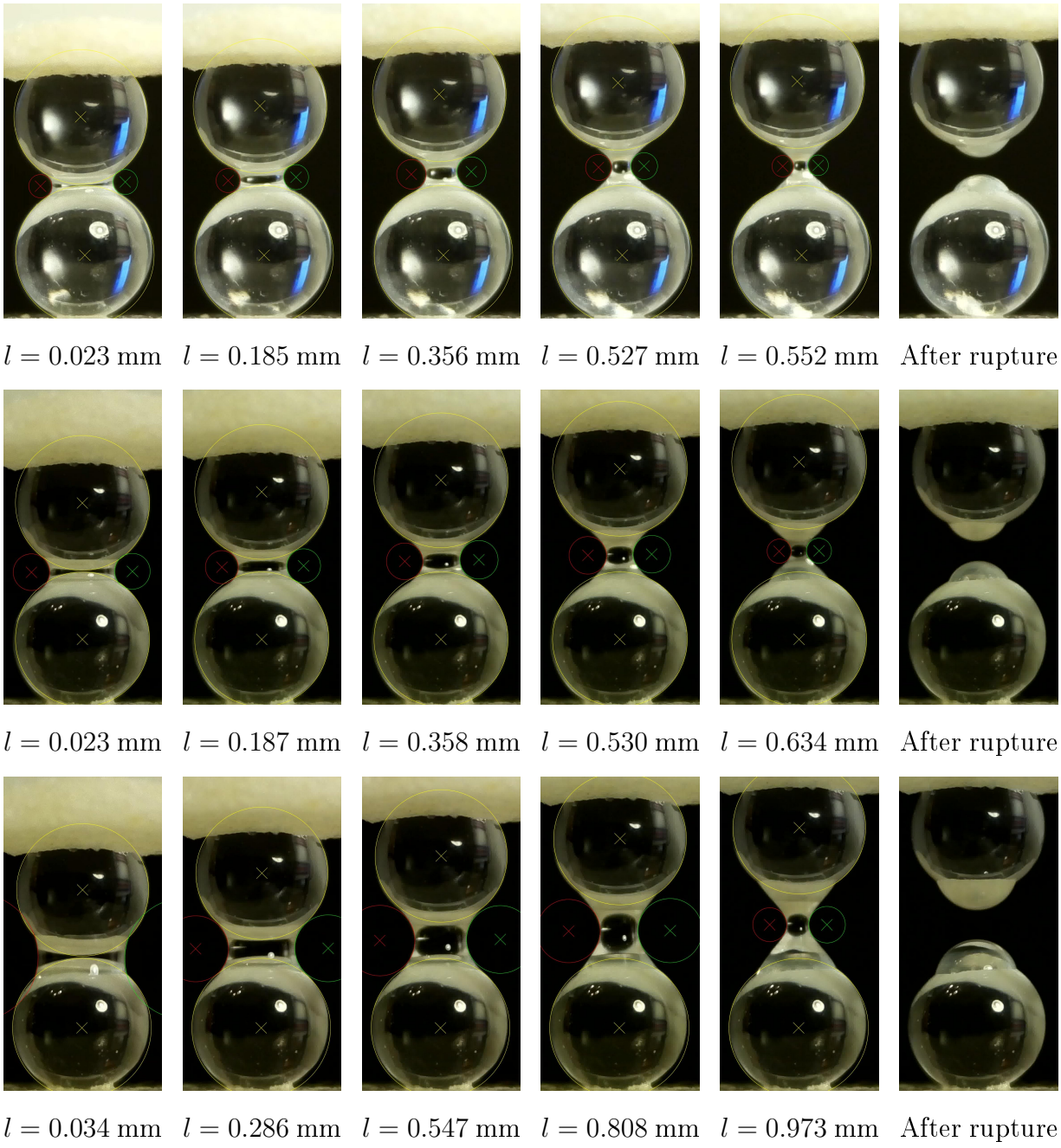
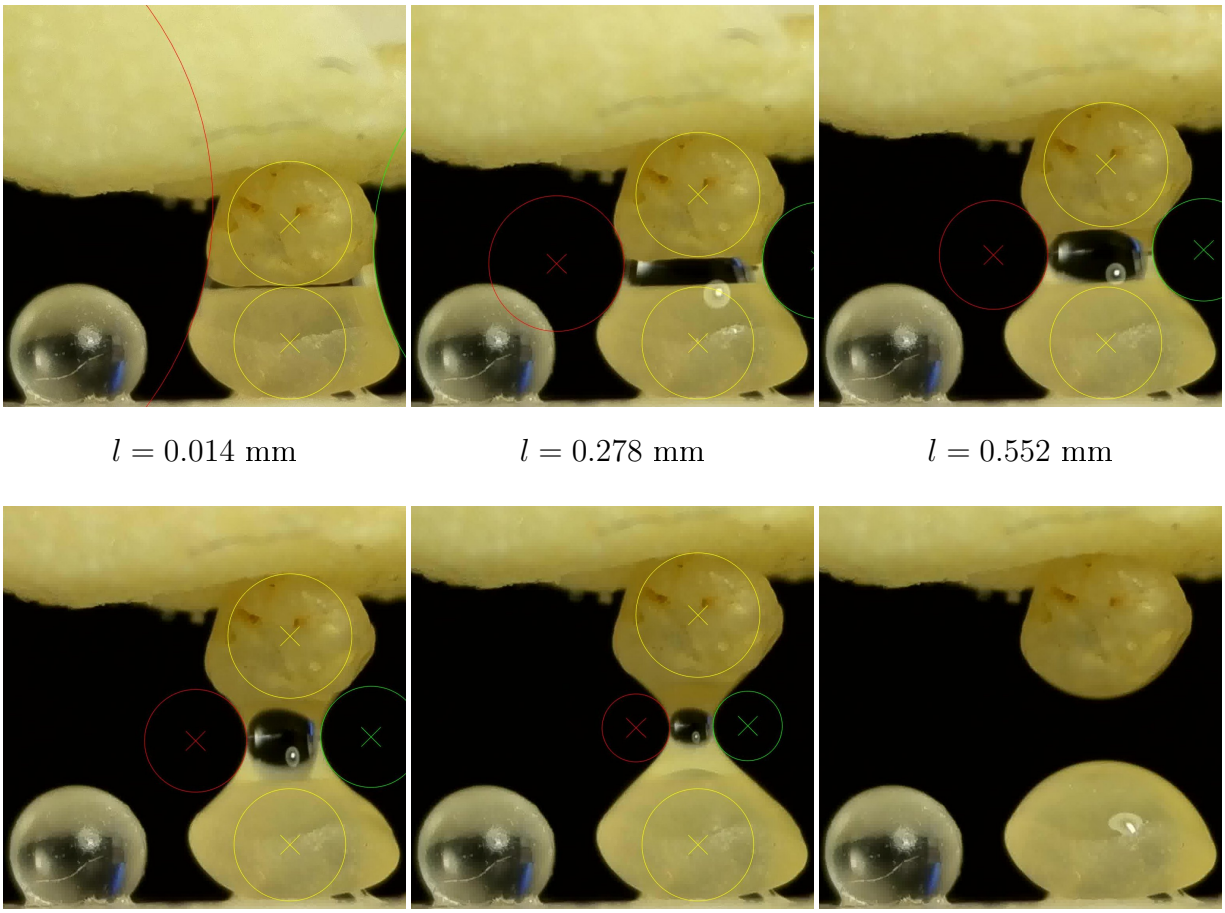


Figure B.8: Image sequences during monotonic straining of capillary bridges with different initial liquid volumes V_{liq} in between glass beads with $d \approx 2$ mm. Top row: $V_{\text{liq}} = 0.106$ mm^3, middle row: $V_{\text{liq}} = 0.122$ mm^3, bottom row: $V_{\text{liq}} = 0.412$ mm^3



$l = 0.014$ mm $l = 0.278$ mm $l = 0.552$ mm

$l = 0.825$ mm $l = 1.016$ mm After rupture

Figure B.9: Image sequence during monotonic straining of a capillary bridge with initial liquid volume $V_{\text{liq}} = 0.451$ mm^3 in between Hamburg Sand grains. The diameter of the reference glass bead in the images is $d \approx 1.25$ mm. The diameter of the yellow circles inscribed to the sand grains is $1.02 \leq d \leq 1.13$ mm

B.5 Evolution of air phase during cyclic drainage and imbibition

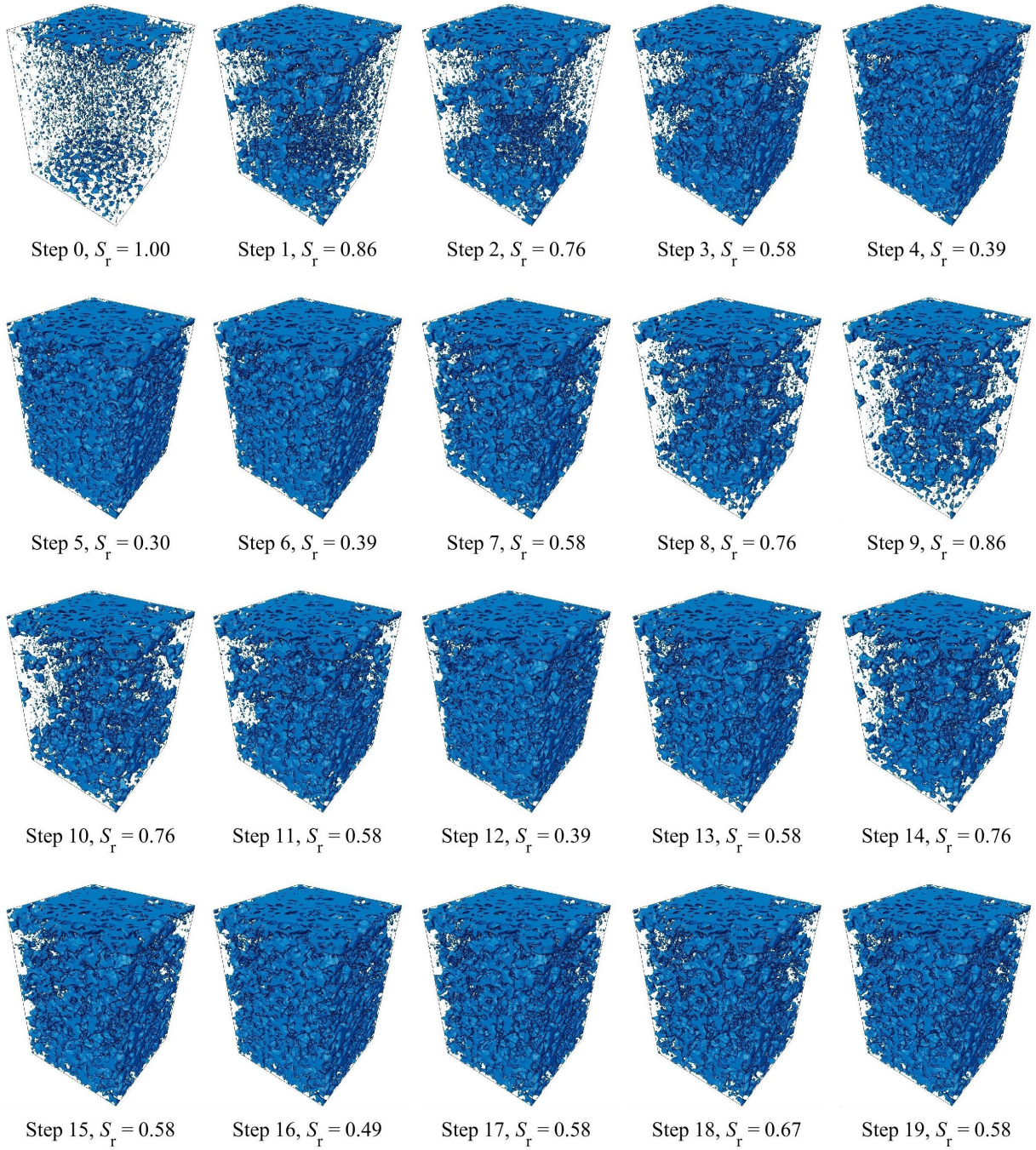


Figure B.10: 3D visualisation of segmented air phase for all 20 time steps in a cyclic drainage and imbibition experiment on a subvolume of 800 px × 800 px × 1145 px (8 mm × 8 mm × 11.45 mm). Step 0 indicates the water saturated initial specimen state. Hydraulic steps and macroscopic degree of saturation according to Fig. 5.14 (Milatz *et al.*, 2022b)

B.6 Evolution of water phase during cyclic drainage and imbibition

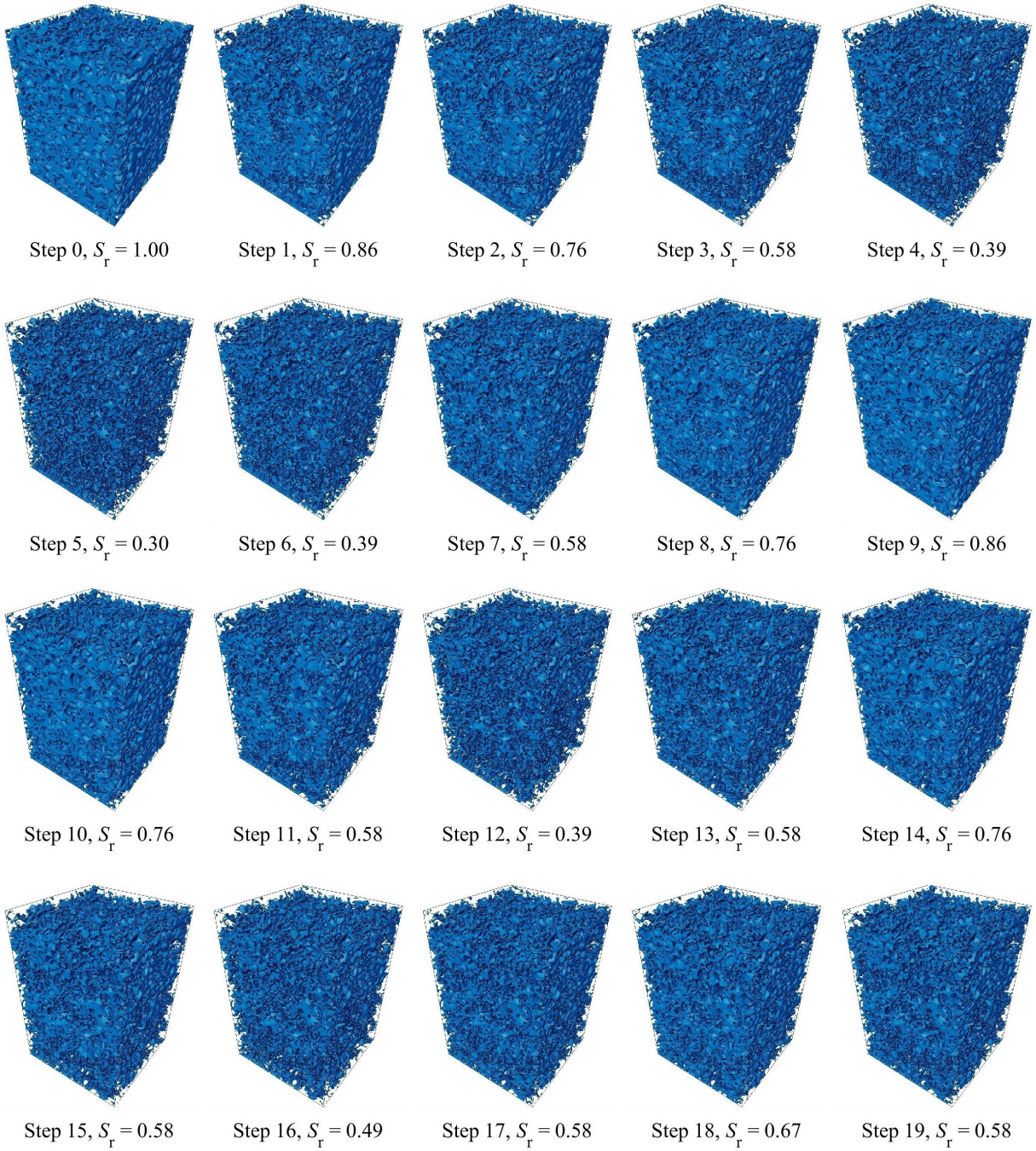


Figure B.11: 3D visualisation of segmented water phase for all 20 time steps in a cyclic drainage and imbibition experiment on a subvolume of 800 px × 800 px × 1145 px (8 mm × 8 mm × 11.45 mm). Step 0 indicates the water saturated initial specimen state. Hydraulic steps and macroscopic degree of saturation according to Fig. 5.14 (Milatz *et al.*, 2022b)

B.7 Evolution of water and air clusters during cyclic drainage and imbibition

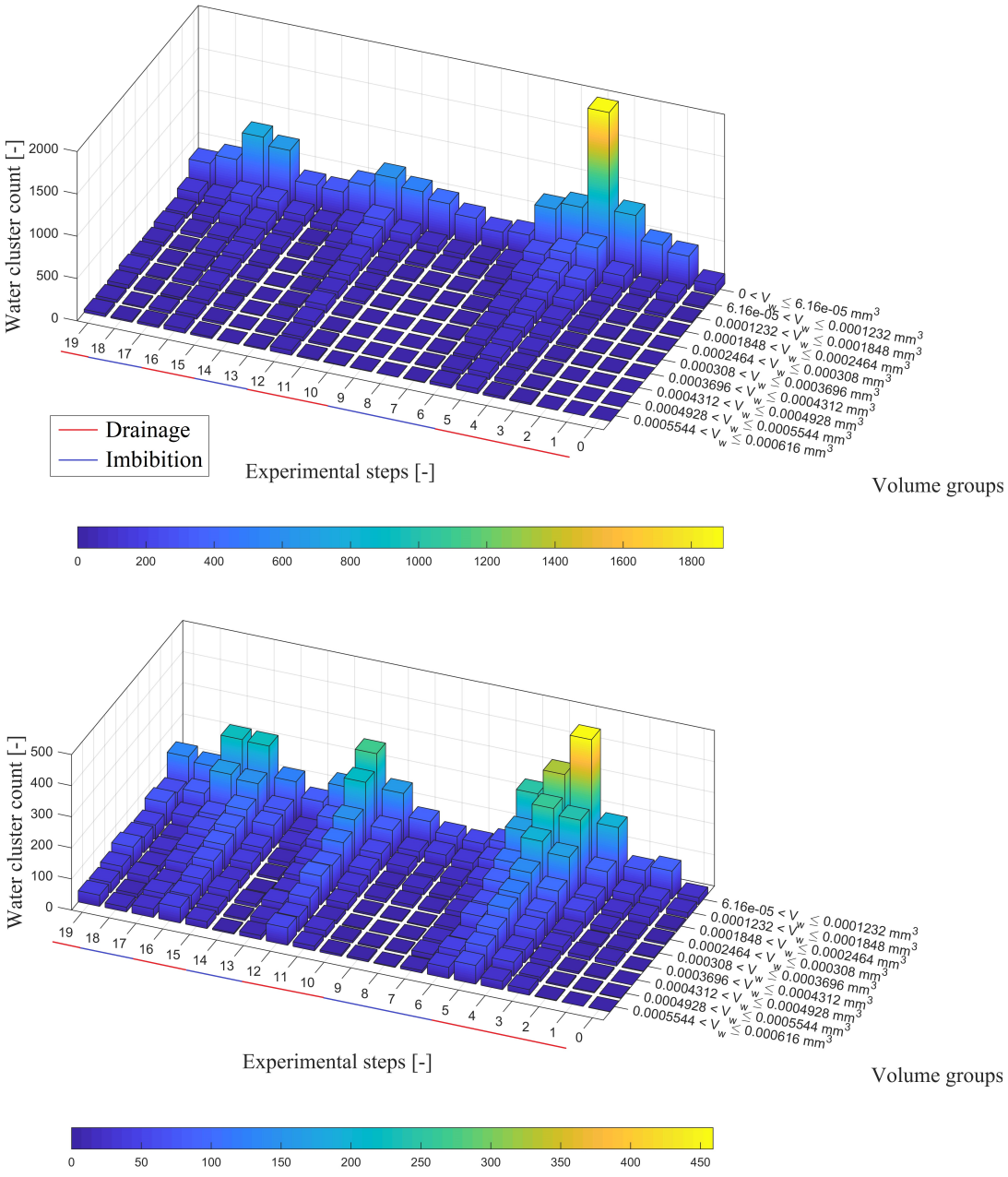


Figure B.12: Histograms showing the evolution of water cluster count in different volume groups. The maximum water cluster volume included is the second largest cluster of the initial configuration with a volume of 0.000616 mm^3 (Milatz *et al.*, 2022b)

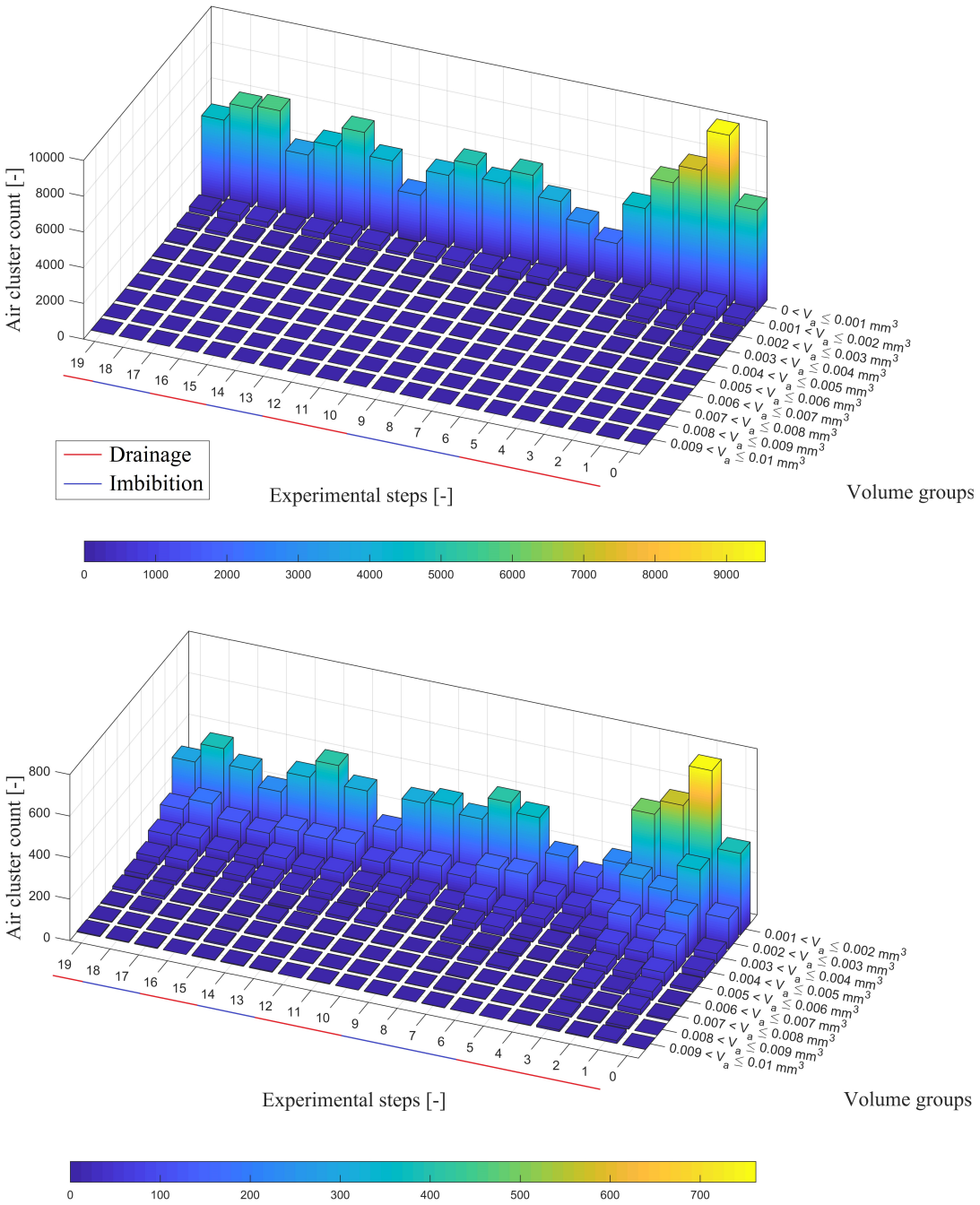
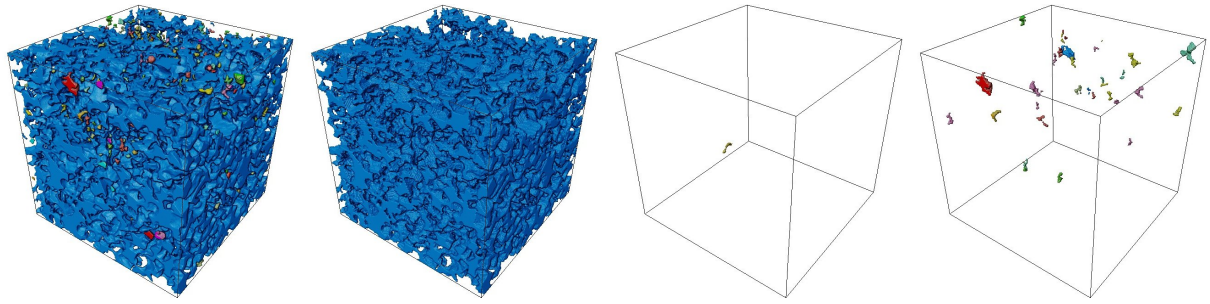
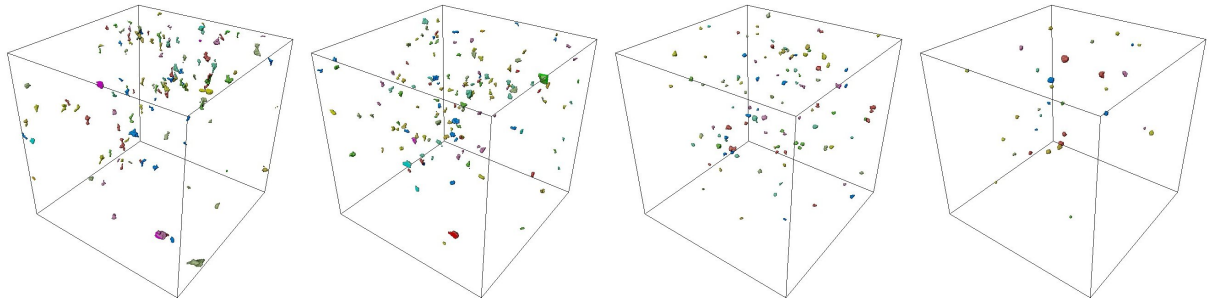


Figure B.13: Histograms showing the evolution of air cluster count in different volume groups. The maximum air cluster volume included is 0.01 mm^3 (Milatz *et al.*, 2022b)

B.8 Characterisation of air clusters by sphericity



All clusters $0.0 < \psi \leq 0.1$ $0.4 < \psi \leq 0.5$ $0.5 < \psi \leq 0.6$



$0.6 < \psi \leq 0.7$ $0.7 < \psi \leq 0.8$ $0.8 < \psi \leq 0.9$ $0.9 < \psi \leq 1.0$

Figure B.14: 3D visualisations of labelled air cluster volumes classified by their sphericity ψ in a central subvolume of 800 px × 800 px × 800 px from CT data after primary drainage. Air clusters with a volume larger than 0.0005 mm^3 are shown. Empty groups classified by ψ are omitted (Milatz *et al.*, 2022b)

B.9 Visualisation of discrete grain motion during primary drainage

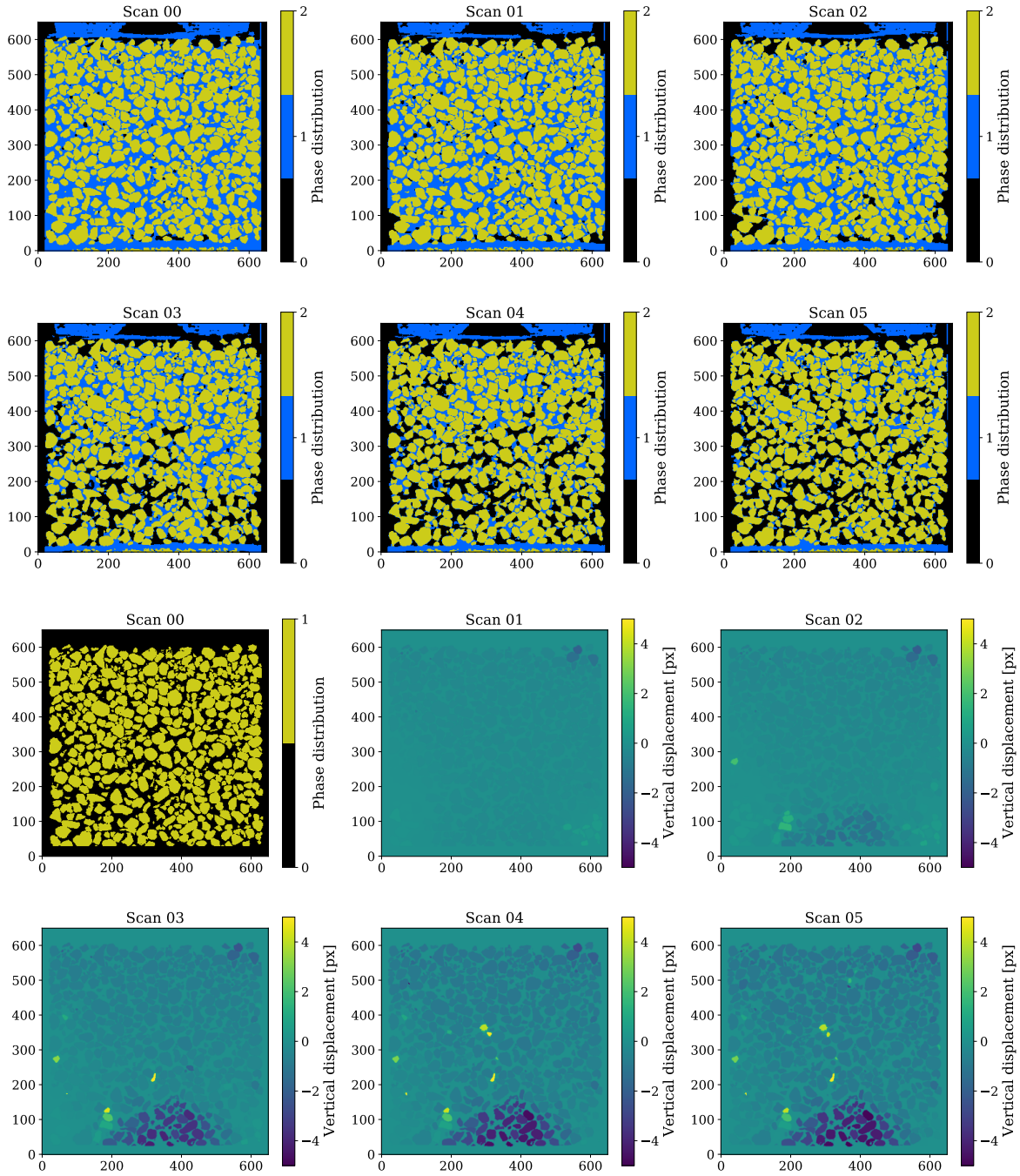


Figure B.15: Phase distributions (top) and corresponding vertical grain displacements (bottom) for the initial state (Scan 00) and five hydraulic steps (Scans 01–05) during primary drainage of Hamburg Sand (view in x-direction) from Milatz *et al.* (2022b)

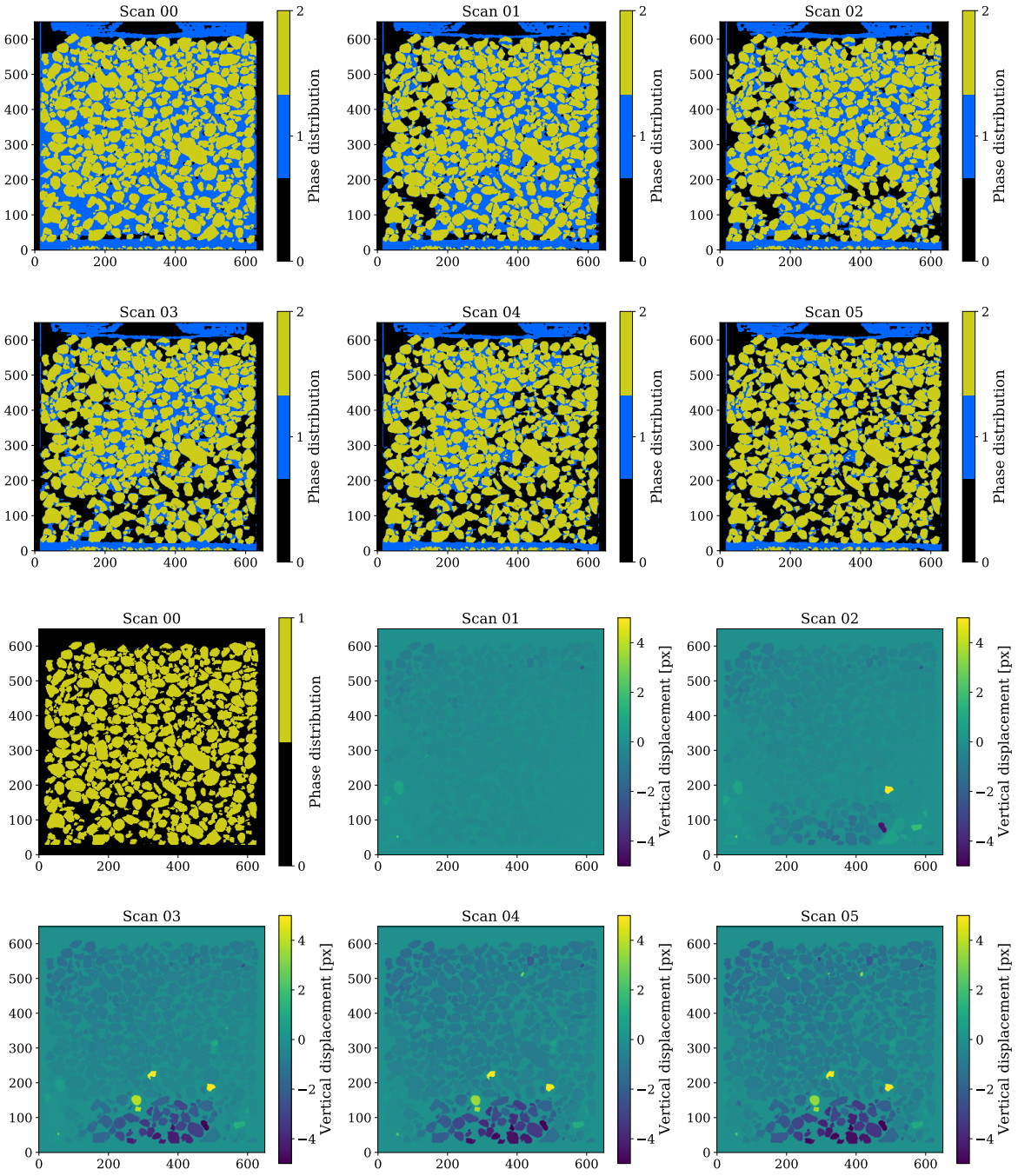
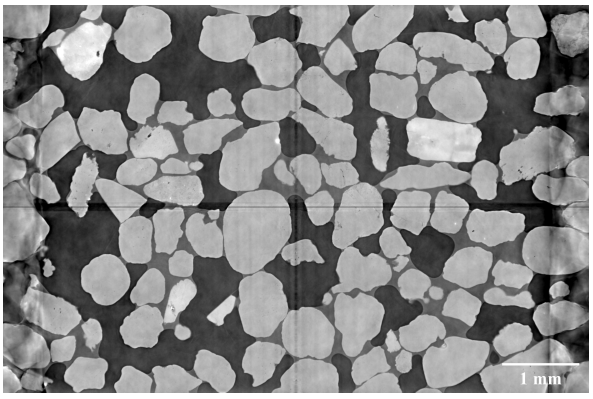
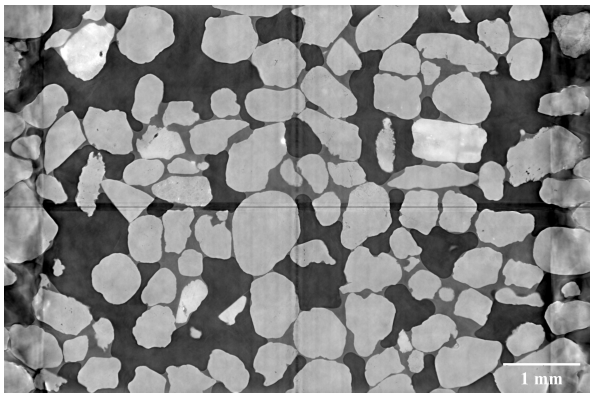


Figure B.16: Phase distributions (top) and corresponding vertical grain displacements (bottom) for the initial state (Scan 00) and five hydraulic steps (Scans 01–05) during primary drainage of Hamburg Sand (view in y-direction) from Milatz *et al.* (2022b)

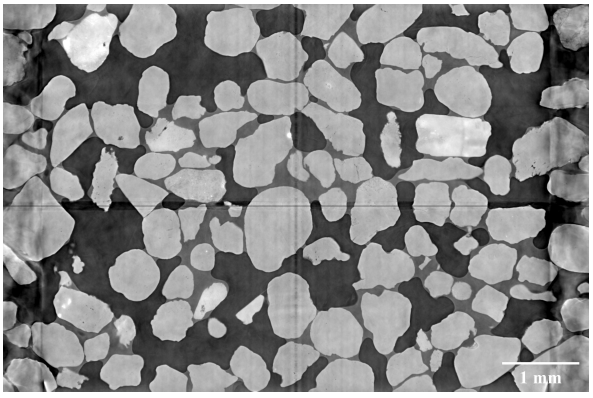
B.10 Synchrotron-based CT imaging of direct shear test



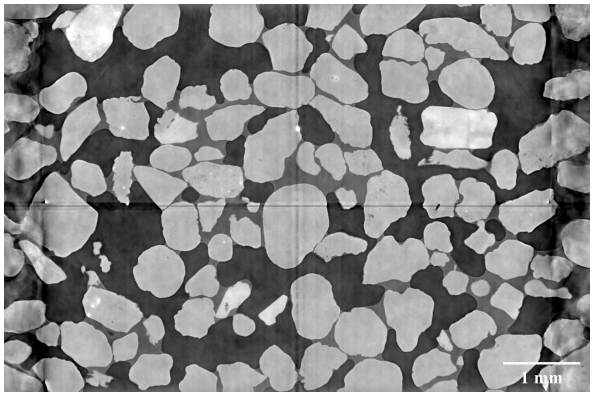
Scan 0: 0.0 mm



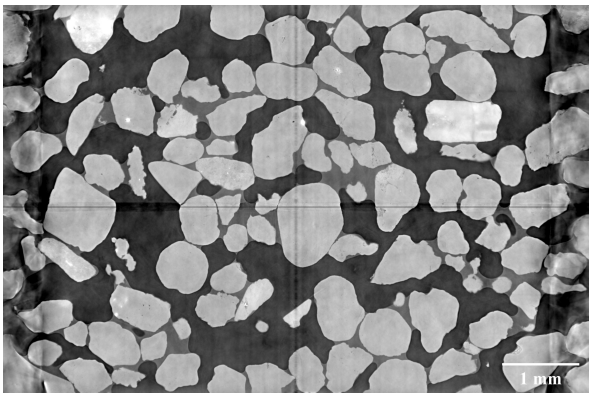
Scan 2: 0.4 mm



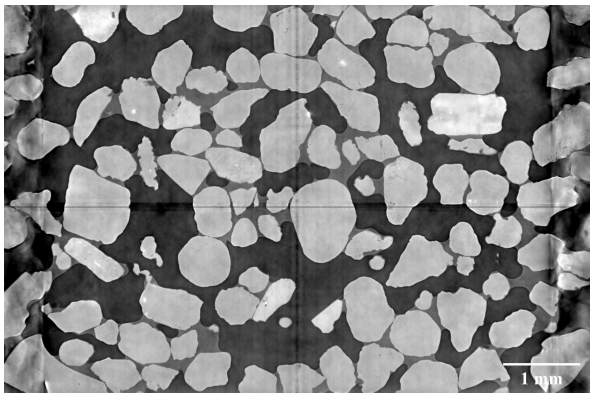
Scan 4: 0.8 mm



Scan 6: 1.2 mm



Scan 8: 1.6 mm



Scan 10: 2.0 mm

Figure B.17: Image sequence during incremental direct shearing of unsaturated Hamburg Sand showing a vertical section through the tomography volume along the shear direction for different shear displacements. The shear plane is indicated by a black horizontal line

Appendix C

Multiphase Lattice Boltzmann Method

In this Appendix, the single-component multiphase Lattice Boltzmann Method (LBM) as an extension to the single-phase LBM for flow simulation is briefly introduced as far as required by the different studies presented in this work. After describing fundamentals of the single-phase LBM, the extension to a single-component multiphase LBM as well as its implementation are presented. The single-component multiphase LBM is applied to simulate capillary phenomena and the water retention behaviour in granular soils with a rigid grain skeleton as described in Chapter 8.

The selected LBM formulation is based on the single-component multiphase formulation and Fortran code presented and discussed in Huang *et al.* (2015). For deeper explanations and further application examples, the interested reader is referred to Huang *et al.* (2015) or other text books, *e. g.*, Krüger *et al.* (2017).

C.1 Fundamentals of single-phase LBM

The LBM as discussed in this work is based on the discretised form of the Boltzmann equation (He and Luo, 1997) given as

$$f_\mathrm{i}(\boldsymbol{x}+\boldsymbol{e}_\mathrm{i}\Delta t,t+\Delta t) = f_\mathrm{i}(\boldsymbol{x},t) - \frac{\Delta t}{\tau}\left(f_\mathrm{i}(\boldsymbol{x},t) - f_\mathrm{i}^\mathrm{eq}(\boldsymbol{x},t)\right) + S_\mathrm{i}(\boldsymbol{x},t) \quad , \tag{C.1}$$

where $f_\mathrm{i}(\boldsymbol{x},t)$ represents the density distribution function and $f_\mathrm{i}^\mathrm{eq}(\boldsymbol{x},t)$ the equilibrium distribution function, both related to discrete velocity direction i. The position vector in discretised space is given by $\boldsymbol{x}$, while $\boldsymbol{e}_\mathrm{i}$ represents the discrete velocity directions of the fluid. τ is the relaxation time and $S_\mathrm{i}(\boldsymbol{x},t)$ represents a possible source term, *e. g.*, for consideration of a body force, such as caused by gravity.

The essence of LBM is a discretisation of space in lattice points or nodes each of which represents a local computation cell for which the discrete Lattice Boltzmann equation is solved over a discretised time t with time steps Δt. Note that generally, $\Delta t = 1$ ts (time step) and τ represents a fraction of Δt, *e. g.*, $\tau = 1.0\ \Delta t$. Besides the lattice for spatial discretisation, the flow velocity of fluid in the computation domain is further

discretised by a so-called velocity model which is named depending on the model dimension N and number of velocity directions M according to the naming convention "$D_N Q_M$". For example, the frequently used 3D velocity model with 19 discrete flow directions (including the 0 flow direction) at each lattice node is labelled the D_3Q_{19}-model. Here, the index i = 0,...,18 represents 18 independent flow directions as shown in Figure C.1 and a 0 direction (zero vector).

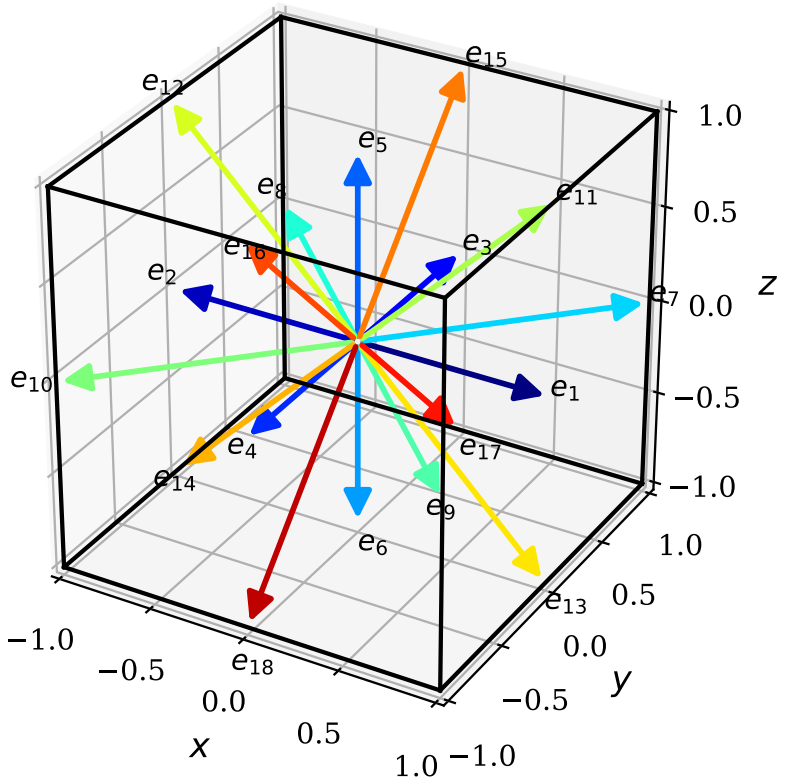


Figure C.1: The D_3Q_{19}-model with its discrete velocity directions highlighted in different colours inside its computation node or cell

The velocity vector $\boldsymbol{e}_i$ represents the i = 0,...,18 discrete velocities included in the D_3Q_{19}-model and is defined as follows.

$$[\boldsymbol{e}_0, \boldsymbol{e}_1, \boldsymbol{e}_2, \boldsymbol{e}_3, \boldsymbol{e}_4, \boldsymbol{e}_5, \boldsymbol{e}_6, \boldsymbol{e}_7, \boldsymbol{e}_8, \boldsymbol{e}_9, \boldsymbol{e}_{10}, \boldsymbol{e}_{11}, \boldsymbol{e}_{12}, \boldsymbol{e}_{13}, \boldsymbol{e}_{14}, \boldsymbol{e}_{15}, \boldsymbol{e}_{16}, \boldsymbol{e}_{17}, \boldsymbol{e}_{18}] \tag{C.2}$$
$$= c \begin{bmatrix} 0 & 1 & -1 & 0 & 0 & 0 & 0 & 1 & -1 & 1 & -1 & 1 & -1 & 1 & -1 & 0 & 0 & 0 & 0 \\ 0 & 0 & 0 & 1 & -1 & 0 & 0 & 1 & 1 & -1 & -1 & 0 & 0 & 0 & 0 & 1 & -1 & 1 & -1 \\ 0 & 0 & 0 & 0 & 0 & 1 & -1 & 0 & 0 & 0 & 0 & 1 & 1 & -1 & -1 & 1 & 1 & -1 & -1 \end{bmatrix}$$

Here, $c = \frac{\Delta x}{\Delta t} = \frac{1 \text{ lattice unit (lu)}}{1 \text{ time step (ts)}}$ is the lattice speed. 1 "lattice unit" (lu) represents the unit of spatial discretisation, while time is given in "time steps" (ts). Furthermore, mass is described in the LBM-specific "mass unit" (mu).

The flow of fluid density is discretised in different directions in which a distribution to neighbouring computation cells is possible. The density transfer between neighbouring cells is performed in a so-called *streaming* step which is repeated in the computation scheme together with the *collision* step as represented by the Bhatnagar-Gross-Krook (BGK)-operator (Bhatnagar *et al.*, 1954) included in Equation C.1. The streaming step of the different vector components of the density distribution from one lattice computation cell to the neighbouring cells in the x-y-plane in between two time steps is illustrated in Figure C.2. The exemplary plot shows the streaming of the components of f from a central lattice node to the neighbouring nodes following the discrete directions of the corresponding velocity directions of vector $\boldsymbol{e}$ from time step t_0 to time step $t_0 + \Delta t$. Using the D_3Q_{19}-model, the streaming step is calculated in 3D for all velocity directions and for all computation cells in the model, *i. e.*, all cells exchange "density flow" or momentum with their neighbours.

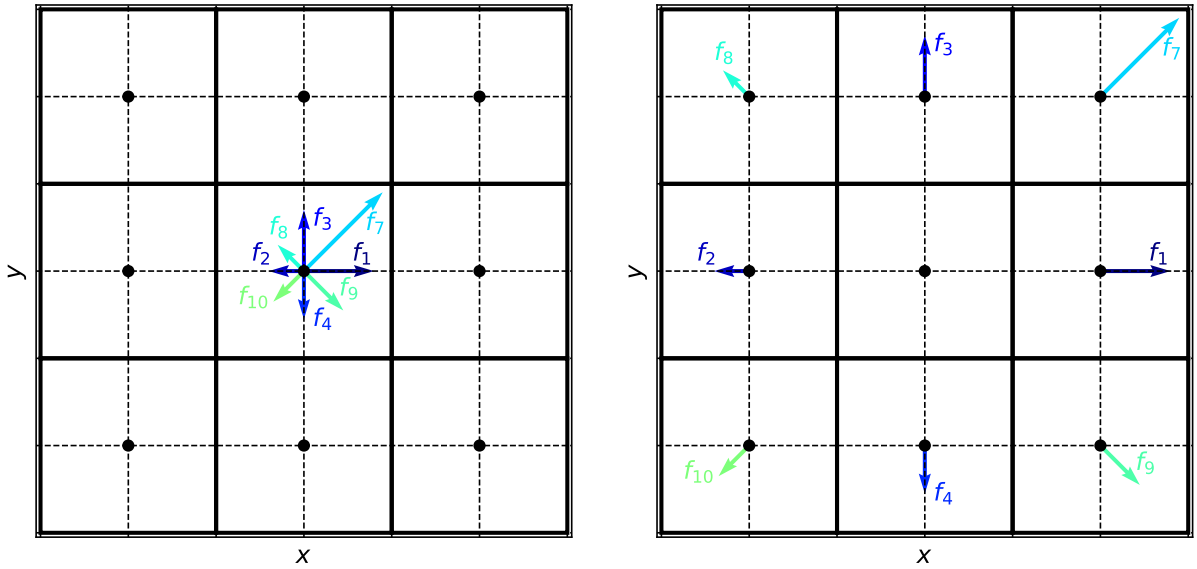


Figure C.2: Exemplary streaming step in between two time steps illustrating the exchange of discrete density distribution components from a central lattice node to its surrounding neighbours (the example is based on the 3D D_3Q_{19}-model as shown in Figure C.1, but shown in the x-y-plane for simplicity)

In the collision step, the density distribution is relaxed towards the equilibrium distribution function using a single relaxation parameter, the relaxation time τ, which is related to the macroscopic kinematic fluid viscosity ν according to

$$\nu = c_s^2 \left(\tau - 0.5\,\Delta t\right) \quad , \tag{C.3}$$

where c_s is the speed of sound. In the case of the D_3Q_{19}-model, the speed of sound c_s is defined as

$$c_s^2 = \frac{c^2}{3} \quad . \tag{C.4}$$

The terms *streaming* and *collision* originate from the gas dynamics background of LBM according to which the streaming and collision of density can also be considered from a particulate point of view with particles or gas molecules moving in between nodes or cells and exchanging momentum during collisions.

The equilibrium density distribution function $f_{\mathrm{i}}^{\mathrm{eq}}(\boldsymbol{x},t)$ is given by Equation C.5 (Luo, 1998).

$$f_{\mathrm{i}}^{\mathrm{eq}}(\boldsymbol{x},t) = \omega_{\mathrm{i}}\,\rho\left(1+\frac{\boldsymbol{e}_{\mathrm{i}}\cdot\boldsymbol{v}}{c_{\mathrm{s}}^2}+\frac{(\boldsymbol{e}_{\mathrm{i}}\cdot\boldsymbol{v})^2}{2c_{\mathrm{s}}^4}-\frac{\boldsymbol{v}^2}{2c_{\mathrm{s}}^2}\right) \quad , \tag{C.5}$$

with the weights ω_{i}. ρ is the macroscopic fluid density present in a computation node or cell, while $\boldsymbol{v}$ indicates the macroscopic fluid velocity vector. For the $\mathrm{D_3Q_{19}}$-model, the weights ω_{i} are defined as

$$\omega_{\mathrm{i}} = \begin{cases} \frac{1}{3} & \text{for i = 0} \\ \frac{1}{18} & \text{for i = 1,...,6} \\ \frac{1}{36} & \text{for i = 7,...,18.} \end{cases} \tag{C.6}$$

The macroscopic density of the fluid in every computation cell is represented by ρ according to

$$\rho = \sum_{\mathrm{i}} f_{\mathrm{i}} \quad , \tag{C.7}$$

revealing it as the sum of all discrete components of the density distribution function.

If the source term $S_{\mathrm{i}}(\boldsymbol{x},t)$ equals to zero, the macroscopic fluid velocity vector $\boldsymbol{v}$ is calculated as

$$\boldsymbol{v} = \frac{1}{\rho}\sum_{\mathrm{i}} f_{\mathrm{i}}\boldsymbol{e}_{\mathrm{i}} \quad . \tag{C.8}$$

C.2 Extension to single-component multiphase LBM

For the multiphase flow, further enhancements of the single-phase LBM formulation presented so far are required. Here, the single-component multiphase Shan-Chen LBM formulation is applied. This formulation is based on the work by Shan and Chen (1993) who have included an attractive or repulsive force between the imaginary particles which form the flow between cells. With the help of this force term, phase separation due to non-ideal gas behaviour of a single chemical component as described by a non-ideal non-monotonic equation of state (EOS) can be modelled (Huang *et al.*, 2015). Although surface tension and the ratio of densities and viscosities of coexisting fluids cannot be adjusted independently, the formulation allows to model evaporation, condensation, and cavitation. Unlike other multi-component multiphase LBM models, the single-component version only uses a single distribution function for a single component that can show gas (vapour) or liquid physical behaviour depending on its pressure and density state as described by the applied EOS. This explains the origin of the name "single-component multiphase formulation". It originates from the fact that phase separation allows multiphase behaviour of a single-component which can coexist in different density states, *e. g.*, as gas and liquid.

In the original model based on the work by Shan and Chen (1993), the attractive force between the "fluid particles" in a computation cell and its nearest neighbour cells $\boldsymbol{F}_{\text{int}}$ is computed according to

$$\boldsymbol{F}_{\text{int}}(\boldsymbol{x},t) = -G\psi(\boldsymbol{x},t)\sum_{\text{i}}\omega_{\text{i}}\psi(\boldsymbol{x}+\boldsymbol{e}_{\text{i}}\Delta t,t)\boldsymbol{e}_{\text{i}}\Delta t \quad , \tag{C.9}$$

where G is a control parameter for the strength of the inter-particle force and ψ is a mean-field potential. Note that this interaction force is a force per volume and that frequently the Δt is omitted.

The EOS, which relates the fluid pressure p to density ρ, used in the classical Shan-Chen model is given as

$$p = c_{\text{s}}^2\rho + \frac{c_{\text{s}}^2\Delta t^2 G}{2}\psi^2(\rho) \quad , \tag{C.10}$$

with ψ originally being an exponential function of ρ further described in Huang *et al.* (2015). In order to implement other EOS, such as the Carnahan-Starling EOS (which is used in this thesis), in the multiphase LBM model, following Huang *et al.* (2015), Equation C.10 is reordered to obtain

$$\psi = \sqrt{\frac{2(p-c_{\text{s}}^2\rho)}{c_{\text{s}}^2\Delta t^2 G}} \quad . \tag{C.11}$$

The Carnahan-Starling EOS (Carnahan and Starling, 1969) relates the pressure of a fluid modelled as hard spheres to its density for a given temperature and is represented by

$$p = \rho\, R\, T\frac{1+\frac{b\rho}{4}+(\frac{b\rho}{4})^2-(\frac{b\rho}{4})^3}{(1-\frac{b\rho}{4})^3} - a\,\rho^2 \tag{C.12}$$

according to Huang *et al.* (2015).

Here, $a = 1\ \frac{\text{lu}^5}{(\text{mu ts}^2)}$, $b = 4\ \frac{\text{lu}^3}{\text{mu}}$, and $R = 1\ \frac{\text{lu}^2}{(\text{ts}^2\ \text{tu})}$ with tu being "temperature units". T is the fluid temperature and R is the gas constant. At temperatures T below the critical temperature $T_{\text{c}} = 0.0943$ tu, the fluid shows subcritical gas behaviour with two coexisting densities being present in the form of gas and liquid. The Carnahan-Starling EOS at $T/T_{\text{c}} = 0.7$ as used for the simulations in this thesis is plotted in Figure C.3.

The different present fluid phases are identified as gas if $\rho < \rho_{\text{boundary, g}} = 0.0484$ mu/lu^3 and as liquid if $\rho > \rho_{\text{boundary, l}} = 0.2726$ mu/lu^3. The intermediate densities represent a transition zone.

In the present LBM formulation, the Carnahan-Starling EOS is considered by plugging p from Equation C.12 into Equation C.11 to compute ψ for the force calculation.

In order to model contact angles which are important for different wetting boundary conditions at the contact of fluid and solid phase, a "wall density" ρ_{wall} was introduced by Benzi *et al.* (2006). Instead of using Equation C.9 which is applied in between fluid nodes, the equation

$$\boldsymbol{F}_{\text{ads}}(\boldsymbol{x},t) = -G\psi(\rho(\boldsymbol{x},t))\sum_{\text{a}}\omega_{\text{a}}\psi(\rho_{\text{wall}})s(\boldsymbol{x}+\boldsymbol{e}_{\text{a}}\Delta t,t)\boldsymbol{e}_{\text{a}}\Delta t \tag{C.13}$$

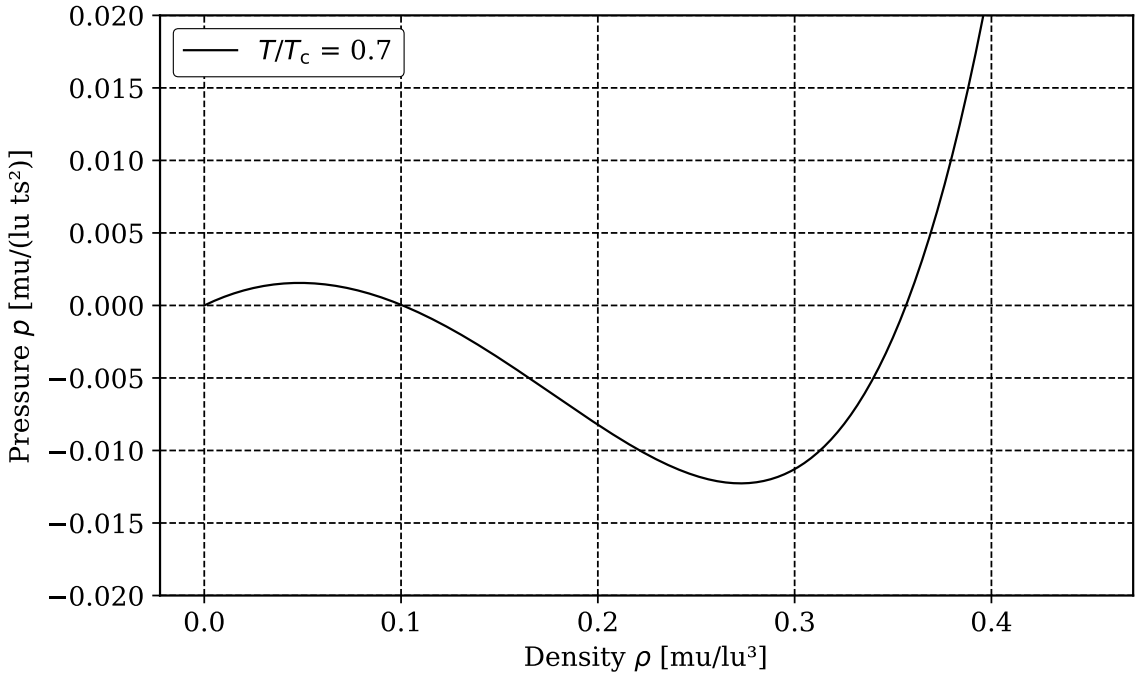


Figure C.3: Carnahan-Starling EOS at $T/T_c = 0.7$ as applied in the multiphase LBM simulations in Chapter 8

is applied to compute the adhesive force $\boldsymbol{F}_{\text{ads}}$ acting between a liquid and a contacting solid node. In this equation, the contact angle can be tuned with ρ_{wall}. $s(\boldsymbol{x} + \boldsymbol{e}_a \Delta t, t)$ represents a switch function yielding 1 if the node in neighbouring "index a-direction" is a solid to interact with or 0 if the node in this direction is liquid thus canceling the adhesion force term.

Boundary conditions used in the LBM implementation are the "bounce back" condition where the flow directions into solid nodes are reflected back into the opposite directions in the collision step as well as periodic boundary conditions at the model boundaries where flow and force components are copied to the corresponding other sides of the model.

As initial condition, typically, a random field of fluid densities with prescribed perturbation is initialised leading to phase separation until equilibrium is reached. Flow boundary conditions prescribing a fluid flow through the borders of the computation domain can be realised as described by Huang *et al.* (2015). However, in the simulations of water retention behaviour presented in this work, a simple "density injection" approach as proposed by Hosseini *et al.* (2021) is applied in which the fluid density is increased or decreased in liquid cells to mimic temporal changes of degree of saturation.

C.3 Implementation of the single-component multiphase LBM

The implementation of the LBM code in C++ used in Chapter 8 follows the LBM model and Fortran code for the simulation of a sessile droplet contacting a wall as published in Huang *et al.* (2015). In order to simulate the water retention behaviour based on CT data as described in Chapter 8, different routines for importing the model geometry from binarised CT data only containing the porous medium, for density injection, and for output of numerical results have been added. Furthermore, the C++ code has been enriched with thread-based parallelisation using OpenMP which enables a faster performance on multi-threaded systems with multiple cores, *e. g.*, by parallelised loops.

The geometry of the porous medium is transferred to a text file by a Python script which reads a binary 3D TIFF image file of the porous medium from CT data containing the integers 0 for a pore node and 1 for a solid node. This geometry text file is then read by the main C++ program. During a simulation, temporal results are written as text files. A results file for temporal data contains the averaged fluid pressures, capillary pressure, the number of gas and liquid nodes as well as degree of saturation in the simulation domain *vs.* simulation time. Furthermore, the densities, the actual velocities and pressures in every node are written to text file for visualisation of spatial results for selected time increments. The spatial results file can be converted to a file for visualisation, *e. g.*, using the open-source *ParaView* software (Ahrens *et al.*, 2005) with every computation node being visualised as a voxel.

The general structure of the C++ code to run a simulation of the water retention behaviour in a virtual porous medium is outlined as follows:

1) Read simulation parameters from a text file
2) Read the geometry of the porous medium from a text file
3) Initialise the density distribution as a random field
4) Run the main calculation loop in time increments repeating the following steps until a maximum time increment is reached:
    - 4a) Write output based on selected time criteria
    - 4b) Call the streaming algorithm
    - 4c) Compute the macroscopic variables
    - 4d) Compute the actual velocities
    - 4e) Compute the interaction forces between fluid nodes and solid and fluid nodes
    - 4f) Call the collision algorithm
    - 4g) Increase or decrease density for selected time increments by density injection.

As a test of the parallelisation of the C++ code, a speedup study is run based on phase separation on a lattice grid with $200 \times 200 \times 200$ lattice nodes representing a porous medium. The Hamburg Sand geometry model from Section 8.2.2 has been used as input in all speedup simulations which are run on the TUHH HPC-cluster. The results of the study are summarised in Figure C.4 showing a satisfactory speedup in the limits of the selected number of threads and for the chosen model size. The speedup using the version of the code applied in Chapter 8 is shown. The runtime also depends on the interval in which field output data is written to disk. This write operation is currently not implemented in parallel. In order to achieve an even better performance, the LBM code could be adapted for GPU computing in future projects using graphics processing units (GPUs) and their high parallelisation performance as described and evaluated by Krüger *et al.* (2017).

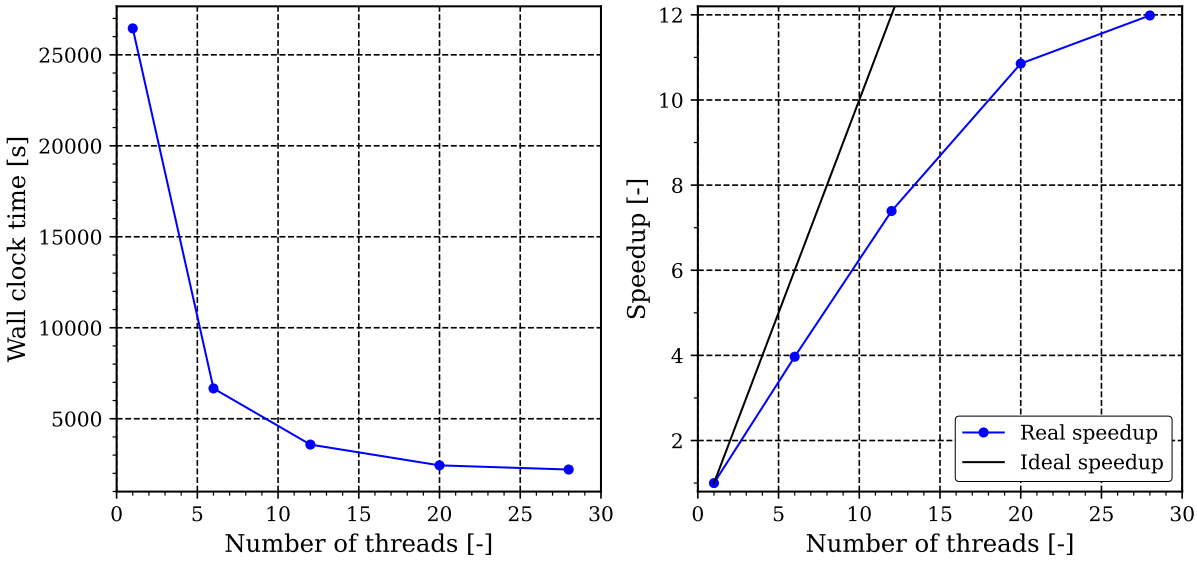


Figure C.4: Dependence of wall clock time and speedup on the used number of threads found in comparative simulations of 1000 ts during the phase separation step on a grid with $200 \times 200 \times 200$ lattice nodes inside a porous medium. Please note that the computations have been partly assigned to different machines on the HPC-cluster leading to slightly different hardware resources

Appendix D

Research data

Research data from investigations presented in this thesis are documented and stored in the research data repository *TUHH Open Research* (TORE) where they can be downloaded.

Research data	Reference and link to repository
Uniaxial compression tests from Milatz *et al.* (2021b): CT data, macroscopic data and results	Milatz *et al.* (2021a): `https://tore.tuhh.de/handle/11420/8791`
Water retention experiment from Milatz *et al.* (2022b): CT data, macroscopic data and results	Milatz *et al.* (2022a): `https://tore.tuhh.de/handle/11420/12296`
LBM simulation of the WRC from Chapter 8: C++ code, example files, results	Milatz (2022): `https://tore.tuhh.de/handle/11420/12806`